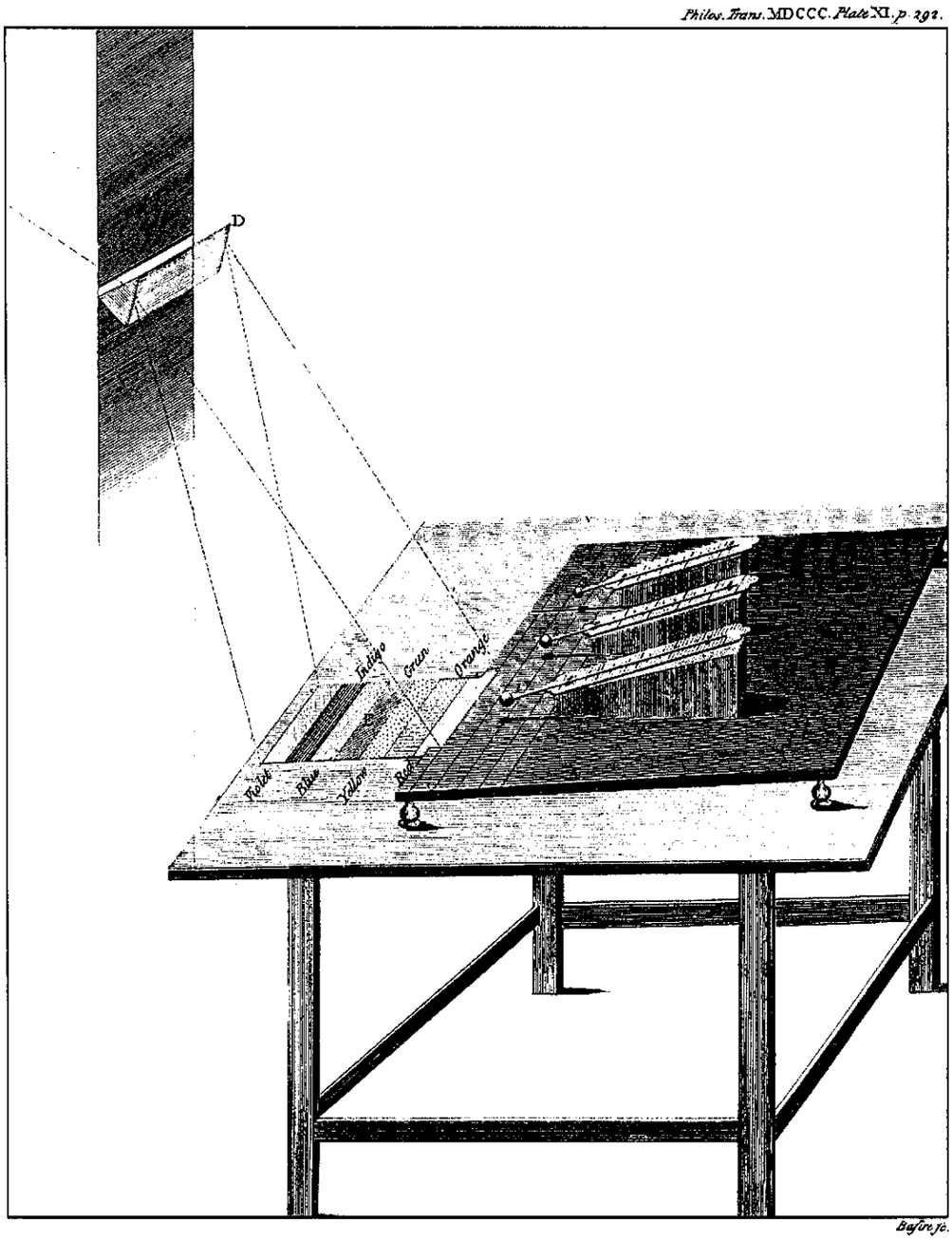

Basire sc.

This thesis was typeset with LaTeX using a modified version of the the University of California PhD dissertation class file, `ucthesis.cls`. Unless otherwise noted, all figures in this thesis were created by the author using IDL® or CorelDraw®.

The image on the cover is Plate XI from "Experiments on the Refrangibility of the Invisible Rays of the Sun," by Sir William Herschel, published in *Philosophical Transactions of the Royal Society of London*, Volume 90 (1800). Plate XI shows the apparatus Herschel used to discover infrared radiation. (Image © the Royal Society.)

SHIFTS: SIMULATOR FOR THE HERSCHEL IMAGING FOURIER TRANSFORM SPECTROMETER

JOHN VYVYAN LINDNER

Bachelor of Science, Physics and Astronomy, University of Victoria (2003)

A thesis submitted to the School
of Graduate Studies of the University
of Lethbridge in partial fulfilment
of the requirements of the degree

MASTER OF SCIENCE

Department of Physics
University of Lethbridge
Lethbridge, Alberta, Canada

To my family

Abstract

The Spectral and Photometric Imaging Receiver (SPIRE) is one of three scientific instruments on the European Space Agency's (ESA's) Herschel Space Observatory (HSO). The medium resolution spectroscopic capabilities of SPIRE are provided by an imaging Fourier transform spectrometer (IFTS). A software simulator of the SPIRE IFTS was written to generate realistic data products, making use of available qualification and test data. We present the design and implementation of the simulator. Component and end-to-end simulations were compared to results from the first SPIRE instrument proto-flight model (PFM1) test campaign conducted at the Rutherford Appleton Laboratory (RAL) in Oxford, England in 2005. Final characterization of the simulator involved the determination of astronomical quantities from the synthetic data products of a simple molecular cloud.

Acknowledgements

First and foremost, I want to thank my supervisor, Professor David Naylor, for giving me this tremendous opportunity. It is impossible to overstate how much I have valued his knowledge, expertise and enthusiasm these past three years. Even with his perennially busy schedule, David always gave me his full attention once he entered the office. I am grateful for his frankness and honesty, as well as his careful editing of my thesis in the final months of this project.

David always said that it takes a family to raise a grad student. So naturally, I am indebted to the Astronomical Instrumentation Group (AIG) at the University of Lethbridge for their help during my studies. The advice and direction I received from Peter Davis, the SPIRE project manager, was instrumental in the design, development and characterization of SHIFTS. Thanks also go to Trevor Fulton, whose tireless efforts with the SPIRE software were a huge help these past few months. I am particularly grateful to Ian Schofield who salvaged my code when the AIG computer server crashed *one week* before I had to submit. In addition, I wish to thank Dr Robin Phillips for his insights into LaTeX and the Einstein A coefficients, and Brad Gom for helping me optimize the SHIFTS code. The development of SHIFTS was also aided by the efforts of Karim Ali, Ian Chapman, Kris Dyke, Andres Rebolledo and Troy Ronda. Finally, thank you to my office mates – Samuel Ronayette, Locke Spencer and Margaret Tahic – for the instructive discussions (both physics and non-physics related) and for providing a enjoyable working atmosphere. Double thanks to Locke for his helpful comments on the final draft of my thesis.

In addition to the AIG at the University of Lethbridge, my work was supported by members of the international SPIRE consortium. Thank you to Dr Bruce Swinyard – my surrogate supervisor during my six months in England – who helped get the first full version of SHIFTS running. In addition, I want to acknowledge members of the SPIRE team at the Rutherford Appleton

Laboratory (RAL; Oxfordshire, England) for their support during my stay: Asier & Mercedes Aramburu, Dr Mark Ferlet, Dr Douglas Griffin, Dr Steve Guest, Dr Ken King, Dr Tanya Lim, Judy Long, Dr Dave Smith and Dr Sunil Sidher. I greatly benefited from numerous discussions with Bruce Sibthorpe (Cardiff University, Cardiff, Wales) about the photometer simulator; many of his ideas found their way into SHIFTS. I am grateful to Professor Peter Ade and Dr Peter Hargrave (both at Cardiff University), who provided documentation and test data on the beamsplitters, CBB, filters and SCAL. For helpful discussions and responses to queries about SMEC and the warm electronics, I want to acknowledge Drs Jean-Paul Baluteau (LAM, Marseille, France), Christophe Cara (CEA Service d'Astrophysique, Saclay, France), Didier Ferrand (LAM) and Frederic Pinsard (CEA). I would also like to thank Dr James Bock (JPL/CalTech, Pasadena, California), Dr Kjetil Dohlen (LAM), Dr Douglas Griffin (RAL), Dr Tanya Lim (RAL), Dr Dominique Pouliquen (LAM) and Brooks Rownd (SAO, Hilo, Hawaii) for providing the photographs and schematics seen in Chapters 3 and 6.

One final member of the SPIRE consortium I want to thank is Professor Jason Glenn (University of Colorado, Boulder, CO), who acted as the external examiner for my thesis defense. In addition to the useful comments and corrections Professor Glenn provided on my thesis, his insight into the operation of the SPIRE detector arrays in the fall of 2005 was very much appreciated. Thank you also to Professors René Boeré and Steve Patitsas, the other half of the Thesis Examination Committee; their experience and guidance were immensely valuable. I am grateful to the entire Supervisory Committee – Professors Boeré, Naylor and Patitsas – for their patience when I (twice) extended my submission deadline.

I also want to thank Professor Doug Johnstone (University of Victoria, Victoria, BC) and Dr Paul Feldman (HIA/DAO, Victoria, BC) for arranging my original interview with David back in 2003. It just goes to show what a simple inquiry and the loan of some comic books can lead to.

Several other individuals also deserve recognition. The discussion of the units of the dipole moment in Appendix C was partially based on correspondence with Drs Laurence Rothman and Marie Šimečková (both at the Harvard-Smithsonian Center for Astrophysics, Cambridge, MA). Permission to reproduce the HST mosaic of the Orion Nebula seen in Chapter 1 was kindly provided by Professor C. R. O'Dell (Vanderbilt University, Nashville, Tennessee). A big thank you to Christine Woollett from the Royal Society in London who secured permission for me to include a plate from a paper by Sir William Herschel as my cover page.

I want to express my gratitude to the 2004/2005 editorial board of the Canadian Undergraduate Physics Journal (CUPJ), especially Iva Cheung. Although volunteering with CUPJ delayed my own research, the experience improved my understanding of the purpose and practice of scientific writing.

Last but certainly not least, I wish to thank my family and friends. The unwavering support and encouragement of my mother and father were anchors during the stormy periods of this work. From first-year physics through today, my big brother's advice and intellect helped me navigate my years of post-secondary education. Thanks to all three of them (particularly Tom) for their comments on the various incarnations of my thesis. My thanks to my friends (in Alberta, BC and Ontario) for their support and for not minding that I've missed everyone's birthday for the past year. Special thanks to Erin Clarke, Saikat Basu, Nicholas Hanson, Margo Killham, Rod Leland, Dr David Logue, Richard Querel, Mark Tipper, Stephen Tipper, and Preston Williams for providing shoulders to lean on in recent months. I am also grateful to Rod for adding a professional polish to the digital images supplied by other authors.

The work covered in this thesis was funded by the School of Graduate Studies and the Office of Research Services (both at the University of Lethbridge), the Canadian Institute for Photonics

Innovations (CIPI), the Canadian Space Agency (CSA) and the National Science and Engineering Research Council (NSERC). I also want to acknowledge the various bursaries and grants received from BMAD during the course of my studies.

-JVL, March 2006

Table of Contents

List of Figures

List of Tables

List of Abbreviations

AC	alternating current
ADC	analog-to-digital converter
ADU	analog-to-digital unit
AIG	Astronomical Instrumentation Group
APE	absolute pointing error
AU	arbitrary units
BDA	bolometer detector assembly
BIPM	Bureau International des Poids et Mesures*
BMAD	Bank of Mom and Dad
BSM	beam steering mirror
CBB	cryogenic blackbody
CGS	centimetre-gram-second
CEA	Commissariat à l'Energie Atomique
CIPI	Canadian Institute for Photonics Innovations
CO	carbon monoxide
CQM	cryogenic qualification model
CSA	Canadian Space Agency
CSL	Centre Spatial de Liège (Liège, Belgium)
CUPJ	Canadian Undergraduate Physics Journal
DAO	Dominion Astrophysical Observatory (Victoria, British Columbia)
DC	direct current
DFT	discrete Fourier transform
DPU	digital processing unit
DQE	detective quantum efficiency
EADS	European Aeronautic Defense and Space
ESA	European Space Agency
FFT	fast Fourier transform
FIR	far-infrared

*International Office of Weights and Measures

FOV	field-of-view
FPU	focal plane unit
FTS	Fourier transform spectroscopy
FWHM	full-width at half-maximum
GEISA	Gestion et Etude des Informations Spectroscopiques Atmosphériques[†]
GSFC	Goddard Space Flight Center (Greenbelt, Maryland)
GUI	graphical user interface
HDPE	high density polyethylene
HIA	Herzberg Institute of Astrophysics (Victoria, British Columbia)
HIFI	Heterodyne Instrument for the Far Infrared
HITRAN	High-resolution Transmission Molecular Absorption Database
HSO	Herschel Space Observatory
HST	Hubble Space Telescope
IDL	Interactive Data Language
IFTS	imaging Fourier transform spectrometer
ILS	instrumental line shape
IR	infrared
IRAS	Infrared Astronomical Satellite
IRF	impulse response function
ISO	Infrared Space Observatory
ISM	interstellar medium
JAXA	Japan Aeronautical Exploration Agency
JCMT	James Clark Maxwell Telescope (Mauna Kea, Hawaii)
JFET	junction field effect transistor
JPL	Jet Propulsion Laboratory (California Institute of Technology, Pasadena, California)
L2	second Lagrangian point
LAM	Laboratoire d'Astrophysique de Marseille (Marseille, France)
LIA	lock-in amplifier
LOS	line of sight
MCP	master control program
MIR	mid-infrared
MKS	metre-kilogram-second
MPD	mechanical path difference
MZ	Mach-Zehnder
N/A	not available
NASA	National Aeronautics and Space Administration

[†]Management and Study of Atmospheric Spectroscopic Information

NEP	noise-equivalent power
NIR	near-infrared
NSERC	National Science and Engineering Research Council
NTD	neutron-transmutation doped
OPD	optical path difference
PACS	Photodetector Array Camera and Spectrometer
PCF	phase correction function
PFM	proto-flight model
PID	proportional-integral-derivative
RAL	Rutherford Appleton Laboratory (Oxfordshire, England)
RAM	random-access memory
RC	resistor-capacitor
RMS	root-mean-square
RPE	relative pointing error
SAO	Smithsonian Astrophysical Observatory (Mauna Kea, Hawaii)
SAS	simulated astronomical source
SCAL	spectrometer calibrator
SCUBA	submillimeter common-user bolometer array
SHIFTS	Simulator for the Herschel Imaging Fourier Transform Spectrometer
SI	Système international
SiC	silicon carbide
Si_3N_4	silicon nitride
SMEC	spectrometer mechanism
SPICA	Space Infrared Telescope for Cosmology and Astrophysics
SPIRE	Spectral and Photometric Imaging Receiver
SST	Spitzer Space Telescope
TE	transverse electric
TM	transverse magnetic
UV	ultraviolet
YSO	young stellar object
ZPD	zero path difference

Notes on Format

This thesis employs the following style conventions:

References External references to works by other authors are denoted by parenthetic citation (e.g., [2-4,9] refers to references 2, 3, 4, and 9). Internal references to different sections of the text are denoted by $x.y.z$ (or $x - y$ in the appendices), where x is the chapter (or appendix), y is the section, and z is the subsection. Figure, table, and equation numbers are denoted by $a.b$ (or $a - b$ in the appendices), where a is the chapter (or appendix) and b is the order in the chapter (or appendix) where the figure, table or equation appears.

Equations Units are included in square brackets after every numbered equation (e.g., [cm s^{-1}] indicates an equation is in units of centimetres per second). If the units of a numbered equation are not given, the equation is unitless. Parenthetic and subscript notation are both employed to denote a functional dependence (e.g., $\phi(\sigma)$ and ϕ_σ both indicate that ϕ is a function of σ); context determines the notation used.

Text Several non-regular fonts are used in this thesis: the *italic* font is employed to emphasize key terms or concepts and to denote an internet web address; the SMALL CAPS font is employed to note the names of IDL routines or SHIFTS modules; and the `courier` font is employed to note the names of electronic files such as LaTeX `.cls` or IDL `.sav` files. Footnotes are employed to list an internet web address or to note the English translation of a non-English title or phrase.

Chapter 1

Introduction

> *"What was observed by us in the third place is the nature or matter of the Milky Way itself, which, with the aid of the splyglass, may be observed so well that all the disputes that for so many generations have vexed philosophers are destroyed by visible certainty, and we are liberated from wordy arguments. For the Galaxy is nothing else than a congeries of innumerable stars distributed in clusters. To whatever region of it you direct your spyglass, an immense number of stars immediately offer themselves to view, of which very many appear rather large and very conspicuous but the multitude of small ones is truly unfathomable."*
>
> - Galileo Galilei, *The Sidereal Messenger*, University of Chicago Press (1989, originally published as "Sidereus Nuncius" in 1610)

On a clear night in Lethbridge, the narrow band of the galactic plane runs from horizon to horizon, inclined with respect to the zenith. The ancient Greeks believed the band was a stream of milk, a gift from the gods [1]. According to the oral tradition of the Blackfoot tribe of southern Alberta, the band is the trail that Wolf takes to and from the spirit world [2]. Based on observations with the first telescope in 1610, Galileo Galilei suggested the band was composed of thousands of stars. However, Galileo was unable to determine why these stars were arranged in a band or the mechanism by which they were created [3]. While our understanding of galaxy and star formation has improved over the past 400 years, a complete answer to these two questions continues to elude astronomers.

Enter the Herschel Space Observatory (HSO). A cornerstone mission of the European Space Agency (ESA), the HSO will observe the electromagnetic spectrum between 60 and 670 μm (1 μm = 10^{-6} m) [4]. Scheduled for launch in 2008, the scientific payload of the HSO consists of three onboard instruments: the Heterodyne Instrument for the Far Infrared (HIFI), the Photodetector Array Camera and Spectrometer (PACS), and the Spectral and Photometric Imaging Receiver (SPIRE) [4–7].

The primary scientific goals of the SPIRE instrument are characterizing the spectral energy distributions of redshifted galaxies and studying interstellar gas and dust before and during star formation [5]. To accomplish these goals, SPIRE contains two sub-instruments: an imaging photometer and an imaging Fourier transform spectrometer (IFTS) [5]. This thesis describes the design, implementation and integration of a software simulator of the SPIRE IFTS written to generate realistic Herschel data products based on existing subsystem qualification data [5, 8]. Chapter 1 outlines the science case for the SPIRE spectrometer, describes the Herschel telescope and the motivation for the SPIRE spectrometer simulator, and provides an overview of this thesis.

1.1 The science case for the SPIRE spectrometer

The design of the SPIRE spectrometer (described in Chapter 3) is well-suited to address two poorly understood areas of modern astronomy: the evolution of the chemical, dynamic and physical properties of the interstellar medium (ISM) and the processes involved in early star formation [5,9]. To demonstrate the scientific motivation for the spectrometer, this section briefly outlines the history and current status of theories describing the ISM and star formation.

Almost 200 years after Galileo, Sir William Herschel conducted an extensive survey of nebulae [10]. Figure 1.1 shows the Orion Nebula, a nearby (430 parsecs; see Appendix A) and well-

studied example of a nebula [11,12]. From his observations of Orion and other nebulae, Herschel suggested these clouds of gas and dust were the locations where stars are born [10, 13]. (The other major contribution Herschel made to astronomy was the discovery of infrared (IR) radiation using spectroscopic observations of the Sun; see cover page [14].)

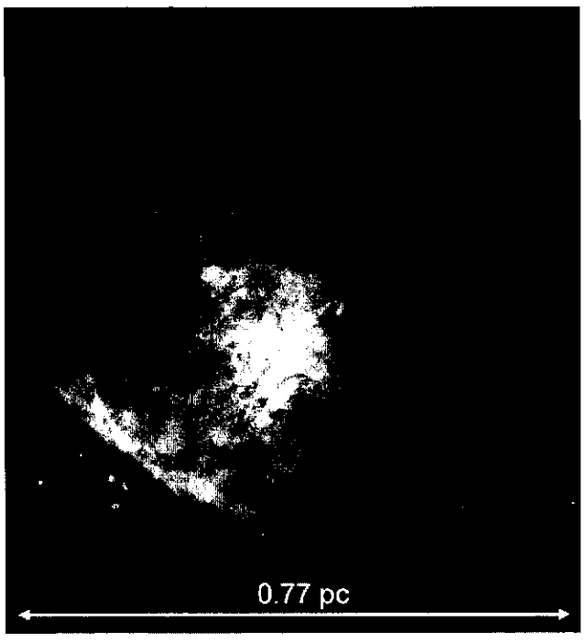

Figure 1.1: Mosaic image of the Orion Nebula constructed from fifteen Hubble Space Telescope pictures. (Figure courtesy of Dr C. Robert O'Dell, Vanderbilt University, Nashville, Tennessee.)

By the mid-1980s, the astronomical community had reached a consensus on the basic life cycle of stars [15–17]. In general, a proto-stellar core forms from the fragmentation and collapse of molecular clouds such as the Orion Nebula [16, 18]. The proto-stellar core accretes material from the surrounding envelope of gas and dust to form a young stellar object (YSO), which eventually develops into a main-sequence star [16]. At the end of their lives, stars eject most of their constituent matter back into the ISM [9, 15]. First observed by Robert Trumpler in 1930, the ISM is composed of highly diffuse dust and gas and is responsible for stellar extinction [12, 18–21].

The mechanisms associated with stellar extinction also occur during the fragmentation stage of star formation [17]. The ultraviolet (UV) and visible photons emitted by the proto-stellar core are absorbed and scattered by the dust and gas in molecular clouds [16, 22]. As such, the earliest stages of star formation are obscured from the view of optical and UV telescopes. The dust

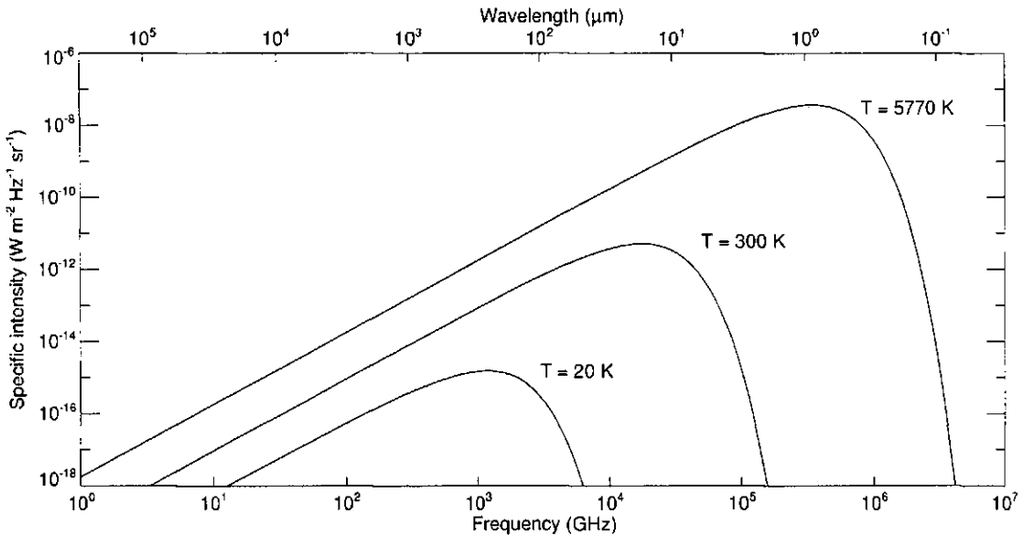

Figure 1.2: Comparison of the emission of different blackbodies (where 1 GHz = 10^9 Hz). Blackbody spectra are shown for three perfect emitters at three different temperatures: an interstellar dust grain at 20 K, a human body at 300 K and the effective surface temperature of the Sun at 5770 K [15].

re-radiates the absorbed energy as a blackbody, whose emission is governed by the Planck equation,

$$B_\nu(T) = \varepsilon_\nu \frac{2h\nu^3}{c^2} \frac{1}{e^{\frac{h\nu}{kT}} - 1}, \qquad [\mathrm{W\,m^{-2}\,Hz^{-1}\,sr^{-1}}] \tag{1.1}$$

where ν is the frequency (in hertz, or Hz), ε_ν is the emissivity as a function of frequency (unitless), T is the temperature (in kelvin, or K), c is the speed of light, h is the Planck constant and k is the Boltzmann constant (see Table A-1) [23, 24]. Figure 1.2 shows the blackbody emission for three different temperatures [15].

The dust grains in molecular clouds and the ISM are cold with temperatures between 10 and 100 K [9, 25]. Therefore, most of their radiation is emitted in the far-infrared (FIR) and submillimetre region between 100 and 1000 μm (see Figure 1.2) [9, 17]. Coincidentally, the gases found in molecular clouds and the ISM (e.g., carbon monoxide, hydrogen cyanide and sulphur dioxide) also have hundreds of emission lines in the FIR and submillimetre region [9, 26, 27].

The exploration and characterization of gas and cold dust has in part driven the develop-

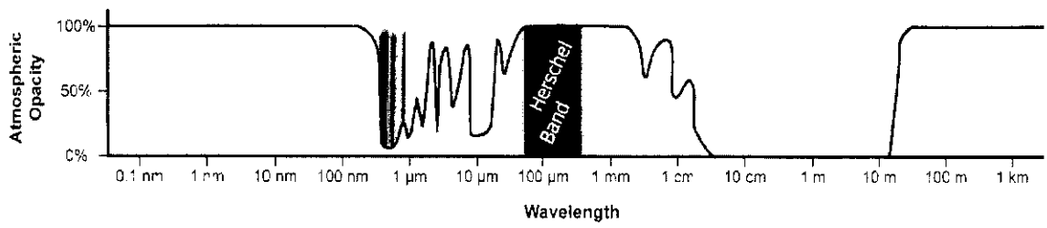

Figure 1.3: Opacity of the atmosphere of the Earth. The rainbow represents the visible spectrum and the solid red band represents the region observed by the Herschel telescope. (Original figure courtesy of Jet Propulsion Laboratory, California Institute of Technology, Pasadena, California.)

ment of infrared instrumentation over the past 20 years [9, 17, 28, 29]. One of the most successful ground-based instruments is the Submillimetre Common User Bolometer Array (SCUBA) mounted on the James Clerk Maxwell Telescope (JCMT) in Mauna Kea, Hawaii [30, 31]. Recent observations in the SCUBA 850 μm band discovered cold (10 – 30 K) proto-stellar cores in the Lynds and ρ Ophiuchi molecular clouds. While these results are encouraging, the measurements only covered a narrow band of radiation [32–34]. Ground-based observations of the entire FIR and submillimetre band are currently impossible because the radiation is absorbed by molecules (mostly water vapour) in the atmosphere of the Earth (see Figure 1.3) [7, 9, 30].

The limited atmospheric transparency in the infrared lead to the 1983 launch of the joint American-British-Dutch Infrared Astronomical Satellite (IRAS) [22, 29]. Among its many accomplishments, IRAS provided the first observational evidence of disks of gas and dust around YSOs [22]. Successors to IRAS include the ESA Infrared Space Observatory (ISO) in 1995, and the National Aeronautics and Space Administration (NASA) Spitzer Space Telescope (SST) in 2003 [29, 35]. The three instruments on Spitzer are currently observing near-infrared (NIR) and mid-infrared (MIR) radiation between 3 and 180 μm [35]. In February 2006, the Japan Aerospace Exploration Agency (JAXA) ASTRO-F satellite joined the SST in orbit with two of its own NIR and MIR cameras [36, 37].

While ASTRO-F and the SST offer unbiased wideband surveys, their cameras cannot observe beyond 200 μm [35, 36]. In order to fully characterize the spectral energy distributions of cold dust, the longer wavelengths observed with SPIRE are essential [9].

1.2 The Herschel Space Observatory and the SPIRE consortium

The Herschel Space Observatory (shown in Figure 1.4) is the ESA follow-up mission to ISO [38]. It will be the first space telescope to observe the FIR and submillimetre region of the electromagnetic spectrum [4, 38]. With a 3.5 m passively cooled primary mirror, cryogenically cooled instrument payload and no atmospheric contributions, Herschel will provide unparallelled sensitivity at these wavelengths. The HSO will orbit at the second Lagrangian point (L2), a stable gravitational well in the Earth-Sun system, with an estimated observing lifetime of three years [4,39].

As indicated at the beginning of the chapter, Herschel contains three instruments: HIFI, PACS and SPIRE [4]. HIFI is a high resolution spectrometer operating at frequencies of 500–1250 GHz (240–600 μm) and 1410–1910 GHz (157–212 μm) [4, 7]. PACS is an imaging photometer and spectrometer operating between 57 and 210 μm [4, 6]. Finally, the two SPIRE sub-instruments will complement PACS with imaging photometry, and low and medium resolution imaging spectroscopy from 200 to 670 μm [4, 5]. (The spectral resolution of a spectrometer is typically given by the resolving power, $R = \frac{\nu}{\Delta\nu}$, where $\Delta\nu$ is the width of the resolving element (in GHz). For low and medium resolution IR spectroscopy, R is on the order of 15 and 1000, respectively [5].)

The SPIRE instrument is being developed by an international consortium led by Professor Matthew Griffin at the University of Cardiff in Cardiff, Wales [4,5]. The lead Canadian institution in the SPIRE consortium is the Astronomical Instrumentation Group (AIG) at the University of Leth-

bridge, under the direction of Professor David Naylor. With funding from the Canadian Space Agency (CSA), the Canadian contribution to SPIRE includes the provision of support personnel for the instrument test campaigns, the development of data analysis software, and the construction and delivery of a test Fourier transform spectrometer [40,41]. In partial fulfilment of the first obligation, I spent the first six months of 2004 at the Rutherford Appleton Laboratory (RAL) in Oxfordshire, England.

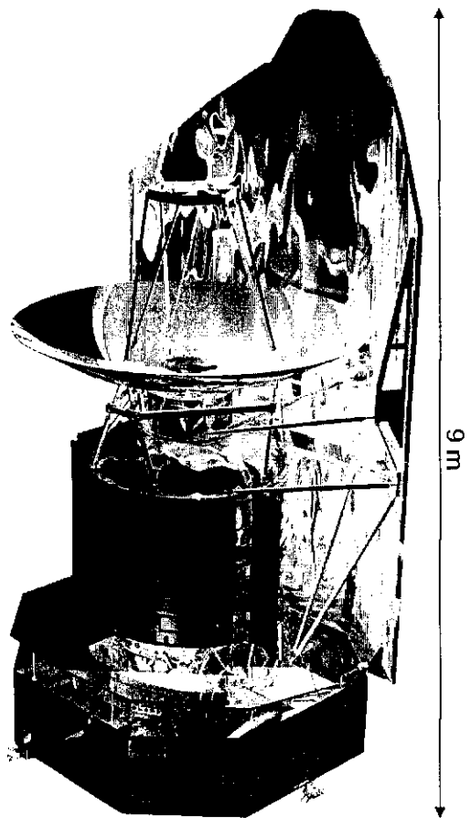

Figure 1.4: Computer rendering of the Herschel Space Observatory. The primary mirror (shown in gold) is mounted above the cylindrical cryostat, which houses the instrument payload, and the octagonal service module. A solar shield is located behind the telescope. (Figure courtesy of the European Space Agency.)

Since repairs of SPIRE are impossible once the telescope is launched, a comprehensive instrument test campaign is currently under way [5,38,43]. The first instrument test, the cryogenic qualification model (CQM), was successfully completed at RAL in 2004. Following cryogenic vibration tests at the Centre Spatial de Liège (CSL) in Liège, Belgium, the first and second proto-flight model (PFM1 and PFM2, respectively) test campaigns were conducted at RAL in 2005 [5,43]. The final instrument test campaign is planned for the spring of 2006 with delivery of the SPIRE flight model to ESA scheduled for August 2006.

1.3 The SPIRE spectrometer simulator

Concurrent to the instrument test campaigns, software simulators of the two SPIRE sub-instruments were written [5, 8, 44]. This thesis describes the Simulator for the Herschel Imaging Fourier Transform Spectrometer (SHIFTS), which built on a simple version initiated by Dr Bruce Swinyard at RAL [45–47]. As indicated at the beginning of this chapter, SHIFTS was designed to generate realistic Herschel data products, making use of available qualification and test data.

There were three primary motivations for this work. First, the SPIRE software teams can evaluate their data reduction programs using the data products generated by SHIFTS (see Section 6.2) [5]. It is essential that the data reduction software is completed prior to launch because of the limited lifetime of the HSO [38]. Second, astronomers can use SHIFTS to predict instrument performance under various operating conditions and plan their observing proposals accordingly (see Chapter 7). Finally, SHIFTS can assist in the characterization and diagnosis of problems encountered in flight.

1.4 Thesis overview

This chapter described the science case for the SPIRE spectrometer, the basic features of the Herschel telescope and the motivation for writing the SPIRE spectrometer simulator. Before the simulator is discussed, Chapters 2 and 3 provide necessary background. First, Chapter 2 describes Fourier transform spectroscopy, the spectroscopic technique employed by the SPIRE spectrometer [5]. Chapter 3 then provides a detailed description of the SPIRE spectrometer.

Given this understanding, Chapter 4 describes the simulator architecture and the components of SHIFTS. Chapter 5 covers the testing and integration of the SHIFTS modules. Chapter 6

compares data products generated by SHIFTS to real data measured during the PFM1 test campaign in 2005. In Chapter 7, SHIFTS is employed to generate the synthetic data product of a simple dust cloud model; the astronomical quantities of the cloud were determined from the resultant spectra. Finally, Chapter 8 summarizes the thesis and outlines the direction of future work.

The three appendices at the end of the thesis provide supplemental information related to the implementation and characterization of SHIFTS. Appendix A lists the constants and units employed in this thesis. Appendix B describes the analysis of the PFM1 test data integrated into SHIFTS. Appendix C compares two different notations of the Einstein A coefficient, a concept introduced in Chapter 7.

Chapter 2

Fourier Transform Spectroscopy

> *"A little over a year ago the scientific world was startled by the announcement that Professor Zeeman had discovered a new effect of magnetism on light. (...) It occurred to me at once to try this experiment by the interference method, which is particularly adapted to the examination of just such cases as this, in which the effect to be observed is beyond the range of the spectroscopic method. (...) The visibility curves that were thus obtained showed that, instead of a broadening, as was first announced by Zeeman, each of the sodium lines appeared to be double."*
>
> - Albert A. Michelson, *Light Waves and their Uses*, University of Chicago Press (1902).

This chapter outlines the theoretical background of Fourier transform spectroscopy (FTS). A thorough grounding in FTS is key to understanding the operation of the Spectral and Photometric Imaging Receiver (SPIRE; see Chapter 3) spectrometer onboard the Herschel Space Observatory (HSO) and the Simulator for the Herschel Imaging Fourier Transform Spectrometer (SHIFTS; see Chapter 4). The concepts introduced in this chapter reappear throughout this thesis.

Section 2.1 introduces the Fourier series and the Fourier transform; Section 2.2 outlines the basic properties of Fourier transforms. With the mathematical foundation in place, the Michelson interferometer and its contributions to spectroscopy are described in Section 2.3. From the ideal

case, Sections 2.4 and 2.5 discuss the techniques used today in Fourier transform spectroscopy.

2.1 The Fourier series and transform

In 1807, J. B. Joseph Fourier submitted "Sur la propagation de la Chaleur dans les corps solides"* to L'Institut de France [48]. To describe heat flow, Fourier proposed that the initial temperature distribution, $f(x)$, of a one-dimensional solid is represented as a infinite sum of sine and cosine terms,

$$f(x) = \sum_{n=0}^{\infty} \left[a_n \cos(nkx) + b_n \sin(nkx)\right], \tag{2.1}$$

where a_n and b_n are the *Fourier coefficients*, x is the position (in units of length) and $k = \frac{2\pi}{\lambda}$ is the angular wavenumber (in radians per unit length) for a wavelength of $\lambda = 2L$ [48, 49]. As derived in Champeney [50], the Fourier coefficients for $f(x)$, periodic over the interval $[-L,L]$, are given by

$$a_n = \frac{1}{L}\int_{-L}^{L} f(x)\cos(nkx)dx, \tag{2.2}$$

$$b_n = \frac{1}{L}\int_{-L}^{L} f(x)\sin(nkx)dx. \tag{2.3}$$

By letting $L \rightarrow \infty$ and replacing k with $2\pi\sigma$ where σ is the spatial frequency or *wavenumber* (in waves per unit length), the discrete Fourier coefficients, a_n and b_n, are replaced with a continuum of coefficients denoted, respectively, by $a(\sigma)$ and $b(\sigma)$. This allows Equation 2.1 to be rewritten as two integrals,

$$f_c(x) = \int_{-\infty}^{\infty} a(\sigma)\cos(2\pi\sigma x)d\sigma, \tag{2.4}$$

$$f_s(x) = \int_{-\infty}^{\infty} b(\sigma)\sin(2\pi\sigma x)d\sigma, \tag{2.5}$$

where $f_c(x)$ is the *inverse Fourier cosine transform* of $a(\sigma)$, and $f_s(x)$ is the *inverse Fourier sine transform* of $b(\sigma)$ [51]. Note that $a(\sigma)$ contains only even terms and $b(\sigma)$ only odd terms. Employing

*On the propagation of heat in solid bodies

Euler's formula, $a(\sigma)$ and $b(\sigma)$ are written as a complex function, $F(\sigma)$, composed of both even and odd terms and given by

$$F(\sigma) = a(\sigma) - ib(\sigma), \tag{2.6}$$

where $i = \sqrt{-1}$ [51, 52]. Therefore, Equations 2.4 and 2.5 are generalized as a single equation,

$$f(x) = \mathcal{F}^{-1}[F(\sigma)] = \int_{-\infty}^{\infty} F(\sigma) e^{i2\pi\sigma x} d\sigma, \tag{2.7}$$

where $\mathcal{F}^{-1}[F(\sigma)]$ is defined as the *inverse Fourier transform* (or reverse Fourier transform) of $F(\sigma)$ [50, 51, 53]. To determine $F(\sigma)$, we perform the (forward) *Fourier transform*,

$$F(\sigma) = \mathcal{F}[f(x)] = \int_{-\infty}^{\infty} f(x) e^{-i2\pi\sigma x} dx, \tag{2.8}$$

where x and σ are called conjugate variables. Equations 2.7 and 2.8 are one of three definitions of the forward and reverse Fourier transform seen in Bracewell [51] and Champeney [50]. While the above definition employs reciprocal units in the spatial and spectral domains, the other two definitions are instead defined in terms of position and angular wavenumber. To normalize the transform, these definitions include a constant before the integral sign; one multiplies the reverse transform by $\frac{1}{2\pi}$ while the other multiplies both the forward and reverse transforms by $\frac{1}{\sqrt{2\pi}}$. To avoid confusion, the definitions of the forward and reverse Fourier transforms given in Equations 2.7 and 2.8 are used exclusively in this thesis.

As can be seen, the Fourier integrals are reversible operations: given $F(\sigma)$, we can determine $f(x)$; and vice-versa [50]. The Fourier transform provides a simple relationship between a function and its frequency components. Waveforms can be manipulated or analyzed in either the spatial or spectral domains (i.e., as a function of x or σ, respectively).

2.2 Properties of Fourier transforms

This section outlines some important properties of Fourier transforms. The field of study devoted to the representation of an arbitrary function by a superposition of sinusoids and cosinusoids is called *Fourier analysis* [49]. Specific topics covered include symmetry and phase, the boxcar and triangle functions, the superposition and convolution theorems, and Parseval's theorem.

The previous section used position, x, and wavenumber, σ, as conjugate variables in the two domains [54]. For reasons which become clear in Section 2.3.2, the most frequently employed conjugate pair in Fourier transform spectroscopy is x in centimetres (cm) and σ in inverse centimetres (cm^{-1}) [49, 55–57]. Another conjugate pair employed in this thesis (see Sections 4.4 and 4.5, and Appendix B) is time (in seconds, or s) and frequency (in Hz), denoted respectively by t and f. However, for the remainder of this chapter, wavenumber and frequency are used interchangeably.

2.2.1 Symmetry

Consider an even function of unit amplitude defined over the range $x = [-\infty,\infty]$ of the form

$$f_e(x) = \cos(2\pi\sigma_o x), \tag{2.9}$$

where $\sigma_o = 5\ cm^{-1}$ is the spatial frequency, as shown in Figure 2.1(a). Following the derivation in Bracewell [51], the Fourier transform of $f_e(x)$ is

$$F_e(\sigma) = \mathcal{F}[f_e(x)] = \frac{1}{2}\delta(\sigma \mp \sigma_o), \tag{2.10}$$

where

$$\delta(\sigma - \sigma_o) = \begin{cases} 1 & \text{for } \sigma = \sigma_o \\ 0 & \text{for } \sigma \neq \sigma_o \end{cases}, \tag{2.11}$$

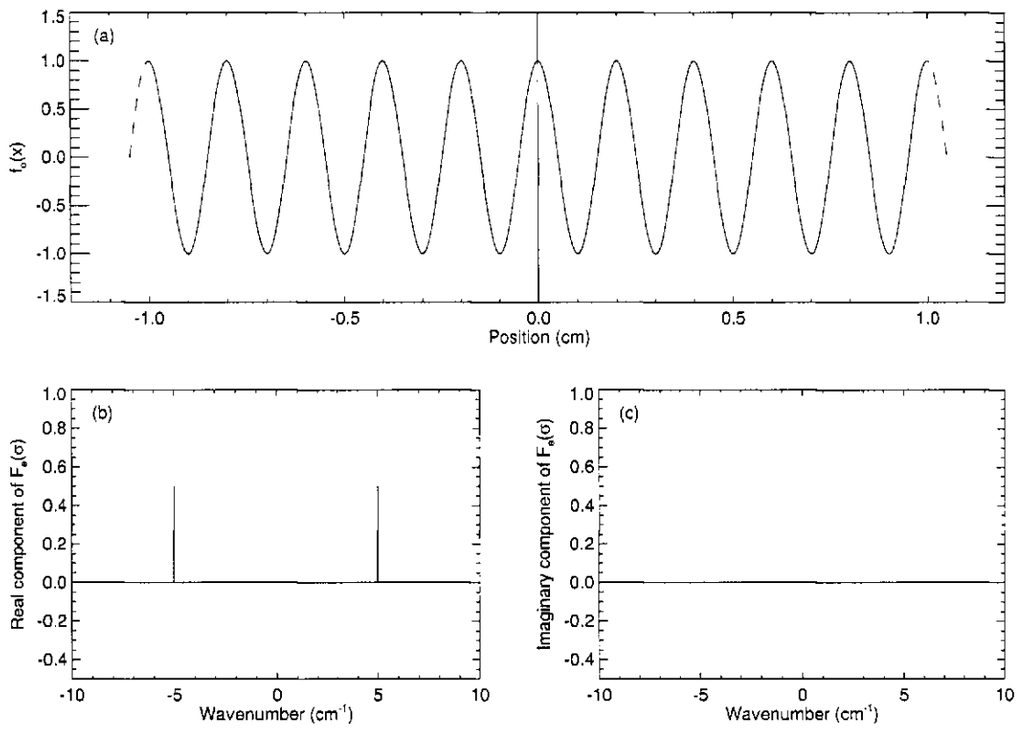

Figure 2.1: Fourier transform of a symmetric function. Panel (a) shows an infinite even function with a frequency of 5 cm^{-1}. Panels (b) and (c) show the real and imaginary components, respectively, of the Fourier transform of Panel (a).

is the Dirac Delta function or simply the *delta function* [49, 51, 58]. As can be seen in Panels (b) and (c) of Figure 2.1, $F_e(\sigma)$ corresponds to two real symmetric delta functions at $\sigma = \pm 5$ cm^{-1}. In fact, the Fourier transform of any symmetric function is symmetric [51].

As shown in Equations 2.7 and 2.8, the limits of the Fourier integrals are symmetric about $x = 0$ cm. Therefore, the Fourier transform of any function produces information at both positive and negative frequencies. Due to the inherent symmetry of the Fourier transform, the unit amplitude of $f_e(x)$ in the spatial domain is split evenly between the two delta functions in the spectral domain. However, in practice, negative frequencies are non-physical and are generally ignored [49].

Conversely, consider an odd function defined over the range $x = [-\infty,\infty]$ of the form

$$f_o(x) = \sin(2\pi\sigma_o x). \tag{2.12}$$

In this case, the Fourier transform of $f_o(x)$ is

$$F_o(\sigma) = \mathcal{F}[f_o(x)] = \pm\frac{1}{2}i\delta(\sigma \mp \sigma_o) = \begin{cases} \frac{1}{2}i & \text{for } \sigma = \sigma_o \\ -\frac{1}{2}i & \text{for } \sigma = -\sigma_o \\ 0 & \text{for } \sigma \neq \pm\sigma_o \end{cases}. \tag{2.13}$$

Contrary to $\mathcal{F}[f_e(x)]$, the Fourier transform of a real and anti-symmetric function is imaginary and anti-symmetric [51]. However, similar to $\mathcal{F}[f_e(x)]$, the unit amplitude of $f_o(x)$ is split evenly between the two delta functions at frequencies of $\sigma = \pm\sigma_o$ in $F_o(\sigma)$.

In the more general case, an arbitrary function is asymmetric. By Fourier decomposition, an asymmetric real function is represented as a sum of even and odd terms [49]. Therefore, its Fourier transform contains a real even component and an imaginary odd component [51]. For example, consider the following real function:

$$f_{oe}(x) = \cos\left(2\pi\sigma_o x + \frac{5\pi}{6}\right). \tag{2.14}$$

As can be seen in Panel (a) of Figure 2.2, this function is asymmetric about $x = 0$ cm. The resultant Fourier transform, shown in Panels (b) and (c), is a combination of the previous two cases: the even component of the waveform corresponds to symmetric delta functions in the real part of the spectrum, and the odd component corresponds to anti-symmetric delta functions in the imaginary part of the spectrum.

Given Figure 2.2, the real and imaginary components can be written in terms of the *magnitude* and *phase* (denoted respectively by $\mathcal{M}$ and ϕ) [52]. On the complex unit circle, this corresponds to converting from cartesian to polar coordinates. The relationship between the real,

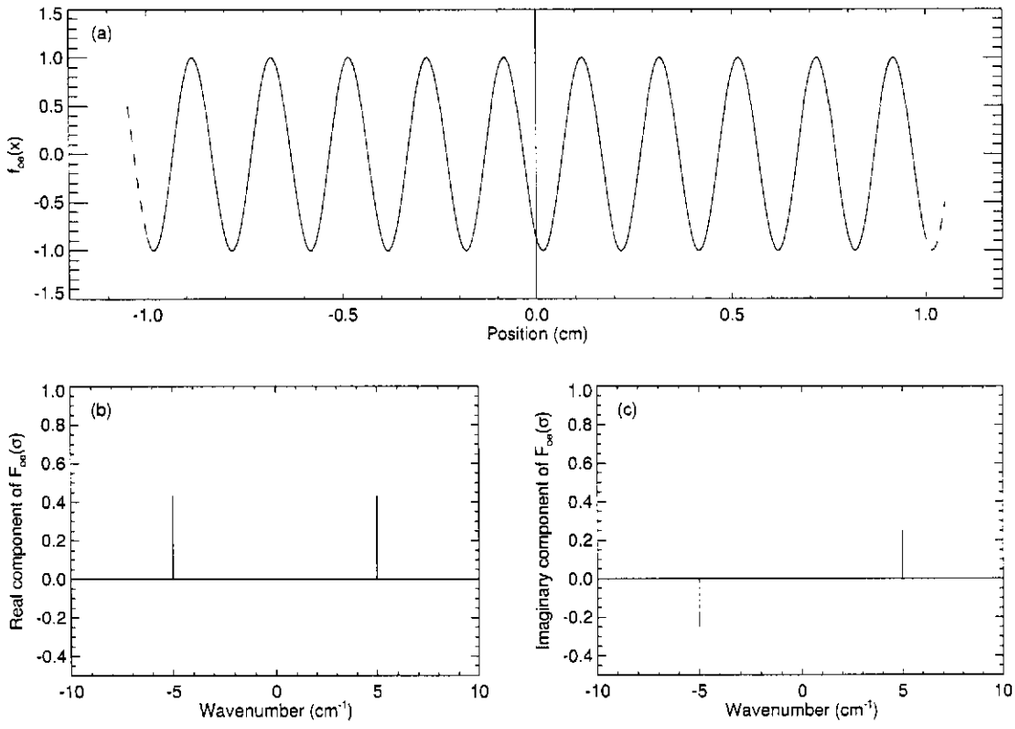

Figure 2.2: Fourier transform of an asymmetric function. Panel (a) shows an infinite function composed of even and odd terms. Panels (b) and (c) show the real and imaginary components, respectively, of the Fourier transform of Panel (a).

$\mathcal{R}_\sigma$, and imaginary, $\mathcal{I}_\sigma$, components of a spectrum is given by

$$\mathcal{M}_\sigma = \sqrt{\mathcal{R}_\sigma^2 + \mathcal{I}_\sigma^2}, \tag{2.15}$$

and

$$\phi_\sigma = \arctan\left(\frac{\mathcal{I}_\sigma}{\mathcal{R}_\sigma}\right). \qquad \text{[radians]} \tag{2.16}$$

As can be seen in Panels (b) and (c) of Figure 2.2, the amplitude of the real and imaginary components at $\sigma = 5\ \text{cm}^{-1}$ are $\frac{\sqrt{3}}{4}$ and $\frac{1}{4}$, respectively. Equation 2.16 yields $\phi = \frac{5\pi}{6}$, identical to the phase term in Equation 2.14 that introduced the asymmetry. Using a technique called *phase correction*, the phase is used to retrieve a real spectrum from an asymmetric waveform (see Section 2.5.3) [59].

Table 2.1: Symmetry properties of Fourier transform pairs, where $f(x)$ is any function, and $\mathcal{F}[f(x)]$ is the Fourier transform of $f(x)$.

$f(x)$		$\mathcal{F}[f(x)]$	
Real	Imaginary	Real	Imaginary
even	0	even	0
odd	0	0	odd
0	even	0	even
0	odd	odd	0
asymmetric	0	even	odd
0	asymmetric	odd	even
even	odd	asymmetric	0
odd	even	0	asymmetric
even	even	even	even
odd	odd	odd	odd

The symmetry properties of Fourier transforms are summarized in Table 2.1 [51, 56]. These properties suggest operations on even and real functions are preferable since their Fourier transforms only require a cosine transform [51]. Fourier transform spectrometers such as the Michelson interferometer (see Section 2.3) exploit this fact because their measurements are inherently real and, for the ideal case, symmetric [55, 56].

2.2.2 Transform pairs

In addition to the sine and cosine, there are other functions whose Fourier transforms are frequently encountered in Fourier analysis [49, 51, 54]. This section lists two common functions seen throughout this chapter. The first is the boxcar function, defined by

$$\Pi(x) = \begin{cases} 1 & \text{for } |x| < L \\ 0 & \text{for } |x| > L \end{cases}, \tag{2.17}$$

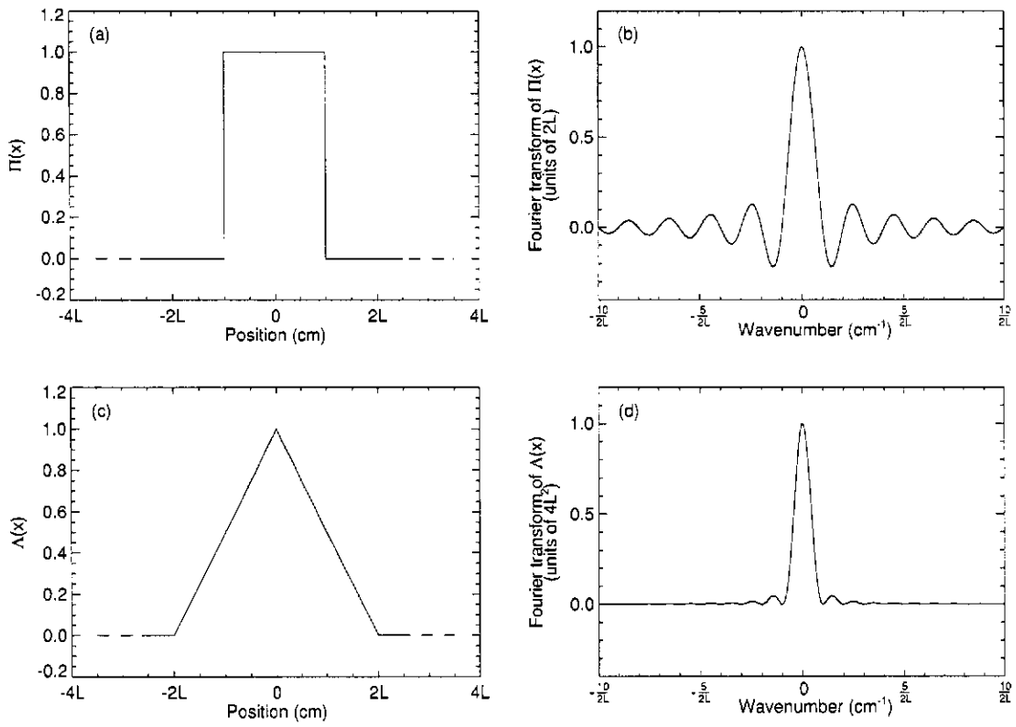

Figure 2.3: Fourier transforms of the boxcar and triangle functions. Panel (a) shows a boxcar function with its Fourier transform, a sinc function, shown in Panel (b). Panel (c) shows a triangle function with its Fourier transform, a sinc^2 function, shown in Panel (d).

and shown in Panel (a) of Figure 2.3. As shown in Bracewell [51] and James [54], the Fourier transform of $\Pi(x)$ is

$$\mathcal{F}[\Pi(x)] = \int_{-\infty}^{\infty} \Pi(x) e^{-i2\pi\sigma x} dx = 2L \frac{\sin(2\pi\sigma L)}{2\pi\sigma L}, \tag{2.18}$$

where $\frac{\sin(2\pi\sigma L)}{2\pi\sigma L}$ is commonly referred to as the *sinc function*, $\text{sinc}(2\pi\sigma L)$, shown in Panel (b). Since the sinc function is frequently encountered in Fourier analysis, its properties are well understood [51, 54]. The sinc function has a full-width at half-maximum (FWHM) of $\frac{1.207}{2L}$ and crosses zero where σ is an integer multiple of $\frac{1}{2L}$. Located at $\frac{1.43}{2L}$, the secondary minimum is -21.7 % of the central maximum [51, 56].

The second common function is the triangle function, defined by

$$\Lambda(x) = \begin{cases} 1 - \frac{|x|}{2L} & \text{for } |x| < 2L \\ 0 & \text{for } |x| > 2L \end{cases}, \tag{2.19}$$

and shown in Panel (c) of Figure 2.3. Shown in Panel (d), the Fourier transform of $\Lambda(x)$ is

$$\mathcal{F}[\Lambda(x)] = \int_{-\infty}^{\infty} \Lambda(x) e^{-i2\pi\sigma x} dx = 4L^2 \text{sinc}^2(2\pi\sigma L). \tag{2.20}$$

The properties of $\text{sinc}^2(2\pi\sigma L)$ are similar to the sinc function. However, since $\text{sinc}^2(2\pi\sigma L)$ is positive-definite for all σ, it is the secondary maximum that occurs at $\frac{1.43}{2L}$. Moreover, the amplitudes of all the secondary lobes are reduced; the amplitude of the secondary maximum is only 4.7 % of the central maximum [51, 56].

2.2.3 Fourier theorems

There are a series of theorems fundamental to Fourier analysis that describe the effect that changes to a function have on its Fourier transform. This section outlines three important theorems employed in this thesis: *superposition*, *convolution* and *Parseval*. (For additional theorems, the reader is referred to Bracewell [51], Brigham [53], Champeney [50] and James [54].) For the remainder of this chapter, $F(\sigma)$ and $G(\sigma)$ are the Fourier transforms of $f(x)$ and $g(x)$, respectively, and only positive frequencies are shown in a spectrum.

Superposition theorem

Fourier transforms obey the superposition theorem [49, 51], which is expressed mathematically as

$$\mathcal{F}[f(x) + g(x)] = \mathcal{F}[f(x)] + \mathcal{F}[g(x)] = F(\sigma) + G(\sigma). \tag{2.21}$$

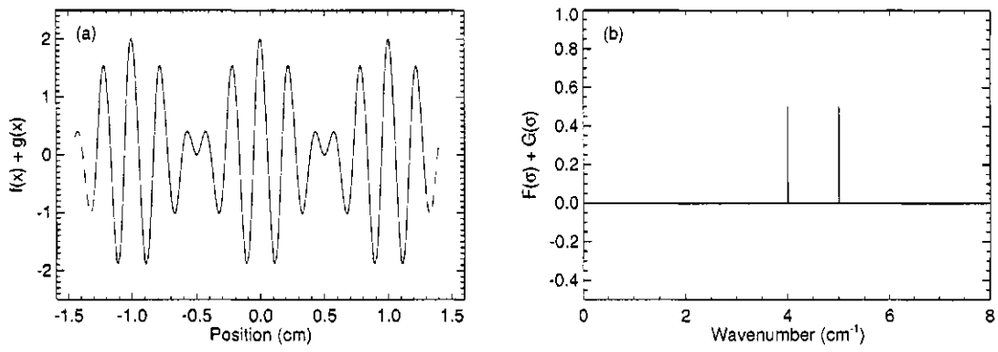

Figure 2.4: Example of the superposition theorem. Panel (a) is the sum of two infinite cosine functions oscillating at 4 and 5 cm^{-1}. Panel (b) is the Fourier transform of Panel (a).

Consider two cosine functions (see Equation 2.9) oscillating at spatial frequencies of σ_1 and σ_2. By employing trigonometric identities, the resultant function of the sum of these two waveforms produces a *beat pattern* given by

$$f_{\sigma_1}(x) + f_{\sigma_2}(x) = 2\cos(\pi x(\sigma_1 - \sigma_2))\cos(\pi x(\sigma_1 + \sigma_2)), \tag{2.22}$$

where the first cosine term is the envelope of the rapidly varying second cosine term. Panel (a) of Figure 2.4 shows the above equation with $\sigma_1 = 5$ cm^{-1} and $\sigma_2 = 4$ cm^{-1}. In agreement with the above equation, the waveform oscillates nine times in a 2 cm spatial period. Panel (b) shows the Fourier transform of Equation 2.22. As can be seen, the Fourier transform of the sum of the two functions is simply the Fourier transform of each of the individual functions.

Convolution theorem

The Fourier transform of the multiplication of two functions in one domain is equivalent to convolution in the other, as given by

$$\mathcal{F}^{-1}(G(\sigma) \cdot F(\sigma)) = f(x) * g(x) = \int_{-\infty}^{\infty} f(z)g(x-z)dz, \tag{2.23}$$

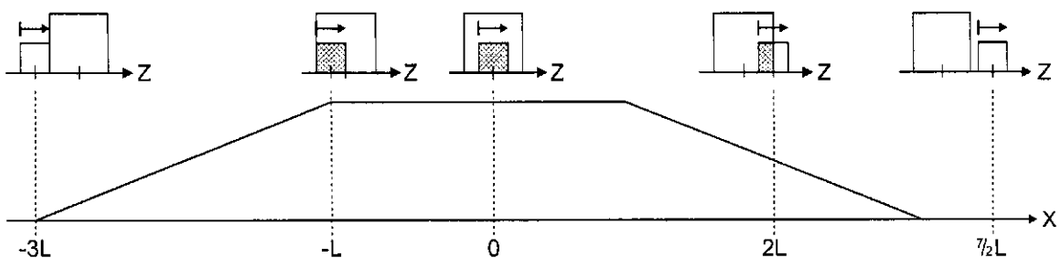

Figure 2.5: Example of the convolution theorem. The lower portion shows a trapezoid, the result of the convolution of two boxcar functions of different widths. The integration over z at each point in x (see Equation 2.23) is shown in the upper portion, where the hatched regions indicates the overlapping area of the two boxcars and the arrows indicate the direction of the shifting boxcar function.

where z is a dummy variable and $f(x) * g(x)$ denotes the convolution of $f(x)$ and $g(x)$ [49, 51]. In effect, convolution shifts the reverse of the second function across the first function; each point in x is the integral of the product of the overlapping regions of $f(z)$ and $g(x - z)$ [51].

Consider the convolution of two boxcar functions, where the reversed function is given by Equation 2.17 and the fixed boxcar funtion, $f(x)$, is twice as wide as $g(x - z)$. As shown in the upper portion of Figure 2.5, the initial overlap occurs at $x = -3L$. The integrated area increases linearly to a plateau that begins at $x = -L$. The overlap is constant until $x = L$ and then decreases linearly to zero [49, 56, 58].

As is clear from the lower portion of Figure 2.5, the convolution of two boxcar functions of different widths is a trapezoid. In the special case where the boxcar functions have the same width L, the convolution yields a triangle function. As indicated in the previous section, the Fourier transform of a boxcar function is a sinc function. The product of two sinc functions naturally yields a sinc^2 function, identical to the Fourier transform of a triangle function [51]. (Several excellent animations of convolution can be found at *http://mathworld.wolfram.com/Convolution.html*.)

Parseval's theorem

The final theorem of interest is Parseval's theorem, which states that the integral of the square of a function equals the integral of the square of its Fourier transform [51,53]. It is expressed mathematically as

$$\int_{-\infty}^{\infty} |f(x)|^2 dx = \int_{-\infty}^{\infty} |F(\sigma)|^2 d\sigma. \tag{2.24}$$

Parseval's theorem is the embodiment of the conservation of energy; information is neither created nor destroyed during a transform. For a derivation of Parseval's theorem, the reader is referred to Champeney [50].

2.3 The Michelson interferometer

As Section 2.2 indicated, the Fourier transform is a powerful mathematical tool that relates any periodic waveform to its component frequencies. This section describes how Fourier transforms are employed to determine the spectral distribution of electromagnetic radiation.

2.3.1 Michelson and the interference of light

Light is composed of transverse waves of electric and magnetic potentials [60]. In 1801, Thomas Young conducted his famous double-slit experiment, proving that light waves interfere with one another [61]. Put simply, the theory of interference states that the superposition of two rays of light of equal amplitude, frequency and phase is simply another waveform of identical frequency and phase but with double the amplitude. This is called constructive interference. However, if those same two rays of light are out of phase by π radians, then when added together they cancel one another out. This is called destructive interference [62].

The concept of interference was firmly established when Albert A. Michelson began his

studies of light in 1878 [63]. In 1881, Michelson invented his now famous interferometer to test for the existence of the luminiferous ether [63,64]. Although the ether experiment returned a negative result (which had a major impact on relativity), the Michelson interferometer has since played a major role in the development of spectroscopy [57,65].

The Michelson interferometer is one example of a *Fourier transform spectrometer*, a two-beam interferometer used to measure spectra [60,65]. The SPIRE imaging spectrometer is based on another two-beam interferometer, the *Mach-Zehnder* (MZ) interferometer (see Chapter 3) [5,60]. However, the Michelson interferometer is the simplest design so our discussion focuses on it.

2.3.2 Theory of an ideal Michelson interferometer

Figure 2.6 depicts a schematic of a Michelson interferometer. Light emitted from the source is collimated and then strikes the *beamsplitter*, a reflective substrate angled 45 degrees with respect to the direction of travel of the light [64,65]. Half of the beam is reflected off the beamsplitter and half is transmitted. The reflected beam is reflected again off a fixed plane mirror back to the beamsplitter. The transmitted beam is reflected off a second plane mirror, which moves in a direction perpendicular to its plane, back to the beamsplitter.

The two beams recombine at the beamsplitter and the reflected light is directed down to an eyepiece, where Michelson observed the resultant intensity. By changing the position of the movable mirror with turns of a millimetre screw, Michelson changed the optical distance the second beam travelled [65]. Note than only half of the radiation entering a Michelson interferometer can be measured since 50 % is transmitted back through the beamsplitter to the source [55,66].

To understand the effect of moving the second mirror, let us examine the optical path of the two beams of light within the interferometer. From the solution to Maxwell's equations for

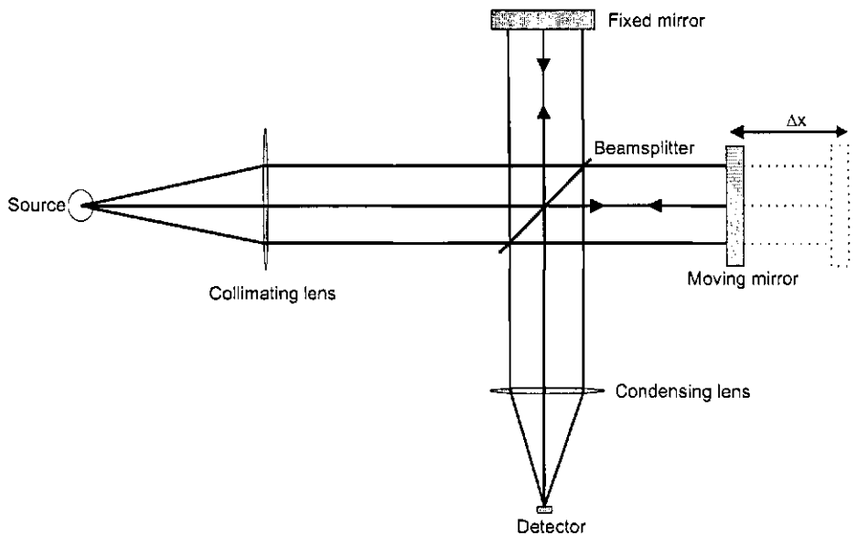

Figure 2.6: Schematic of a Michelson interferometer. Arrows indicate the direction of motion of light rays. The dotted section of the moving mirror corresponds to a movement of Δx in the position of the mirror.

one-dimensional free space, the wave equation of the electric field is given by

$$E(x,\sigma) = E_o(\sigma)e^{i2\pi(\sigma x - \nu t)}, \qquad [\mathrm{V\,m^{-1}}] \tag{2.25}$$

where x is the position (in cm), σ is the wavenumber (in $\mathrm{cm^{-1}}$), t is the time (in s), ν is the frequency (in Hz) and $E_o(\sigma)$ is the maximum amplitude of the electric field (in volts per metre, or $\mathrm{V\,m^{-1}}$) [60].

Following a reflection from and a transmission through the beamsplitter, the two beams are observed at the eyepiece, having travelled optical paths x_1 and x_2. The resultant electric field at the detector is

$$E_d(x,\sigma) = rtE_o(\sigma)\left[e^{-i2\pi(\sigma x_1 - \nu t)} + e^{-i2\pi(\sigma x_2 - \nu t)}\right], \qquad [\mathrm{V\,m^{-1}}] \tag{2.26}$$

where r and t are the *amplitude coefficients* of reflection and transmission, respectively, of the beamsplitter [67]. The intensity, $I_d(x,\sigma)$, measured at the eyepiece is proportional to the time average of

the square of the measured electric field,

$$I_d(x,\sigma) = \frac{c\epsilon_o}{2} E_d(x,\sigma) E_d^*(x,\sigma), \qquad [\mathrm{W}] \tag{2.27}$$

where c is the speed of light and ϵ_o is the permittivity of free space (see Table A-1) [67]. For the remainder of this chapter, the constant factor $\frac{c\epsilon_o}{2}$ is ignored and the intensity measured at the eyepiece is simply given by

$$I_d(x,\sigma) \propto E_d(x,\sigma) E_d^*(x,\sigma) = 2RTE_o^2(\sigma)\left[1 + \cos(2\pi x\sigma)\right], \qquad [\mathrm{W}] \tag{2.28}$$

where $R = r^2$ is the *reflectance*, $T = 1 - r^2$ is the *transmittance* and $x = x_1 - x_2$ is the *optical path difference* (OPD) between the two beams (in cm), which depends solely on the position of the movable mirror [49, 60]. Since x is an observable quantity, it is natural to use wavenumber (in cm^{-1}) as the conjugate variable in the spectral domain.

The unique position corresponding to $x = 0$ cm is called *zero path difference* (ZPD) because both mirrors are equidistant from the beamsplitter [55]. At ZPD, both beams of light travel the same distance so all frequencies are in phase and yield the maximum intensity [49].

As the second mirror moves away from ZPD, the optical path distance for the second beam of light increases. Since the light travels between the movable mirror and the beamsplitter twice, a change of Δx in the moving mirror's position results in a change of $2\Delta x$ in the optical path (see Figure 2.6) [49, 55, 56]. The power, $I(x)$, at the eyepiece is the integral of all the component intensities:

$$\begin{aligned} I(x) &= \int_0^\infty I_d(x,\sigma)\,d\sigma, \\ &\propto 2RT\left[\int_0^\infty E_o^2(\sigma)\,d\sigma + \int_0^\infty E_o^2(\sigma)\cos(2\pi\sigma x)\,d\sigma\right], \\ &= \frac{1}{2}I(0) + 2RT\int_0^\infty B(\sigma)\cos(2\pi\sigma x)\,d\sigma, \qquad [\mathrm{W}] \end{aligned} \tag{2.29}$$

where $E_0^2(\sigma)$ is proportional to our measure of interest, the spectrum $B(\sigma)$ [60]. For an ideal interferometer, $R = T = 0.5$. Therefore, it can be seen by inspection that half the maximum power is contained in the constant term above [49]. It is customary to ignore the offset since it contains no spectral information. Instead, we focus on the modulating term, rewritting Equation 2.29 as

$$I(x) = \int_0^\infty B(\sigma)\cos(2\pi\sigma x)d\sigma. \qquad [\mathrm{W}] \tag{2.30}$$

Changes in the optical path difference introduce phase shifts of $\cos(2\pi\sigma x)$ into the second beam. At a given OPD, higher frequency components experience greater phase shifts [56]. Mirroring the spectrum to include negative frequencies, using the definition $B(\sigma) = B(-\sigma)$, yields

$$I(x) = \frac{1}{2}\int_{-\infty}^\infty B(\sigma)\cos(2\pi\sigma x)d\sigma, \qquad [\mathrm{W}] \tag{2.31}$$

which is the inverse Fourier cosine transform of $B(\sigma)$ (see Equation 2.4) [55].

The function $I(x)$ is a measure of the interference of all the frequency components of $B(\sigma)$ as the OPD is varied. Therefore, $I(x)$ is termed an *interferogram* [49]. By the symmetry requirements of Fourier transforms (see Section 2.2.1), the measured interferogram is *double-sided*; i.e., it is evenly sampled at both positive and negative optical path differences [49, 56]. The spectrum, $B(\sigma)$, is recovered by performing the Fourier cosine transform on the interferogram,

$$B(\sigma) = \int_{-\infty}^\infty I(x)\cos(2\pi\sigma x)dx. \qquad [\mathrm{W}] \tag{2.32}$$

2.4 Sampling an interferogram

Since Michelson observed with an eyepiece, he never measured an interferogram, only its visibility curve [57, 65]. Heinrick Rubens and Robert W. Wood measured the first true interferogram in 1911 [68]. However, they were still unable to compute the Fourier transform of their

interferogram directly [49, 57, 68]. Another forty years passed before Peter B. Fellgett published results of the first numerical Fourier transform of an interferogram [57]. The first successful use of a Fourier transform spectrometer in astronomy came in 1966 when Janine and Pierre Connes used one to measure the near-infrared (NIR) spectrum of the atmosphere of Venus [69].

This section focuses on the basic features of an interferogram and how interferograms are measured. The topics discussed include discrete sampling, the Nyquist theorem, aliasing, natural apodization, instrumental line shape and broadband spectra. The recovery of a spectrum from an interferogram is covered in Section 2.5.

2.4.1 Discrete sampling

In practice, it is not possible to sample a continuous interferogram. Instead, interferograms are usually sampled at equal intervals of optical path difference [56]. Mathematically, this is equivalent to multiplying the interferogram by the Shah function given by

$$\text{Ш}(x) = \sum_{n=-\infty}^{\infty} \delta(x - n\Delta x), \tag{2.33}$$

where Δx is the sampling interval (in cm).

As a consequence of discrete sampling, there is no guarantee that the position of zero path difference is measured [49]. Figure 2.7 illustrates this problem for an infinite cosine wave with a frequency of $\sigma_o = 3$ cm^{-1} sampled at $\Delta x = 0.1$ cm (as denoted by the red circles). As can be seen, the sampled interferogram is asymmetric, such that its Fourier transform cannot be computed using the Fourier cosine transform (see Section 2.5.1).

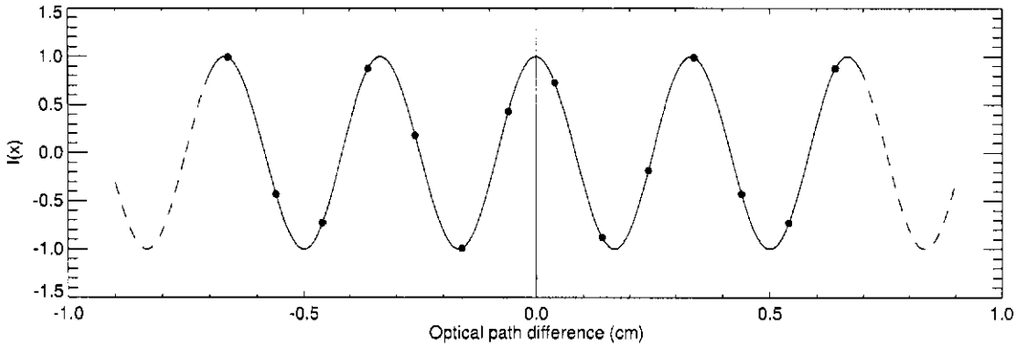

Figure 2.7: Example of a discretely sampled cosine wave. The solid line denotes a infinite cosine wave with a frequency of $\sigma_o = 3$ cm^{-1} sampled every 0.1 cm, where the red circles represent the samples.

2.4.2 Nyquist sampling theorem

Discrete sampling also sets limits on the spectral information recoverable from an interferogram [49, 70]. To sample a spectrum without any loss of information, the *Nyquist criteria* states the sampling interval, Δx, must be less than or equal to the inverse of twice the bandwidth of the spectrum:

$$\Delta x \leq \frac{1}{2(\sigma_N - \sigma_L)}, \qquad \text{[cm]} \tag{2.34}$$

where σ_N is the maximum wavenumber and σ_L is the minimum wavenumber of the spectrum (both in cm^{-1}) [49, 56, 70]. The maximum wavenumber, σ_N, is called the *Nyquist frequency* [55]. In practice, the lower bound, σ_L, is taken as a null term and the above equation is simply written as

$$\Delta x \leq \frac{1}{2\sigma_N}. \qquad \text{[cm]} \tag{2.35}$$

2.4.3 Aliasing

If the maximum frequency in the spectrum is not sampled twice per oscillation period (i.e., the Nyquist criteria is not satisfied), the interferogram is aliased. Information beyond the Nyquist frequency is folded into the interferogram at a lower frequency location [55, 56]. Consider

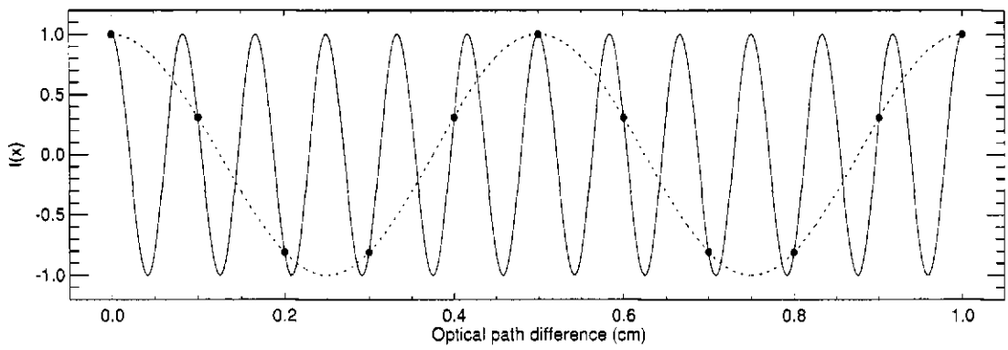

Figure 2.8: Example of aliasing. The solid line corresponds to a cosine function with a frequency of 12 cm^{-1}; the dotted line corresponds to a cosine function with a frequency of 2 cm^{-1}; the red circles represent the 0.1 cm sampling of the waveforms.

a spectrum with a frequency component located at σ_o. The corresponding interferogram is sampled such that $\sigma_o < \sigma_N$. If the spectrum also contains information beyond the Nyquist frequency, spectral features located at $\sigma = 2N\sigma_N \pm \sigma_o$, where N is an integer, are shifted to a frequency of σ_o [56].

Figure 2.8 is a graphical demonstration of this phenomenon. For an interferogram sampled every 0.1 cm (as denoted by the red circles), the corresponding Nyquist frequency is 5 cm^{-1} (see Equation 2.35). The spectrum has two frequency components at 2 and 12 cm^{-1}, represented by the dashed and solid lines, respectively. As can be seen, the amplitudes of the cosine functions are indistinguishable when sampled every 0.1 cm [55].

2.4.4 Natural apodization

The *finite entrance aperture* of a Fourier transform spectrometer produces an effect termed natural apodization [49]. In an ideal interferometer, an infinitesimal entrance aperture ensures the resultant interference is produced by two plane waves moving in the same direction. However, to increase the light-collecting power, the entrance aperture of a Fourier transform spectrometer has a finite size [49]. From geometric optics, radiation exiting the aperture at different angles travels

different optical paths prior to detection [67, 71]. It can be shown that the optical path difference of an off-axis beam is $x\cos(\alpha')$, where α' is the half-cone angle between the off- and on-axis beams (in radians) [66]. To determine the interference fringe intensity at a given OPD, we integrate over the beam size,

$$I(x) = \int_0^{\Omega} \cos[2\pi\sigma x\cos(\alpha')]d\Omega', \qquad [\mathrm{W}] \tag{2.36}$$

where $d\Omega'$ is an element of solid angle (in steradians, or sr) and Ω is the solid angle of the beam, defined as

$$\Omega = \pi\alpha^2, \qquad [\mathrm{sr}] \tag{2.37}$$

where α is the maximum value of α'. Using the small angle identity ($\cos(\alpha) \sim 1 - \frac{\alpha^2}{2}$ for small α) and the above equation, Equation 2.36 yields

$$I(x) = \Omega\mathrm{sinc}\left(\frac{\sigma x\Omega}{2\pi}\right)\cos\left(2\pi\sigma x\left[1 - \frac{\Omega}{4\pi}\right]\right), \qquad [\mathrm{W}] \tag{2.38}$$

as shown in Davis, Abrams & Brault [49].

Two consequences are evident from the above equation. First, the optical path difference grid is shorter for off-axis beams [55]. However, the scale change is generally small and can be ignored (see Section 3.6.2) [49]. The second effect is the modulation of the interferogram by a sinc function. From Sections 2.2.2 and 2.2.3, this is equivalent to the convolution of spectral features by a boxcar function of width $\frac{\Omega\sigma}{2\pi}$. If the aperture of the interferometer is increased such that the width of the boxcar function is larger than the spectral resolution, $\Delta\sigma$, then the linear independence of the spectral features is lost [49, 72]. This fixes an upper limit on the resolving power, R, of the instrument, known as the *Jaquinot criteria* and given by

$$R \leq \frac{2\pi}{\Omega}, \tag{2.39}$$

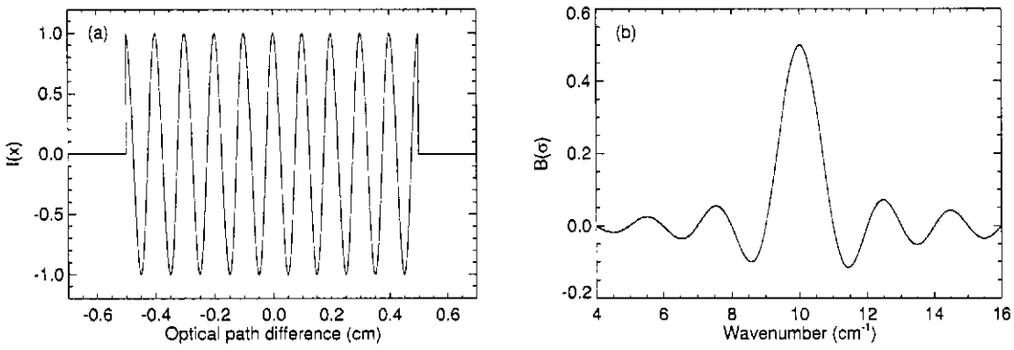

Figure 2.9: Example of finite path difference. Panel (a) shows a cosine waveform with a frequency of 10 cm^{-1} measured over a finite optical path difference from -0.5 to 0.5 cm. Panel (b) is the Fourier transform of the waveform, a sinc function centered at 10 cm^{-1}.

where $R = \frac{\sigma}{\Delta\sigma}$ (see Section 1.2) [49,57]. The Jaquinot criteria is evaluated for the SPIRE spectrometer in Section 3.6.2.

2.4.5 Instrumental line shape

Another instrumental effect to consider is the *finite path difference*, which introduces the instrumental line shape (ILS) of a Fourier transform spectrometer. The ILS of any spectrometer defines the shape of a spectral line given a monochromatic input. An ideal interferometer has an infinite optical path difference. In such a case, a single emission line of unit strength oscillating at a frequency of σ_o has a corresponding interferogram of $I(x) = \cos(2\pi\sigma_o x)$ defined over $x = [-\infty,\infty]$ (see Sections 2.2.1 and 2.3.2) [49].

However, practical limitations dictate that interferograms are only measured out to a finite optical path difference [49,55,56]. Mathematically, this is equivalent to multiplying $I(x)$ by a boxcar function (see Equation 2.17), where L is the maximum OPD. As per Section 2.2.3, the spectrum is then convolved by a sinc function [51].

Panel (a) of Figure 2.9 shows a truncated interferogram where $L = 0.5$ cm and $\sigma_o =$

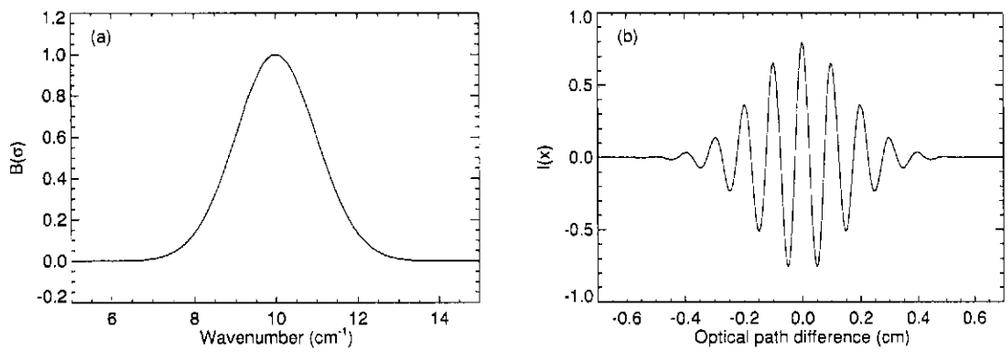

Figure 2.10: Example of a broadened line profile. Panel (a) shows a broadband spectrum given by Equation 2.40 and Panel (b) is its Fourier transform.

10 cm^{-1}. In Panel (b), the corresponding spectrum clearly shows a sinc function centered at $\sigma = \sigma_o$. This sinc profile determines the spectral resolution (see Section 2.5.1) and introduces troublesome secondary lobes (see Section 2.5.2), sometimes referred to as *ringing* [49, 56].

2.4.6 Broadband spectrum

While the finite path difference defines the instrumental line shape for a monochromatic input, spectra are rarely composed of infinitely narrow emission (or absorption) features. In reality, light is emitted over a continuum of frequencies [15]. An interferogram composed of broadband radiation is noticeably different from one due only to a monochromatic source.

Consider the gaussian emission feature shown in Panel (a) of Figure 2.10 and given by

$$B(\sigma) = e^{-(\sigma-\sigma_o)^2/2\mu^2}, \qquad [\mathrm{W}] \tag{2.40}$$

where $\sigma_o = 10\ \mathrm{cm}^{-1}$ is the center of the line and $\mu = 1\ \mathrm{cm}^{-1}$ is the standard deviation. The FWHM of a gaussian function is 2.35μ. The corresponding interferogram is shown in Panel (b). Similar to Panel (a) of Figure 2.9, the peaks of the oscillations are spaced 0.1 cm apart. But unlike the interferogram of the narrow line, the envelope of the broadband spectrum decays with OPD [49].

Furthermore, the secondary lobes seen in Panel (b) of Figure 2.9 are not present in broadband spectral features; ringing is only evident when the width of a spectral feature is on the order of a resolution element [49].

2.5 Recovering a spectrum

By definition, a spectrum is real [49]. Section 2.4 unfortunately demonstrated that while a measured interferogram is real, it is also discretely sampled, finite and asymmetric. This section describes the basic techniques employed to recover a spectrum and account for the instrumental effects introduced by the interferometer.

2.5.1 The discrete Fourier transform

Given a discretely sampled asymmetric interferogram, the spectrum cannot be computed using the continuous Fourier cosine transform (as was suggested in Section 2.3.2). Instead, the spectrum is computed using the complex form of the discrete Fourier transform (DFT) [49,55,56]. Using the DFT, the discretely sampled spectrum is given by

$$B(\sigma_j) = \sum_{j=0}^{N-1} I(x_j) e^{-2\pi i \sigma_j x_j / N}, \qquad [\mathrm{W}] \tag{2.41}$$

where N is the number of elements in the interferogram (and the spectrum), and $I(x_j)$ is the interferogram (in watts, or W) sampled at discrete optical path differences, x_j, separated by a sampling interval of Δx (in cm). Each element in $B(\sigma_j)$ is linearly independent of every other element [56]. To determine the corresponding σ_j values, we define the spectal resolution as

$$\Delta\sigma = \frac{\sigma_N}{N}, \qquad [\mathrm{cm}^{-1}] \tag{2.42}$$

where σ_N is the Nyquist frequency introduced in Section 2.4.2 (in cm^{-1}). Combining the above equation with a complementary definition of the sampling interval, $\Delta x = \frac{L}{N}$, and Equation 2.35, the spectral resolution is written as

$$\Delta\sigma = \frac{1}{2L}, \qquad [cm^{-1}] \tag{2.43}$$

where L is the maximum OPD (in cm) [55, 56].

The instrumental line shape further modifies the spectral resolution [56]. Consider once again a single emission line of unit strength oscillating at a frequency of σ_o. Given the above equation, its full-width at half-maximum is one spectral resolution element, $\Delta\sigma$ [55]. Because of the finite path difference and finite entrance aperture of a Fourier transform spectrometer, the emission line is convolved by a boxcar function of width $\frac{\Omega\sigma_o}{2\pi}$ (see Section 2.4.4) and a sinc function of FWHM $\sim \frac{1.207}{2L}$ (see Section 2.4.5) [49]. In a well-designed Fourier transform spectrometer, the sinc profile dominates and the minimum resolvable element is therefore

$$\Delta\sigma = \frac{1.207}{2L}. \qquad [cm^{-1}] \tag{2.44}$$

It is important to note that Fourier transforms are rarely calculated by the DFT today [49, 53]. Using the DFT, the computation of a N-point Fourier transform requires on the order of N^2 operations [53, 73]. This computational limitation led to the 1965 development of the fast Fourier transform (FFT) by James W. Cooley and John W. Tukey [73]. Using factorization to eliminate repetitive multiplications, the FFT algorithm reduces the number of operations to, in the best case, $N\log_2 N$ [53, 73]. In this thesis, all Fourier transforms were computed using the fast Fourier transform. For a complete treatment of the FFT algorithm, the reader is referred to Brigham [53].

2.5.2 Apodization

Another problem introduced by the ILS is ringing in the spectrum [49]. As can be seen in Panel (b) of Figure 2.9, the broadened emission line has symmetric side lobes due to the cutoff of the interferogram at $x = \pm 0.5$ cm, as shown in Panel (a). These side lobes may be mistaken as spectral lines, or may mask real spectral features [49, 55].

Apodization is a mathematical filtering technique used to reduce the amplitude of these secondary lobes [55]. An interferogram is apodized by multiplying it by an apodizing function, which is equivalent to convolving the spectrum by the Fourier transform of the apodization function [55]. A correctly chosen apodizing function smooths the edge discontinuities in the interferogram, which in turn minimizes the side lobes in the spectrum [49]. The cost associated with apodization is a reduction in the spectral resolution, as was seen with the ILS (see Section 2.5.1) [55].

Various apodizing functions are currently employed in FTS, such as the triangle, Norton-Beer and Blackman-Harris functions [56, 74–76]. Margaret Tahic recently determined ten optimal apodizing functions that reduce secondary lobes with a minimum loss in spectral resolution [74, 77].

2.5.3 Phase correction

As indicated at the beginning of Section 2.5, a spectrum is an observable quantity and therefore real. Measured interferograms are generally asymmetric such that their Fourier transforms are complex (see Section 2.4.1). Phase correction modifies an asymmetric interferogram to produce a real spectrum [56, 59].

Consider a moving stage with a scan length of $2L$. Given a double-sided interferogram measured from $-L$ to L, the magnitude of the complex spectrum is computed by Equation 2.15.

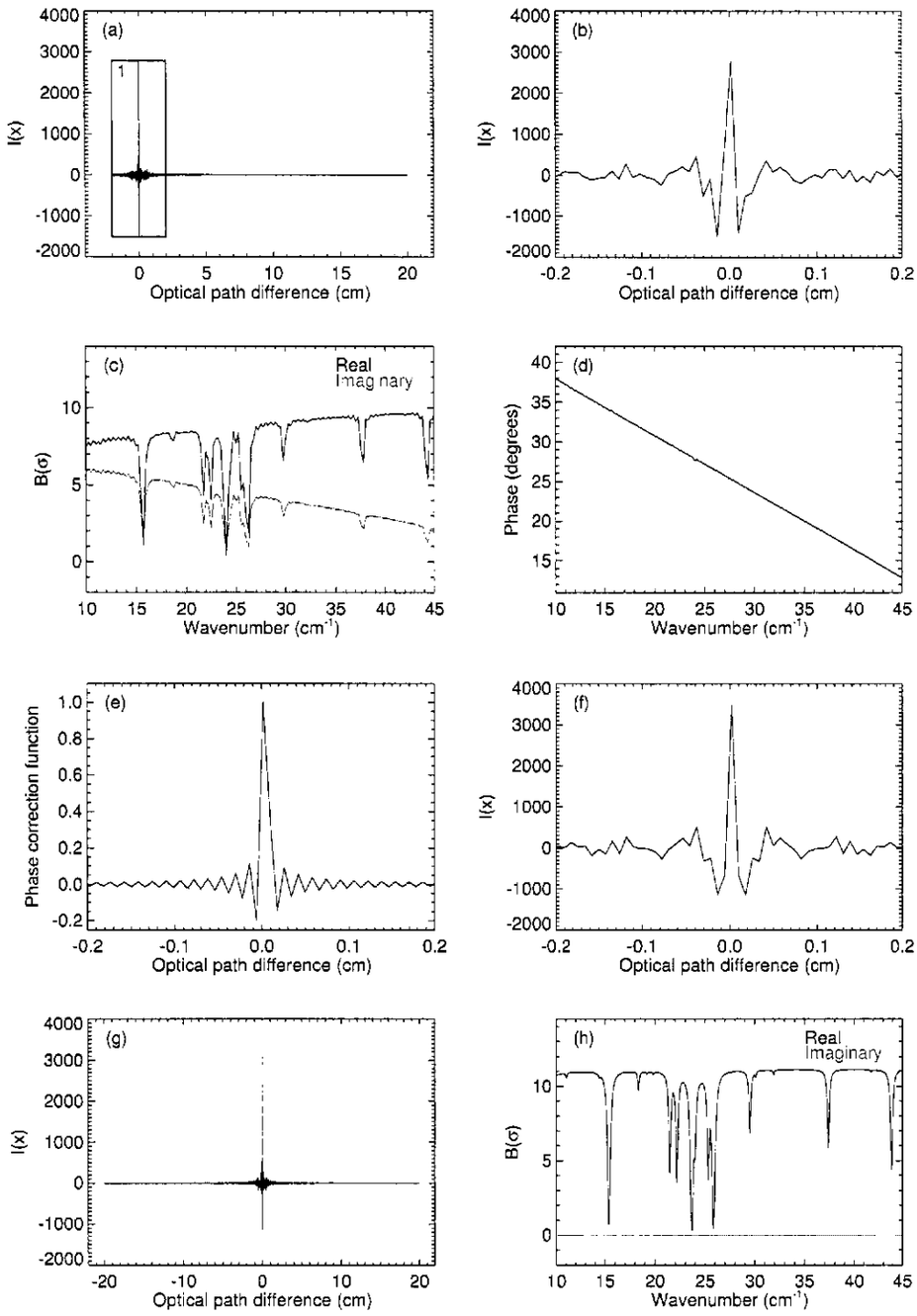

Figure 2.11: Phase correction by the Forman method. Panel (a) shows an asymmetric single-sided interferogram of a model spectrum of atmospheric transmission [78]. The blue box marked "1" denotes the double-sided component. Panel (b) shows the interferogram around ZPD. Panel (c) shows the Fourier transform of the double-sided interferogram. From the phase in Panel (d), the phase correction function is calculated in Panel (e). Panels (f) and (g) show the phase corrected interferogram. The spectrum of the phase-corrected interferogram is shown in Panel (h).

The magnitude contains the same information as the real component of the spectrum if the interferogram were symmetric [56]. However, scanning from $-L$ to L limits the spectral resolution to $\frac{1.207}{2L}$ (see Equation 2.44). By employing phase correction, the maximum OPD is greater, thereby increasing the spectral resolution [56]. The Forman method, explained below, utilizes a *single-sided* interferogram (i.e., an interferogram not sampled to equal OPDs on either side of ZPD) to correct for phase errors [56, 59].

Figure 2.11 is a graphical representation of the Forman method for a linear phase error. Panel (a) shows a single-sided interferogram of a model spectrum of atmospheric transmission [78]. As indicated by the blue box marked "1", a double-sided interferogram of $L = 2$ cm is extracted; Panel (b) shows the double-sided interferogram around ZPD where the asymmetry is clearly visible. The double-sided interferogram is Fourier transformed to yield the real and imaginary components, as shown in black and red, respectively, in Panel (c). The phase, shown in Panel (d), is determined using Equation 2.16. From the phase, ϕ, the phase correction function (PCF) is given by

$$PCF = \mathcal{F}^{-1}[e^{-i\phi}] = \int_{-\infty}^{\infty} e^{-i\phi} e^{i2\pi\sigma x} d\sigma. \tag{2.45}$$

The PCF, shown in Panel (e), is convolved with the single-sided interferogram. This convolution shifts information from the imaginary domain to the real, leaving only noise in the imaginary. As can be seen in Panel (f), the asymmetric interferogram from Panel (b) is now symmetric. Finally, the double-sided component is dropped and the interferogram is mirrored at negative positions, as shown in Panel (g). The spectrum of the phase-corrected interferogram contains only real elements, as shown in Panel (h) [59].

Using phase correction, only a short double-sided component is required in an interferogram. The remainder of the mechanical scan length is used for high resolution spectroscopy, thereby increasing the resolving power of the instrument (see Equation 2.44). Note that the phase correc-

tion shown in Figure 2.11 is for a linear phase error due to a sampling error (see Section 2.4.1). Other sources of phase error (such as electronics and optics) introduce higher-order phase errors (see Sections 3.7, 4.9, 5.7, 6.3 and 6.4). For an in-depth discussion of phase correction, the reader is directed to Spencer [79].

2.5.4 Zero filling

The last processing technique of note is zero filling [49, 56, 80]. As indicated in Section 2.5.1, each independent element in a discrete spectrum is $\frac{1.207}{2L}$ cm^{-1} away from its nearest neighbours [49]. However, there are situations where a narrower wavenumber spacing is advantageous or even necessary. (see Sections 4.4 and 4.5) [49, 56]. Zero filling is a computationally efficient technique of interpolating a spectrum onto a finer spectral resolution. [56, 80].

To zero fill an interferogram, new elements of value zero are added to the end of an interferogram. Without adding any new information, zero filling increases the maximum path length of the interferogram. By Equation 2.43, a longer path length corresponds to a finer wavenumber grid [55]. Note that the Nyquist frequency of the spectrum remains the same because zero filling does not change the sampling interval, Δx, of the interferogram [49]. Zero filling is the preferred interpolation technique in FTS because it preserves the sinc function instrumental line shape of the Fourier transform spectrometer [49, 72].

2.6 Summary

Chapter 2 provided a basic overview of Fourier transform spectroscopy. The mathematics underlying Fourier transforms (see Sections 2.1 and 2.2) were introduced to understand the instrumental effects present in an interferogram (see Section 2.4) measured by an ideal Michelson

interferometer (see Section 2.3). Section 2.5 outlined the significant post-processing needed to recover a spectrum from a measured interferogram.

Supplemental topics in FTS are introduced in later chapters as needed. For a more in-depth discussion of Fourier transforms, the reader is directed to Bracewell [51]; Brigham [53]; Champeney [50]; James [54]; and Walker [58]. For texts specifically covering FTS, the reader is directed to Bell [55]; Davis, Abrams & Brault [49]; and Griffiths & de Haseth [56].

With this background in place, Chapter 3 examines the Fourier transform spectrometer used in the SPIRE imaging spectrometer.

Chapter 3

The SPIRE imaging Fourier transform spectrometer

> *"It being now evident that there was a refraction of rays coming from the sun, which though not fit for vision, were yet highly invested with a power of occasioning heat. (...) If we call* light, *those rays which illuminate objects, and* radiant heat, *those which heat bodies, it may be inquired, whether light be essentially different from radiant heat."*
>
> - Sir William Herschel, "Experiments on the Refrangibility of the Invisible Rays of the Sun," *Philosophical Transactions of the Royal Society of London*, Volume 90 (1800).

The Herschel Space Observatory (HSO) and the Spectral and Photometric Imaging Receiver (SPIRE) were introduced in Chapter 1. SPIRE consists of two complementary sub-instruments: a three-band imaging photometer and a two-band imaging Fourier transform spectrometer (IFTS) [5]. Chapter 2 described Fourier transform spectroscopy (FTS), the spectroscopic technique used in the SPIRE spectrometer. This chapter outlines the spectrometer itself, focusing on the subsystems modelled in the Simulator for the Herschel Imaging Fourier Transform Spectrometer (SHIFTS; see Chapter 4). Several versions of SPIRE will be built prior to launch; this chapter describes the SPIRE model used in the first proto-flight model (PFM1) test campaign conducted in 2005 at the Ruther-

ford Appleton Laboratory (RAL) in Oxfordshire, England [5,43]. Any differences between the PFM1 and flight models are noted when necessary.

Section 3.1 provides an overview of the instrument; Sections 3.2 through 3.7 describe the individual subsystems. The successful implementation of SHIFTS frequently relied on research performed by members of the international SPIRE consortium. When results from other institutions are presented in this chapter, appropriate credit is given. The latter sections also include results from the PFM1 test campaign; Chapter 6 and Appendix B detail the analysis of PFM1 data performed for this thesis. (It should also be noted that elements of this chapter are based on internal SPIRE technical documents because complete descriptions of certain subsystems were not available in the scientific literature at the time of publication.)

3.1 Overview of the SPIRE spectrometer

This section describes the optical layout of the SPIRE spectrometer and outlines several important design considerations. Figure 3.1 shows a schematic of the spectrometer side of the SPIRE focal plane unit (FPU; the structure containing the SPIRE optics and detection systems) and Figure 3.2 shows the physical and optical layouts of the spectrometer. Note the symmetry of the spectrometer about an imaginary line between the two beamsplitters in Figure 3.1 and Panels (b) and (c) of Figure 3.2; these figures show the position of zero path difference (ZPD) described in Section 2.3.2.

The compact size of the SPIRE FPU ($690 \times 410 \times 410$ mm) introduces challenging optical constraints [31,66,83]. The use of powered mirrors within the interferometer maintains small beam sizes [66]. Oversized optical components are required to limit the diffraction effects of the long wavelengths observed in SPIRE [83, 84]. Alignment issues are also important because of the 22

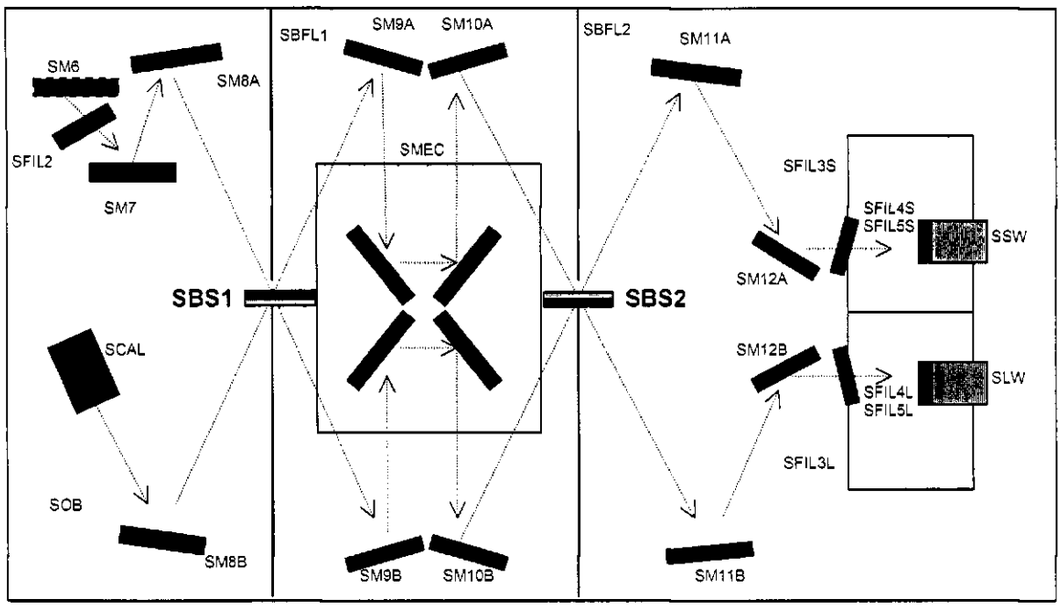

Figure 3.1: Schematic of the SPIRE spectrometer [81,82]. The dotted arrows denote the direction light travels; the dark blue boxes denote mirrors; the dark green boxes denote filters; the light blue boxes denote the spectrometer mechanism and the 1.7 K enclosure (from left to right); the orange boxes denote the bolometer detector assemblies; the pink box denotes the spectrometer calibrator; and the red/green boxes denote the beamsplitters (red corresponds to the inductive side and green to the capacitive side of the beamsplitter). The SM6 mirror is dashed to indicate its location on the photometer side of the focal plane unit. (Figure courtesy of Dr Douglas Griffin, Rutherford Appleton Laboratory, Oxfordshire, England.)

components in the optical path of the sky port [66,85,86]. These considerations are all balanced in the optical design to optimize image quality and maximize throughput [66,83,86].

Following reflections from the Herschel primary and secondary mirrors (see Panel (a) of Figure 3.2), light enters the SPIRE FPU through a filter (CFIL1; optics common to both the photometer and the spectrometer are prefixed by C) with a high wavenumber cutoff at 100 cm^{-1} (see Section 3.6.1) [87]. Aside from the primary and secondary mirrors (see Section 3.2.2), all mirrors in the SPIRE optical path are made of Aluminum 6061 and have a reflectance of 99 % at SPIRE wavelengths [5]. The SPIRE focal plane unit must be cooled to 4.5 K by the Herschel cryostat because the peak blackbody emission (see Equation 1.1) of any surface between 7 and 25 K falls within the SPIRE band [86].

Inside the SPIRE FPU, the first common mirror (CM3 in Panel (c) of Figure 3.2) projects an image of the telescope pupil onto the beam steering mirror (BSM; CM4 in Panel (c) of Figure 3.2), which controls the fine pointing of the telescope field-of-view (FOV) [88, 89]. The final common mirror (CM5) images the beam onto the spectrometer pickoff mirror (SM6 in Figure 3.1 and Panel (c) of Figure 3.2) that folds the beam into the spectrometer half of the SPIRE FPU [5, 86].

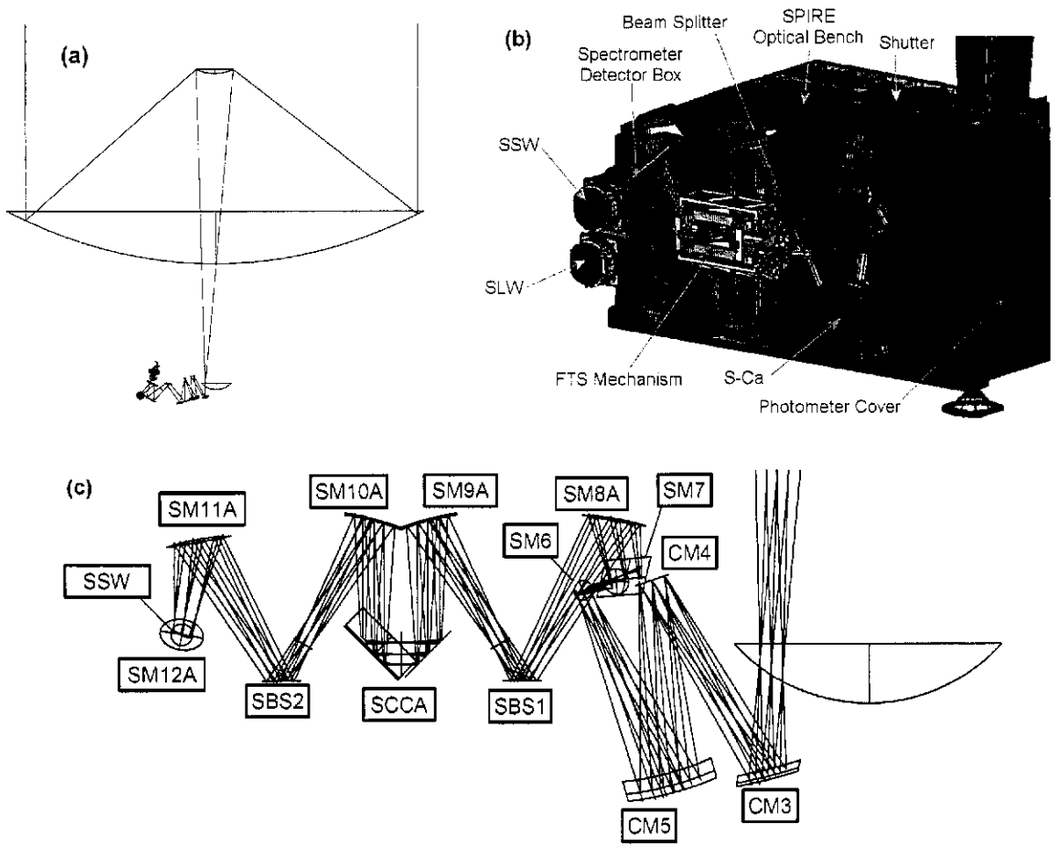

Figure 3.2: Physical and optical layouts of the SPIRE spectrometer [66, 81]. Panel (a) shows an optical raytrace of the Herschel primary and secondary mirrors with the optical path of the SPIRE photometer shown to scale. Panel (b) shows a computer rendering of the spectrometer side of the SPIRE focal plane unit with the cover removed; the red conic sections represent the beams. Panel (c) shows the optical path of the spectrometer; the symmetric lower half is generated by reflection about an imaginary line joining the two beamsplitters (SBS1 and SBS2). In Panel (c), common optics (prefixed by C) are located on the photometer side of the FPU. (Figures courtesy of Dr Douglas Griffin, Rutherford Appleton Laboratory, Oxfordshire, England; and Dr Kjetil Dohlen, Laboratoire d'Astrophysique de Marseille, Marseille, France.)

The SPIRE spectrometer employs a modified *Mach-Zehnder* (MZ) design, first proposed in Ade, Hamilton & Naylor [90] and field tested in Naylor *et al.* [91] and Swinyard *et al.* [46]. Like the Michelson interferometer (see Section 2.3), the modified MZ design measures an interferogram to determine a spectrum (see Sections 2.4 and 2.5) [90]. But in contrast to the Michelson interferometer, the modified MZ design provides access to all the two input and two output ports of the interferometer. The use of novel intensity *beamsplitters* (explained in Section 3.4) doubles the theoretical optical efficiency of the modified MZ design over that of a classic Martin-Puplett interferometer because light of all polarizations is detected [46, 66, 90–93]. In the modified MZ design, the arms of the classic MZ interferometer are folded, reducing the mass and volume of the interferometer (critical parameters for any space mission) [60, 90]. This folding allows a single translation stage to simultaneously modulate the optical path of both beams. Therefore, a change of Δx in stage position changes the optical path difference (OPD) between the two beams by $4\Delta x$ [46]. (Section 4.8.3 provides a mathematical treatment of the optical paths in the modified MZ design.)

Inside the spectrometer cavity, the telescope beam passes through a second low-pass filter (SFIL2 in Figure 3.1) and is folded by several mirrors (SM7 and SM8A in Figure 3.1 and Panel (c) of Figure 3.2) onto the first beamsplitter. Incident on the opposite face of the beamsplitter is light from the *spectrometer calibrator* (SCAL; explained in Section 3.3). The reflected and transmitted beams are directed to complementary collimating mirrors (SM9A and SM9B in Figure 3.1) that fold the light onto the back-to-back roof-top mirrors mounted on the *spectrometer mechanism* (SMEC; explained in Section 3.5). Following reflection from the roof-top mirrors, light is folded back to the camera mirrors (SM10A and SM10B in Figure 3.1) and then directed to the second beamsplitter (SBS2 in Figure 3.1 and Panel (c) of Figure 3.2) [5, 86].

Two pairs of mirrors (SM11A and SM12A, and SM11B and SM12B, both in Figure 3.1)

focus the beams through separate low-pass filters (SFIL3S and SFIL3L in Figure 3.1) into the 1.7 K enclosure of the bolometer detector assemblies (BDAs), which house the detection systems for the two spectrometer bands [94]. According to the design specifications, the *spectrometer long wavelength* (SLW) band covers 315 – 670 μm (14.9 – 31.7 cm^{-1}); the *spectrometer short wavelength* (SSW) band covers 200 – 325 μm (30.8 – 50.0 cm^{-1}). Inside the BDAs, each beam passes through a *low-pass filter stack* (explained in Section 3.6.1) and is focused onto the *feedhorns*. The feedhorns (explained in Section 3.6.2) act as high-pass filters and couple the light to the *spider-web bolometers*. Cooled to 300 mK by an internal Helium-3 refrigerator, the bolometers (explained in Section 3.6.3) detect the incident radiation. The measured signal is then filtered, digitized and read out by the detector electronics (explained in Section 3.7) [5].

The remaining sections of this chapter (3.2 to 3.7) describe individual components of the SPIRE spectrometer, concentrating on elements modelled in SHIFTS. For a complete description of the optical layout of the SPIRE spectrometer and associated design considerations, see Caldwell *et al.* [83]; Dohlen *et al.* [66]; Dohlen, Origné & Ferlet [86]; Griffin, Swinyard & Vigroux [5]; and Swinyard *et al.* [46].

3.2 Herschel telescope

Though not a subsystem of SPIRE, the Herschel Space Observatory will have a considerable effect on the signal measured by the SPIRE spectrometer [5]. The contributions of telescope pointing and thermal background are included in SHIFTS; their implementation is covered in Sections 4.6, 4.7 and 4.8.2.

3.2.1 Pointing effects

The orientation of Herschel will determine the FOV that SPIRE observes [5]. The large inertial mass of Herschel will ensure the pointing is relatively stable and not subject to high-frequency variations [62]. The one standard deviation pointing errors included in SHIFTS are as follows:

Absolute pointing error (APE) The angular difference between the commanded line of sight (LOS) and the actual LOS may be 3.7 arcsec per axis [95].

Relative pointing error (RPE) The telescope may drift off the LOS by 0.3 arcsec per axis in a one minute period [95].

3.2.2 Thermal effects

As stated in Section 1.2, the Herschel telescope has a 3.5 m diameter passively cooled primary mirror [4, 5]. The mirror is composed of 12 petals of silicon carbide (SiC) manufactured by the European Aeronautic Defense and Space (EADS)-Astrium in Toulouse, France [4, 96, 97]. Also constructed by EADS-Astrium, the 30.8 cm diameter secondary mirror is composed of a single piece of SiC [97].

The primary and secondary mirrors will emit radiation as blackbodies (see Equation 1.1) with temperatures between 70 and 90 K and emissivities between 1 and 3 % [85, 96, 98]. The exact temperature and emissivity of the mirrors cannot be determined until the HSO is in orbit because the thermal conditions at the second Lagrangian point (L2) are largely unknown [66, 99]. However, the temperature will be stable because of their large thermal masses. A drift rate of no more than 180 $\mathrm{mK\,hr^{-1}}$ is expected; see Griffin, Griffin & Swinyard [81, 96]. In addition, the emissivity and temperature are anti-correlated; if the emissivity is high, the mirrors radiate energy more efficiently and thus their equilibrium temperature is lower, and vice-versa [72].

Emission from the primary and secondary mirrors is expected to be the dominant source of noise in the SPIRE spectrometer [5, 96]. The background emission from these mirrors dramati-

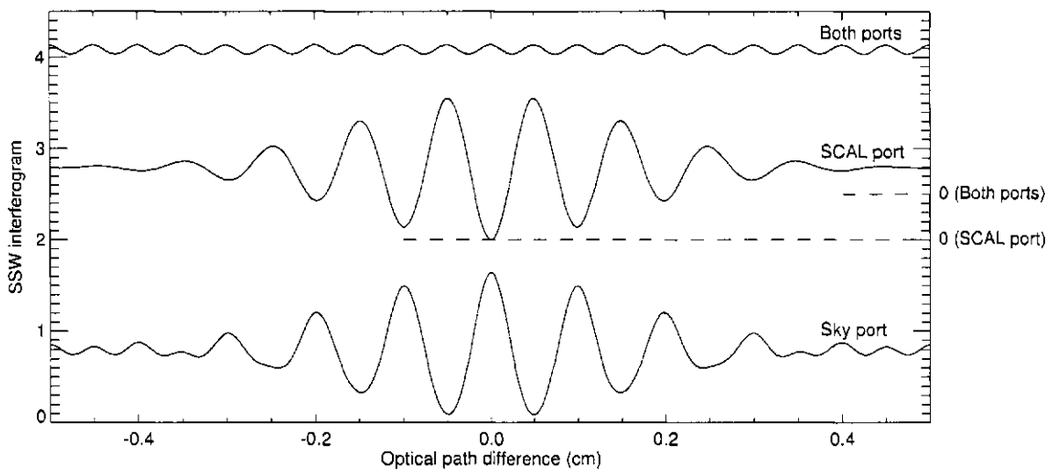

Figure 3.3: Compensation at the first output port. The interferogram representing the spectrometer calibrator port is offset by 2 units while the interferogram representing both ports is offset by 2.5 units.

cally increases the loading on the bolometers and the dynamic range on the interferogram [5, 99]. The solution to this problem is addressed below.

3.3 Spectrometer calibrator

The large telescope emission noted above strictly limits the dynamic range available for digitization of the interferogram. A small dynamic range (i.e., low modulation of the interferogram) is especially important when observing a weak astronomical signal (e.g., 20 K low emissivity dust). By including a continuum source at the second input port with similar spectral characteristics as the background signal, the astronomical signal is better matched to the data acquistion system [5, 100]. The spectrometer calibrator (marked by the pink box in Figure 3.1) provides this compensation in the SPIRE spectrometer.

To explain compensation, we return to the concept of interference introduced in Section 2.3. If we consider the SPIRE spectrometer as an ideal interferometer, conservation of energy

requires that the total energy entering the two input ports equals the total energy exiting the two output ports. Electromagnetic radiation entering the first input port interferes constructively at the first output port and destructively at the second output port; vice-versa for the second input port. The output ports are therefore said to be complementary [49, 101].

Figure 3.3 shows the result of compensation at the first output port (i.e., the SSW port). The interferogram of the astronomical source was represented by a cosine function (see Equation 2.9) while the interferograms of the SCAL and Herschel primary mirror emission were represented by the Fourier transform of the gaussian-broadened emission line shown in Figure 2.10. These interferograms were chosen for demonstrative purposes and are not representative of the inteferograms measured by the SPIRE spectrometer. Radiation from the first input port (i.e., the sky port) interferes constructively at the first output port; however, radiation from the opposite input port (i.e., the SCAL port) interferes destructively at the first output port. In the ideal case, the sum of the interferograms of the two input ports is an interferogram due only to the astronomical source. While a well-compensated background reduces the dynamic range requirements of the interferogram for sampling the astro-

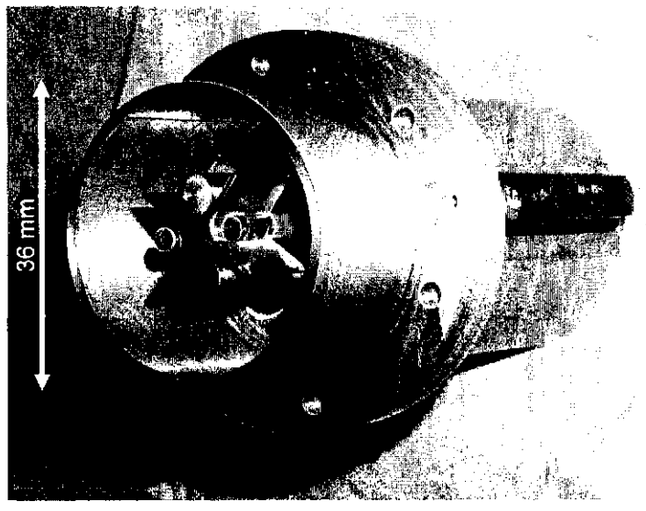

Figure 3.4: Photograph of the first proto-flight model of spectrometer calibrator (without the black coating) [99]. A redundant pair of sources is visible next to the primary pair; all four sources are thermally isolated from one another by the cross shape in the middle of the cavity. (Figure courtesy of Dr Peter Hargrave, Cardiff University, Cardiff, Wales.)

nomical signal, the use of SCAL doubles the background loading on the bolometers (i.e., the offset is twice as high) [45]. Section 4.8.3 provides a mathematical treatment of compensation; Sections 5.6.2 and 6.4 demonstrate simulated and real compensation, respectively.

Figure 3.4 shows a photograph of the PFM1 model of SCAL [99]. Built by the Astronomical Instrumentation Group (AIG) at Cardiff University in Cardiff, Wales, SCAL employs two sources, each consisting of an Aluminum end cap mounted on a Torlon strut [99, 100]. Following the notation of Hargrave & Griffin [100], SCAL-A denotes the larger source and SCAL-B denotes the smaller source. While only these two sources are heated, the entire mechanism is painted with a black coating with an emissivity that varies between 93 and 98 % [100]. Since SCAL is located at a pupil (and is therefore seen equally by all pixels), the geometric area of the sources defines their effective emissivity. Therefore, the two sources produce effective emissivities of 2 and 4 % because they fill 2 and 4 % of the pupil area [98, 99]. However, recent results indicate that the emissivity of the Herschel primary mirror is lower than suggested in Section 3.2.2 [96]. As such, the flight model of SCAL will likely employ 1 and 2 % sources [98].

Measured by a series of Lakeshore Cernox CX-1030 thermistors each with a temperature resolution of 5 mK, the operating range of the SCAL sources is $4-120$ K [100, 102]. The temperature is controlled by a digital feedback loop, which employs a proportional-integral-derivative (PID) controller [88]. Updating at 2.5 kHz, the PID controller utilizes the present measurement, the derivative of the present measurement and the integral of past measurements to maintain a constant temperature [88, 103]. Similar to the Herschel primary and secondary mirrors, the temperature of the SCAL sources is stable; the output intensity drifts by no more than 1 % over one hour of continuous operation [100]. Appendix B-2 analyzes the temperature stability of the SCAL sources used in the PFM1 test campaign. From that analysis, Section 4.5 describes how the SCAL temperatures

were simulated in SHIFTS.

3.4 Beamsplitters

Light from the two input ports of the intereferometer is split at the first intensity beamsplitter [5]. As indicated in Section 3.1, the successful implementation of the SPIRE spectrometer design relies entirely on the high and uniform efficiency of these beamsplitters over a wide spectral range [90, 91].

Built by the AIG at Cardiff University, the beamsplitters (SBS1 and SBS2 in Figure 3.1 and Panel (c) of Figure 3.2) are composed of inductive and capacitive metal meshes sandwiched on either side of a hot-pressed polypropylene substrate in a Fabry-Perot configuration [46, 87, 90, 91, 104, 105]. Differences in the optical properties of the capacitive and inductive grids produce different reflectance profiles for reflections from either side of the beamsplitter (see Figures 3.1 and 3.5) [72, 105].

In the discussion of the ideal Michelson interferometer in Section 2.3.2, we assumed the beamsplitter has 50 % reflectance and transmittance; in reality, no beamsplitter has such characteristics [49, 55]. Figure 3.5 shows the reflectance and transmittance of the flight model beamsplitters measured at a temperature of 300 K using a pair of Martin-Puplett interferometers [82, 93]. As can be seen, the beamsplitter efficiencies are high and uniform over the SSW band and vary between 0.4 and 0.6 over the SLW band. The reflectance and transmittance of the one flight model beamsplitter were also measured at 77 K and were in good agreement with the 300 K data [82]. The profiles shown in Figure 3.5 were used in SHIFTS to represent the beamsplitter reflectance and transmittance at their 4.5 K operating temperature (see Section 4.8.3).

In addition to the magnitude of the reflectance and transmittance, the phase of the re-

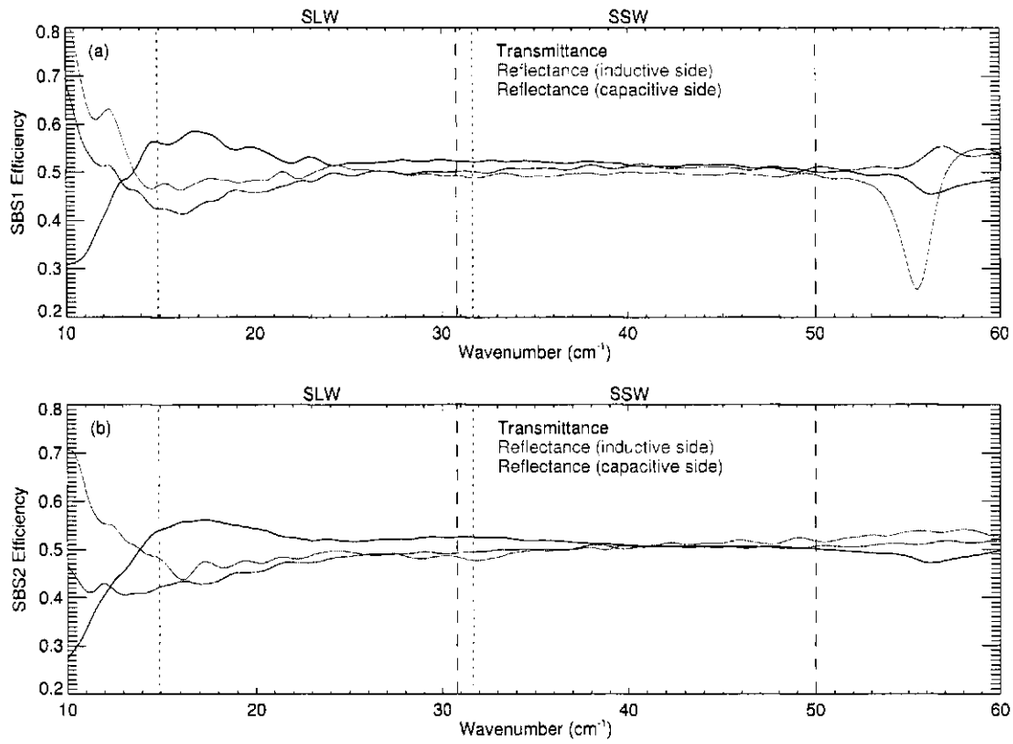

Figure 3.5: Transmittance and reflectance of the SPIRE beamsplitters. Panels (a) and (b) shows the reflectance and transmittance, at 300 K, for the *flight model beamsplitters* SBS1 and SBS2, respectively. The dotted lines denote the long wavelength array band edges and the dashed lines denote the short wavelength array band edges. (Data courtesy of Dr Peter Hargrave, Cardiff University, Cardiff, Wales.)

flected and transmitted electric fields is shifted by the beamsplitters. Since the polypropylene substrate is a dielectric with a higher refractive index than the surrounding medium, Fresnel's equations dictate that the phase of the reflected beam is shifted by π radians while the phase of the transmitted beam is unchanged [60]. Measurements of prototype beamsplitters with a free-standing grid deposited on a Mylar substrate also suggested that extra reflections in the air gap introduced additional phase shifts. However, no unidentified phase terms were measured in the beamsplitters with hot-pressed polypropylene substrates during the PFM1 test campaign in 2005 [72].

3.5 Spectrometer mechanism

Between the two beamsplitters, optical retardation is introduced with the spectrometer mechanism [5]. The development model of SMEC used in the PFM1 test campaign had a stage travel of 4 cm and was positioned such that zero path difference was located at 0.823 cm [106]. Because of the modified MZ design (see Section 3.1), the maximum mechanical path difference (MPD) of 3.177 cm corresponds to a maximum optical path difference of 12.708 cm [5, 90]. The variable scan length produces spectral resolutions up to 0.047 cm^{-1} (see Equation 2.44). The remaining stage travel provides the double-sided interferogram required for phase correction (see Section 2.5.3) [46]. In the SMEC flight model, the stage travel will be 3.85 cm with ZPD located at 0.35 cm [5, 107].

The spectrometer mechanism was designed by Dr Don Jennings at the Goddard Space Flight Center (GSFC) in Greenbelt, Maryland, and is being built by the Laboratoire d'Astrophysique de Marseille (LAM) in Marseille, France. Figure 3.6 shows a photograph of the development model of SMEC. As can be seen, SMEC consists of a translation stage suspended from a porch swing mechanism [5, 45, 107]. Back-to-back roof-top mirrors are mounted on the translation stage. Linear actuators provide frictionless stage movement while flexible pivots on the double parallelogram structure provide the restoring force and guarantee the motion remains parallel to the optical axis [46, 107]. This sophisticated assembly operates at 4.5 K and dissipates minimal power.

The stage position is measured by a Heidenhain LIP401A linear optical encoder mounted underneath the mirror carriage [45, 46, 108]. The encoder determines the stage position from the interference fringes of two complementary glass gratings, one fixed and one moving [107]. At cryogenic temperatures, the 4 μm spacing of the gratings provides an interpolated accuracy of 10 nm [45]. Instead of being sampled at regular intervals in position, the stage is time sampled at

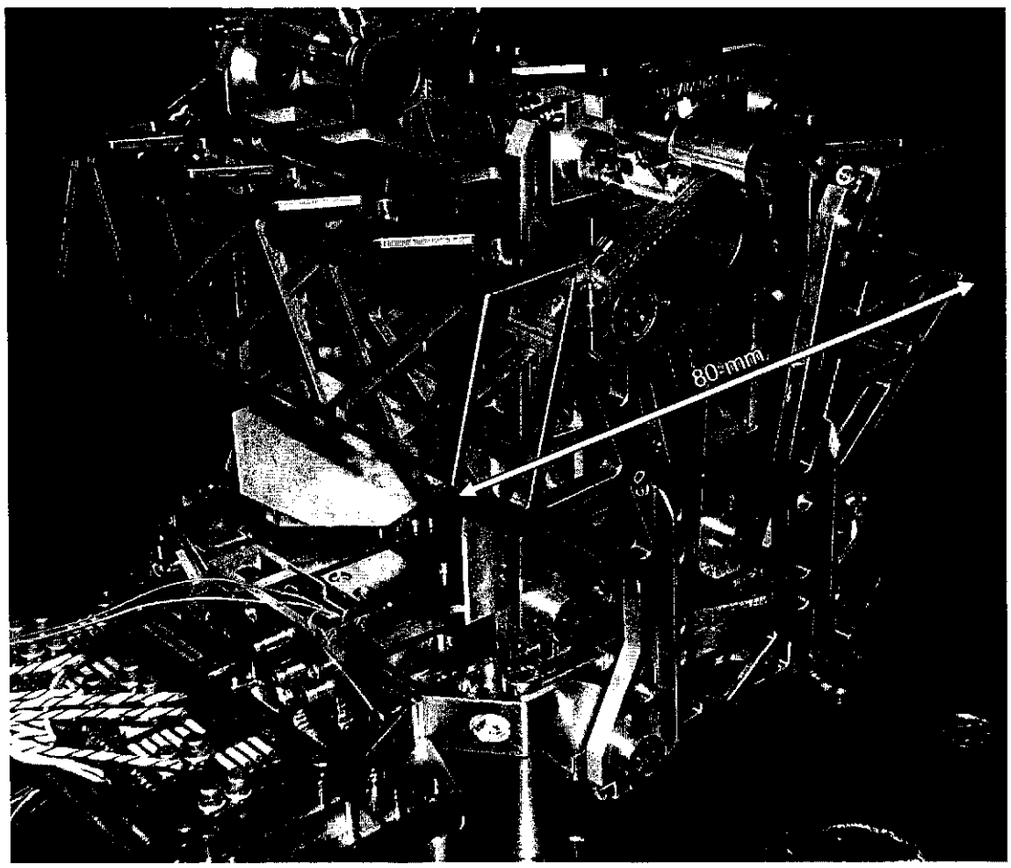

Figure 3.6: Photograph of the spectrometer mechanism development model, showing the double parallelogram structure with the translation stage and the back-to-back roof-top mirrors underneath. (Figure courtesy of Dr Dominique Pouliquen, Laboratoire d'Astrophysique de Marseille, Marseille, France.)

226 Hz [5]. While time sampling simplifies the readout electronics, it requires sophisticated Fourier analysis techniques to recover the spectrum (see Section 6.2) [109].

By varying the scan conditions of SMEC, the IFTS can be operated in two different modes: *continuous scan* or *step-and-integrate*. In continuous scan mode, the roof-top mirrors move at a constant speed for the duration of a scan. The measured signal is thus modulated at a frequency of

$$f = 4v_{\text{mech}}\sigma, \tag{3.1}$$

where v_{mech} is the mechanical speed of the stage (in $\text{cm}\,\text{s}^{-1}$) and σ is the wavenumber (in cm^{-1}).

Given an electrical cutoff frequency of 24.44 Hz (see Section 3.7) and a Nyquist frequency of 60 cm^{-1} (see Section 2.4.1), Equation 3.1 yields a maximum stage speed of 0.1 $cm\,s^{-1}$. During the PFM1 test campaign, the stage was operated at speeds between 90 and 900 $\mu m\,s^{-1}$ (see Section 6.1 and Appendix B-1). Utilizing the same feedback loop as SCAL (see Section 3.3), a PID controller uses successive encoder fringes to compensate for velocity drifts [46]. Although continuous scan dramatically shortens the scan time, uncertainties in the stage velocity will limit the performance of the spectrometer unless they are properly characterized [45]. Section 4.4 describes the simulation of the SMEC stage position based on PFM1 data analyzed in Appendix B-1.

In step-and-integrate mode, the stage moves sequentially from one stage position to the next and the integrated signal is measured at each location. However, this mode is unlikely to be used for actual observations because of the long time required for each scan [5]. As such, step-and-integrate mode was not implemented in SHIFTS; continuous scan mode was used exclusively.

3.6 Signal detection

As indicated in Section 3.1, the bolometer detector assemblies are placed at the two output ports of the interferometer [5]. Aside from the filter stacks, which are built by the AIG at Cardiff University, the entire BDAs are manufactured by the Jet Propulsion Laboratory (JPL) at the California Institute of Technology in Pasadena, California.

Figure 3.7 shows a photograph of a SPIRE bolometer detector assembly. Located inside the 1.7 K enclosure, the long wavelength BDA has 19 pixels and covers a wavelength range of 315 – 670 μm (14.9 – 31.7 cm^{-1}), and the short wavelength BDA has 37 pixels and covers a wavelength range of 200 – 325 μm (30.8 – 50.0 cm^{-1}) [5]. The bands were chosen to give approximately the same background power to each array [46]. As is shown in the following two sections, the mean

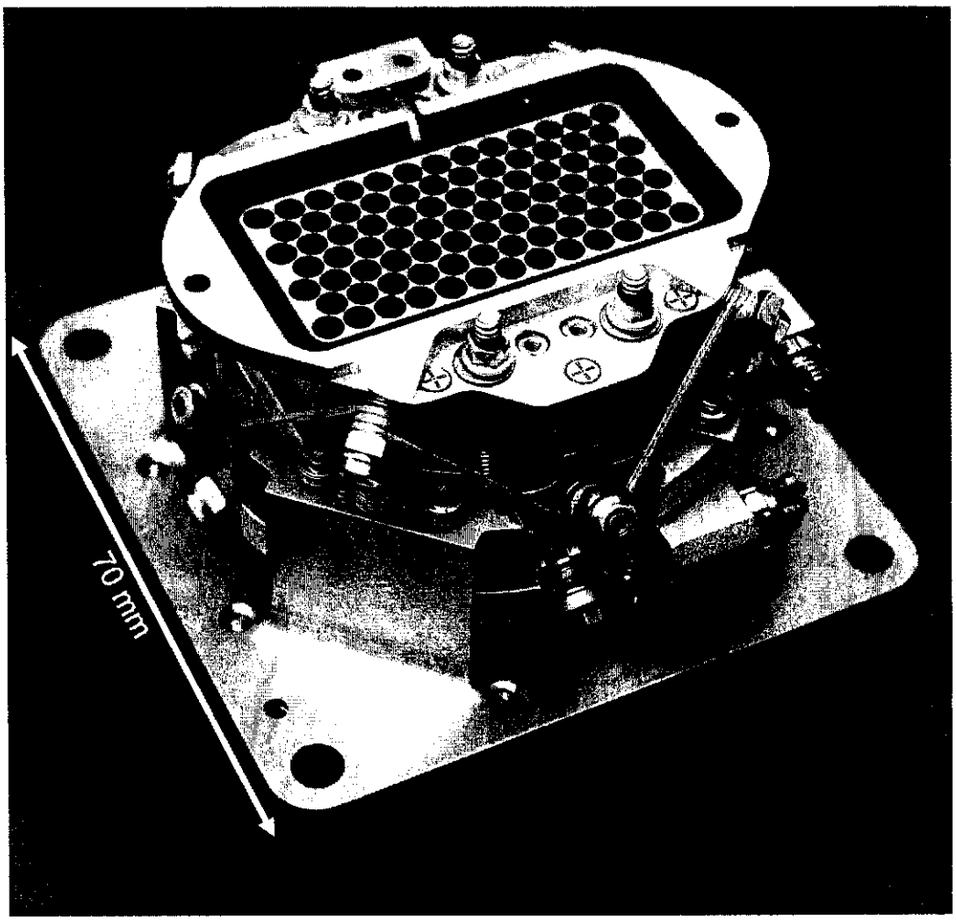

Figure 3.7: Photograph of a SPIRE bolometer detector assembly unit. The figure shows the photometer medium wavelength unit with the filter stack removed; the spectrometer arrays employ a nearly identical design. The hexagonally packed holes are the circular apertures of the feedhorns. (Figure courtesy of Dr James Bock, Jet Propulsion Laboratory, California Institute of Technology, Pasadena, California.)

bandpasses measured from the PFM1 data differ from the above design values by 1 or 2 cm^{-1}. To ensure a realistic result, the measured values were employed in SHIFTS.

3.6.1 Band-limiting filters

To limit the power on the detectors and control out-of-band radiation, a filter stack is mounted in front of each feedhorn array [45]. Each stack includes two low-pass filters (SFIL4 and SFIL5 in Figure 3.1) and a high density polyethylene (HDPE) field lens [87, 110]. Manufactured using the same technique as the beamsplitters (see Section 3.4), the lens and filters transmit 87 % of in-band radiation and reject over 99 % of out-of-band frequencies [5, 81, 104, 105].

As noted in Section 3.1, the telescope beam passes through three low-pass filters prior to entering the BDA modules: CFIL1, SFIL2 and SFIL3. Figure 3.8 shows the transmittance of these filters as well as the combined transmittance of the two filter stacks. The filter properties were measured by the AIG at Cardiff University using a Martin-Puplett interferometer [93, 110].

Figure 3.9 shows the total low-pass transmittance of the two detector arrays for each input port of the SPIRE spectrometer. As can be seen, the SLW and SSW transmittances begin to fall off at 30 and 50 cm^{-1} and drop below 1 % transmittance by 34 and 55 cm^{-1}, respectively. Moreover, due to its location in the optical path (see Figure 3.1), the SCAL beam does not pass through CFIL1 or SFIL2. Therefore, its total transmittance is approximately 23 % higher than the port that views the Herschel primary mirror and the astronomical source [87]. Section 4.8.3 outlines the integration of these filter profiles into SHIFTS.

3.6.2 Feedhorns

After transmission through the filter stack, radiation enters the circular aperture feedhorns [5]. As shown in Figure 3.10, the feedhorns are arranged in a hexagonal pattern to maximize

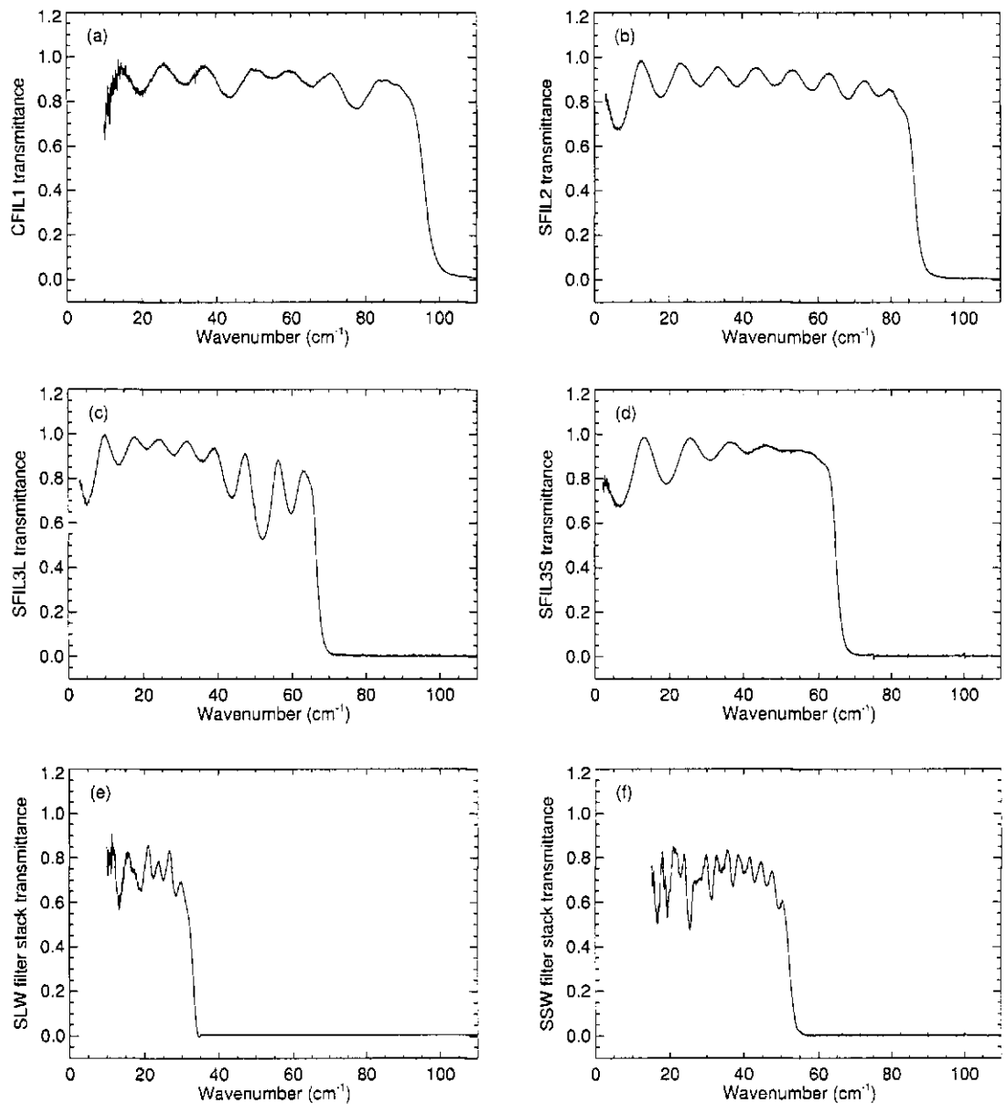

Figure 3.8: Transmittance of individual spectrometer low-pass filters. Panels (a)–(d) show the transmittance for individual filters CFIL1, SFIL2, SFIL3L and SFIL3S, respectively. Panels (e) and (f) show the combined transmittance for the long and short wavelength filter stacks, respectively. (Data courtesy of Dr Peter Hargrave, Cardiff University, Cardiff, Wales.)

use of the available area [111]. All but six of the SLW feedhorns are coaligned with SSW feedhorns [5]. To reference individual pixels, we follow the JPL naming scheme seen in Figure 3.10 (e.g., C3 is the central pixel in the SLW array) [112].

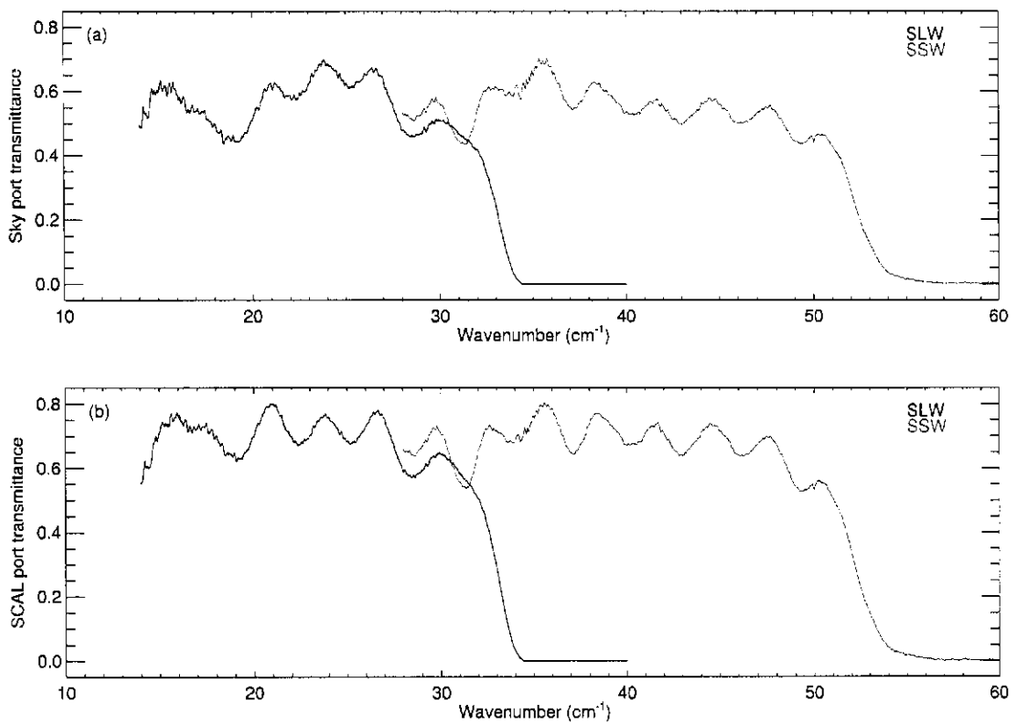

Figure 3.9: Total transmittance of the spectrometer low-pass filters. Panel (a) shows the transmittance for the first input port (astronomical source and Herschel primary and secondary mirrors) and Panel (b) shows the transmittance for the second input port (spectrometer calibrator). For clarity, the short wavelength transmittance is not plotted below 28 cm^{-1} in either panel. (Data courtesy of Dr Peter Hargrave, Cardiff University, Cardiff, Wales.)

Each gold-plated copper feedhorn is composed of a smooth-walled cone with a short circular waveguide connected at the base; the waveguide couples radiation into the integrating cavity containing the spider-web bolometers (explained in Section 3.6.3) [113, 114]. As shown in Figure 3.11, each conic section acts as a light collector, concentrating incident radiation onto a smaller area [115–117]. The response of a feedhorn to incident radiation is complex and depends on two interrelated factors: the radiation *modes* that propagate in the horn and circular waveguide, and the coupling of the *telescope diffraction pattern* to the *feedhorn antenna pattern* [83, 116–118]. The performance of the feedhorns is currently being investigated by members of the SPIRE consortium; the discussion below summarizes the accepted understanding at the time of publication [5, 119].

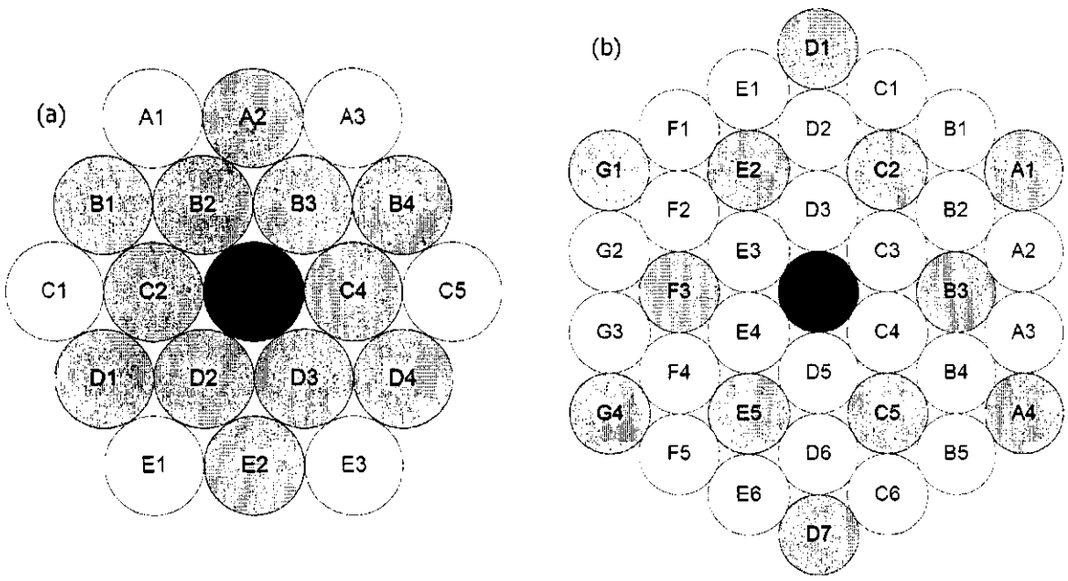

Figure 3.10: Pixel maps of the spectrometer arrays. Panel (a) shows the long wavelength pixels and Panel (b) shows the short wavelength pixels. In both panels, the blue pixels indicate the pixels that overlap in both arrays and the red pixel indicates the central pixel. (Figures courtesy of Dr Tanya Lim, Rutherford Appleton Laboratory, Oxfordshire, England.)

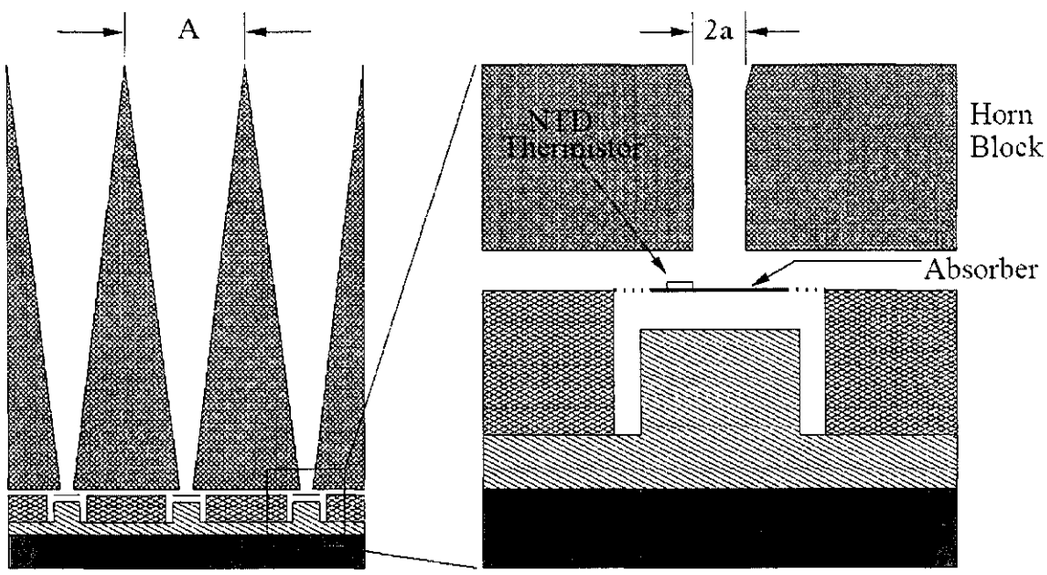

Figure 3.11: Cross section of a feedhorn block and an integrating cavity. The left-hand panel shows the close-packed feedhorns each with a circular opening of diameter A. The right-hand panel shows an integrating cavity fed by a circular waveguide of radius a. (Figure courtesy of Brooks Rownd, Smithsonian Astrophysical Observatory, Hilo, Hawaii.)

Radiation modes

To introduce the concept of radiation modes, we begin with the circular waveguide, which provides the long wavelength rejection for the two spectrometer bands [83, 113, 114]. The propagation of electromagnetic fields in a waveguide is described by Maxwell's equations [60, 120]. For a cylindrical geometry as shown in Figure 3.12, the general form of the electric and magnetic fields in a vacuum is derived in Waldron [120]. As per Waldron, the tangential electric field is given by

$$E_z = E_o J_m(kr) e^{i\omega t} e^{-i\beta z} e^{-im\phi}, \qquad [\mathrm{V\,m^{-1}}] \tag{3.2}$$

where E_o is a normalization constant (in $\mathrm{V\,m^{-1}}$), $\omega = 2\pi\nu$ is the angular frequency of the radiation (in radians $\mathrm{s^{-1}}$), t is the time (in s), β is the propagation constant (in radians $\mathrm{m^{-1}}$), $J_m(kr)$ is a Bessel function of the first kind of order m, and

$$k = \sqrt{\omega^2 \epsilon_o \mu_o - \beta^2} \qquad [\mathrm{radians\,m^{-1}}] \tag{3.3}$$

is the angular wavenumber introduced in Section 2.1, where ϵ_o and μ_o are the permittivity and permeability, respectively, of free space (see Table A-1) [120–122].

In Equation 3.3, the propagation constant is imaginary for frequencies less than $\sqrt{\frac{k^2}{\mu_o \epsilon_o}}$ [120, 121]. When β is imaginary, the tangential electric field in Equation 3.2 decays exponentially with z (i.e., no light propagates) [121]. To satisfy the boundary condition that $E_z = 0$ at the surface of a conductor, $J_m(k_o r)$ is zero for $r = a$, where a is the radius of the waveguide [120, 121]. Using $\beta = 0$ in Equation 3.3 with this boundary condition, we

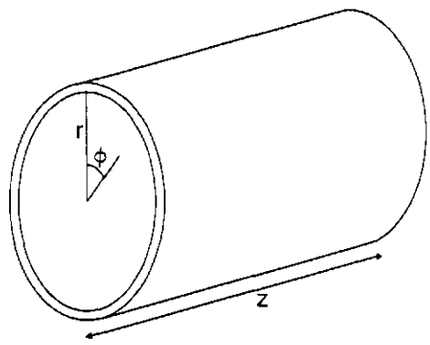

Figure 3.12: Cylindrical coordinate system for a circular waveguide.

Table 3.1: Feedhorn and circular waveguide properties for the two SPIRE spectrometer bands.

	Feedhorn diameter A (mm)[a]	Beam separation θ (arcsec)[b]	Waveguide radius a (μm)[a]	TE_{11} cutoff wavenumber σ_c (cm^{-1})	
				Theoretical	Measured[c]
SLW	3.80	49.0	197.5	14.9	15.60 ± 0.81
SSW	2.15	28.3	95.0	30.8	31.44 ± 0.26

[a] Source: Chattopadhyay *et al.* [113] and Rownd *et al.* [114].
[b] Source: Griffin, Swinyard & Vigroux [5].
[c] Source: Davis, Fulton & Naylor [125].

define a low spatial frequency cutoff,

$$\sigma_c = \frac{\chi_{mn}}{2\pi a}, \qquad [\mathrm{cm}^{-1}] \tag{3.4}$$

where χ_{mn} is the nth non-vanishing root of the Bessel function of the first kind of order m [122,123].

This solution to the wave equation produces a set of eigenfunctions, known as *transverse electric* (TE), defined by unique combinations of mode numbers m and n [120–122, 124]. A complimentary set of eigenfunctions known as *transverse magnetic* (TM) is derived given the second boundary condition that E_ϕ is zero at $r = a$ [120, 122]. Any arbitrary spatial configuration of the electric and magnetic fields in the waveguide is represented by the weighted sum of individual modes [124]. Note that Equation 3.4 applies to both TE and TM modes [122]. (For a graphical representation of individual field configurations, the reader is directed to Marcuvitz [122].)

For the fundamental TE_{11} mode ($m = 1$, $n = 1$), $\chi_{11} = 1.841$ [122–124]. Using the waveguide radii from Table 3.1, Equation 3.4 yields a theoretical cutoff wavenumber of 14.9 cm^{-1} for the SLW band and 30.8 cm^{-1} for the SSW band [119, 122, 124]. For comparison, Table 3.1 lists the mean cutoff wavenumbers measured from PFM1 data [125]. The inconsistency between the measured and theoretical values is not surprising considering the machining tolerances of the small diameter waveguides.

Multi-mode waveguides

In general, waveguides are designed to propagate only a single mode of light [121]. However, to accomodate the wide bandpass of the two spectrometer bands, the SLW and SSW waveguides are multi-moded [83, 113, 114]. Higher order modes have higher cutoff frequencies (i.e., higher order modes are attenuated at low spatial frequencies) because χ_{mn} increases with the order of the mode [122, 124]. For example, radiation propagating in the TM_{01} mode ($m = 0$, $n = 1$) in an SLW waveguide has a cutoff frequency of 19.4 cm^{-1} [119, 124]. Near the filter-stack cutoff wavenumber (see Section 3.6.1), five modes propagate in the SLW waveguide (TE_{11}, TM_{01}, TE_{21}, TE_{02} and TM_{11}) and three modes propagate in the SSW waveguide (TE_{11}, TM_{01} and TE_{21}) [85, 113, 114].

While multiple modes propagate in the feedhorns, each mode couples to the antenna system with a different efficiency [113, 114]. The *feedhorn efficiency*, $\eta_{\rm feed}$, is defined as the ratio of the power coupled to the bolometers to the power entering the feedhorn [85, 113]. For the TE_{11} mode propagating at short wavelengths, feedhorn efficiencies above 0.9 are seen in the simulations discussed in Chattopadhyay *et al.* [113] and Rownd *et al.* [114]. However, $\eta_{\rm feed}$ drops for long wavelengths and higher order modes. Furthermore, when multiple modes are present (i.e., at high spatial frequencies), interaction between the modes lowers the total power transmitted [113, 114].

Feedhorn antenna pattern

Given this understanding of modes and mode coupling, we now introduce the feedhorn antenna pattern. Similar to a radio telescope, each feedhorn produces an antenna pattern with sidelobes and a main beam perpendicular to the plane of the feedhorn aperture [118, 121]. To describe the feedhorn's response to incident light, we define the *main-beam efficiency*, η_s, as the

fraction of the feedhorn antenna pattern contained in the main beam.

In SPIRE, the center of the feedhorns are spaced $2F\lambda$ apart at a wavelength of 390 μm for the SLW band and 225 μm for the SSW band. The focal ratio of the final optics, denoted by F, is 5 [5, 83, 114]. The actual diameters of the feedhorn apertures are smaller than $2F\lambda$ because of the 10 μm-thick walls between the horns (see Table 3.1) [5, 113, 114]. For a $2F\lambda$ feedhorn, the main-beam efficiency is approximately 0.8. At longer wavelengths, η_s drops because more of the feedhorn antenna pattern is contained in the sidelobes. For example, at 670 μm (14.9 cm^{-1}), an SLW feedhorn is $1.13F\lambda$, which corresponds to a main-beam efficiency of 0.4 [111].

Incident radiation only couples to the main beam because the sidelobes view the cold 4.5 K SPIRE focal plane unit [5]. Measurements indicate that the main beam antenna pattern (or beam shape) for the TE_{11} mode is gaussian [83, 113, 114, 119]. However, the width of the beam shape was seen to vary with frequency [113, 114]. The presence of multiple modes further complicates the beam shape because higher order modes are not centrally peaked [83, 113, 114]. Therefore, the resultant beam shape has a more flattened top, especially for higher frequencies where more modes propagate [83, 113, 114, 119].

The feedhorn antenna pattern also defines the angular size of the sky seen by each feedhorn. As noted in Table 3.1, the SLW and SSW beams are spaced 49.0 and 28.3 arcsecs apart. After accounting for vignetting, the angular diameter of the SPIRE spectrometer beam is 2.6 arcmin [5]. From Equation 2.37, this corresponds to a solid angle of 4.5×10^{-7} steradians. As indicated in Section 2.4.4, the finite size of the entrance aperture convolves the spectrum by a rectangle function of width $\frac{\Omega\sigma}{2\pi}$ [49]. However, the resultant scale change is small (4.30×10^{-6} cm^{-1} at 60 cm^{-1}) and was therefore ignored in SHIFTS. Furthermore, the small solid angle shows that the Jaquinot criteria (see Equation 2.39) is satisfied in the SPIRE spectrometer

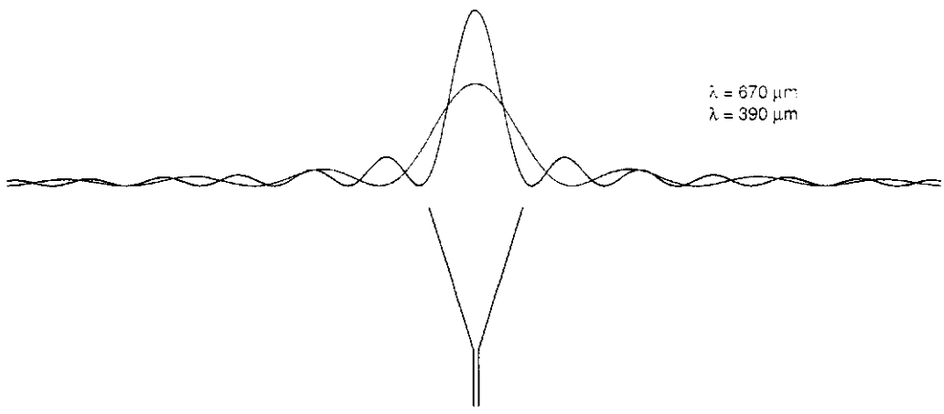

Figure 3.13: Example of aperture efficiency. The figure shows a spectrometer long wavelength feedhorn and the Airy profiles of two wavelengths within the SLW band.

Aperture efficiency

The final efficiency related to the beam shape and the size of the feedhorn aperture is the *aperture efficiency*. To define this term, we first introduce the telescope diffraction pattern. As derived in Born & Wolf [60], the Fraunhofer diffraction pattern due to a circular aperture of diameter d (in this case, the Herschel primary mirror) is the *Airy profile*, given by

$$I(x) = I_o \left[\frac{2J_1(r)}{r}\right]^2, \qquad [\mathrm{W}] \tag{3.5}$$

where I_o is the maximum power (in W), $J_1(r)$ is the first order Bessel function of the first kind and $r = \frac{\pi d\theta}{\lambda}$, where θ is the angular radius. The first minimum of Equation 3.5, located at $r = 1.22\pi$, defines the radius of the Airy disc,

$$\theta = \frac{1.22\lambda}{d}. \qquad [\mathrm{radians}] \tag{3.6}$$

The aperture efficiency, η_A, defines the coupling of the feedhorn beam shape to the Airy disc of the telescope diffraction pattern [83, 111]. The aperture efficiency is at a maximum of 0.76 for a $2F\lambda$ feedhorn [111]. As the wavelengths increases, the radius of the Airy disc increases and the aperture efficiency drops. Figure 3.13 is a graphical representation of the aperture efficiency at two

different wavelengths. At a wavelength of 670 μm, the Airy disc is oversized in comparison to the feedhorn so less energy is coupled to the feedhorn antenna pattern [83, 111]. At that wavelength, the aperture efficiency falls to 0.4 [111].

In summary, this section demonstrated the complexity of coupling light through the feedhorns to the integrating cavity. Each of the three interconnected efficiencies (aperture, feedhorn and main-beam) have mode and wavelength dependencies [5, 66, 83, 85, 113, 114, 118–122, 124, 126]. As indicated at the beginning of this section, SPIRE consortium members are analyzing the PFM1 results to characterize the feedhorn performance [5, 119]. Given our current understanding, Sections 4.8.1 and 4.8.3 outline how the feedhorns were modelled in SHIFTS.

3.6.3 Bolometers

The spider-web bolometers, located in the integrating cavity below the circular waveguide, are used to detect the incident radiation [5, 113, 127]. By definition, a bolometer measures radiation by measuring changes in resistance generated by the absorbed radiation [127–129].

Figure 3.14 shows a photograph of an array of SPIRE bolometers. A temperature sensitive absorber with a low heat capacity is connected to a heat sink through a thermal conductance [5, 127, 130]. In the case of SPIRE, the absorbing element is a metallized silicon nitride (Si_3N_4) micromesh in a spider-web pattern. An alternating current (AC)-biased current flows through a neutron transmutation doped (NTD) germanium thermistor bonded to the Si_3N_4 [131, 132]. Incident radiation is absorbed by the micromesh, increasing its temperature with a characteristic time constant (in s) denoted by τ. The temperature increase lowers the absorber's resistance, which is measured as a change in voltage by the NTD thermistor [127, 130, 131]. The bolometers are cooled to 300 mK to limit detector noise [127].

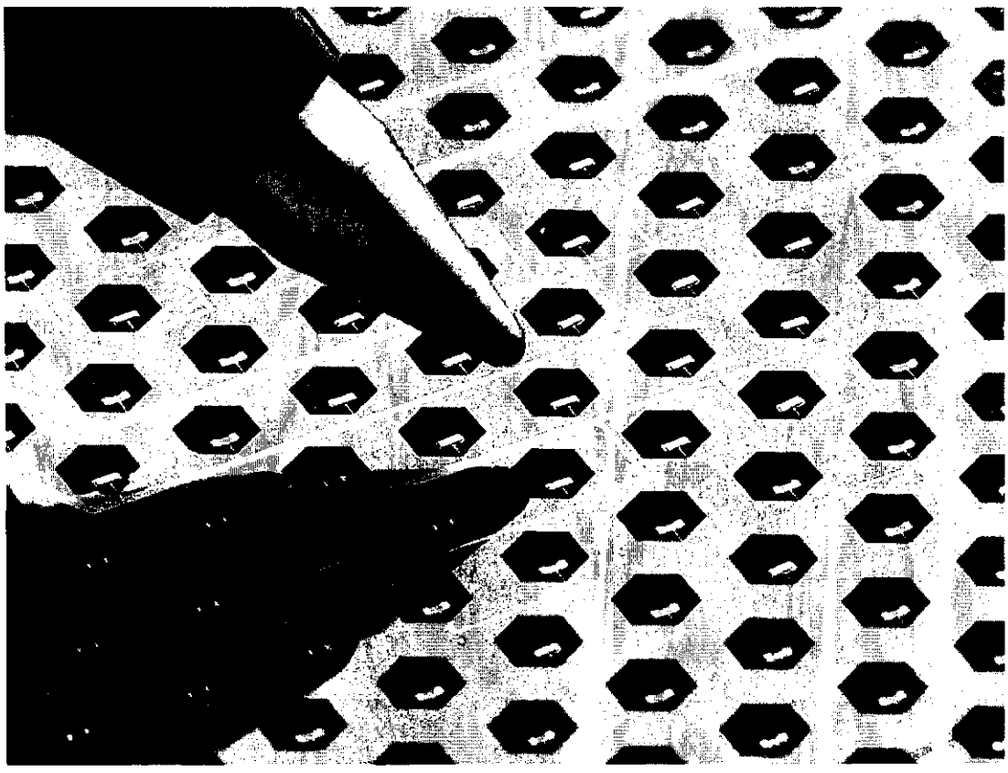

Figure 3.14: Microscope photograph of an array of SPIRE bolometers. The neutron transmutation doped germanium thermistor (in white) is located on the edge of the metallized silicon nitride micromesh absorber. For a scale reference, note the pen in the top left-hand corner of the image. (Figure courtesy of Dr James Bock, Jet Propulsion Laboratory, California Institute of Technology, Pasadena, California.)

Using a technique outlined in Sections 5.7 and 6.3, the bolometer thermal time constants were determined from the measured phase of PFM1 data. The time constants of the 19 SLW bolometers ranged between 1.6 and 10.9 ms with a mean of 5.1 ms, while the 37 SSW bolometers ranged between 1.2 and 13.9 ms with a mean of 7.4 ms [133]. Like any detector, the bolometers are not perfect absorbers; the detective quantum efficiency (DQE) is 0.7 [5]. According to Griffin, Griffin & Swinyard [81], an absorbed power of 10 pW changes the measured voltage by 4 mV. However, no citation was found for this value in Griffin, Griffin & Swinyard [81] so its accuracy cannot be confirmed.

The largest noise contribution in the SPIRE spectrometer is *photon noise* due to emission from SCAL and the primary and secondary mirrors [5, 127]. Caused by random fluctuations in the arrival time of incident radiation, photon noise is proportional the square root of the number of absorbed photons [130]. The photon noise is generally given as a noise-equivalent power (NEP), which is defined as the incident power on a detector required to produce a signal output equivalent to the root-mean-square (RMS) noise output [134]. Expressed as a NEP, the photon noise is

$$NEP_{\text{photon}} = \sqrt{2hc\sigma Q}, \qquad [\text{W Hz}^{-1/2}] \tag{3.7}$$

where Q is the incident radiation (in W), σ is the wavenumber of the radiation (in cm^{-1}), c is the speed of light, and h is the Planck constant (see Table A-1) [111, 128].

3.7 Electronics and readout

Once photons are detected by the bolometers, the signal is converted into an electrical form and transmitted from the telescope back to Earth [5]. Cryogenic readout cables connect each bolometer to a junction field effect transistor (JFET) module [94]. Mounted outside the 4.5 K SPIRE

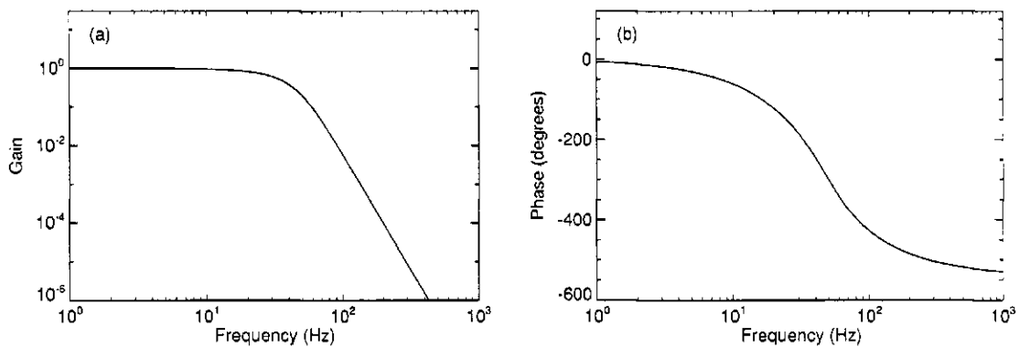

Figure 3.15: Transfer function of the six-pole Bessel filter of the first proto-flight model electronics. Panel (a) shows the gain of the transfer function while Panel (b) shows the phase.

enclosure and operating at a temperature of 120 K, the JFET modules amplify the detector signals and transmit them to the warm readout electronics located on the Herschel service module [94,135].

Lock-in amplifiers (LIAs) in the warm electronics read the AC signal from the bolometers and convert it to a direct current (DC) signal [135]. The LIAs then pass the signal through a 6-pole Bessel filter with a -3dB cutoff frequency of 24.44 Hz [135]. The transfer function of the electrical filter used in the PFM1 test campaign is given by

$$\begin{aligned} H_E(p) = &\left(\frac{1}{1+(7.58\times10^{-3})p+(16.03\times10^{-6})p^2}\right) \\ &\times\left(\frac{1}{1+(3.22\times10^{-3})p+(10.89\times10^{-6})p^2}\right) \\ &\times\left(\frac{1}{1+(6.26\times10^{-3})p+(14.65\times10^{-6})p^2}\right), \end{aligned} \tag{3.8}$$

where $p = i2\pi f$ is the Laplace variable (in radians s^{-1}) for a frequency f (in Hz) [106, 135]. The flight model electronics will include an additional low-pass filter [135]. Figure 3.15 shows the gain and phase of the PFM1 transfer function. In the warm electronics, the electrical noise is 5 nV $Hz^{-1/2}$ (1 nV = 10^{-9} V) and the total gain is approximately 3600 [135]. After being sampled at 80 Hz, voltages between 0 and 5 volts are digitized by a 16-bit analog-to-digital converter (ADC) [94,135].

3.8 Summary

This chapter introduced the design of the SPIRE spectrometer onboard the Herschel Space Observatory. The spectrometer employs a modified Mach-Zehnder interferometer to measure far-infrared (FIR) and submillimetre spectra. Sections 3.3 to 3.7 described the various optical, mechanical and electrical subsystems of the spectrometer.

However, it should be noted that this chapter is not a complete description of the SPIRE spectrometer instrument. Due to the lack of empirical data (e.g., pointing errors from the beam-steering mirror, bolometer crosstalk, etc.), the inadequate models or the limited impact (e.g., FIR and submillimetre emission from cold mirrors), various elements were not discussed [5, 83, 86, 88, 113, 126]. The following chapter describes how the components described in this chapter were integrated into SHIFTS.

Chapter 4

The Simulator for the Herschel Imaging Fourier Transform Spectrometer

> *"When the models are given a mathematical formulation, but analytic predictions are not possible, then quite often simulation can prove to be a useful tool, not only for describing the model itself, but also for investigating how the behaviour of the model may change following a change in the model."*
>
> - Byron J. T. Morgan, *Elements of Simulation*, Chapman and Hall (1984).

This chapter describes the design and implementation of the Simulator for the Herschel Imaging Fourier Transform Spectrometer (SHIFTS). Based on a simple conceptual model developed by Dr Bruce Swinyard at the Rutherford Appleton Laboratory (RAL) in Oxfordshire, England, SHIFTS was written to simulate the Spectral and Photometric Imaging Receiver (SPIRE) spectrometer onboard the Herschel Space Observatory (HSO) [5,45–47]. This chapter draws on the theoretical understanding of Fourier transform spectroscopy (FTS) described in Chapter 2 and the overview of the SPIRE spectrometer given in Chapter 3.

Section 4.1 describes the software architecture of SHIFTS. Sections 4.2 and 4.3 outline the initialization of the simulator and the creation of its master time grid, respectively. Sections 4.4

to 4.9 describe each of the six timelines generated by SHIFTS. Finally, Section 4.10 describes how the signal and positions were read out asynchronously and saved as a Herschel data product. It is important to note that the focus of this chapter is the physics underlying SHIFTS. Aside from the discussion of the simulator architecture and initialization in the following two sections, discussion of specific algorithms or code is limited and included only when necessary.

4.1 Simulator architecture

SHIFTS is the primary focus of this thesis; its development accounted for a substantial portion of my Masters program. The motivation for this work is given in Section 1.3. At completion, the entire program included 2000 lines of code in over two dozen sub-programs. To understand its overall operation, this section outlines the simulator architecture of SHIFTS.

SHIFTS was written to model the components and subsystems of the first proto-flight model (PFM1) version of the SPIRE spectrometer outlined in Chapter 3. As indicated in Section 3.8, not every element of the SPIRE spectrometer was included in SHIFTS. The elements included represent the subsystems that have the greatest effect on the measured interferogram and for which characterization data were available.

The simulator was written in version 6.2 of the Interactive Data Language® (IDL) distributed by Research Systems Inc [136]. IDL was well-suited to a project such as SHIFTS because of its powerful array manipulation capabilities and extensive visualization tools. Since SHIFTS operated on large data sets, the optimized array multiplications in IDL largely eliminated the use of loops in the program, dramatically lowering the execution time of the simulator. While every provision was taken to ensure SHIFTS executed quickly and with a minimal use of computer memory, the program remained computationally intensive. As an example, a single high resolution scan (defined

Table 4.1: Description of SHIFTS modules.

Module	Description
SMECMPD	Simulated the mechanical path difference of the spectrometer mechanism given a noise profile (see Section 4.4).
THERMALSCAL	Simulated the temperature of the two spectrometer calibrator sources given a noise profile (see Section 4.5).
THERMALHPM	Calculated the temperature of the Herschel primary mirror given a drift rate (see Section 4.6).
POINTINGHSO	Calculated the pointing of the Herschel telescope given the absolute and relative pointing errors (see Section 4.7).
POWERBOLO	Simulated the modified Mach-Zehnder interferometer by calculating the power on each bolometer given the simulated astronomical source and the above four timelines (see Section 4.8).
DETECTORSIG	Calculated the signal measured by the bolometer and the electronics given the power incident on each bolometer (see Section 4.9).

in Section 4.4) took ten minutes to generate on a 2.52 GHz computer with 1 gigabyte of RAM.

Some of the software architecture of SHIFTS was based on the structure of the SPIRE photometer simulator, which is currently being written by Bruce Sibthorpe at Cardiff University in Cardiff, Wales, as part of his doctoral thesis [44]. SHIFTS was composed of a series of independent modules. Each module was self-contained and simulated a physical quantity of the SPIRE spectrometer. Coupled to each module was a unique data structure, which contained a collection of scalars, arrays and sub-structures (a structure is analogous to an object in C++ or Java) [136, 137]. Like the SPIRE photometer simulator, the output of each module was a single timeline representing the physical quantity being simulated (e.g., the position of the spectrometer mechanism). Table 4.1 lists the primary modules in SHIFTS and offers a brief description of each.

Interaction between the modules was controlled by a core routine called the master control program (MCP) . The MCP passed input structures to the modules and retrieved output structures with a new or modified timeline. The modular nature of SHIFTS means a new version of

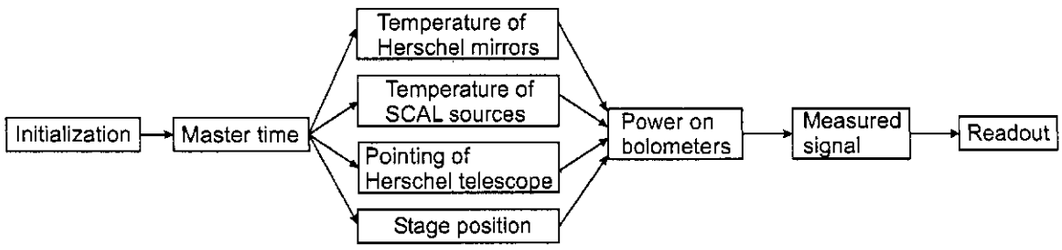

Figure 4.1: Order of execution of the SHIFTS master control program (from left to right). Each box represents a distinct component of the simulator.

a module can easily be implemented without affecting the rest of the simulator. To achieve this modularity, a well-defined set of input and output parameters was implemented for each module.

The order of execution of the MCP is shown in Figure 4.1. SHIFTS first executed an initialization routine, which initiated the run and populated the data structures mentioned above (the initialization routine was not considered a module because it produced no timeline). Next, a *master time* grid was created to ensure each timeline was sampled on the same interval (see Section 4.3). The timelines for the stage position, the pointing of the Herschel telescope, and the temperature of the primary mirror and SCAL sources were all simulated in parallel because of their independence from one another (see Sections 4.4 to 4.7). Given the above four timelines, a radiative transfer model was employed to simulate the propagation of radiation through the SPIRE spectrometer (see Section 4.8). The measured signal was calculated from the power incident on the bolometer (see Section 4.9). Finally, the measured signal was sub-sampled and saved into a Herschel data product (see Section 4.10).

The MCP was executed through an IDL command line script. The command line script operated in two user modes: common and expert. In the expert user mode, an extensive set of parameters were available, allowing the user (i.e., a SPIRE consortium member) to control every element of the simulation. In the common user mode, a limited subset of these parameters were

available for a user. This mode was designed so astronomers can explore the capabilities of the SPIRE spectrometer without having to understand the precise operation of the instrument. The command line interface was a functional yet temporary solution: future releases of SHIFTS will include a graphical user interface (GUI) that is currently under development.

The following two sections describe the initialization of SHIFTS. Each of the six primary modules in SHIFTS are then described in turn, beginning with Section 4.4.

4.2 Initialization

As indicated in the previous section, the primary goal of the initialization step was to initiate a run and populate the data structures used in each module. To perform this purpose, SHIFTS first read two files into memory: `user_settings.sav` and `ifts_settings.sav`. The former file contained user-controlled parameters (e.g., number of scans, location of calibration files) while the latter contained physical and optical parameters of the SPIRE spectrometer (e.g., the diameter of the feedhorns, the emissivity of the Herschel primary mirror). Controlled by the IDL command line script introduced above, the `user_settings.sav` file defined the conditions used for a specific run of SHIFTS.

To populate the data structures, SHIFTS read in several calibration files (all stored in the IDL `.sav` format) into memory. The calibration files included the noise profile of the spectrometer mechanism (SMEC; see Section 4.4), the noise profile of the spectrometer calibrator (SCAL; see Section 4.5), the reflectance and transmittance of the beamsplitters (see Sections 4.8.3), the transmittance of the filters (see Section 4.8.3), the various efficiencies of the optical and feedhorn systems (see Section 4.8.3) and a simulated astronomical source (SAS). Once SHIFTS read all the calibration files into memory, each data structure was populated. Aside from the file containing

the SAS, the precise contents of the calibration files are described in their respective sections. An internal housekeeping structure was also created to note important diagnostic parameters useful in debugging the code.

For the remainder of this section, we focus on the simulated astronomical source, the most complex input file. The SAS was a static (i.e., time-independent) three-dimensional data cube where each element of the cube was a specific intensity given in janskies (see Appendix A) per steradian [15, 23, 67]. Coupled to each specific intensity were three values: a right ascension denoted by α, a declination denoted by δ, and a wavenumber denoted by σ. Each right ascension-declination pair defined the spatial location of every element of specific intensity (for a rectangular coordinate system) while the wavenumber array defined the spectral location.

Figure 4.2 is a simple representation of the simulated astronomical source for a five-by-five pixel section of sky. Each associated array was defined by an initial value, a step size and a number of elements. Given these three values, the right ascension, declination, and wavenumber were

$$\alpha_i = \alpha_o + (i-1)\Delta\alpha - \left(\frac{\alpha_N - \alpha_o}{2}\right), \qquad \text{[arcsec]} \tag{4.1}$$

$$\delta_j = \delta_o + (j-1)\Delta\delta - \left(\frac{\delta_N - \delta_o}{2}\right), \qquad \text{[arcsec]} \tag{4.2}$$

$$\sigma_k = \sigma_o + (k-1)\Delta\sigma_{\text{sim}}, \qquad [\text{cm}^{-1}] \tag{4.3}$$

where α_o, δ_o and σ_o were the initial values of the right ascension, declination and wavenumber, respectively; $\Delta\alpha$, $\Delta\delta$ and $\Delta\sigma_{\text{sim}}$ were the step sizes of the right ascension, declination and wavenumber, respectively; and α_N and δ_N were the maximum value of the right ascension and declination, respectively. Due to the symmetry requirements of Fourier analysis (see Section 2.2), the initial value of the wavenumber grid was always fixed at 0 cm^{-1}. The indices i, j, k were incremented in integer steps between one and the number of elements for each respective array. The maximum

wavenumber was given by the Nyquist frequency, σ_N (see Section 2.4.2). The parenthetical terms in Equations 4.1 and 4.2 shifted the right ascension and declination so that, in the absence of pointing errors, the center of the data cube was aligned with the central pixel of each detector array. The size of the associated arrays was limited only the memory and processor speed of the computer running SHIFTS.

The initialization routine also performed two important checks on the spectral information contained in the SAS. First, SHIFTS ensured the line width of the SAS spectrum, $\Delta\sigma_{sim}$, was smaller than the spectral resolution defined by the maximum optical path difference (OPD) of the interferogram (see Equation 2.44) [49]. If $\Delta\sigma_{sim}$ was too coarse, we discovered that this produced an "anti-aliasing" effect. As described in Section 2.4.3, aliasing shifts spectral information beyond the Nyquist frequency (the highest sampled frequency in an interferogram) to a lower frequency position. In the case of anti-aliasing, the coarse sampling of the SAS spectrum provided insufficient frequency components to properly compute the discrete Fourier transform (DFT). Beyond an OPD of $\frac{1}{2\Delta\sigma_{sim}}$, the interferogram became periodic. In addition to checking the spectral line width, the initialization routine confirmed that the spectrum was sampled to a Nyquist frequency of 60 cm^{-1}, which is the highest wavenumber decade measured by the short wavelength array.

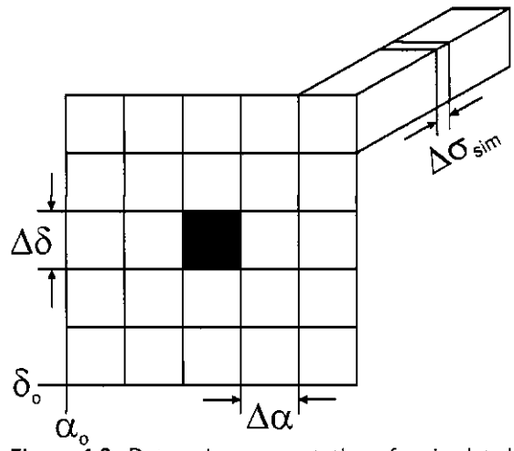

Figure 4.2: Data cube representation of a simulated astronomical source for a five-by-five pixel section of sky. The values α_o and δ_o define the initial positions of the right ascension and declination, respectively. The variables $\Delta\alpha$ and $\Delta\delta$ define the spatial spacing between each pixel; the spectral step size is given by $\Delta\sigma_{sim}$. The red pixel represents the center of the sky section.

Finally, the SAS data cube was converted into the units required by the POWERBOLO module (see Section 4.8). First, each spectrum was scaled by the ratio of the solid angle of a single SAS pixel and the fixed solid angle of the feedhorns (see Table 3.1) [5]. Next, the simulated astronomical source was converted from a specific intensity to an electric field. The specific intensity is a scalar field and does not undergo interference; however, the wave nature of the electric field does [60]. The specific intensity was first converted to a power per unit wavenumber given the speed of light (see Table A-1) and the throughput of the instrument. In a well-designed optical system, the throughput is constant. Given the geometric area of the entrance aperture (i.e., the Herschel primary mirror) and the diffraction-limited minimum resolvable point source (see Equation 3.6), the throughput is approximated by

$$A\Omega = \lambda^2, \qquad [\mathrm{m^2\ sr}] \tag{4.4}$$

where $\lambda = \frac{1}{100\sigma}$ is the wavelength (in m) [5, 85]. By reversing Equation 2.27, the electric field per unit wavenumber is given by

$$\mathrm{E} = \sqrt{\frac{2I}{c\epsilon_o A_f}}, \qquad [\mathrm{V\,m^{-1}\,(cm^{-1})^{-1}}] \tag{4.5}$$

where I is the irradiance (or the time-average of the Poynting vector) per unit wavenumber (in $\mathrm{W\,m^{-2}\,(cm^{-1})^{-1}}$), A_f is the area of circular aperture of feedhorn f (in $\mathrm{m^2}$; see Table 3.1), c is the speed of light and ϵ_o is the permittivity of free space (see Table A-1) [60, 67, 138].

An important consequence of using the electric field instead of the specific intensity relates to reflection and transmission in the optical system. As noted in Chapter 2.3.2, the efficiency of the beamsplitters is defined as either an amplitude reflection (or transmission) coefficient or a reflectance (or transmittance) [49, 60]. In Chapter 3, the efficiencies of the beamsplitters and low-pass filters were quoted as transmittances and reflectances. Since interference is performed on electric fields, the efficiencies in SHIFTS were defined in terms of the amplitude reflection and

transmission coefficient (see Section 2.3.2) [67].

4.3 The master time grid

As indicated in Section 4.1, the six timelines simulated by SHIFTS used the same master time grid, which ensured that all the timelines could be manipulated together. The clock speed of the Herschel digital processing unit (DPU) is 312.5 kHz. However, it was computationally prohibitive to sample the master time at the DPU clock speed. Instead, the SHIFTS master time clock was set to 500 Hz (312.5 kHz is a multiple of 500 Hz) and was assumed to have no error. As indicated in Section 2.4.2, to sample unambiguously a broadband spectrum, the highest frequency component must be measured at least twice per oscillation period [49]. The highest frequency component modelled in SHIFTS is 112.06 Hz (see Section 4.4). With the clock frequency of SHIFTS set at 500 Hz, the highest frequency component was oversampled by a factor of slightly more than two. For the remainder of this chapter, the master time grid is denoted by t_m, the master time spacing by Δt_m, and master time intervals by subscript m (e.g., z_m defines the position of the stage at a time interval m).

4.4 SMECMPD: timeline of the mechanical path difference of the spectrometer mechanism

This section outlines the simulation of the mechanical path difference (MPD) of the spectrometer mechanism (SMEC) for a single observation in the continous scan mode. The SMECMPD module utilized SMEC data measured during the SPIRE instrument PFM1 test campaign conducted at RAL in 2005.

Section 3.5 provided an overview of the SMEC subsystem. As described there, the back-to-back roof-top mirrors mounted on SMEC provide the optical retardation necessary to generate an interferogram [5, 107]. In the continuous scan mode, the SMEC stage translates at a fixed speed [5]. In SHIFTS, the elapsed time for a single scan was defined by the stage speed and the scan length, parameters set in `user_settings.sav`. In the common user mode, three scan lengths were permitted: low, medium and high resolution. Following SPIRE notation, a low resolution scan covered -0.07 to 0.07 cm relative to zero path difference (ZPD), a medium resolution scan covered -0.35 to 0.35 cm, and a high resolution scan covered -0.35 to 3.5 cm [139]. (Note that the above definition of resolution is employed for the remainder of this thesis even though it differs from the definition seen in Chapter 1.) In the expert user mode, any scan range between -0.35 and 3.5 cm was permitted.

To mimic normal stage motions, SHIFTS reversed the scan direction after each scan by changing the sign of the velocity. Following SPIRE notation, we defined a forward scan to have a positive velocity and begin at a negative stage position relative to ZPD; vice-versa for a reverse scan [139, 140]. A single run of SHIFTS consisted of one or multiple scans where each scan yielded one interferogram. The total run time was the product of the time for a single scan and the total number of scans. An additional half second was added between each scan, to represent the deceleration and acceleration phases of the stage [140]; during that time, the stage position was fixed.

The description of SMEC in Section 3.5 also noted that the stage position is time-sampled and controlled by a digital feedback loop [5, 88]. The combination of natural stage resonances, encoder errors and the feedback loop introduces a *velocity jitter* whereby equal increments in time do not correspond to equal increments in position [45, 46].

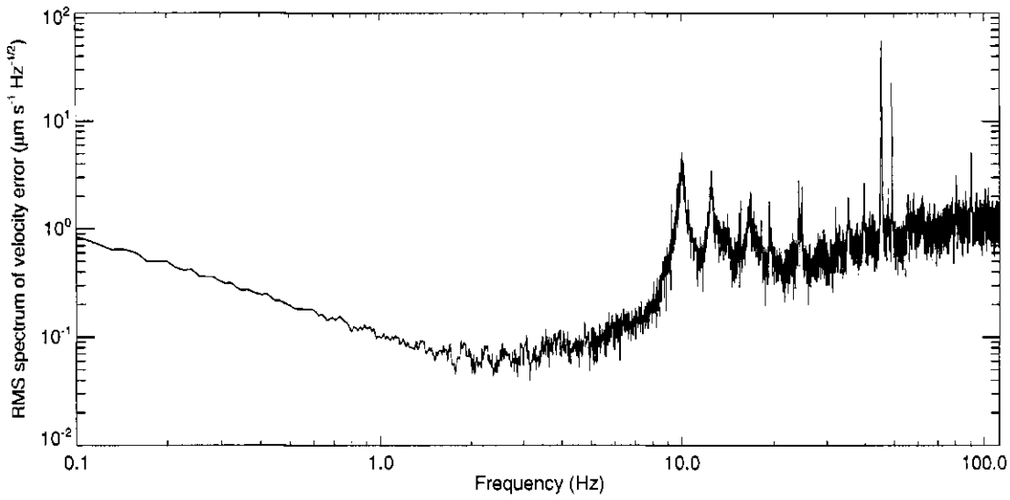

Figure 4.3: Model profile of velocity error from the spectrometer mechanism. The profile was determined from the velocity error spectra of eight scans taken at 452 $\mu m\,s^{-1}$ during the first proto-flight model test campaign conducted in 2005 at the Rutherford Appleton Laboratory in Oxfordshire, England (see Appendix B-1).

In order to properly model the stage position, it was first necessary to investigate the velocity jitter. The analysis of the velocity jitter from PFM1 data was conducted over several months and is described in detail in Appendix B-1. The result of this analysis was the noise profile (stored as a calibration file) shown in Figure 4.3. As indicated in the appendix, the noise profile was determined from the velocity error of eight scans taken at a mean stage speed of 452 $\mu m\,s^{-1}$. The Nyquist frequency of the profile was 113.06 Hz and the frequency spacing was 0.014 Hz.

Since the profile was determined from ground-based measurements, it cannot include the effects of the spacecraft environment. Recent finite element analysis indicates that micro-vibrations of the reactions wheels (used to control the orientation of the Herschel telescope) may produce accelerations on the order of 0.245 $m\,s^{-2}$ [141]. Subsequently, SPIRE consortium members at the Laboratoire d'Astrophysique de Marseille (LAM) in Marseille, France, suggested that these accelerations may excite resonances in SMEC [62, 142]. Unfortunately, the nature of these vibrations cannot

be fully understood until the spacecraft is launched. Once the effects are characterized in flight, a new noise profile similar to the one shown in Figure 4.3 can be substituted in SHIFTS.

Before the noise profile in Figure 4.3 was employed to simulate the MPD of the SMEC stage, the profile was first converted onto the time grid used in SHIFTS. As noted in Appendix B-1, the PFM1 data were sampled at 226.12 Hz for an average of 72.97 s. However, SHIFTS employed a sampling interval of 2 ms and a scan time that varied depending on the stage speed and scan length (e.g., a low resolution scan taken at a speed of 0.1 cm s^{-1} lasted only 1.4 s while a high resolution scan taken at 0.01 cm^{-1} lasted 385 s). Given Equation B-4, the Nyquist frequency for SHIFTS was 250 Hz; the frequency interval changed with the scan time (see Equation B-3) [49, 56].

The model profile was interpolated onto the SHIFTS frequency grid using the IDL INTERPOL routine, which employs a four-point cubic spline interpolation [136, 143]. Since the Nyquist frequency of the SMEC data from the PFM1 test campaign was only 113.06 Hz, any Fourier components present beyond 113.06 Hz were aliased to lower frequency locations when the stage positions were sampled (see Section 2.4.3). Therefore, no information could be determined on the stage performance between the 113.06 and 250 Hz. Instead, the simulated profile was zero-filled between those frequencies (see Section 2.5.4). In addition to the interpolation and the zero-filling, the simulated profile was normalized by multiplying each point in the interpolated spectrum by the square root of the SHIFTS frequency interval (which, as stated above, could vary from run to run).

To simulate realistic MPDs, SHIFTS then performed the following operations:

1. The interpolated spectrum was used as a noise envelope and was multiplied by random phase. As seen in Figure B-1(d), the phase of the measured SMEC data was random. A random number, ϕ, was generated between $-\pi$ and π radians for each frequency interval. The random numbers were created using the IDL RANDOMU routine, which is based on a technique de-

veloped by Park & Miller [136, 143, 144]. Each value in the interpolated profile was then multiplied by $(\cos\phi + i\sin\phi)$.

2. In the raw spectrum of the velocity error in Figure B-1, information was present at both positive and negative frequencies [49, 50]. However, data was only present in positive frequencies in the randomized spectrum. To mimic the measured spectrum, the randomized profile was butterflied so that the real component was symmetric about 0 Hz and the imaginary component was anti-symmetric; i.e., $\mathcal{R}(-f) = \mathcal{R}(f)$ and $\mathcal{I}(-f) = -\mathcal{I}(f)$.

3. A simulated velocity error, Δv_m, was determined by computing the Fourier transform of the randomized and butterflied spectrum. Since the real component of the simulated spectrum was even and the imaginary component was odd, the resulting velocity error was asymmetric and real (see Table 2.1) [51].

4. The simulated velocity error was converted from microns per second to centimetres per second. Then the mechanical path difference at each master time interval m was calculated by

$$z_m = v_m \Delta t_m + z_{m-1} - z_o, \qquad \text{[cm]} \tag{4.6}$$

where z_o was the initial position of the scan (in cm) and $v_m = \bar{v} + \Delta v_m$ was the sum of the user-defined stage velocity and the simulated velocity error (in $\mathrm{cm\,s^{-1}}$).

These four steps were repeated for each scan using the same interpolated profile. The simulated positions varied for each scan because a different random phase was employed for each iteration. Section 5.2 compares the mechanical path differences simulated using this technique with the results of the PFM1 data analyzed in Appendix B-1.

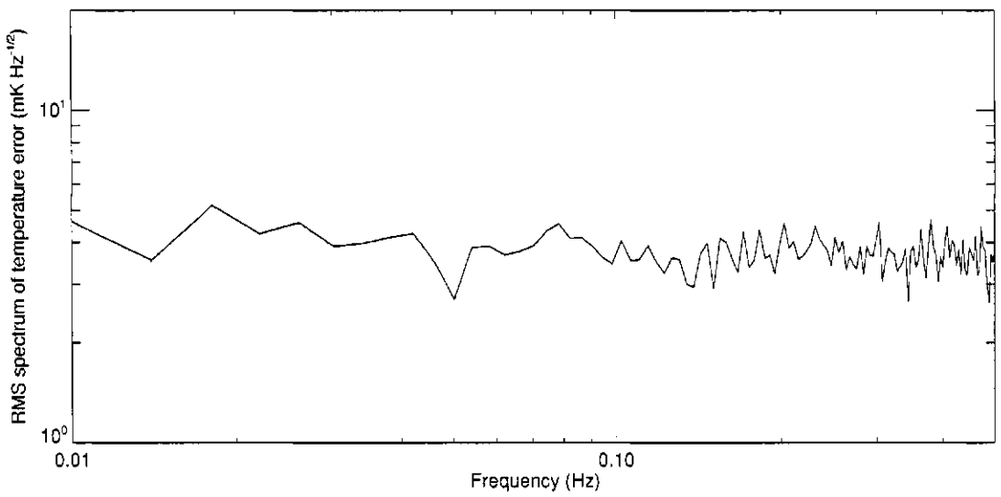

Figure 4.4: Model profile of temperature error from the spectrometer calibrator. The profile was determined from 19 temperature measurements of SCAL-A taken at 38.15 K on March 24, 2005 during the first proto-flight model test campaign conducted at the Rutherford Appleton Laboratory in Oxfordshire, England (see Appendix B-2).

4.5 THERMALSCAL: timeline of the temperature of the spectrometer calibrator

This section describes the simulation of the temperature of the two sources of the spectrometer calibrator (SCAL). Section 3.3 outlined the design and operation of SCAL. As explained there, the two sources, denoted SCAL-A and SCAL-B, are heated to temperatures up to 120 K and are used to compensate for the large background emission of the Herschel primary and secondary mirrors [5, 99]. Similar to SMEC, the temperature of the SCAL sources is controlled by a digital feedback loop. But unlike SMEC, the SCAL timelines were not split into individual scans. The THERMALSCAL module produced the temperature timelines of SCAL-A and SCAL-B for a single SHIFTS run given a noise profile (stored as a calibration file) and a base temperature set in `user_settings.sav`.

Appendix B-2 describes the analysis of SCAL data measured from PFM1 data. Like the

SMEC data, this analysis produced a noise profile, shown in Figure 4.4. The noise profile was based on 19 temperature measurements of SCAL-A taken at 38.15 K on March 24, 2005. Each measurement lasted 250 s and was sampled once per second. From Equations B-3 and B-4, the frequency interval and Nyquist frequency in the spectral domain were 0.004 and 0.5 Hz, respectively.

In the appendix, Figure B-3(c) showed that the phase of the SCAL temperature error spectra was random. This fact allowed us to repeat the technique outlined in the previous section to simulate the temperatures of the two SCAL sources. Like the SMEC profile, the SCAL profile was first interpolated, zero-filled and normalized. Using Steps 1 – 3 from Section 4.4, we calculated a temperature error (in K) denoted by ΔT_m. The temperature at each master time interval m was then given by

$$T_m = \overline{T} + \Delta T_m, \qquad [\mathrm{K}] \tag{4.7}$$

where $\overline{T}$ was the user-defined temperature of the source (in K). This technique was employed twice, once for SCAL-A and once for SCAL-B. Since Figure B-4 demonstrates that there was little variation between the sources, the same noise profile was employed for both sources. Section 5.3 compares the temperature timelines simulated using this technique with the results of the PFM1 data analyzed in Appendix B-2.

4.6 THERMALHPM: timeline of the temperature of the Herschel primary mirror

The Herschel primary mirror will reflect incoming radiation and direct it to the SPIRE instrument. However, as indicated in Section 3.2.2, the primary mirror emits radiation as a blackbody at a temperature of approximately 80 K and an emissivity of approximately 2 % [85, 96]. The

spectrometer calibrator, discussed above, is used to compensate for the large emission from the Herschel primary and secondary mirrors. For simplicity, SHIFTS did not model the temperature of the Herschel secondary mirror. Instead, the effect of the secondary mirror was modelled in SHIFTS by doubling the emissivity of the primary mirror.

It is believed that the temperature of the primary and secondary mirrors will be largely stable [81, 96]. The THERMALHPM module simulated the temperature of the mirror as a simple linear drift, characterized by an initial temperature T_o (in K) and a drift of ΔT (in K) over a time period P (in seconds). Therefore, the temperature was given by

$$T = T_o + \frac{\Delta T}{P} t_m. \qquad \text{[K]} \tag{4.8}$$

The initial temperature was set to 80 K and the drift rate, $\frac{\Delta T}{P}$, to 180 mK hr^{-1} (see Section 3.2.2) [81].

4.7 THERMALHPM: timeline of the pointing of the Herschel telescope

The pointing of the HSO determines the field-of-view (FOV) seen by the detectors [5]. This section describes the simulation of the pointing of Herschel generated by the POINTINGHSO module of SHIFTS. The pointing errors of the beam steering mirror (BSM; potentially a larger source of noise) were not included in SHIFTS because there was insufficient test data available to characterize its effect [88, 89].

Pointing only affects the astronomical signal because the Herschel and SCAL beams are internal to the Herschel telescope and are thus unaffected by changes in the orientation of the HSO. Similar to the temperature of the Herschel primary mirror, the pointing will be relatively stable. Two pointing errors were included in SHIFTS: the absolute pointing error (APE) and the relative pointing error (RPE) [95]. Following Section 3.2.1, the APE was defined as an initial offset with a

one standard deviation error of 1.2 arcsec per axis while the RPE was defined as a drift over 60 s with a one standard deviation error of 0.3 arcsec per axis [95].

To simulate the pointing, the magnitude of the RPE and APE were determined using random Gaussian noise. Four separate random numbers were generated with the IDL RANDOMN routine, which employs the Box-Muller method to produce a normally distributed random array with a mean of zero and a standard deviation of one [136, 145]. Each random number was multiplied by the pointing errors specifications given above. For a single run, the right ascension and declination of the HSO at a time interval m were then defined as

$$\alpha_{\mathrm{HSO}_m} = \alpha_{\mathrm{APE}} + \left(\frac{\alpha_{\mathrm{RPE}}}{60} t_m\right), \qquad \text{[arcsec]} \tag{4.9}$$

$$\delta_{\mathrm{HSO}_m} = \delta_{\mathrm{APE}} + \left(\frac{\delta_{\mathrm{RPE}}}{60} t_m\right), \qquad \text{[arcsec]} \tag{4.10}$$

where α_{APE} and α_{RPE} denote the right ascension of the APE and RPE, respectively, and δ_{APE} and δ_{RPE} denote the declination of the APE and RPE, respectively (all four in arcsec).

Note that the equations given above specifically describe the pointing of the HSO. They differ from the right ascension and declination given by Equations 4.1 and 4.2, which define the location on the sky of the simulated astronomical source.

4.8 POWERBOLO: timeline of the power incident on the bolometers

This section describes the POWERBOLO module, the most complex module in SHIFTS. Given the four timelines described in Sections 4.4 to 4.7, this module simulated the entire optical system of the SPIRE spectrometer to determine the power incident on the bolometer f at each master time interval m. As indicated in Section 3.6, the spectrometer long wavelength (SLW) array has 19 bolometers and the spectrometer short wavelength (SSW) array has 37 bolometers [5]. Therefore,

the POWERBOLO module produced 56 timelines, one for each bolometer.

This module accounts for the blackbody emission of SCAL, and the Herschel primary and secondary mirrors; the reflection and transmission of the beamsplitters; the optical retardation of the SMEC stage; the transmittance of the low-pass filters and the waveguides; and the various efficiencies of the detector system. However, the time-dependent nature of some of these values made it impossible to simply perform an inverse Fourier transform on the SAS spectra. Instead, the power was calculated one master time interval at a time, beginning at $m = 0$.

The first four parts of Section 4.8 describe the calculations performed to determine the power incident on each bolometer f. Section 4.8.1 describes how the spatial pixels of the simulated astronomical source were grouped into their respective feedhorns. Section 4.8.2 explains the calculation of the blackbody emission of SCAL and the Herschel primary mirror given their respective temperature timelines. Section 4.8.3 models the transmission of the broadband radiation through the optical path of the SPIRE spectrometer to the bolometers. Section 4.8.4 then integrates the broadband spectra to determine the power incident on each bolometer f at each master time interval m, the result of which is an interferogram. The addition of photon noise is described in Section 4.8.5.

4.8.1 Determining the field-of-view of each feedhorn

Before the radiation from the SAS was propagated through the optical system, the spatial pixels were first grouped into their respective feedhorns. The grouping was performed at each master time interval because the pointing of the Herschel telescope shifted the input data cube such that a SAS pixel could drift across several feedhorns during a single scan.

The FOV of the SPIRE spectrometer was 2.6 arcmin across; the angular spacing between

the SLW and SSW feedhorns was 49 and 28.3 arcsec [5]. As indicated in Section 4.2, the angular size and resolution of the input spectral cube was arbitrary. If the SAS filled the spectrometer FOV, was sampled every arcsecond and contained sufficient spectral information for a high resolution scan, the data cube would contain approximately 30 million elements. Even for a single scan sampled at 500 Hz, the execution time would last several days. For that reason, SHIFTS employed the simplified version described below.

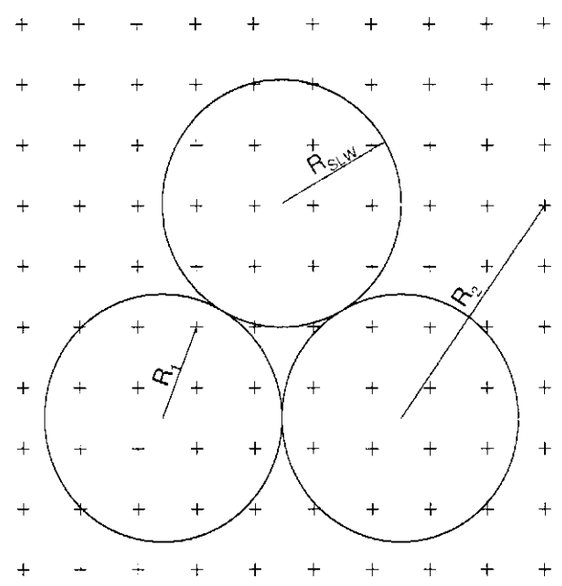

Figure 4.5: Example of the binning of the spatial pixels of the simulated astronomical source. The circles represent the feedhorn apertures and the crosses represent the spatial pixels of the SAS.

As shown in Figure 3.10, the SSW and SLW feedhorns are packed hexagonally [5]. A basic algorithm was written to determine which feedhorn each SAS pixel eventually entered. The angular distance of each SAS pixel ij from the center of each feedhorn f was iteratively calculated by

$$r_{ijf} = \sqrt{(\alpha_f - \alpha_{im})^2 + (\delta_f - \delta_{jm})^2}, \qquad \text{[arcsec]} \tag{4.11}$$

where α_f and δ_f were the angular positions (in arcsec) of the center of feedhorn f (relative to the central feedhorn),

$$\alpha_{im} = \alpha_i + \alpha_{\mathrm{HSO}_m}, \qquad \text{[arcsec]} \tag{4.12}$$

was the right ascension of the SAS pixel ij at time interval m, and

$$\delta_{jm} = \delta_i + \delta_{\mathrm{HSO}_m}, \qquad \text{[arcsec]} \tag{4.13}$$

was the declination of SAS pixel ij at time interval m. If the distance r_{ijf} was less than the angular radius of the feedhorn, then the spectrum of SAS pixel ij was considered inside feedhorn f. An example of this binning is shown in Figure 4.5. Clearly, the angular distance R_1 is less than the radius of the feedhorn, R_{SSW}, while the angular distance R_2 was greater. Once SHIFTS determined which pixels were grouped into each feedhorn, their respective spectra were summed together. Section 5.6 validates this component of the POWERBOLO module by scanning a single source across the FOV of the SSW array.

It should be noted that there are several drawbacks to this technique, which will be addressed in future releases of SHIFTS. Most obviously, this technique does not account for the partial overlap of an SAS pixel. In addition, any off-axis radial dependence in the transmission of the SAS pixels were smoothed out by binning the spectra before transmission.

4.8.2 Modelling the background emission

One of the largest noise sources in the SPIRE spectrometer is the blackbody emission from the Herschel primary mirror and SCAL [5, 99]. As indicated in Section 3.2.2, the thermal emission from these sources accounts for most of the loading on the bolometers. Therefore, it was important that their emissions were properly simulated in SHIFTS. Since the temperatures of the Herschel primary mirror and the SCAL sources changed over time, the corresponding changes in their blackbody emission had to be calculated.

As stated in Section 3.1, the Mach-Zehnder (MZ) interferometer design utilizes both input ports [90]. Light from the first input port is a combination of the Herschel primary mirror and the astronomical source. The second input port is illuminated by SCAL. The thermal emission from both the Herschel primary mirror and the SCAL sources is described by the Planck equation (see

Equation 1.1) [60, 62].

In the case of the Herschel primary mirror, its largely stable temperature timeline was determined in Section 4.6. As indicated there, the temperature of the secondary mirror was not computed. Its considerable effect was included as an additional contribution to the emissivity of the primary mirror. The total emissivity of the mirrors was assumed to be a constant 4 % (2 % from each mirror) over the SPIRE wavelength range [5, 96, 99].

As for the emission from the calibration port, the temperature timelines of the two heated sources, SCAL-A and SCAL-B, were simulated in Section 4.5. As indicated in Section 3.3, the SCAL model used in the PFM1 test campaign employed sources with a fill factor of 2 and 4 % [99]. We ignored the minor wavelength dependence of the black coating and assumed that both sources were perfect emitters [99, 146]. The same assumption was made for the third component of the SCAL emission, the remaining 94 % of the pupil. The temperature of this contribution was fixed at 4.5 K (i.e., the temperature of the SPIRE focal plane unit) [5, 99]. The blackbody emission of each component was summed together to produce the total emission of SCAL. To mimic the SAS, the specific intensities of the thermal sources were converted to electric fields per unit wavenumber using Equation 4.5 where the throughput was given by Equation 4.4.

The thermal emission from other components in the SPIRE spectrometer was not included in SHIFTS. At 80 K with an emissivity of 4 %, the Herschel primary mirror emits approximately 75 pW (1 pW = 10^{-12} W) in the SPIRE band [85]. In contrast, a 4.5 K mirror with an emissivity of 1 % (see Section 3.1) emits only 0.006 pW in the SPIRE band. While the emission from these components is sufficiently small that it can be ignored, their transmission effects were substantial enough to be included (see next section).

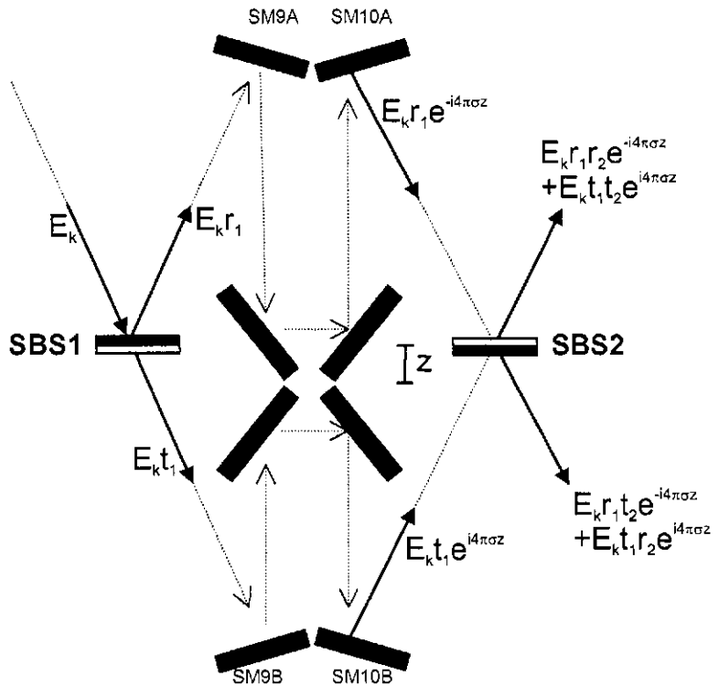

Figure 4.6: Optical path of an electromagnetic wave in the SPIRE spectrometer [81]. The arrows denote the direction light travels; the blue boxes denote mirrors (where the blue cross in the center represents the back-to-back rooftop mirrors of the spectrometer mechanism); the red/green boxes denote the beamsplitters (red corresponds to the inductive side and green to the capacitive side of the beamsplitter). (Original figure courtesy of Dr Douglas Griffin, Rutherford Appleton Laboratory, Oxfordshire, England.)

4.8.3 Optical retardation and signal attenuation

From the calculations in the previous two sections, each radiation source (the astronomical signal, the Herschel primary mirror and the spectrometer calibrator) yielded two pairs of spectral beams. One pair was detected by the SLW bolometers while the other was detected by the SSW bolometers. Each pair represented the two optical paths that radiation took between the source and the detector. Since the beams originate from different sources, their amplitudes and phase fluctuations are uncorrelated [60]. Therefore, the beams were incoherent and were treated independently. This section describes the calculation of the interference patterns produced by radiation propagating in the two optical paths of the SPIRE spectrometer.

To simulate the optical retardation of each beam, let us examine the optical path taken by an electromagnetic wave of amplitude E_k entering the first input port (i.e., the sky port) of the SPIRE spectrometer, as shown in Figure 4.6. While the path of the wave is similar to the path taken in the Michelson interferometer (see Section 2.3.2), there are specific differences in the modified MZ design [45, 46, 90, 91]. Similar to the Michelson interferometer, the electric field is split into two separate beams at the first beamsplitter (SBS1 in Figure 4.6). The *up beam* is reflected off the inductive side of SBS1 while the *down beam* passes through SBS1. As can be seen, the back-to-back rooftop mirrors are not located at the point of zero path difference (ZPD) but a distance z (in cm) away. Unlike the Michelson interferometer, the mirror location in the modified MZ interferometer modulates both beams simultaneously [90, 91]. In Figure 4.6, the up beam travels a longer optical distance between the two beamsplitters so its phase lags by a factor of $e^{-i4\pi\sigma z}$ relative to ZPD, where σ is the wavenumber (in cm^{-1}). Complementing the up beam, the phase of the down beam led by a factor of $e^{i4\pi\sigma z}$ relative to ZPD. Upon recombination at the second beamsplitter, the optical path difference between the two beams is $4z$ (twice the optical retardation of the Michelson interferometer) [46, 90, 91].

Focusing on the portion of the beam directed to the SSW bolometers (i.e., the first output port), the up beam is reflected off the capacitive side of SBS2 while the down beam is transmitted through SBS2. This results in an electric field of wavenumber k incident on the SSW bolometer f_s at a master time interval m,

$$E_{f_s mk} = E_{f_s mk}\left(r_{1_i} r_{2_c} e^{i4\pi\sigma_k z_m} + t_1 t_2 e^{-i4\pi\sigma_k z_m}\right), \quad [\mathrm{V\,m^{-1}\,(cm^{-1})^{-1}}] \quad (4.14)$$

where r and t are the complex amplitude reflection and transmission coefficients, respectively, (defined in Section 2.3.2), σ_k is given by Equation 4.3 and z_m is given by Equation 4.6. The subscripts denote the beamsplitter (SBS1 or SBS2) where i denotes the inductive side and c the capacitive (only

relevant for reflection). Similarly, the electric field of wavenumber k incident on the SLW bolometer f_ℓ at a master time interval m is

$$E_{f_\ell mk} = E_{f_\ell mk}\left(r_{1_i} t_2 e^{i4\pi\sigma_k z_m} + t_1 r_{2_i} e^{-i4\pi\sigma_k z_m}\right), \quad [\mathrm{V\,m^{-1}\,(cm^{-1})^{-1}}] \quad (4.15)$$

The magnitudes of r and t were taken from the values shown in Figure 3.5 [99]. As for the phase, Section 3.4 listed that the phase change of r was π radians while the phase change of t was zero [67].

Equations 4.14 and 4.15 were used to simulate the optical retardation of the astronomical signal and the blackbody emission of the Herschel primary mirror. For radiation entering the second input port (i.e., the SCAL port), the same equations were employed but they were reversed (i.e., Equation 4.14 corresponded to the electromagnetic wave exiting the second output port, and vice-versa for Equation 4.15). To account for the complementary nature of the two ports (see Section 3.3), we refer the reader to Chamberlain [101] and Davis, Abrams & Brault [49].

In addition to the optical properties of the beamsplitter and the optical retardation introduced by the SMEC stage, the other efficiencies of the optical system were also simulated in SHIFTS. These include the reflectance of the SPIRE mirrors, the low-pass filters and the various efficiencies of the feedhorn system [5, 87, 110, 111]. These efficiencies were combined into a single frequency-dependent amplitude transmission coefficient given by

$$\eta_k = \sqrt{\eta_A \eta_{\mathrm{feed}} \eta_s T_{\mathrm{waveguide}} T_{\mathrm{filter}} T_{\mathrm{mirror}}}, \quad (4.16)$$

where η_A, η_{feed} and η_s were the aperture, feedhorn and main-beam efficiencies, respectively (see Section 3.6.2); $T_{\mathrm{waveguide}}$ was the transmittance of the feedhorn cutoff (see Section 3.6.2); T_{filters} was the combined transmittance of the SPIRE low-pass filters (see Section 3.6.1); and T_{mirror} was the total reflectance of the mirrors in the SPIRE optical path (see Section 3.1). Similar to the beamsplitters, the above efficiency was defined as an amplitude transmission coefficient (and not a transmittance)

because the propagating radiation was expressed as an electric field (and not a power) [60].

The transmittances T_{filters} and $T_{\text{waveguide}}$ defined the bandpass of each array. The total transmittance of the low-pass filters is given for each port in Figure 3.9. As indicated in Section 3.6.1, the second input port (i.e., the SCAL port) passes through two less filters than the first input port; therefore, its total efficiency is higher. The long-wavelength cutoff of the waveguide (described in Section 3.6.2) was simulated as a unity transmittance at high wavenumbers with a sharp rollover at the cutoff frequency. Since the weighting of the propagating modes is currently unknown, we assumed all the radiation propagated in the fundamental TE_{11} mode [114, 119]. As such, the SLW and SSW cutoff frequencies were fixed at 15.60 and 31.44 cm^{-1}, respectively, the values measured during the PFM1 test campaign (see Table 3.1) [125].

The reflectance of the SPIRE mirrors was simulated as a single transmittance value, constant at all wavenumbers. As indicated in Section 3.1, the reflectance of each mirror was 99 % [5]. As can be seen in Figures 3.1 and 3.2, the sky beam reflects off 14 mirrors and the SCAL beam off 7 mirrors [87, 110]. Therefore, T_{mirror} was 0.869 for the first input port and 0.932 for the second input port.

Finally, to model the efficiencies of the detection system, we employed values given in Griffin [85] and Rownd *et al.* [114]. Following Griffin [85], the main-beam efficiency was set at 0.8 between 0 and 450 μm; between 450 and 670 μm, η_s dropped linearly to 0.6. The aperture efficiency was 0.1 lower than the main-beam efficiency for all wavenumbers [111]. As indicated above, we assumed that only the TE_{11} mode propagated in the detection system [114, 122]. For simplicity (and due to the lack of broadband empirical data), we assumed a constant feedhorn efficiency of 0.7 [5, 113, 114, 119].

By including all the above efficiencies, we determined a value of η_k for each input and

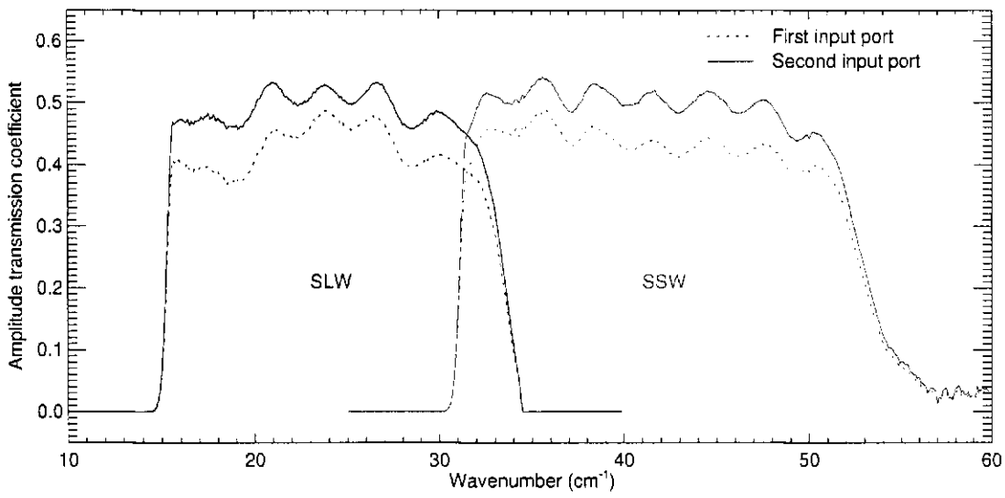

Figure 4.7: Transmission efficiency for the input and output ports of the SPIRE spectrometer. These profiles include the effects of the feedhorn, aperture and main-beam efficiencies of the detection system; the beamsplitters; the low-pass filters; and the mirrors.

output port for all wavenumbers σ_k. The four efficiencies were stored as calibration files and are shown in Figure 4.7. As can be seen, the transmission was higher for the second input port (i.e., the SCAL port) since there were less optical components (filters and mirrors) in its path [87, 110]. The product of η_k and their respective electric fields (given by either Equation 4.14 or 4.15) yielded the electric field of wavenumber k incident on each bolometer f at a master time interval m.

4.8.4 Integrating the power

Following transmission through the various optical paths of the SPIRE spectrometer, broadband radiation was incident on the bolometers. To determine the total power incident on each bolometer, we combined discrete versions of Equation 2.26 and 2.27. As such, the power incident on bolometer f at a master time interval m was given by

$$I_{fm} = \Delta\sigma_{\mathrm{sim}} \sum_{\sigma_0}^{\sigma_N} \left(\frac{2A_f}{c\epsilon_o} E^*_{fmk} E_{fmk} \right), \qquad [\mathrm{W}] \tag{4.17}$$

where $E_{fm,k}$ was the electric field at a wavenumber k incident on bolometer f at a master time interval m (in $\mathrm{V\,m^{-1}\,(cm^{-1})^{-1}}$); $\Delta\sigma_{\mathrm{sim}}$ was the line width of the SAS spectrum (in $\mathrm{cm^{-1}}$; see Section 4.2); σ_o and σ_N were the lower and upper bounds, respectively, of the wavenumber grid (in $\mathrm{cm^{-1}}$); A_f was the area of the circular aperture of feedhorn f (in $\mathrm{m^2}$; see Table 3.1); c was the speed of light and ϵ_o was the permittivity of free space (see Table A-1). Note that in contrast to Equation 2.26, Equation 4.17 was defined in terms of time instead of position.

The summation of Equation 4.17 was the final step in each instance of the iteration process introduced at the beginning of Section 4.8. Following the integration, the master time interval was incremented to $m + 1$. At the next master time interval, the MPD of the SMEC stage, the temperature of SCAL and the Herschel primary mirror, and the poining of the HSO were all different. The calculations of Sections 4.8.1 to 4.8.4 were repeated and the master time interval was then incremented again. This iterative process continued until the power incident on each bolometer was calculated for every master time interval. The result of these iterations was effectively a discrete Fourier transform (DFT) of the electromagnetic waves entering the two input ports. It was not possible to take advantage of the computional speed gains of the fast Fourier transform (FFT) in our case because the MPD was not evenly spaced and the spectra entering the input ports varied in time [53].

4.8.5 Photon noise

Once a raw interferogram was determined for each bolometer, SHIFTS added the photon noise. As indicated in Section 3.6.3, the photon noise from the thermal emission of SCAL, and the Herschel primary and secondary mirrors is expected to be the largest source of noise in the SPIRE spectrometer [5, 127]. Proportional to the square root of the number of photons, the photon noise

is given in Equation 3.7 as a noise-equivalent power (NEP) [111, 130]. In SHIFTS, the power of the photon noise was estimated by

$$\Delta I_{fm} = \sqrt{\left(\frac{2hc\sigma_o}{\Delta t_m}\right) I_{fm}}, \qquad \text{[W]} \tag{4.18}$$

where h was the Planck constant, c was the speed of light (see Table A-1), σ_o was the center wavenumber of each band, Δt_m was the master time interval (see Section 4.3) and I_{fm} was the power incident on bolometer f at a master time interval m. For the SLW and SSW arrays, σ_o was set to 22.2 and 40 cm^{-1} (450 and 250 μm), respectively.

Photon noise follows Poisson statistics which, for large photon counts, can be approximated by a Gaussian distribution [138, 147, 148]. Each value of ΔI_{fm} was multiplied by random Gaussian noise to simulate the random arrival time of each photon. Generated with the IDL RANDOMN routine, the Gaussian noise had a mean of zero and a standard deviation of one (see Section 4.7) [136]. This simulated photon noise was added to the raw interferogram, I_{fm}, determined in the previous section. Noise, in the form of detector electrical noise, is discussed further in Section 4.9.2. An example of the photon noise calculation is given in Section 5.6.

4.9 DETECTORSIG: timeline of the measured signal

From the results of Section 4.8, SHIFTS determined the power incident on each bolometer at every instance of the master time grid. The DETECTORSIG module determines the actual signal measured by the SPIRE detection system. Section 4.9.1 describes the impulse response function (IRF) of the detection system while Section 4.9.2 outlines the calculation of the electrical noise and the introduction of several conversion factors. After the calculations performed by this module, SHIFTS asynchronously sampled the signal and position and saved their values to an external electronic file (see Section 4.10).

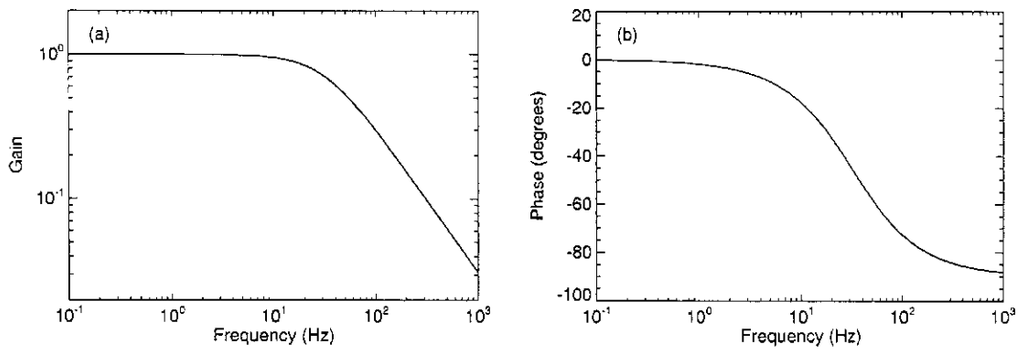

Figure 4.8: Transfer function of the resistor-capacitor filter response of a bolometer with a time constant of 5.1 ms. Panel (a) shows the gain while Panel (b) shows the corresponding phase.

4.9.1 Impulse response function

Section 3.6.3 outlined the operation of the SPIRE bolometers. As indicated there, the absorption of photons increases the temperature of the micromesh, thereby changing the resistance of the neutron-transmutation doped (NTD) germanium thermistors. However, this change is not instantaneous but occurs with a characteristic time constant, τ (in ms). Due to the complexity of the bolometer manufacturing process, the time constants varied from pixel to pixel [106]. The version of SHIFTS described in this thesis employed a single time constant for each array; future releases will include a provision for a different time constant for each bolometer.

The thermal response of the bolometer was simulated as a simple resistor-capacitor (RC) circuit [106]. Represented as a complex Laplace function, the response of a RC circuit is given by

$$H_B(p) = \frac{\omega}{p+\omega}, \tag{4.19}$$

where ω is the inverse of the thermal time constant (in Hz) and $p = i2\pi f$ was the complex Laplace variable for a frequency f (in Hz) [106, 149]. Figure 4.8 shows the gain and phase of the RC circuit for a thermal time constant of 5.1 ms ($\omega = 196.1$ Hz).

In addition to the thermal response of the bolometer, the warm electronics in the Herschel

service module have a characteristic response, given by Equation 3.8 and shown in Figure 3.15 [94, 135]. Note the similarity between the transfer function of the warm electronics and the bolometer transfer function shown in Figure 4.8. The product of Equations 3.8 and 4.19 yielded the total transfer function for the detector system. SHIFTS separated the total transfer function into partial fractions and performed an inverse Laplace transform (Laplace transforms are similar to Fourier transforms except that the spectral variable is complex and the temporal variable is real) [51]. The result of the inverse Laplace transform (denoted by $\mathcal{L}^{-1}$) of the partial fractions is the *impulse response function* (IRF), given by

$$\begin{aligned} h(t) = \mathcal{L}^{-1}[H_B(p)H_E(p)] = Ae^{-\omega t} &+ 2Be^{-\alpha_1 t}\cos(\beta_1 t + \angle B) \\ &+ 2Ce^{-\alpha_2 t}\cos(\beta_2 t + \angle C) \\ &+ 2De^{-\alpha_3 t}\cos(\beta_3 t + \angle D), \end{aligned} \tag{4.20}$$

where the coefficients varied depending on the bolometer thermal time constant [106]. For a time constant of 5.1 ms, the coefficients A, B, C and D were 99.80, 148.17, 4.63 and 61.244, respectively; ω, α_1, α_2 and α_3 were 196.08, 236.65, 147.79 and 213.56 Hz; β_1, β_2 and β_3 were -79.83, -264.54 and -150.44 radians s^{-1}; and $\angle B$, $\angle C$ and $\angle D$ were -3.03, 1.58 and -0.66 radians. Figure 4.9 shows the IRF corresponding to these coefficients.

The response of the detection system is equivalent to a low-pass spectral filter [135]. Using the IDL CONVOL routine, the IRF was convolved with the interferogram incident on each bolometer to produce a synthetic interferogram [136]. As outlined in Section 2.2.3, a convolution in one Fourier domain corresponds to a multiplication in another. The length of the IRF was fixed at 100 ms, which was seven times longer than the largest thermal time constant determined from the PFM1 data (see Section 3.6.3) [125]. Due to the finite width of the IRF, information was lost at the beginning of the interferogram during the convolution. To account for the lost information, an

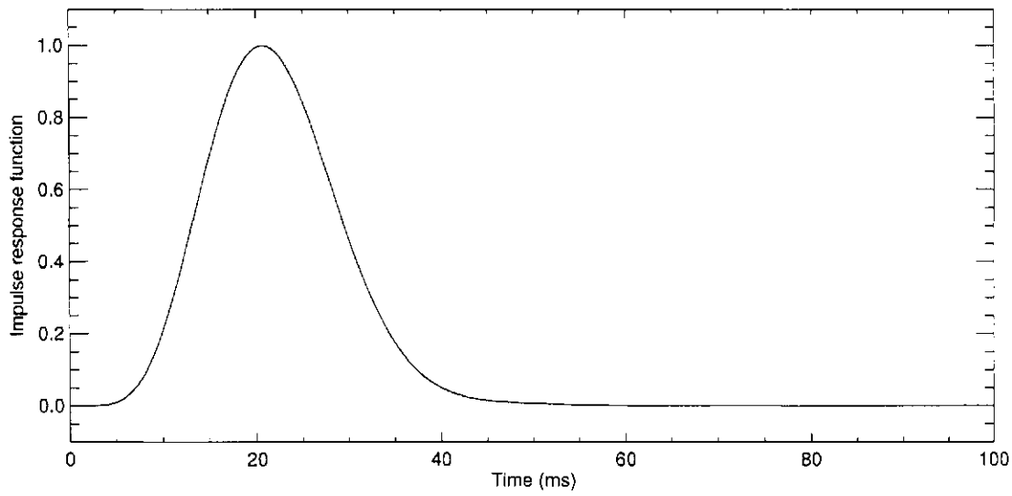

Figure 4.9: Impulse response function for a thermal time constant of 5.1 ms.

extra 100 ms was added to the beginning of the first scan.

4.9.2 Electrical noise and gain

Following the convolution of the impulse response function, the interferogram was converted from a power to a voltage. Each element in the interferogram was multiplied by the detective quantum efficiency (DQE) of 0.7 and the responsivity of the SPIRE bolometers, 40 GV W^{-1} [5,81].

The next step added the electrical noise. As indicated in Section 3.7, the electrical noise was 5 nV Hz$^{-1/2}$ [135]. In comparison, a photon loading of 10 pW (the approximate power from the 80 K, 4 % Herschel primary mirror reaching the detectors) yielded a noise-equivalent power (NEP) of 50 nV Hz$^{-1/2}$ given Equation 4.18 and the DQE and responsivity quoted above [5,85]. To include the electrical noise, we repeated the calculation of Section 4.8.5. Given the master time interval, Δt_m, the base noise level was converted to a voltage. This value was multiplied by random Gaussian noise (using the IDL RANDOMN routine) to produce a noise voltage at each master time interval m for each bolometer f [136]. This scaled random noise was added to the interferogram

signal (in V). A point of clarification: uncorrelated noise sources (such as electrical and photon noise) are added in quadrature [148]. Multiplying the noise sources by random Gaussian noise and summing them in a time series was equivalent to adding them in quadrature.

After the introduction of the electrical noise, SHIFTS multiplied each interferogram by a gain of 3600 to simulate the SPIRE detector amplifier.

4.10 Readout and data product

The end result of Section 4.9 was a synthetic interferogram for each bolometer f, measured in volts and sampled at equal increments of time. The stage position was also sampled on the same time grid. Together, the position and signal define an interferogram [49].

However, while equal time sampling was necessary in SHIFTS, it does not reflect the actual sampling of the SPIRE spectrometer. As indicated in Sections 3.5 and 3.7, the stage metrology and the detector signal are sampled at 226.12 and 80 Hz [5]. To mimic this asynchronous sampling, SHIFTS again employed the IDL INTERPOL routine (see Section 4.4) to interpolate the signal and position onto their proper grids [136]. However, in contrast to the actual signal measurements, the SHIFTS detector signal was not then digitized.

Once the position and signal were interpolated onto their respective time grids, the results were saved to an external electronic file. When telemetry data is returned to the Earth from the HSO, each component timeline (e.g., detector signal) is saved to an individual Flexible Image Transport System (FITS) file, a standard format in astronomy [150]. Each set of FITS files defines a Herschel data product for a single observation. To create synthetic data products, SHIFTS saved the stage metrology and detector signal timelines to FITS files. The FITS files were created using the

IDL Astronomy Users Library* maintained by the NASA Goddard Space Flight Center (GSFC) in Greenbelt, Maryland. The exact format of the Herschel FITS files is still being determined by members of the SPIRE consortium. Once the format is finalized, SHIFTS will be updated to conform to that standard.

4.11 Summary

This chapter outlined the design and implementation of SHIFTS, the SPIRE spectrometer simulator. Section 4.1 described the software architecture of the program and provided an overview of the execution order of the individual modules. Sections 4.2 and 4.3 discussed the initialization of SHIFTS. Sections 4.4 to 4.9 covered each of the individual modules of SHIFTS. The final section discussed the creation of Herschel data products.

Chapters 5 – 7 of this thesis explore the data generated produced by SHIFTS. To characterize SHIFTS, Chapter 5 examines the output of each of the six timelines produced by SHIFTS. After this characterization, Chapter 6 compares synthetic interferograms generated by SHIFTS with real interferograms from the first SPIRE proto-flight model test campaign conducted in 2005. Finally, SHIFTS was used to simulate the measured interferograms of a realistic astronomical source (as described in Chapter 7).

*Web address: *http://idlastro.gsfc.nasa.gov/homepage.html*

Chapter 5

Module testing of the SPIRE spectrometer simulator

> *"The second [rule], to divide each of the difficulties under examination into as many parts as possible, and as might be necessary for its adequate solution. The third, to conduct my thoughts in such order that, by commencing with objects the simplest and easiest to know, I might ascend by little and little, and, as it were, step by step, to the knowledge of the more complex; assigning in thought a certain order even to those objects which in their own nature do not stand in a relation of antecedence and sequence."*
>
> - René Descartes, *Discourse on the Method of Rightly Conducting One's Reason and Seeking Truth in the Sciences*, Hackett Publishing Company (1980, originally published as "Le Discours de la méthode pour bien conduire sa raison et chercher la vérité dans les sciences" in 1637).

This chapter describes the module tests of the Simulator for the Herschel Imaging Fourier Transform Spectrometer (SHIFTS). SHIFTS simulates the Spectral and Photometric Imaging Receiver (SPIRE) spectrometer onboard the Herschel Space Observatory (HSO). As outlined in Chapter 4, SHIFTS was composed of six primary modules; the output of each module was a single timeline representing an observable quantity of the SPIRE spectrometer. The simulator was sufficiently complex that it was necessary to test SHIFTS on a module-by-module basis. Therefore, we

Table 5.1: Summary of modules tests.

Module	Test description
SMECMPD	Compared the simulated stage position to measured data analyzed in Appendix B-1 (see Section 5.2).
THERMALSCAL	Compared the simulated spectrometer calibrator source temperatures to measured data analyzed in Appendix B-2 (see Section 5.3) .
THERMALHPM	Compared the simulated temperature of the Herschel primary mirror to technical specifications (see Section 5.4).
POINTINGHSO	Compared the simulated pointing of the Herschel Space Observatory to technical specifications (see Section 5.5).
POWERBOLO	Analyzed the imaging capabilities by introducing a large pointingdrift; compared interferometric capabilities and absolute power to published results; compared the simulated photon noise to theory (see Section 5.6).
DETECTORSIG	Compared the simulated detector response to theory (see Section 5.7).

developed a series of modules tests to validate the performance of each component. Section 5.1 provides an overview of these tests and their figures of merit. The six sections that follow describe the module tests performed for each of the six SHIFTS modules.

5.1 Overview of module tests

Each test outlined in Chapter 5 analyzes the output timeline generated by one of the six primary SHIFTS modules. Without a clear understanding of the performance of each individual module, it could be difficult to interpret the integrated test results of SHIFTS presented in Chapter 6. This section provides a brief overview of the module tests and outlines how they were qualified.

In the case of the spectrometer mechanism and the spectrometer calibrator, real measurement data were available for comparison (see Appendix B). As such, their module tests ensured that the simulated errors were in agreement with the measured ones. For the other four modules, qualification data were unavailable. The tests for these modules compared the resultant timelines

against error specifications listed in Chapter 3 or theoretical expectations determined from Chapter 2. Table 5.1 briefly summarizes the tests performed on each module.

Except for the SMECMPD and POWERBOLO modules, there was only a single test performed per module. Section 5.2 outlines two comparisons carried out on simulated position data, while four distinct tests were conducted to characterize the POWERBOLO module in Section 5.6. To disentangle the competing effects of the POWERBOLO module, the tests discussed in that section simplified certain elements of that module.

5.2 The SMECMPD module

The spectrometer mechanism (SMEC) provides the optical retardation for the SPIRE spectrometer [5]. Section 3.5 described the operation of SMEC while Section 4.4 described SMECMPD, the SHIFTS module that simulated the stage position. To simulate the stage position, we employed a stage noise profile (shown in Figure 4.3) determined from SMEC data measured during the first proto-flight model (PFM1) test campaign conducted at the Rutherford Appleton Laboratory (RAL) in Oxfordshire, England in 2005. The stage position simulated in Section 4.4 was sampled every 2 ms. The SHIFTS READOUT routine (see Section 4.10) sub-sampled the simulated stage position to the PFM1 sampling frequency of 226.12 Hz.

To test the SMECMPD module, we repeated the analysis of the measured subsystem data (outlined in Appendix B-1) on the SHIFTS-simulated stage positions returned by the READOUT routine. Figure 5.1 shows the analysis of a single SMEC scan generated by SHIFTS, which can be directly compared to Figure B-1 in the appendix. The stage speed and scan length were set to 452 μm s^{-1} and 3.3 cm, respectively.

Given the four scans shown in Panel (a), the first scan was extracted (as denoted by the

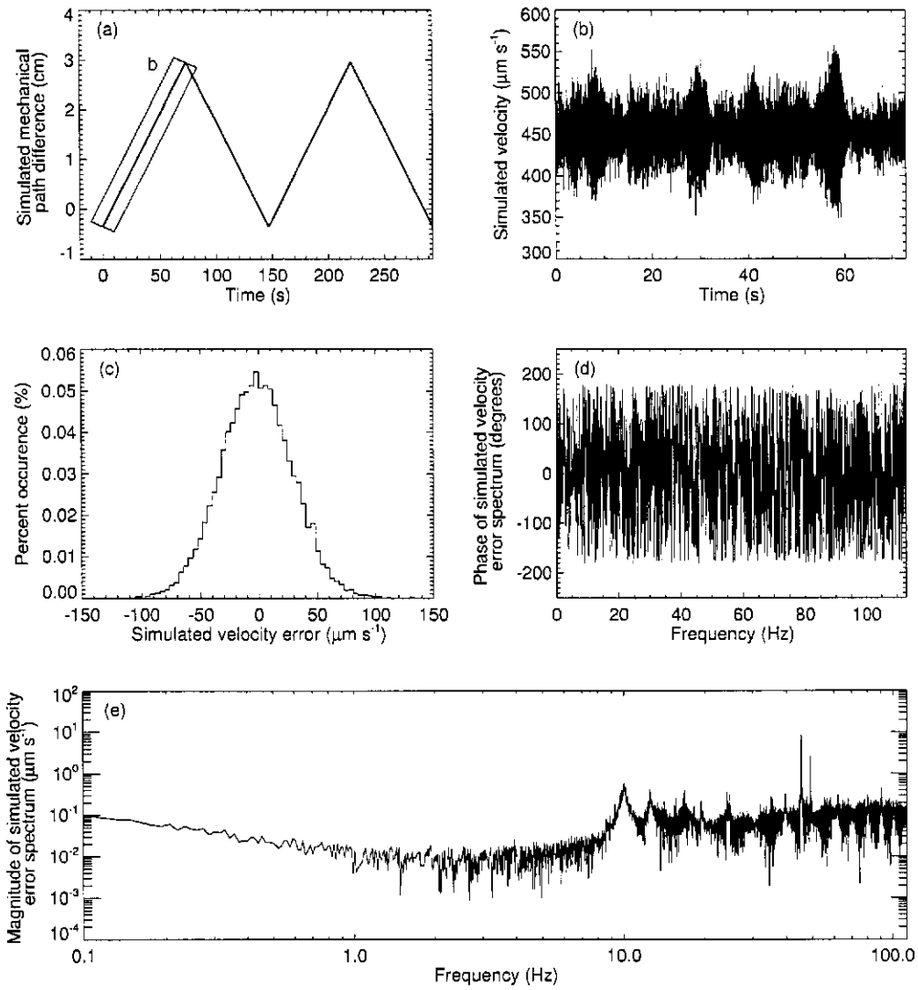

Figure 5.1: Analysis of the velocity error from a single simulated spectrometer mechanism scan. Panel (a) shows four simulated high resolution scans taken at a speed of 452 $\mu m\,s^{-1}$. The blue box marked "b" represents the 3.3 cm segment under analysis. Panel (b) shows the velocity of the segment from Panel (a). Panel (c) shows the distribution of the velocity error of the segment; the bin size is 4 $\mu m\,s^{-1}$. Panels (d) and (e) show the phase and magnitude, respectively, of the Fourier transform of the velocity error. For clarity, only every fifth point is plotted in Panel (d).

blue box marked "b"). The velocity between each pair of position values was determined using Equation B-1 with $\Delta t = 0.0044\,s$. As can be seen in Panel (b), the simulated velocity exhibited similar beat patterns as the velocity of the PFM1 data shown in Figure B-1(b). The mean speed of the simulated data was measured at 452.0 $\mu m\,s^{-1}$ with a normally distributed 1-σ error of 30.5 $\mu m\,s^{-1}$;

in contrast, the speed of the real data in Figure B-1 was 452.2 ± 38.0 $\mu m\,s^{-1}$. Using Equation B-2, we determined the velocity error of the simulated data. The distribution of the simulated velocity error, shown in Panel (c) of Figure 5.1, was in agreement with the distribution of the measured data in Figure B-1(c). The synthetic velocity error was Fourier transformed to determine the noise profile. The phase and magnitude of the simulated velocity error are shown in Panels (d) and (e), respectively, of Figure 5.1. In agreement with the PFM1 data, the phase was random. In addition, the magnitude of the simulated velocity error spectrum contained the same spectral features (with similar amplitudes) at 10, 12.5, 17 and 45.5 Hz as seen in Figure B-1(e).

Figure 5.1 showed the velocity error for a single scan; however, the results varied for each scan because a unique random number array was computed in each case. To fully characterize the SMECMPD module , we next compared the velocity error of 100 simulated scans to the velocity error of the 8 real scans that defined the SMEC model profile shown in Figure 4.3. Like the first comparison, the stage was scanned over a 3.3 cm range at a speed of 452 $\mu m\,s^{-1}$.

The result of this comparison is shown in Figure 5.2. The black distribution in Panel (a) corresponds to the eight real scans taken at a stage speed of 452.3 ± 35.5 $\mu m\,s^{-1}$ (see Table B-1); the red distribution corresponds to the 100 simulated scans taken at 452 $\mu m\,s^{-1}$ and had a standard deviation of 30.5 $\mu m\,s^{-1}$. The secondary peaks symmetric at ± 50 $\mu m\,s^{-1}$ were thought to be due to the PID feedback loop. Panel (b) shows the root-mean-square (RMS) spectra of the 100 simulated scans and the 8 real scans. Determined using Equation B-5, the RMS spectrum of the eight scans (in black) is the SMEC profile shown in Figure 4.3. The agreement between the spectra below 50 Hz was excellent; the mean difference between the two spectra was 0.08 $\mu m\,s^{-1}$. Above 50 Hz, the RMS spectra of the simulated scans dropped off and the mean difference was 0.20 $\mu m\,s^{-1}$. The drop in amplitude of the simulated RMS spectra at high frequencies was responsible for the lower standard

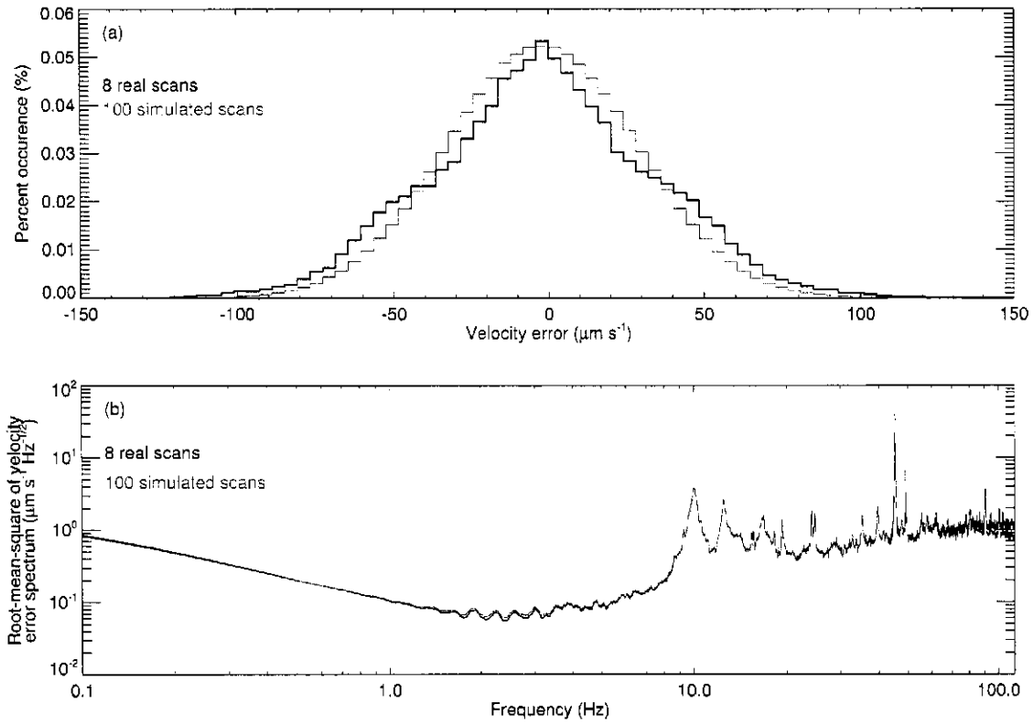

Figure 5.2: Comparison of measured and simulated spectrometer mechanism stage position data. Panel (a) shows the velocity error distribution for a bin size of 4 $\mu m\, s^{-1}$. Panel (b) shows the root-mean-square average of the measured and simulated velocity error spectra. For clarity, the spectra were smoothed by a ten point wide averaging function.

deviation seen in the simulated velocity. Upon further investigation, it was determined that the drop was caused by the sub-sampling of the stage position in the READOUT routine (see Section 4.10). The weighting of the cubic spline interpolation used in the READOUT routine smoothed out high frequency features.

In summary, these results demonstrate that the SMECMPD module performed as expected. Qualitatively, the stage position and noise profile of the simulated data in Figure 5.1 displayed the same features as seen in the measured data (see Appendix B-1). More quantitatively, the difference between the measured and simulated standard deviations was approximately 15 %. Finally, Figure 5.2 proved that the results of the SMECMPD module were repeatable: 100 simulated scans

produced the same standard deviation and noise profile as the measured data.

5.3 The THERMALSCAL module

The spectrometer calibrator (SCAL) is used in the SPIRE spectrometer to compensate for the large background emission of the Herschel primary and secondary mirrors. As indicated in Section 3.3, SCAL is composed of two blackbody sources, denoted SCAL-A and SCAL-B, that emit thermal radiation into the second input port of the SPIRE spectrometer (see Figures 3.1 and 3.2) [99]. Section 4.5 described THERMALSCAL, the SHIFTS module that simulated the temperature of the two sources. Similar to the stage position module (see above), the simulation of the temperature of the SCAL sources employed a noise profile (shown in Figure 4.4) determined from PFM1 data.

Similar to the previous section, the THERMALSCAL module was characterized by repeating the Appendix B-2 analysis on SHIFTS-simulated temperatures. To mimic the 1 Hz sampling of the PFM1 data, the simulated temperature was sub-sampled (using the IDL INTERPOL routine; see Section 4.2) from the 500 Hz sampling of the SHIFTS master time grid.

Figure 5.3 shows the analysis of the simulated SCAL-A temperature, mirroring Figure B-3 in the appendix. In this simulation, SCAL-A was set to 38 K and the temperature was simulated for 250 s (i.e., the same scan time and temperature as the original PFM1 data). The temperature error was determined using Equation B-6 where $\Delta t = 1$ Hz. The standard deviation of simulated data was 3.8 mK, in perfect agreement with the mean standard deviation of the 19 SCAL-A temperatures measured on March 24, 2005 (see Table B-2). The distribution of the simulated temperature was also in agreement with the distribution shown in Figure B-3(b). The phase and the magnitude of the spectrum of the simulated temperature error are shown in Panels (c) and (d), respectively, of Figure 5.3. In agreement with the PFM1 data, the phase was random.

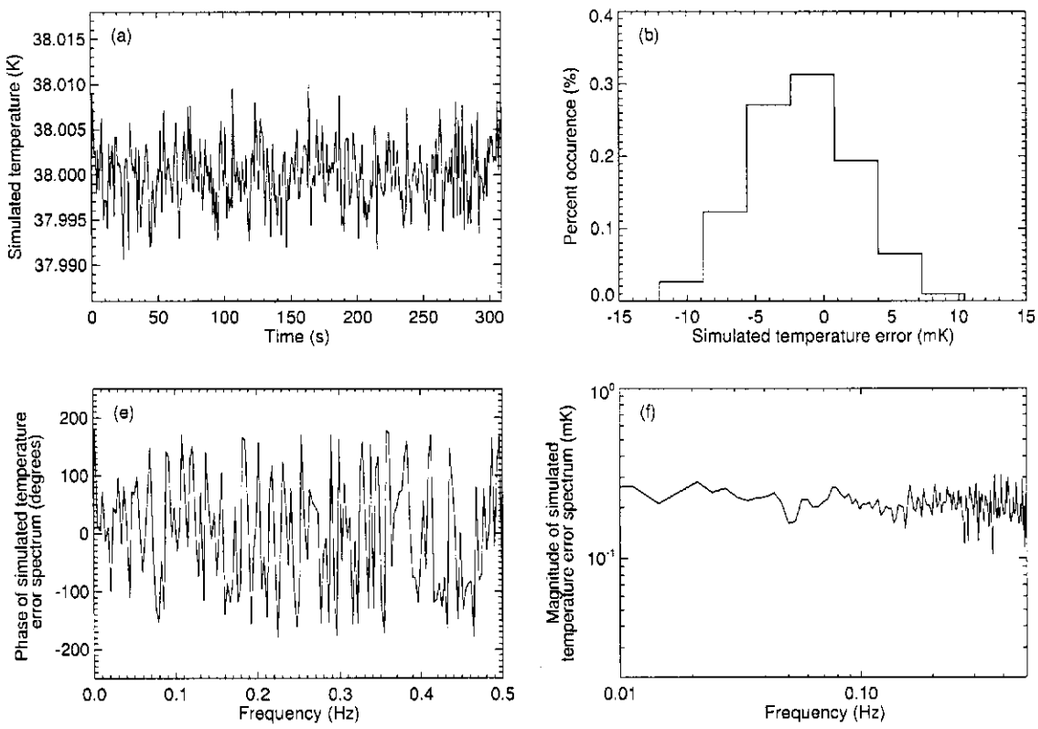

Figure 5.3: Analysis of the temperature error from simulated spectrometer calibrator data. Panel (a) shows the simulated SCAL-A temperature sampled at 1 Hz (σ_N = 0.5 Hz). The distribution of the simulated temperature error in Panel (b) has a bin size of 3.2 mK. Panels (c) and (d) show the phase and the magnitude, respectively, of the Fourier transform of the simulated temperature error.

The characterization of the THERMALSCAL module closely followed the analysis of the SMECMPD module. While the variations in the magnitude in Figure 5.3(d) were smaller than in Figure B-3, the agreement between the simulated and measured standard deviations proved that the THERMALSCAL module correctly models the SCAL temperatures.

5.4 The THERMALHPM module

In contrast to the analysis of the previous two sections, the characterization of the temperature of the Herschel primary mirror module, THERMALHPM, was straightforward. As described in

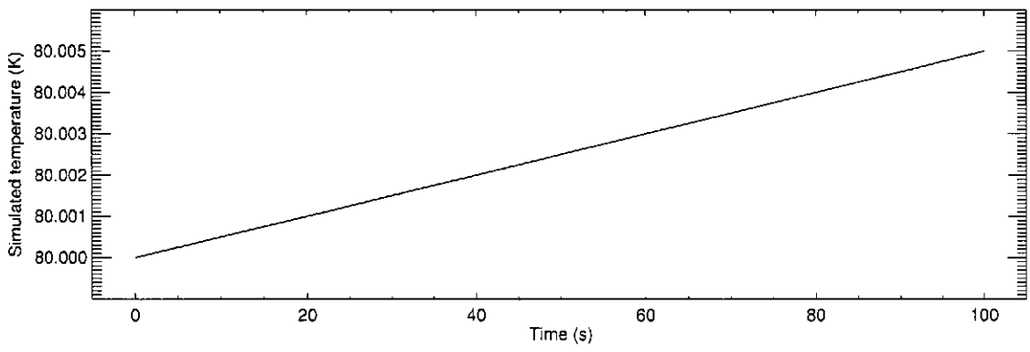

Figure 5.4: Simulated temperature of the Herschel primary mirror.

Section 3.2.2, the photon noise due to the primary mirror of the HSO is expected to be the largest noise source in the SPIRE spectrometer [5, 96, 99]. Due to its large mass, the temperature will be relatively stable. However, the THERMALHPM module simulated a simple linear temperature drift of the mirror for a fixed drift rate. Figure 5.4 shows the temperature of the Herschel primary mirror for a base temperature of 80 K and the drift rate given in Section 4.6. As can be seen, the temperature changes by 5 mK in 100 s. The slope therefore equals 0.05 $\mathrm{mK\,s^{-1}}$ or 180 $\mathrm{mK\,hr^{-1}}$, identical to the drift rate given in Section 4.6.

5.5 The POINTINGHSO module

The other component of the Herschel Space Observatory (HSO) simulated by SHIFTS was the telescope pointing error. The pointing determines the field-of-view (FOV) that the feedhorns observe (see Section 3.2.2). The POINTINGHSO module simulated the pointing using two pointing error specifications: the absolute pointing error (APE) and the relative pointing error (RPE) [5, 95]. As covered in Section 3.2.1, both errors were given as one standard deviation errors; the APE was 3.7 arcsec per axis and the RPE was 0.3 arcsec per axis [95]. The simulation of the APE and the

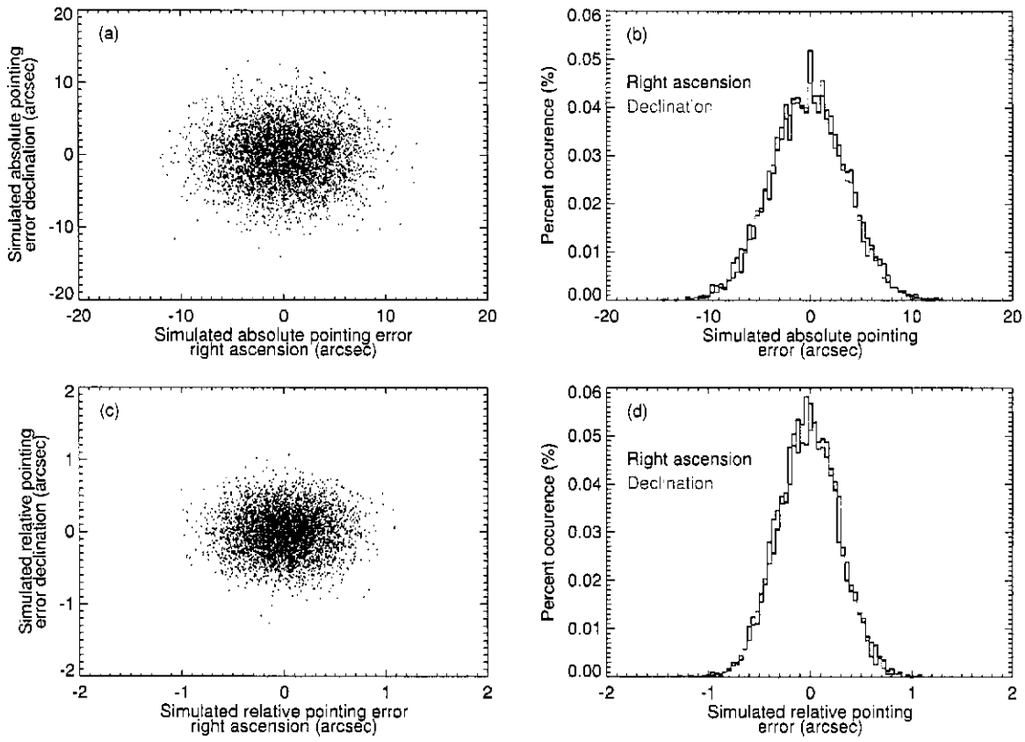

Figure 5.5: Simulated pointing errors of the Herschel telescope. Panels (a) and (c) shows 500 iterations of the absolute and relative pointing errors, respectively, simulated by the POINTINGHSO module. Each black dot corresponds to a single iteration of the module. Panel (b) and (d) shows the distribution of the right ascension and declination for the 500 iterations, for bin sizes of 0.4 and 0.04 arcsec, respectively.

RPE was described in Section 4.7.

To characterize POINTINGHSO, the module was executed 500 times. Figure 5.5 shows the results of these 500 simulations. Each black dot in Panels (a) and (c) represent one iteration of the POINTINGHSO module. Panels (b) and (d) show the distribution of the 500 iterations for bin sizes of 0.4 and 0.04 arcsec, respectively. The distributions for each orthogonal direction, right ascension and declination, are shown. In the case of the APE, the standard deviation of the declination was 3.65 arcsec while the right ascension was 3.74 arcsec. As for the RPE, the standard deviation of the declination was 0.29 arcsec while the right ascension was 0.30 arcsec. The difference between these

simulated values and the specifications given above was less than 1 %. This result confirmed that the POINTINGHSO module performed as expected.

5.6 The POWERBOLO module

The POWERBOLO module was the most complex component of the SPIRE spectrometer simulator. To determine the power incident on the each of the 56 SPIRE bolometers at every instant in the master time grid, this module employed the simulated astronomical source (SAS; see Section 4.2) and the timelines produced by the four previous modules [5, 8]. As explained in Section 4.7, POWERBOLO accounted for the following effects: the background emission of SCAL and the Herschel primary mirror; the optical retardation of the SMEC stage; the FOV of the feedhorns on the sky; and the transmission charateristics of the beamsplitters, filters and feedhorns.

Five separate tests were conducted to characterize this module, each focusing on a different component of the module. These tests, summarized in Table 5.1, were considered sufficient to fully characterize the POWERBOLO module. To simplify the interpretation of the test results, several assumptions were utilized in this section (and Section 5.7). Except for Section 5.6.1, the noise sources of the previous four sections were not included. In other words, the stage velocity, the temperature of the SCAL sources and the Herschel primary mirror, and the pointing of the HSO were all constant. In addition, the beamsplitters were assumed to be ideal (i.e., 50 % reflectance and transmittance). When a test included a non-zero SAS, the data cube contained a single spectrum with a solid angle of 100 arcsec^2 and either one or two emission lines of specific intensity 10^5 MJy sr^{-1}. This specific intensity resulted in an irradiance of approximately 235 Jy on the bolometers, a very strong source [15].

Table 5.2: Summary of POWERBOLO module tests. When included, the spectrum of the simulated astronomical source was a single pixel with a solid angle of 100 arcsec^2 and emission lines of specific intensity 10^5 MJy sr^{-1}. When the stage was scanning, the scan length was -0.35 to 0.35 cm. The symbols T and ε (columns 8 and 9) denote the temperature and emissivity, respectively, of the Herschel primary mirror. Column 10 (Bandpass) includes the circular waveguide cutoff, the transmittance of the low-pass filters and the reflectance of the SPIRE mirrors. Column 11 (Detector system efficiencies) include the aperture, feedhorn and main-beam efficiencies.

Test Description	SAS[a] spectral lines (cm^{-1})		Temperature of sources (K)		Herschel primary mirror		Stage speed (cm s^{-1})	Pointing of HSO[b]	Band-pass	Detection system efficiencies
	Center(s)	Width	SCAL-A	SCAL-B	T (K)	ε (%)				
Scanning HSO[b] (Section 5.6.1)	25	0.33	0	0	0	0	0	on	unity	unity
Ideal compensation (Section 5.6.2)	25,40	0.33	80	0	80	4	0.05	off	ideal	unity
Realistic compensation (Section 5.6.2)	25,40	0.33	13	105	80	varied	0.05	off	realistic	realistic
Absolute power (Section 5.6.3)	off	off	80	0	80	4	0	off	ideal	realistic
Photon noise (Section 5.6.4)	off	off	0	0	25	varied	0.01	off	unity	unity

[a] Simulated astronomical source.
[b] Herschel Space Observatory.

5.6.1 Scanning the Herschel telescope across an unresolved source

To explore the imaging capabilities of SHIFTS, the first test of the POWERBOLO module focused on the binning algorithm outlined in Section 4.8.1. The only variable element in this test was the pointing of the HSO; all other effects were either not included or were assumed to be constant. The transmittance of the optical system (i.e., mirrors, filters and feedhorn system) was unity; photon noise and the thermal emission of SCAL and the Herschel primary mirror were not included; the SMEC stage was stationary at the position of zero path difference (ZPD).

The SAS spectrum contained a single emission line of line width 0.33 cm^{-1} centered at 25 cm^{-1} (see Table 5.1). To simulate the scanning of the HSO, the pointing at each master time interval m was defined as

$$\alpha_{\text{HSO}_m} = at_m + b, \qquad \text{[arcsec]} \tag{5.1}$$

$$\delta_{\text{HSO}_m} = at_m + b, \qquad \text{[arcsec]} \tag{5.2}$$

where $a = 60$ arcsec s^{-1}, $b = -90$ arcsec, t_m was the master time (in s), and α_{HSO_m} and δ_{HSO_m} were the right ascension and declination of the Herschel telescope, respectively (defined in Section 4.7). The position of the source is shown in red in Figure 5.6 with the circular apertures of the spectrometer short wavelength (SSW) feedhorns overplotted in black.

Figure 5.7 shows the resultant power incident on the SSW bolometers. As can be seen, power was only incident on the bolometers whose feedhorns the source passed over in Figure 5.6. Moreover, the length of time where power was incident on a bolometer corresponded to the source crossing time over each feedhorn.

While these figures certainly demonstrate that the binning routine in the POWERBOLO module performed as expected, they also demonstrate the limitations of our current technique. It

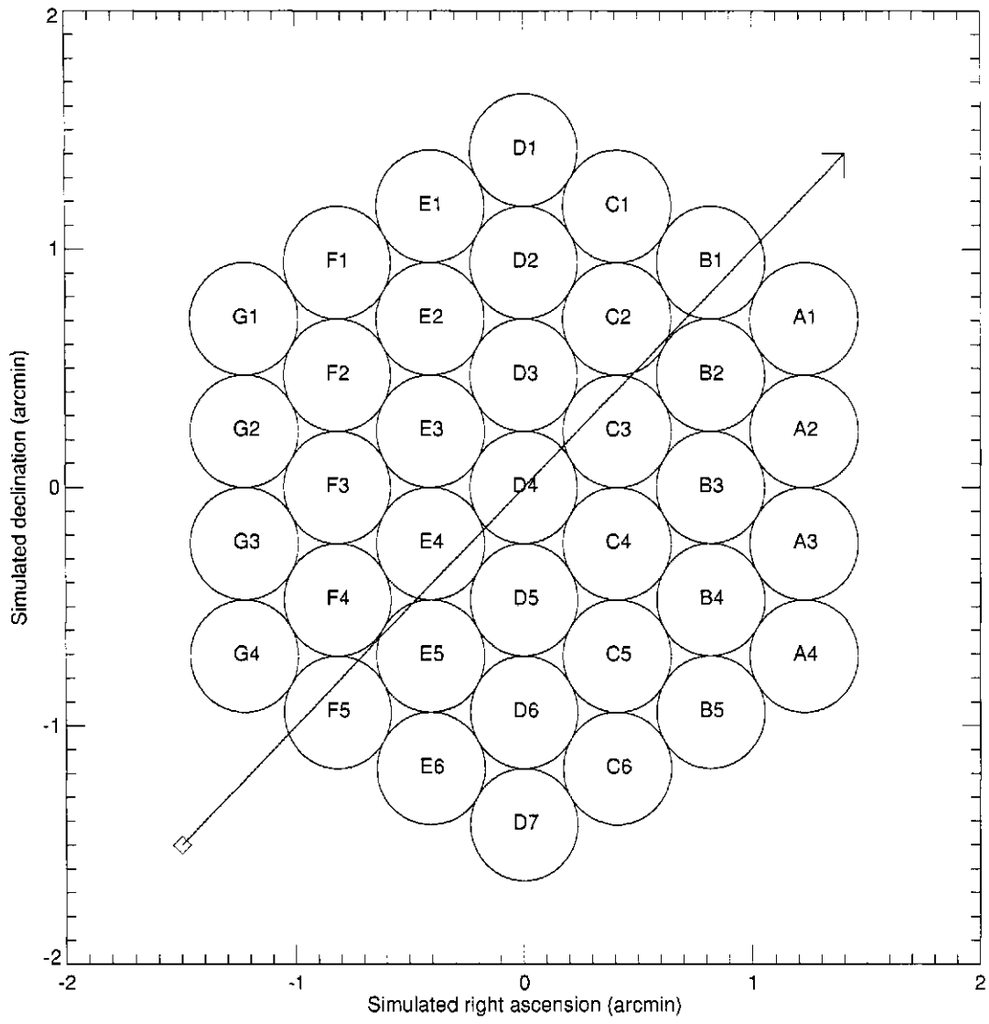

Figure 5.6: Simulation of Herschel Space Observatory scanning. This figure shows an unresolved 10^5 MJy sr^{-1} source drifting across the field-of-view of the spectrometer short wavelength array. The red line shows the motion of the source, where the diamond represents its initial position and the arrow its direction. The black circles represent the circular apertures of the feedhorns.

is clearly unrealistic that the power would only be incident on a single bolometer. The diffraction pattern of the Herschel primary mirror would broaden any unresolved source such that some power would be incident on adjacent pixels [60, 138]. We are currently exploring the possibility of including a full diffraction analysis to incorporate the effects of radiation broadening. For the remainder

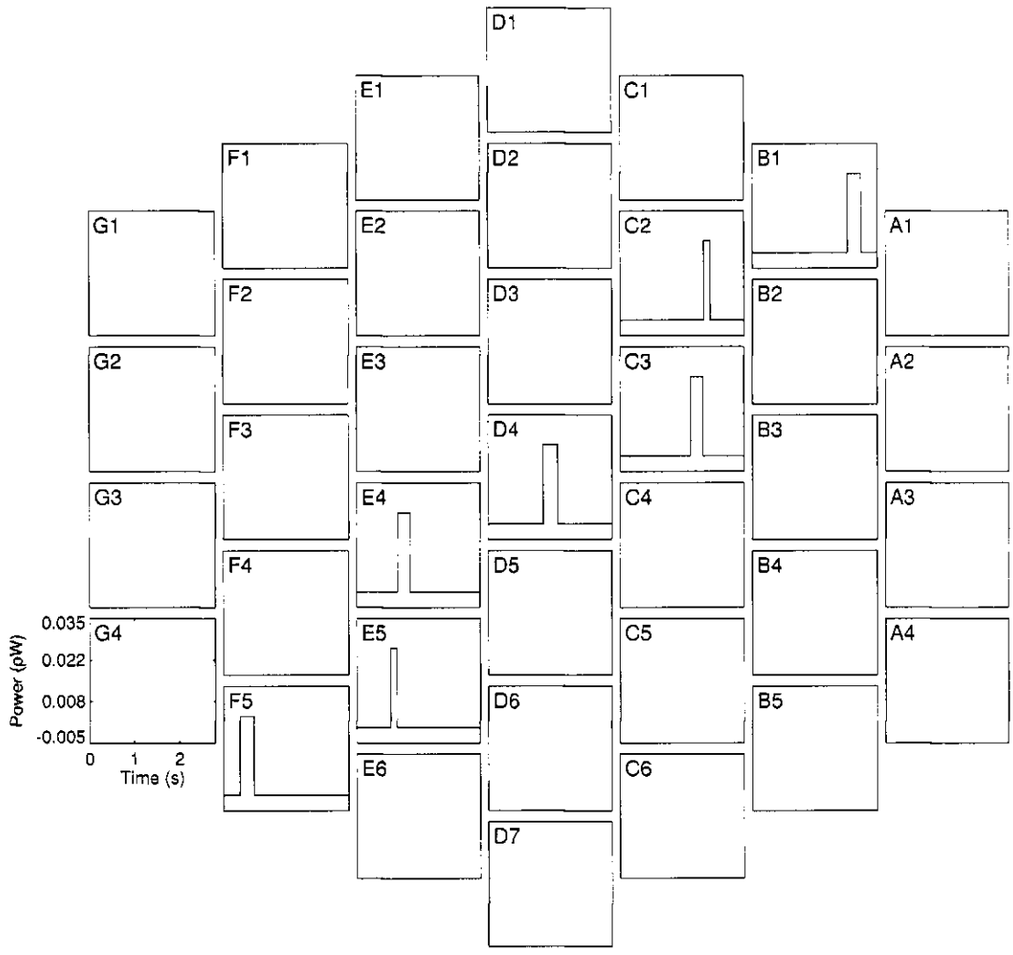

Figure 5.7: Incident signal due to the simulated scanning of the Herschel Space Observatory. This figure shows the power incident on the bolometers of the spectrometer short wavelength band due to the simulated scanning shown in Figure 5.6. The scale for each panel is identical to Panel G4.

of this chapter, the HSO drift was not included.

5.6.2 Compensating for the background emission

Given our confidence in the imaging capabilities of SHIFTS, we turned to the important interferometric capabilities. These next module tests focused on the use of the spectrometer calibrator (seen earlier in Section 5.3) [99]. This section encompassed two tests, one ideal and one

realistic, involving the compensation process outlined in Section 3.3.

In both cases, the emission lines of the SAS spectrum were located at 25 and 45 cm^{-1} with a spectral resolution of 0.33 cm^{-1} (see Panel (a) of Figure 5.8). Moreover, the thermal emission of the Herschel primary mirror was included, at a temperature of 80 K and an emissivity of 4 %. In the ideal case, two medium resolution scans (-0.35 to 0.35 cm, relative to ZPD) was measured at a stage speed of 0.05 $cm\,s^{-1}$; five scans were performed for the realistic case.

Ideal case

In addition to the scan conditions mentioned above, the ideal compensation test modified another SHIFTS parameter. While the efficiencies of the detector system and the mirrors were still assumed to be unity, the bandpass of the spectrometer long wavelength (SLW) and spectrometer short wavelength arrays were included (see Panel (b) of Figure 5.8). However, the filter profiles were assumed unity in-band and were identical for both input ports (in contrast to the real transmission profiles discussed in Section 4.8.3).

Panels (c) and (d) show the SLW and SSW interferograms, respectively, around ZPD due to the SAS and the thermal emission of the Herschel primary mirror. Due to the complementary nature of the output ports and the fact that only the first input port was illuminated, the SLW interferogram was inverted and thus a minimum at ZPD while the SSW interferogram was a maximum at ZPD [49]. As expected, an offset of half the maximum power (of the SSW port) was present in both interfergrams. Furthermore, the SLW band contains lower frequency information so its interferogram does not oscillate as quickly as the SSW interferogram, which contains higher frequency components.

After the offset was removed, the spectrum of each interferogram was computed and is

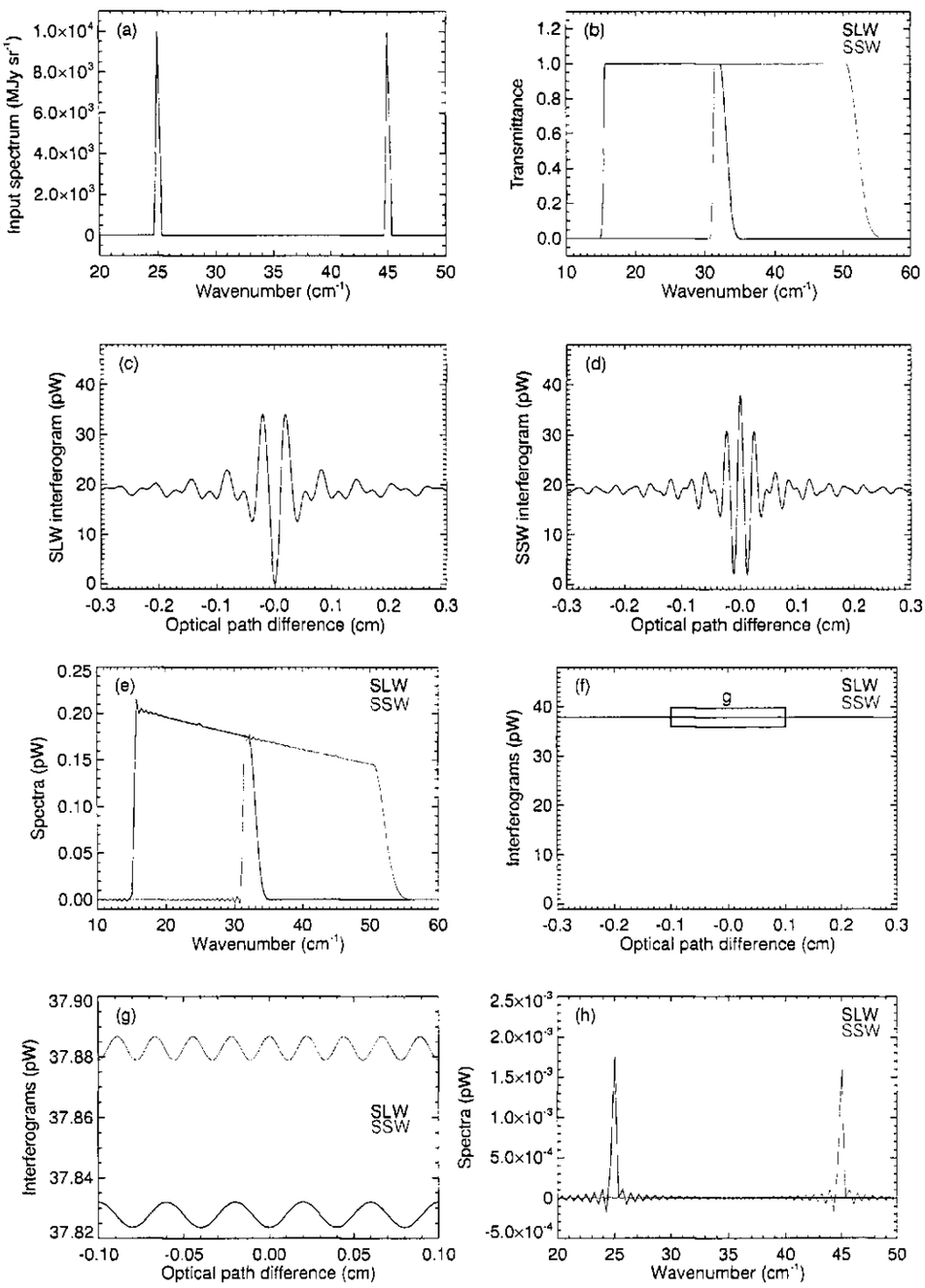

Figure 5.8: Simulation of ideal compensation. Panel (a) shows the spectrum of the simulated astronomical source. Panel (b) shows the transmittance of the two detector bands. Panels (c) and (d) show the simulated long and short wavelength interferograms, respectively, due to the SAS spectrum and the blackbody emission of the Herschel primary mirror. Panel (e) shows the spectra corresponding to Panels (c) and (d). Panel (f) shows the simulated SLW and SSW interferograms due to the SAS and the blackbody emission of the Herschel primary mirror and the spectrometer calibrator. The blue box marked "g" represents the 0.2 cm segment shown in Panel (g). Panel (h) shows the spectra corresponding to Panel (f).

shown in Panel (e). Naturally, energy was only present in the regions allowed by the bandpasses shown in Panel (e). The SAS emission lines were visible as small spikes at 25 and 45 cm^{-1}. However, the amplitude of the lines was small in comparison to the background due to the Herschel primary mirror.

A second scan was simulated under nearly identical conditions. To counteract the strong background signal, the second input port was now illuminated by the SCAL-A source (i.e., the 4 % source) heated to 80 K. The radiation from SCAL-B and the remainder of the SCAL cavity were not included [99]. Since we illuminated the complementary input port, the resulting SLW interferogram due to SCAL experienced constructive interference at ZPD while the SSW interferogram due to SCAL experienced destructive interference [49,90]. Since the input beams (e.g., SCAL, the SAS and the Herschel primary mirror) are incoherent, the resulting interferogram was the sum of the three interferograms present in each output port.

Panel (f) shows the SLW and SSW interferograms for the ideal case of uniform and equal transmission through the two ports. The interferograms were perfectly compensated; the large modulation seen in Panels (c) and (d) disappeared. By extracting a 0.2 cm segment from both interferograms (denoted by the blue box marked "g"), Panel (g) clearly shows the compensated interferograms due to the SAS emission lines (i.e., the cosine waves). Panel (h) shows the Fourier transform of the two compensated interferograms after removal of the offset. The ringing of the sinc function was visible in the spectra because the spectral resolution of the 0.35 cm scan (0.43 cm^{-1} by Equation 2.44) was of the order of the line width of the input SAS spectrum (see Sections 2.4.5 and 2.5.2).

Realistic case

Figure 5.8 showed the compensation of the Herschel primary mirror for the ideal case where the transmission efficiency for both input ports were identical. In other words, it did not account for the differential transmission of the two input ports. As indicated in Sections 4.8.3, radiation from the SCAL port passes through two fewer filters and reflects off seven less mirrors [99, 100]. Correspondingly, its total transmittance is much higher. Therefore, heating the SCAL-A source to the same temperature as the Herschel primary mirror would not compensate, it would dominate.

The second compensation test repeated the first test but with realistic transmission values. The temperature of the Herschel primary mirror, the SAS spectrum, the scan length and the stage speed were unchanged in this test. To simulate the transmittance of the optical system, we employed the profiles shown in Figure 4.7, which included the detector system efficiencies, the transmittance of the low-pass filters, the cutoff frequency of the circular waveguide and the reflectance of the SPIRE mirrors. However, to avoid the ripples in the transmittance due to the low-pass filters, the transmittance was averaged over the bandpass of each detector array. For the SLW output port, an average transmittance of 0.56 and 0.67 were used for the sky and SCAL ports, respectively. For the SSW output port, an average transmittance of 0.55 and 0.68 were used for the sky and SCAL ports, respectively. Even though the temperature of the Herschel primary mirror was fixed, the emissivity was varied between 3.5 and 4.5 %, in increments of 0.25 %. Following Hargrave *et al.* [99], SCAL-A and SCAL-B were heated to 13 and 105 K, respectively.

Figure 5.9 shows the compensated interferograms and spectra under these realistic conditions. Panel (a) shows the SLW interferograms for each emissivity of the Herschel primary mirror. As can be seen, the central peak of the $\varepsilon_{tel} = 3.5\,\%$ interferogram was not inverted, indicating the SCAL port was dominant. With each increase in the primary mirror emissivity, the total power in-

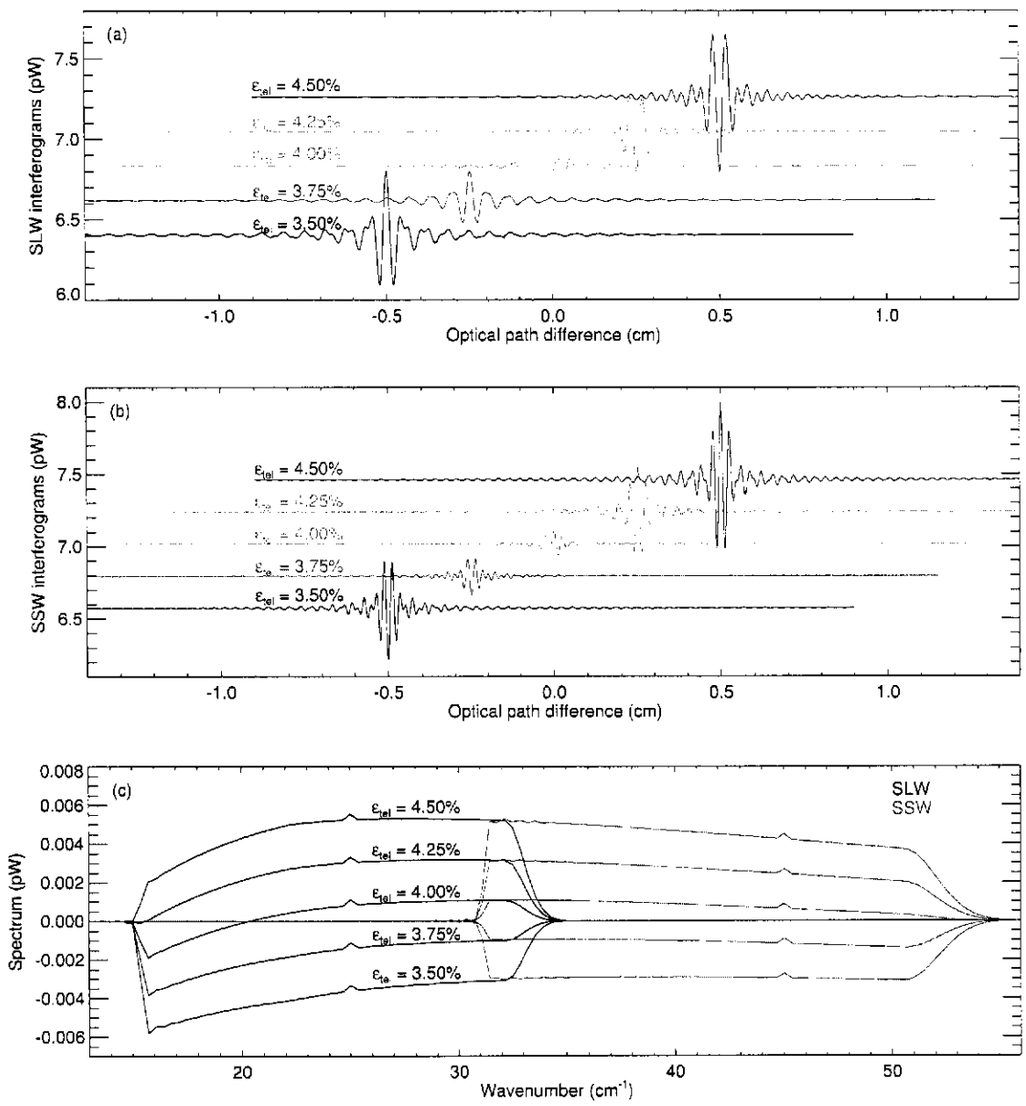

Figure 5.9: Simulation of realistic compensation. Panels (a) and (b) show the long and short wavelength interferograms, respectively, where each plot corresponds to a different emissivity of the Hershel primary mirror (denoted by $\varepsilon_{\mathrm{tel}}$). For clarity, each interferogram (except the 4 % emissivity case) is shifted horizontally relative to one another; the central peak of each interferogram is actually located at zero path difference. Panel (c) shows the spectra corresponding to the interferograms in Panel (a) and (b). In all three panels, the SCAL-A and SCAL-B sources were heated to 13 and 105 K, respectively, and the Herschel primary mirror was heated to 80 K.

creased (evidenced by the rising offset) and the Herschel primary mirror gained in dominance. At a telescope emissivity of 4.5 %, the central peak was inverted, indicating the sky port was now dom-

inant. A similar but reversed picture was seen in Panel (b), which shows the SSW interferograms under the same conditions. In the SSW port, the SCAL dominance at $\varepsilon_{tel} = 3.5\,\%$ was denoted by an inverted central peak, and vice-versa for the Herschel dominance at 4.5 %. In both bands, the modulation of the interferograms was smallest for a telescope emissivity of 4 %, an outcome that matched the result found in Hargrave *et al.* [99].

Panel (c) shows the spectra corresponding to the interferograms in Panels (a) and (b). Similar to Figure 5.8, the power in each band was restricted by the combination of the low-pass filters and the circular waveguide low-frequency cutoff. In each spectrum, the emission lines were clearly visible at 25 and 45 cm^{-1}. In both bands, a negative spectrum represented a dominant SCAL port. As expected, the spectra mirrored the interferograms; SCAL was dominant at low emissivities and the Herschel primary mirror was dominant at high emissivities. One spectrum of note was the $\varepsilon_{tel} = 4\,\%$ SLW spectrum, which switched from negative to positive at 20 cm^{-1}. First of all, this was reflected in its interferogram in Panel (a), where the central peak was neither the maximum nor the minimum of the interferogram. More importantly, the negative component of the spectrum could easily lead to problems when the interferogram was phase-corrected (see Section 2.5.3).

These two tests validated the interferometric component of the POWERBOLO module (see Sections 4.8.2 and 4.8.3). First of all, the line centers of the two SAS emission lines were measured at the correct locations. Furthermore, the complementary nature of the two output ports was evidenced in Figures 5.8 and 5.9. Those figures also clearly demonstrated the advantages and disadvantages associated with compensation: reduced modulation at the cost of a larger offset. Finally, the results of the second compensation test were in agreement with the results found in Hargrave *et al.* [99].

5.6.3 Absolute power calibration

Section 5.6.2 investigated the quantitative aspects of the interference routine in the POWERBOLO module. The test outlined in this section quantified the background power on the SPIRE bolometers and compared those values to a radiative transfer model estimate found in the literature [5, 85].

Griffin, Swinyard & Vigroux [5] lists the background power on each bolometer due to SCAL and the Herschel primary mirror. For the SLW bolometers, the background power was 14 pW and for the SSW bolometers, 15 pW. However, these values included the contribution from each radiation mode propagating in the circular waveguide. As stated in Section 3.6.2, up to five modes propagate in the SLW waveguides and up to three modes propagate in the SSW waveguides. In contrast, SHIFTS only modelled the propagation of the fundamental transverse electric mode (TE_{11}). While the TE_{11} mode contains the majority of the energy in each band, a direct comparison of SHIFTS to the results of Griffin, Swinyard & Vigroux [5] would underestimate the background power.

Instead, our comparison focused on the values given in Griffin [85], which listed the estimated background power in each mode. The simulation described in that SPIRE technical document included the blackbody emission of every thermal source present in the SPIRE spectrometer. In Griffin's [85] analysis, the transmittance of the low-pass filters was fixed at 0.87, the transmittance of the high density polyethelene lens (HDPE; see Section 3.6.1) was set to 0.9 and the reflectance and transmittance of the beamsplitters were set to 0.474. The band edges of the SLW array were 14.92 and 30.77 cm^{-1} and the band edges of the SSW array were 33.33 and 52.63 cm^{-1}. The temperature of the primary mirror and SCAL were both set to 80 K with associated emissivities of 4 %. The aperture, feedhorn, main-beam and optical efficiencies matched the values used in the

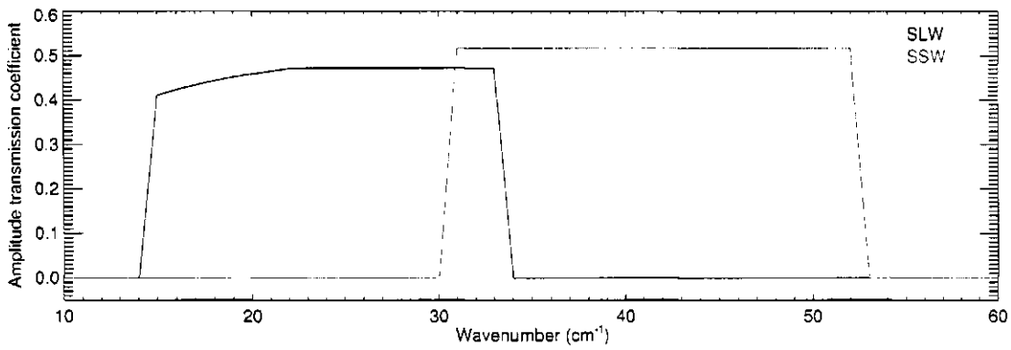

Figure 5.10: Transmission bandpass for absolute power calibration.

previous section. The throughput was given by Equation 4.4. With these values, Griffin [85] determined that the background power in the TE_{11} mode was 7.9 pW in the SLW band and 9.8 pW in the SSW band.

To reproduce the results of Griffin [85], the POWERBOLO module was executed using the conditions listed above. The SAS spectrum was not included (i.e., the HSO observed a blank patch of sky) and the stage was stationary at the ZPD location. To simulate the SCAL emission, only the SCAL-A source was heated. The combination of the detector system efficiencies, band edges, and optical and low-pass filter transmittances yielded the total efficiency, η_k (see Section 4.8.3), shown in Figure 5.10. This figure was similar to the band transmittance used in Section 5.6.2. While the profiles used in the previous section were based on the measured data (see Figure 4.7), the values from Griffin [85] were employed to produce a more direct comparison. Upon execution of SHIFTS, the returned values were 7.66 pW for the SLW bolometer and 9.43 pW for the SSW bolometer.

While the results were encouraging, we note that the SHIFTS values were approximately 5 % lower than the values found in Griffin [85]. This minor difference was due exclusively to the fact that SHIFTS did not model the thermal emission of any sources other than SCAL and the Herschel

primary mirror. Even though Section 4.8.2 demonstrated that the emission of a 1 % emissive 4.5 K blackbody was small, the sum of the emission from all the optical components in SPIRE is sufficient to account for this small discrepancy. This result justifies our decision to ignore the blackbody emission from the cold sources.

5.6.4 Photon noise

The final component of the POWERBOLO module determined the photon noise. Introduced in Section 3.6.3, photon noise is caused by random fluctuations in the arrival time of incident photons and is proportional to the square root of the number of photons [130].

To test the photon noise simulation, we assumed once again that the SPIRE spectrometer was an ideal interferometer. The system efficiency, η_k, was assumed to be unity across the whole band and the beamsplitter reflectance and transmittance were both 50 %. The SAS and the thermal emission from SCAL were not included. The temperature of the Herschel primary mirror was fixed at 60 K for two emissivities: 0.01 and 0.0001 %. While these Herschel primary mirror emissivities are unrealistic, they were useful for demonstrative purposes. Varying the emissivity was a simple method of linearly scaling the power incident on the bolometers at each instant of time. Four medium resolution scans were run at a speed of 0.01 $\mathrm{cm\,s^{-1}}$, two with photon noise and two without.

Figure 5.11 shows the simulated interferograms. Panels (a) and (b) show the SLW and SSW interferograms, respectively, for a telescope emissivity of 0.01 %. Panels (c) and (d) show the SLW and SSW interferograms, respectively, for a telescope emissivity of 0.0001 %. All four panels include both the photon noise and no photon noise cases. Since there are fewer total photons at $\varepsilon_{\mathrm{tel}} = 0.0001$ %, the photon noise was relatively higher for this case. Panels (e) and (f) fo-

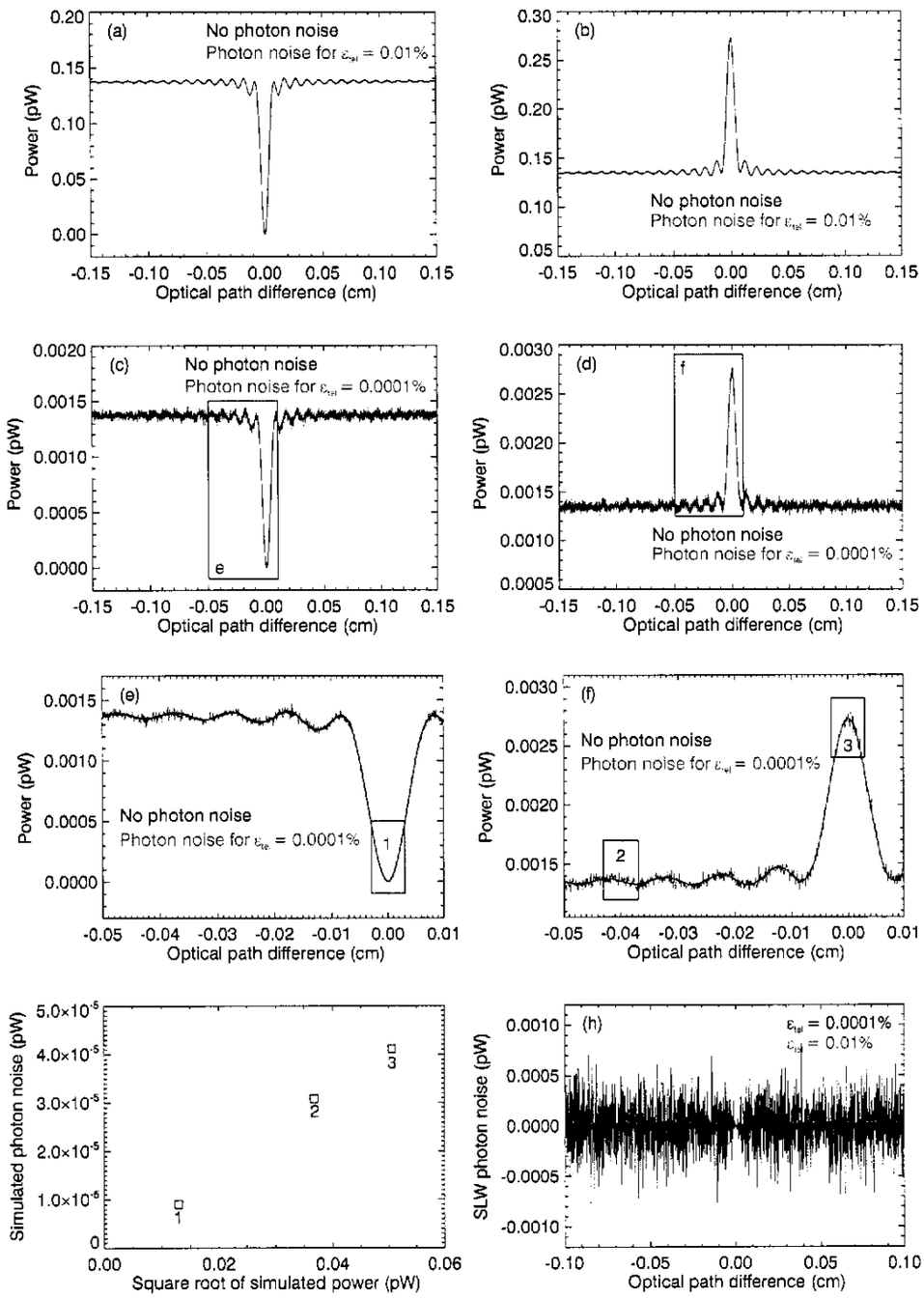

Figure 5.11: Simulation of photon noise. Panels (a) and (b) show the long and short wavelength interferograms, respectively, for a telescope emissivity (denoted by ε_{tel}) of 0.01 %. Panels (c) and (d) show the SLW and SSW interferograms, respectively, for a telescope emissivity of 0.0001 %. The blue boxes denote the 0.6 cm segments shown in Panels (e) and (f). The numbered blue boxes in Panels (e) and (f) represent the mean photon noise values shown in Panel (g). Panel (h) shows the SLW photon noise at each emissivity value.

cused on the boxed sections of Panel (c) and (d). The boxes marked "1", "2" and "3" correspond to the inverted and non-inverted central peaks of the interferograms, as well as the offset. The standard deviation of the photon noise was calculated for each box; the photon noise was defined as the difference between the interferograms with and without photon noise (i.e., Equation 4.18). These standard deviations were plotted against the square root of the mean power in those boxes in Panel (g). As expected, there was a linear relationship between these values. Finally, Panel (h) shows the photon noise in the SLW band at the two emissivities. The ratio of the standard deviation of the 0.01 and 0.0001 % sources was 10.14 (or approximately $\sqrt{100}$).

Several conclusions were drawn from these results. The results shown in Panels (g) and (h) proved that the photon noise was simulated correctly by SHIFTS. Moreover, these results further demonstrate one of the drawbacks of using SCAL to compensate for the thermal emission of the primary mirror. While Section 5.6.2 proved that employing SCAL lowers the modulation in the interferogram, its use will increase the photon noise by approximately a factor of $\sqrt{2}$.

5.7 The DETECTORSIG module

The final SHIFTS module, DETECTORSIG, converted the power incident on the bolometers into a measured signal. To simulate the response of the bolometers and the six-pole Bessel filter in the warm electronics, the signal was convolved by an impulse response function (IRF; see Figure 4.9). To characterize this module, we determined the thermal time constant from the phase of the convolved interferogram and compared it to the set value. We deemed it unnecessary to test the simulation of the electrical noise (since it was calculated in a similar fashion to the photon noise) or the various scaling factors (e.g., responsivity, electrical gain, detector quantum efficiency). SHIFTS was executed under similar conditions to the previous test (see Table 5.2). The only differences

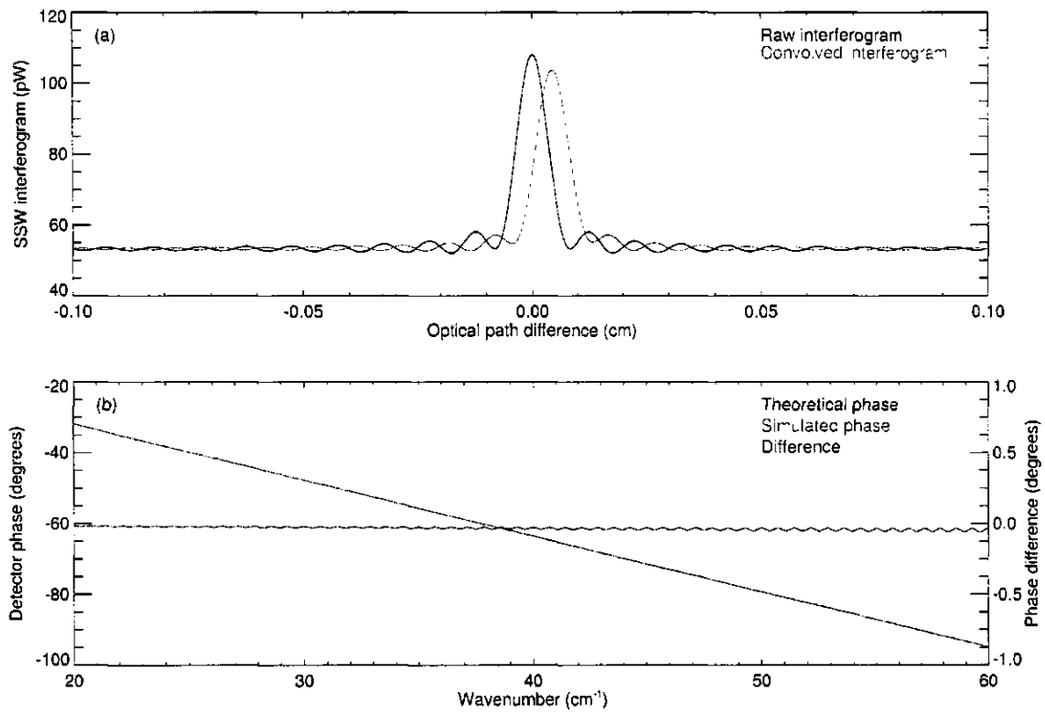

Figure 5.12: Simulated response of the bolometer and warm electronics. Panel (a) shows a raw interferogram and an interferogram convolved by the impulse response function shown in Figure 4.9. Panel (b) shows the simulated and theoretical phase associated with the convolved interferogram; as well as the difference between the two. In Panel (b), the black and red curves follow the left-hand ordinate while the blue curve follows the right hand ordinate.

were that the emissivity of the Herschel primary mirror was increased to 4 %, the stage speed was increased to 0.05 $\mathrm{cm\,s^{-1}}$ and the photon noise was not included.

The impulse response function is given by Equation 4.20. This test employed a thermal time constant of 5.1 ms, which corresponds to the IRF shown in Figure 4.9. Figure 5.12 shows the result of the convolution of the interferogram and the phase. In Panel (a), we note that the convolved interferogram was no longer symmetric about ZPD. As the stage scans from left to right, the power incident on the bolometers changes due to the interference of the beams. The thermal and electrical lag of the detectors moved the maximum measured signal to an optical path difference (OPD) of approximately 50 μm (i.e., after the stage passed the position of maximum incident signal). As is

discussed in more detail in Section 6.3.1, the OPD location of the maximum value of the measured interferogram depends on the scan direction and the stage speed.

The spectrum was determined from the convolved interferogram in Panel (a). From the real and imaginary components of the spectrum, the phase was calculated using Equation 2.16 and is shown in black in Panel (b). Since the raw interferogram was symmetric about ZPD, the phase was entirely due to the IRF.

The theoretical phase of the IRF is equal to the phase of the product of the bolometer and electrical transfer functions (Equations 3.8 and 4.19, respectively). After converting frequency to wavenumber with Equation 3.1, the theoretical phase is shown in red in Panel (b). Note the close agreement between the simulated and theoretical phase.

Finally, the simulated phase was fit to the theoretical phase using MPFITFUN, an external IDL least-squares fitting routine written by Craig Markwardt* [136]. This routine uses the Levenberg-Marquardt method to determine the free parameters of an explicit function (in our case, the equation for the theoretical phase) [136, 143]. From this least-squares fit, we determined a τ value of (5.097 ± 0.001) ms.

The calculated thermal time constant differed from the set value by 0.06 %. This result conclusively proved that the DETECTORSIG module realistically simulated the response of bolometer and electrical response. The fitting technique outlined above reappears in Chapter 6 when we determine the thermal time constants of the PFM1 data.

*Web address: *http://cow.physics.wisc.edu/~craigm/idl/idl.html*

5.8 Summary

Chapter 5 outlined the first qualification tests of the SPIRE spectrometer simulator. Each of the six modules were validated by comparing their output to either measured values or theoretical predictions. In every case, the modules performed as expected. Moreover, the results of the module tests demonstrated some of the advantages and challenges associated with the SPIRE spectrometer, specifically with regards to the use of the spectrometer calibrator. Confident that all the SHIFTS modules work individually, the next chapter performs a full integration test of SHIFTS by comparing simulated interferograms to real data measured during the PFM1 test campaign.

Chapter 6

Comparing SHIFTS with the first SPIRE proto-flight model test results

> *"First you guess. Don't laugh, this is the most important step. Then you compute the consequences. Compare the consequences to experience. If it disagrees with experience, the guess is wrong. In that simple statement is the key to science. It doesn't matter how beautiful your guess is or how smart you are or what your name is. If it disagrees with experience, it's wrong. That's all there is to it."*
>
> - Richard Feynman, *NOVA: The Best Mind since Einstein*. Public Broadcasting Service (1993).

This chapter compares real and synthetic data products for the Spectral and Photometric Imaging Receiver (SPIRE) spectrometer. The real instrument data was collected during the first SPIRE proto-flight model (PFM1) test campaign conducted at the Rutherford Appleton Laboratory (RAL) in Oxfordshire, England in 2005. The synthetic data was generated by the Simulator for the Herschel Imaging Fourier Transform Spectrometer (SHIFTS). The previous chapter characterized each of the six modules of SHIFTS and ensured they performed as expected.

Section 6.1 briefly describes the PFM1 test campaign and Section 6.2 introduces the data-processing pipeline employed to reduce and analyze the PFM1 results. Sections 6.3 and 6.5 analyze

three sets of PFM1 data and compare them to the complementary SHIFTS data. It should be noted that this chapter focuses on the interferogram data products generated during the PFM1 tests campaign. While Appendix B also contains results from the PFM1 test campaign, it deals only with subsystem qualification data.

6.1 The first proto-flight model test campaign

In any space mission, several test campaigns are conducted on the instrument models to determine the expected operation in a space environment. As noted in Section 1.2, the cryogenic qualification model (CQM) test campaign conducted at RAL in 2004 provided a preliminary charaterization of the optical, thermal and electrical systems of SPIRE [43]. The PFM1 tests were the first test campaign where a complete SPIRE model was operated under nominal flight conditions.

To simulate the thermal environment that will be experienced by SPIRE at the second Lagrangian point (L2), the PFM1 model was mounted inside a test cryostat [151]. Figure 6.1 shows a photograph of the test cryostat. The sky port of the SPIRE spectrometer viewed the test facility through the cryostat window or, by insertion of a flip mirror, an internal cryogenic blackbody (CBB) source [43, 151, 152]. Manufactured in a similar fashion to the spectrometer calibrator (SCAL; see Section 3.3), the CBB was a blackened source that filled the field-of-view (FOV) and was used to mimic the thermal emission of the Herschel primary mirror [43, 151]. The 300 K atmospheric radiation of the test facility was attenuated by neutral density filters placed after the cryostat window [152]

Cooling of the cryostat began on February 24, 2005 and the final instrument test was completed on April 6, 2005. During those six weeks, SPIRE consortium members performed hundreds of tests on both the photometer and the spectrometer. Since the PFM1 tests were the first

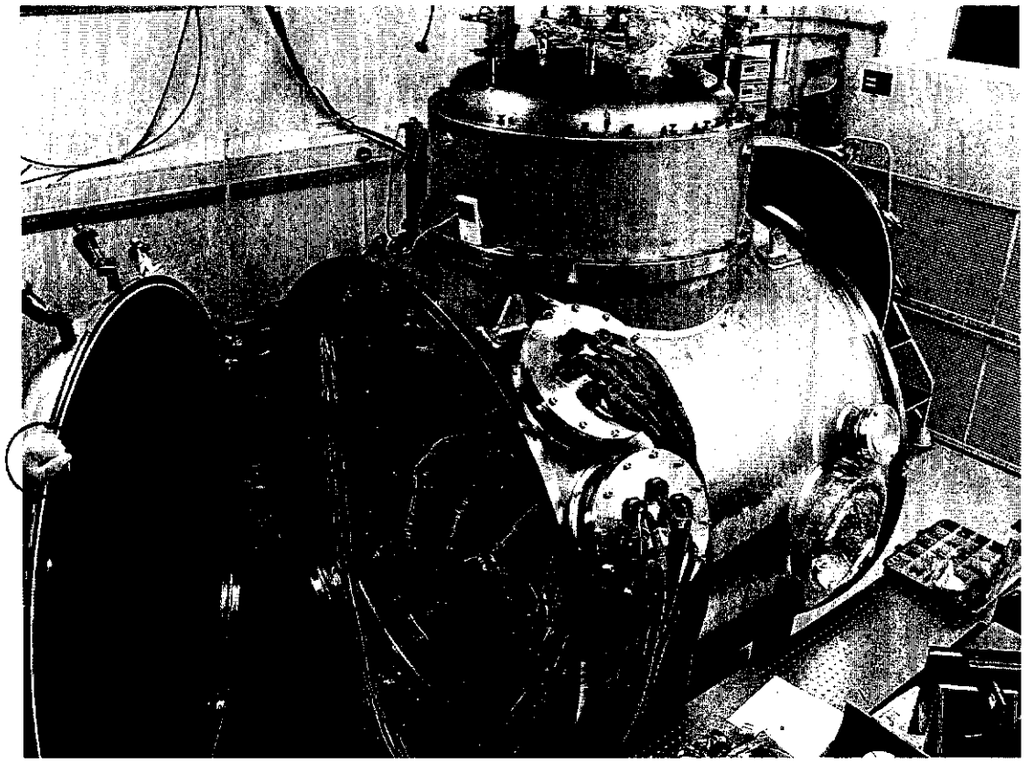

Figure 6.1: Photograph of the test cryostat at the Rutherford Appleton Laboratory in Oxfordshire, England [43]. The figure shows the cryogenic qualification model of SPIRE mounted inside the cryostat during the CQM test campaign in 2004. For a scale reference, note the cotton-gloved hand (circled in red) on the far left of the photograph. (Figure courtesy of Dr Tanya Lim, Rutherford Appleton Laborary, Oxfordshire, England.)

of three major test campaigns (see Section 1.2), the results were naturally incomplete. To perform integrated tests with SHIFTS, we selected three datasets (summarized in Table 6.1) where the SPIRE spectrometer was operated under a variety of scan conditions.

As indicated in the table, sixteen high resolution scans were measured on March 8, 2005 with the CBB source heated to 7.5 K. Section 6.3 analyzes the results of these scans, highlighting the basic features of the interferograms and spectra, and conducting a detailed analysis of the spectral phase. On March 24, a set of scans tested the compensation of the CBB source with the spectrometer calibrator (SCAL). Section 6.4 compares these results to the synthetic data products generated by SHIFTS. Finally, we examined a series of scans taken on April 8, where each group of scans was

Table 6.1: Summary of the first proto-flight model results measured in 2005. For the errors on the speeds, see Table B-1; for the errors on the spectrometer calibrator temperatures, see Table B-2.

Date	Scan start time	Number of scans	Length per scan (cm)	Stage speed ($\mu m\,s^{-1}$)	Temperature (K)		
					SCAL-A	SCAL-B	CBB[a]
March 8	23:09	16	3.439	454.49	4.612	5.035	7.5[b]
March 24	17:46	10	0.646	302.65	38.142	6.480	11.543
	17:58	10	0.646	302.78	38.146	6.494	12.029
	18:20	10	0.646	302.86	38.151	6.507	12.517
April 6	13:59	4	3.498	90.45	4.316	4.552	off
	15:03	4	3.499	271.35	4.173	4.416	off
	15:17	4	3.499	452.25	4.178	4.418	off
	15:24	4	3.500	633.16	4.184	4.425	off
	15:32	4	3.501	904.56	4.184	4.424	off

[a] Cryogenic blackbody.
[b] Source: PFM1 logbook (temperature measurements unavailable).

measured at a different stage speed. During these scans, a far-infrared laser (FIR) was placed in the optical path of the cryostat aperture. Sections 6.5 explores changes in the strength of the laser line due to the increasing scan speed. Before examining the PFM1 data, the following section briefly describes the data-processing pipeline employed to reduce both the real and synthetic data products.

6.2 SPIRE data-processing pipeline

In partial fulfillment of its obligations to the SPIRE project, the Astronomical Instrumentation Group (AIG) at the University of Lethbridge is currently developing a data-processing pipeline for the SPIRE spectrometer [40]. The pipeline is necessary due to the complexity of the mathematical methods used to recover a spectrum (see Section 2.4 and 2.5). This section introduces the pipeline and describes how it was employed to analyze the real and synthetic PFM1 data.

While the current version of the pipeline is robust, some data-processing artifacts are still present in the resultant spectra. The qualification of SHIFTS highlighted several minor problems

in the pipeline, thereby satisfying one of the motivations for the development of SHIFTS (see Section 1.3). My own involvement in the development of the pipeline was minor and is not addressed in this thesis. The discussion here focuses on how the data presented in Chapters 6 and 7 were reduced and analyzed.

The input to the pipeline are the Herschel data products described in Section 4.10. The pipeline accepts both real (e.g., PFM1) and SHIFTS-simulated data products. In the case of real data, the detectors signals were given in analog-to-digital units (ADUs). Section 3.7 indicated that a 16-bit analog-to-digital converter (ADC) in the SPIRE warm electronics digitizes voltages between 0 and 5 V [135]. To allow absolute power comparisons, we converted all the real detector signals from ADUs to voltages using this scaling factor.

Written in Java, the pipeline is composed of a series of data-processing modules [125, 153, 154]. Each module performs a single mathematical operation on the input data product. The first module accounts for the asynchronous sampling of the stage position and detector signals. As indicated in Section 3.5, the irregularly spaced stage position of the spectrometer mechanism, $z(t)$, was sampled at 226.12 Hz. Section 3.7 noted that the detector signal, $I(t')$, was sampled on a different time grid, t', at a frequency of 80 Hz [5]. The mathematics of the fast Fourier transform (FFT) requires that the interferogram be sampled at equal intervals of optical path difference (OPD) [53]. Therefore, the first step in the processing re-samples the stage position onto a uniform OPD spacing by means of a cubic spline interpolation [109, 143]. The detector signals are then interpolated onto the uniform OPD grid. For more on this interpolation step, see Naylor *et al.* [109]. The remaining modules in the pipeline are optional (except for the final single-sided Fourier transform). The optional modules include a DC offset removal (see Section 2.3.2) and phase correction (see Section 2.5.3). These modules are employed in various combinations in Sections 6.3 through 6.5 (and

in Chapter 7).

6.3 Cryogenic blackbody

The first set of PFM1 data analyzed was measured between 23:09 and 23:29 on March 8. Sixteen high resolution scans (eight forward and eight reverse) were taken at a stage speed of 452 $\mu m\,s^{-1}$ (see Table 6.1). During the scans, the CBB was heated to a temperature of 7.5 K while the two SCAL sources were not heated. This section examines the interferograms of the two central pixels in each spectrometer band (SLWC3 and SSWD4; see Figure 3.10) and compares their spectra to simulated spectra generated by SHIFTS.

To generate the synthetic data products, SHIFTS was executed under the conditions outlined in Table 6.1. The stage velocity jitter and the electrical and photon noise were included, as were the bolometer and electrical responses (see Sections 4.4, 4.8.5 and 4.9). The measured values of the thermal time constants were determined using a technique outlined in Section 6.3.2. From this analysis, the SLWC3 and SSWD4 thermal time constants were set to 12.40 and 5.97 ms. Although the SCAL sources were not heated, the SCAL assembly still fills the FOV of the second input port. The SCAL sources were simply fixed at the temperatures given in Table 6.1; the remaining 94 % of the area of the pupil was set to 4.5 K.

Section 6.3.1 compares the real and synthetic interferograms under these scan conditions. Section 6.3.2 then compares the real and synthetic spectra and uses the phase to determine the bolometer time constants. Finally, Section 6.3.3 investigates the high resolution spectra of the real and synthetic data following phase correction.

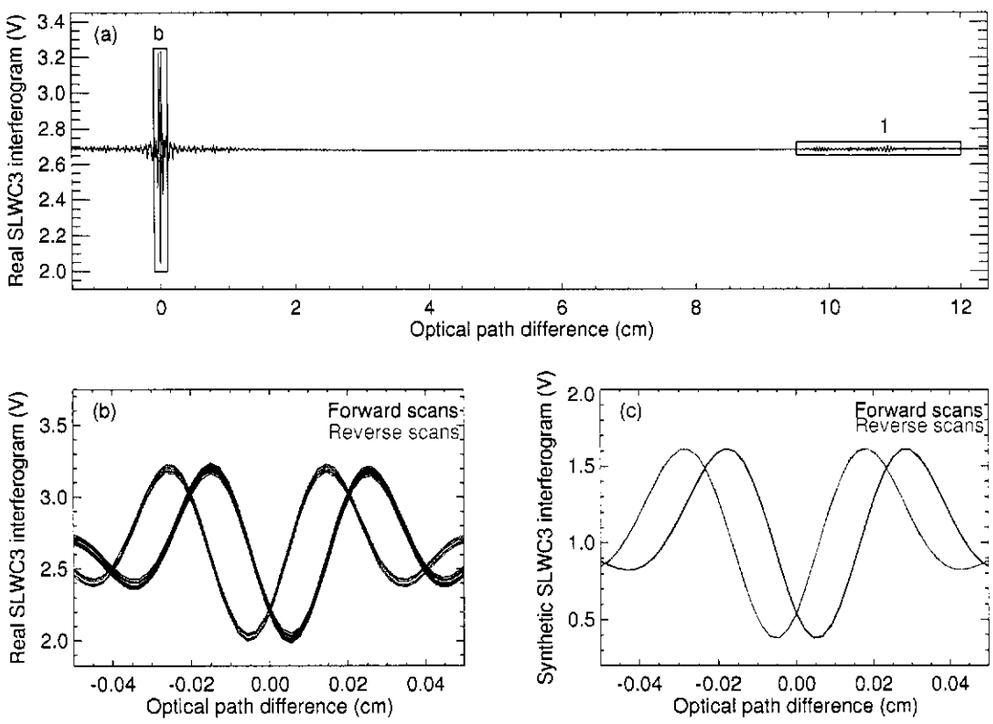

Figure 6.2: Real and synthetic SLWC3 interferograms due to the cryogenic blackbody. Panel (a) shows a single SLWC4 interferogram measured on March 8, 2005 during the first proto-flight model test campaign. The blue box marked "1" denotes the channel fringes (explained in the text) while the blue box marked "b" denotes the region of the interferogram shown in Panel (b). Panel (b) shows all sixteen real SLWC3 interferograms; Panel (c) shows all sixteen synthetic SLWC3 interferograms.

6.3.1 Raw interferograms

The interpolated interferograms were extracted from the pipeline prior to the removal of the DC offset. Figure 6.2 shows the real and synthetic SLWC3 interferograms. As is denoted by the blue box marked "1" in Panel (a), features were present in the interferograms at large OPDs. These channel fringes were not an artifact of the data-processing; the AIG at the University of Lethbridge traced them to resonant cavities in the detector system [72]. However, these are beyond the scope of modelling and were therefore not included in SHIFTS.

The second blue box in Panel (a) denotes the region near zero path difference (ZPD)

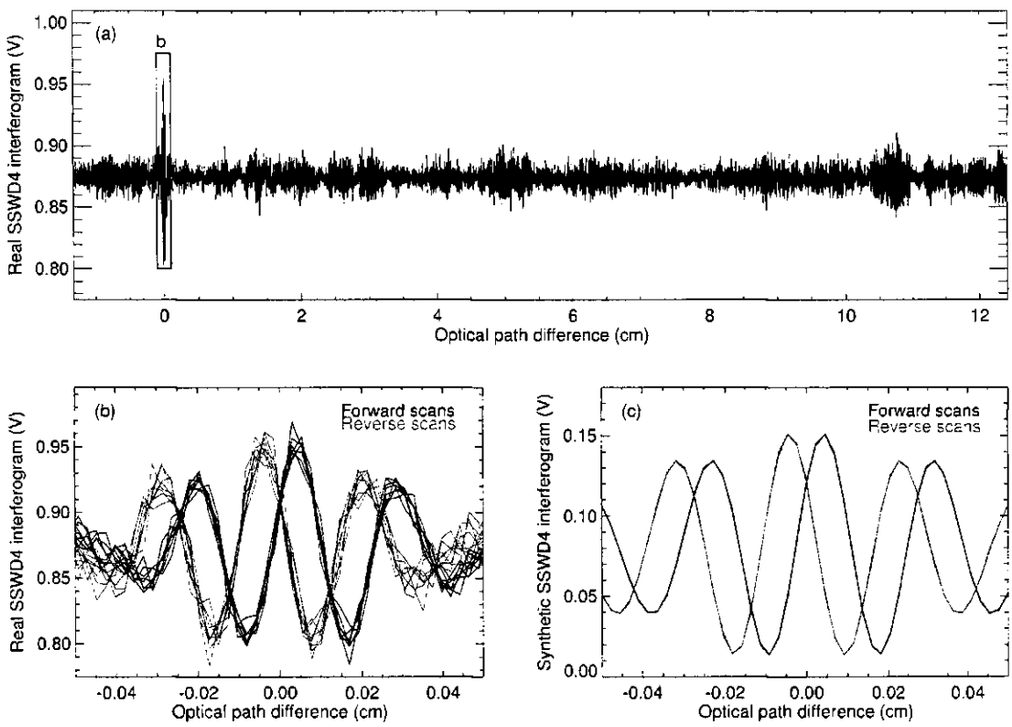

Figure 6.3: Real and synthetic SSWD4 interferograms due to the cryogenic blackbody. Panel (a) shows a single SSWD4 interferogram measured on March 8, 2005 during the first proto-flight model test campaign. The blue box marked "b" denotes the region of the interferogram shown in Panel (b). Panel (b) shows all sixteen real SLWC3 interferograms, while Panel (c) shows all sixteen synthetic SLWC3 interferograms.

which is shown in Panel (b). All sixteen real SLWC3 interferograms are shown in that panel. There are two features to note in Panel (b): the interferograms were inverted and split into two distinct groups on either side of ZPD. The interferograms were inverted because the CBB illuminated the first input port and the SLW array is located at the second output port (see Section 5.6.2) [49]. The two groups of interferograms were displaced from one another due to the bolometer and electrical response discussed in Section 5.7. As indicated there, the thermal lag of the detection system results in the maximum power being detected after the stage has passed ZPD. Therefore, when the stage was moving with a positive velocity (i.e., a forward scan), the peak intensity occurs to the right of

ZPD; vice-versa for a reverse scan.

Panel (c) shows the SLWC3 interferograms generated by SHIFTS. As can be seen, the synthetic interferograms were also inverted and split into two separate groups symmetric about ZPD. The separation between the central peaks of the forward and reverse scan interferograms was approximately the same for both the real and synthetic data ($\sim$ 100 μm). Furthermore, the dynamic range of the real and synthetic data were also in general agreement.

Similar results were found when we investigated the interferograms in the SSW array. Panel (a) of Figure 6.3 shows a single SSWD4 interferogram measured on March 8, 2005. As can be seen, this interferogram was noisier than the SLW interferogram shown in Figure 6.2(a). This noise was not investigated because unaccounted noise sources not related to the sources listed in Chapter 3 were present in the PFM1 data. Panel (b) shows the sixteen scans around ZPD. Once again, the interferograms were split into two groups. In contrast to Figure 6.2, the interferograms were not inverted because the SSW port was located at the first output port of the SPIRE spectrometer. As expected, the SLW and SSW interferograms also contained different frequency components.

Panel (c) shows the synthetic SSWD4 interferograms. As before, the sixteen interferograms showed good agreement with the real data, displaying the same dynamic range, orientation, and separation of forward and reverse scans as in Panel (b). In the next section, we employ the grouping of the forward and reverse scans to determine the bolometer thermal time constants from the phase.

6.3.2 Phase and bolometer time constant

Given the interferograms shown in Figures 6.2 and 6.3, we extracted the double-sided component, removed the DC offset and determined the corresponding spectra. From the 1.3 cm

maximum OPD of the double-sided component, the spectral resolution was 0.46 cm^{-1} (see Equation 2.44).

Figure 6.4 shows the real and synthetic spectra for the SLWC3 bolometer and Figure 6.5 shows the real and synthetic spectra for the SSWD4 bolometer. The spectra were grouped into forward and reverse scans. The left-hand panels in both figures show a single representative spectrum for each group while the right-hand panels show the phase of each scan in that group. Both real and imaginary components were contained in each spectra because of the asymmetry of the double-sided component of the interferogram (see Table 2.1).

We now turn our attention to a discussion of the phase. As can be seen in Panels (a) and (e) of both Figures 6.4 and 6.5, the percentage of energy contained in the real and imaginary components is approximately the same for the real and synthetic forward scan spectra. Correspondingly, the forward scan phases in Panels (b) and (f) were in close agreement. While the reverse scans showed a similar relation between the real and synthetic data, the phases of the forward and reverse scans were noticeably different.

This discrepancy was due to the way different phase sources manifest themselves in an interferogram. Several sources have already been seen in this thesis: Section 2.4.1 introduced the linear phase error due to a mis-sampling of ZPD and Section 5.7 investigated the phase due to the response of the detection system. The total frequency-dependent phase, $\phi_{\rm tot}(\sigma)$, in any spectrum is the sum of all the phase terms,

$$\phi_{\rm tot}(\sigma) = \phi_{\rm ZPD}(\sigma) + \phi_{\rm det}(\sigma) + \phi_{\rm other}(\sigma), \qquad \text{[radians]} \tag{6.1}$$

where $\phi_{\rm ZPD}(\sigma)$ is the linear phase component due to an error in the sampling of ZPD, $\phi_{\rm det}(\sigma)$ is the phase due to the detection sytem and $\phi_{\rm other}(\sigma)$ is any other phase term (all three in radians). Since none of the optical components in the SPIRE spectrometer (e.g., beamsplitters, filters) were

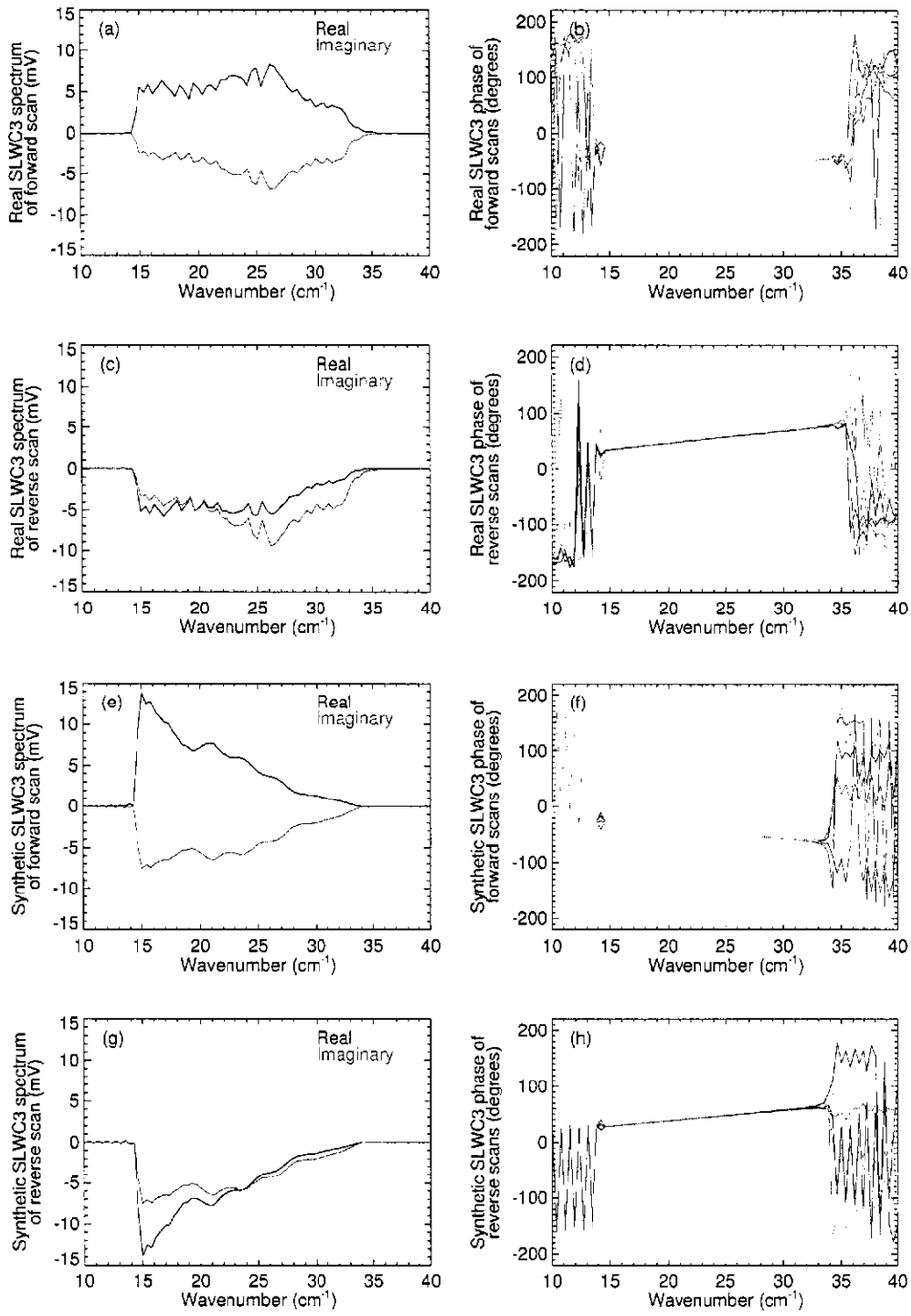

Figure 6.4: Real and synthetic SLWC3 spectra due to the cryogenic blackbody. The left-hand panels show the real and imaginary components of a single SLWC3 spectrum; the right-hand panels show the phase of eight SLWC3 spectra. Panels (a)–(d) correspond to real data; Panels (e)–(h) correspond to synthetic data. Panels (a), (b), (e) and (f) correspond to forward scans; Panels (c), (d), (g) and (h) correspond to reverse scans.

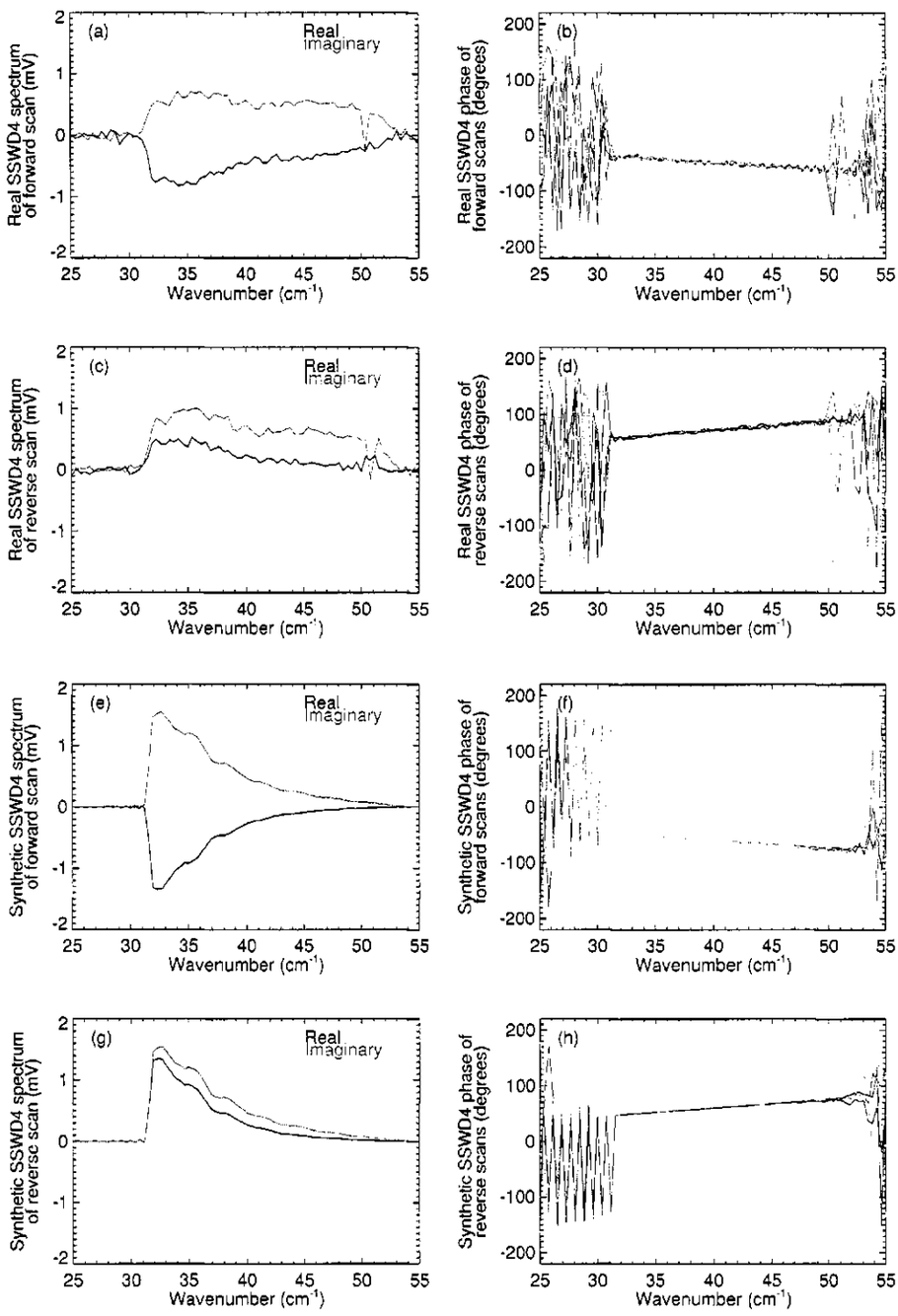

Figure 6.5: Real and synthetic SSWD4 spectra due to the cryogenic blackbody. The left-hand panels show the real and imaginary components of a single SSWD4 spectrum; the right-hand panels show the phase of eight SSWD4 spectra. Panels (a)–(d) correspond to real data; Panels (e)–(h) correspond to synthetic data. Panels (a), (b), (e) and (f) correspond to forward scans; Panels (c), (d), (g) and (h) correspond to reverse scans.

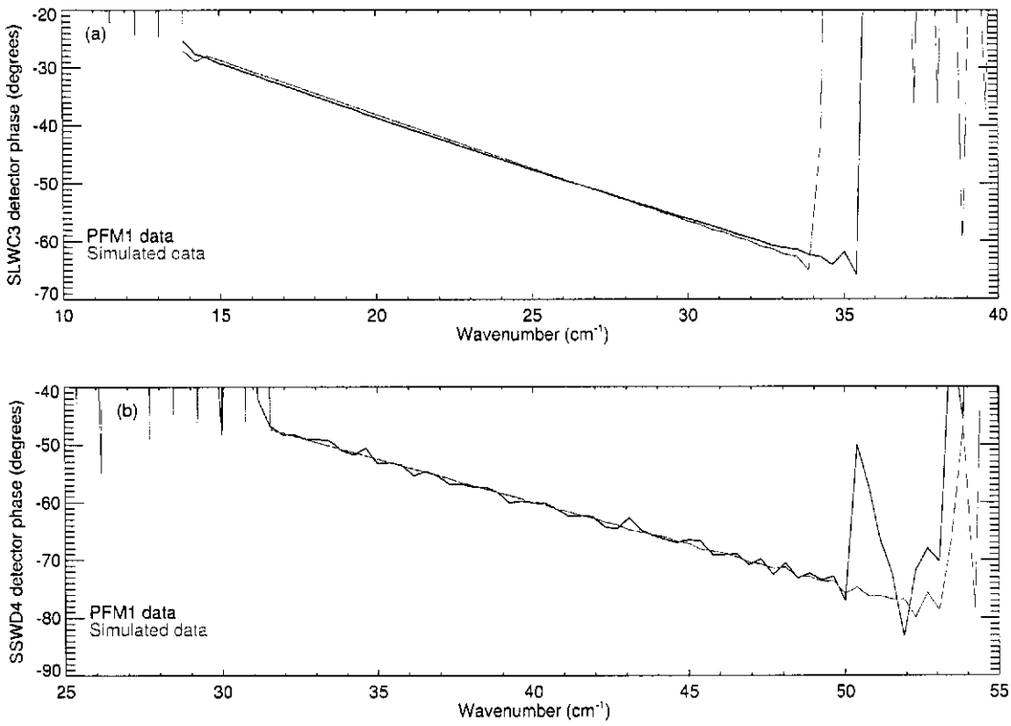

Figure 6.6: Real and synthetic phase due to the detection system. Panel (a) and (b) show the phase of the detection system for the SLWD4 and SSWC3 pixels, respectively.

known to introduce phase errors, we assumed that the $\phi_{\text{other}}(\sigma)$ term was zero.

From Figures 6.2 and 6.3, we can see that the phase due to the detection system depends on the time-varying nature of the measured interferogram signal. In contrast, the phase contribution due to the mis-sampling of ZPD depends only on the position and is independent of time. Therefore, the phase of the forward and reverse scans was written as

$$\phi_{\text{forward}}(\sigma) = \phi_{\text{ZPD}}(\sigma) + \phi_{\text{det}}(\sigma), \qquad \text{[radians]} \tag{6.2}$$

$$\phi_{\text{reverse}}(\sigma) = \phi_{\text{ZPD}}(\sigma) - \phi_{\text{det}}(\sigma). \qquad \text{[radians]} \tag{6.3}$$

By subtracting the above equations, the detector system phase is then given by

$$\phi_{\text{det}}(\sigma) = \frac{1}{2}(\phi_{\text{forward}}(\sigma) - \phi_{\text{reverse}}(\sigma)). \qquad \text{[radians]} \tag{6.4}$$

Using Equation 6.4, the mean phase due to the detection system was determined for the real and synthetic data in each band. These four phases are shown in Figure 6.6. As can be seen, the agreement between the real and synthetic phases is good within the bandpass of each array.

To quantify this agreement, we repeated the analysis of Section 5.7 to determine the bolometer thermal time constant. Using the IDL MPFITFUN routine, the two synthetic phases due to the detection system were fitted to the theoretical phase. As indicated in Section 5.7, the theoretical phase of the detection system is given by the phase of the product of the transfer functions given by Equations 3.8 and 4.19. The bolometer time constant was the only parameter in the fit; more variability was expected in the time constants than in the electronics because the bolometers are custom made in a complex manufacturing process. This fitting technique returned τ values of (12.35 ± 0.02) and (5.96 ± 0.01) ms for the synthetic SLWC3 and SSWD4 pixels, respectively. These values differed by less than 0.5 % from the measured values given at the beginning of Section 6.3. Accurate knowledge of the phase allows high resolution interferograms to be phase-corrected; the following section compares and contrasts the high resolution spectra of the real and synthetic data.

6.3.3 Phase-corrected spectra

From the phases shown in Figure 6.4 and 6.5, the data-processing pipeline phase-corrected the raw interferograms using the Forman method (see Section 2.5.3) [59]. The resulting single-sided interferograms were Fourier transformed to produce spectra with spectral resolutions of 0.05 cm^{-1} (see Equation 2.44 with a maximum OPD of 12 cm).

Figure 6.7 shows the phase-corrected spectra for the real and synthetic data. First of all, we note that the real and synthetic spectra were band-limited; the SLWC3 spectra between 17 and

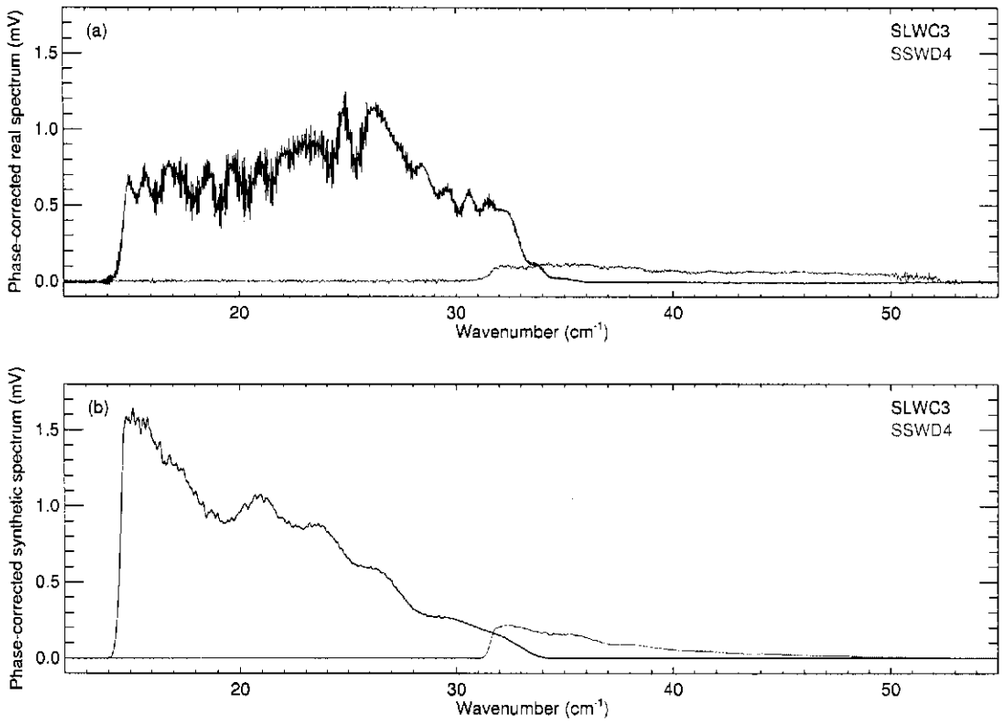

Figure 6.7: Phase-corrected spectra of real and simulated data. Panel (a) shows the SLW and SSW spectra measured from the first proto-flight model test data; Panel (b) shows the SLW and SSW spectra simulated by SHIFTS.

34.5 cm^{-1} and SSWD4 between 31.5 and 52 cm^{-1}. These bands were consistent with the design values given in Section 3.1.

Particularly pleasing was the agreement in the ordinate scales, which included contributions from many terms. The integrated area of the real spectra was 25.7 mV for the SLW band and 3.2 mV for the SSW band. For the synthetic data, the integrated areas were 27.8 and 2.8 mV, respectively. Another method of analyzing the data compared the relative power in the two bands, which is less sensitive to calibration uncertainties. For the real and SHIFTS-simulated spectra, these ratios were 8 and 10, respectively. More energy was contained in the SLW band because the peak of the Planck function (see Equation 1.1) for a 7.5 K blackbody occurs at 14.7 cm^{-1}.

Examining the distribution of energy within each band, it was clear from Figure 6.7 that the synthetic spectra in Panel (b) contained more energy at low wavenumbers than was seen in the real data in Panel (a). One potential explanation for this result was the invalidity of the the single mode approximation employed in SHIFTS. In Section 4.8.3, we argued that since the broadband wavelength-dependent weighting of the radiation modes is currently unknown, we assumed all radiation propagated in the fundamental mode (i.e., TE_{11}). However, Griffin [85] suggests that at least 30 % of the radiation absorbed by the bolometers will be contained in higher order modes. Only present at higher frequencies, the higher order modes would tend to flatten out the SHIFTS spectra, as was seen in the real data. While modelling the power in the other modes is beyond the scope of this thesis, the next section examines the PFM1 results in relation to the assumption of a constant optical throughput.

6.4 Compensation with the spectrometer calibrator

The second data set under analysis was measured on March 24, 2005 when the two SCAL sources were heated. As has been indicated throughout this thesis, accurate compensation of the Herschel primary mirror is an extremely important component of calibration in the SPIRE spectrometer. This comparison investigated 30 medium resolution scans taken at a stage speed of 302 $\mu m\,s^{-1}$.

As indicated in Table 6.1, the SCAL-A and SCAL-B sources were fixed at 38 and 6 K, respectively, for the duration of these scans. The CBB temperature was incremented, in steps of 0.5 K, from 11.5 to 12.5 K. Remember that the CBB source had an effective emissivity of 100 %, which explains why SCAL-A was heated to a temperature four times high than the CBB. (It should also be noted that other scans were taken at higher and lower CBB temperatures on March 24.

Unfortunately, the high temperature measurements were saturated and the low temperature data were unavailable.)

To generate the March 24 data, SHIFTS was executed under the conditions outlined above and using the values listed in Table 6.1. The other settings in SHIFTS were unchanged from Section 6.3. Figure 6.8 shows a single interferogram at each CBB temperature for the SLWC3 and SSWD4 pixels. Panel (a) shows the real SLWC3 interferograms. As can be seen, the DC offset increased as the CBB port became more dominant, repeating the trend seen in Figure 5.9. In the SLW band, the modulation was lowest when the CBB temperature was 11.5 K. Similar results were seen with the synthetic SLWC3 interferograms shown in Panel (b). If we examine the SSWD4 interferograms in Panels (c) and (d), it was once again clear that the DC offset increased with the CBB temperature. In the SSW band, however, the best compensation occured at a CBB temperature of 12.5 K.

It is important to note that the dynamic range of the synthetic interferograms was no longer matched by the real inteferograms. The exact cause of this disagreement is unknown but was likely due to a change in the gain of the warm electronics. Between the March 8 and 24 measurements, the lock-in amplifiers (LIAs; see Section 3.7) failed and were replaced by spare electronics whose exact amplification characteristics are unknown.

The results seen in the interferograms were well reproduced in the spectra returned by the data-processing pipeline. Panel (a) of Figure 6.9 shows the real spectra determined from the double-sided interferograms shown in Panels (a) and (c) of Figure 6.8. In Figure 6.9, negative spectra indicate that the SCAL port was dominant (see Section 5.6.2). For CBB temperatures of 11.5 and 12.0 K, the dominance of the ports in the real SLWC3 spectra switched at approximately 28 and 29 cm^{-1}, respectively.

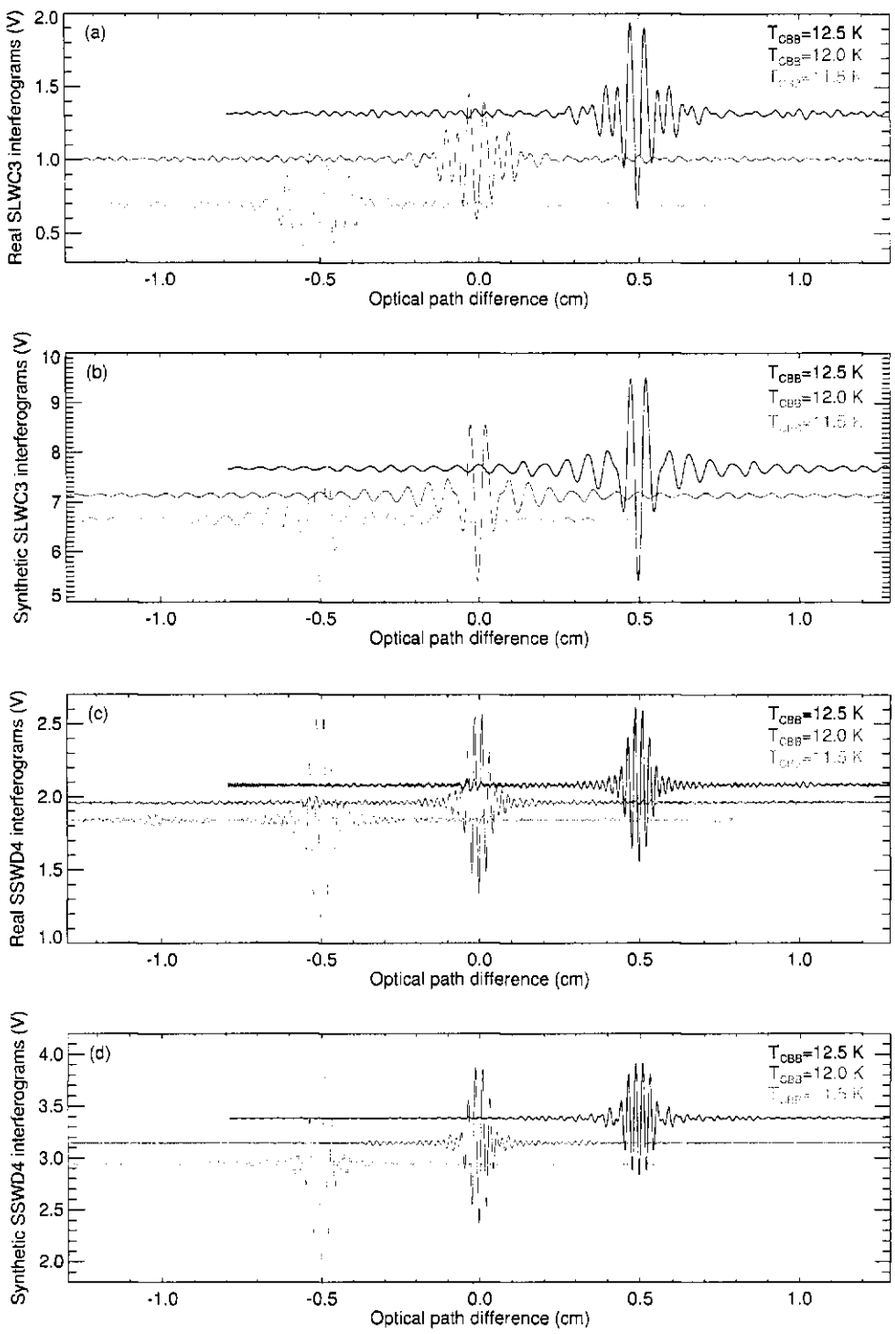

Figure 6.8: Compensation of real and synthetic interferograms. Panels (a) and (c) represent the real SLWC3 and SSWD4 interferograms, respectively, while Panels (b) and (d) represent the synthetic interferograms for the same respective pixels. In each case, the SCAL-A and SCAL-B sources were heated to 38 and 6 K, respectively; the cryogenic blackbody temperatures varied. For clarity, the 11.5 and 12.5 K interferograms are shifted horizontally relative to the 12 K interferogram.

Panel (b) shows the synthetic spectra corresponding to the interferograms shown in Panels (b) and (d) of Figure 6.8. As can be seen, the synthetic spectra reproduce the basic features of the real spectra: a net positive spectra was seen for low frequencies and a net negative spectra was seen for high frequencies. Furthermore, the SLWC3 spectrum for a CBB temperature of 11.5 K became dominated by the SCAL port at approximately 28 cm^{-1}, in agreement with the real spectrum.

However, There were distinct differences between the spectra. Similar to the synthetic spectra shown in Figure 6.7, the power in Panel (b) was too high at low frequencies and too low at high frequencies. As suggested in the previous section the contribution of higher order modes may account for this disagreement. Since a full multi-modal analysis was beyond the scope of this thesis, we also investigated the effect of assuming a constant throughput. As indicated in Section 4.8.2, SHIFTS assumed a diffraction-limited throughput that varied with the square of the wavelength. Panel (c) shows the resultant compensation when the throughput was assumed constant. As can be seen, the energy content across the two bands was more uniform.

The radiation mode characteristics of the SPIRE spectrometer remain a point of debate among SPIRE consortium members. While a constant throughput demonstrated a better overall agreement with the real data, neither Panel (b) or (c) perfectly replicate the real results. In reality, the precise throughput will likely fall between the two extreme cases. Nevertheless, this section demonstrated that SHIFTS well represents the spectral behaviour of the compensation scheme.

6.5 Laser line measurements

The final data set analyzed from the PFM1 test campaign was laser measurements taken on April 6, 2005. Twenty scans at five different speeds were investigated. This section demonstrates the effect of the different scan speeds on the strength of the laser line.

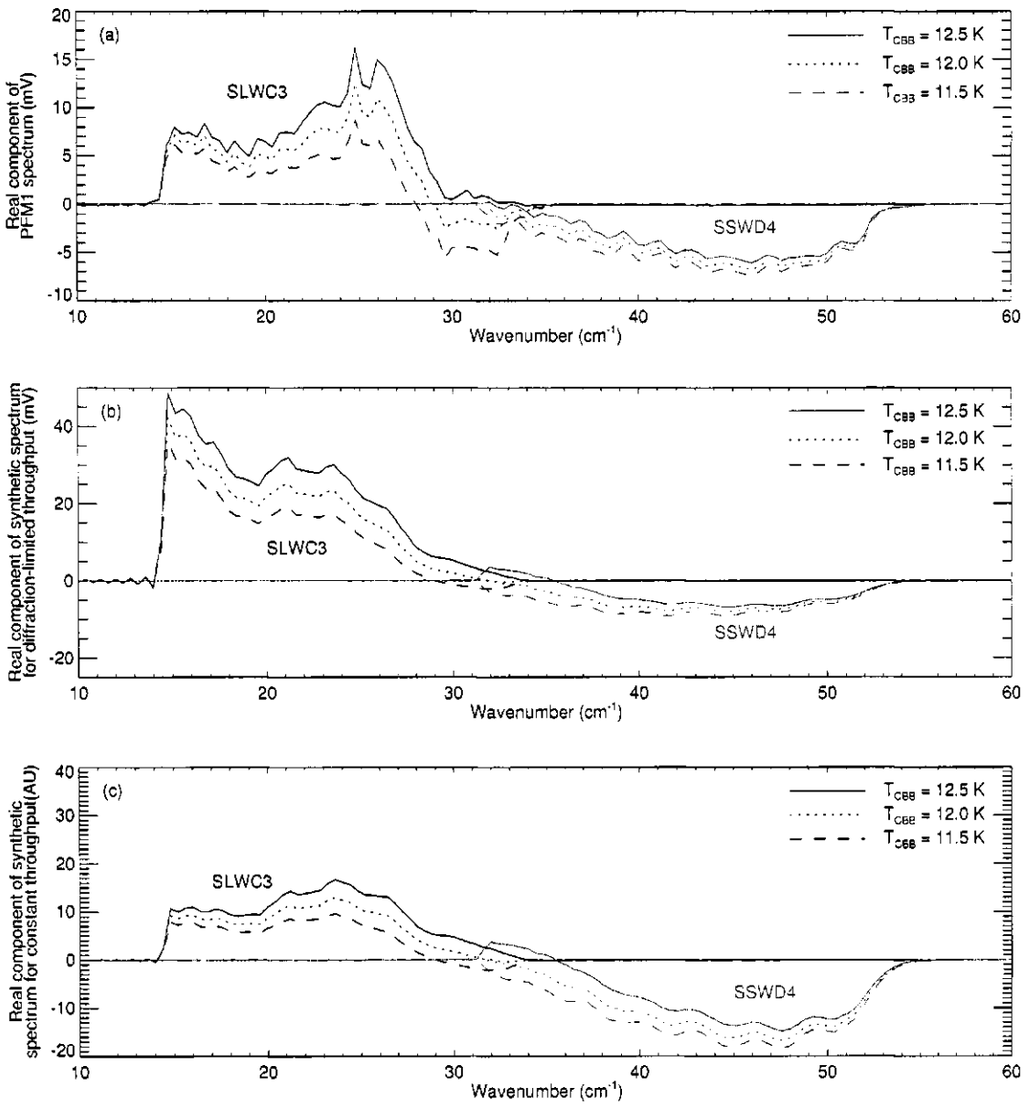

Figure 6.9: Compensation of real and synthetic spectra. Panel (a) shows the real spectra for the three cryogenic blackbody temperatures. Panels (b) and (c) represent the synthetic spectra generated by SHIFTS. In Panel (b), the throughput was diffraction-limited while in Panel (c), the throughput was constant.

As indicated in Section 6.1, a FIR laser was located in the optical path of the cryostat window. The Edinburgh Instruments model PL295 laser was pumped by a PL5 carbon dioxide laser [43,155]. During these tests, the laser was tuned to the 232 μm line of methanol [43,156] and was aligned over the SSWD3 pixel (see Figure 3.10). Unfortunately, even with an active stabilization system, the intensity of the laser drifted throughout the scans [43].

The five speeds scanned are given in Table 6.1. (Incidentally, the stage metrology of these scans was employed to determine the stage noise profile for SHIFTS; see Section 4.4.) In the rapid scan mode, Equation 3.1 indicates that the frequency at which radiation is measured changes with speed. While the wavenumber of the line did not increase with the speed, the audio frequency at which the line was encoded did. Therefore, we expect the line strength to decrease with speed as it moved to higher audio frequencies along the combined gain curve of the bolometer and warm electronics (see Figures 3.15 and 4.8).

Figure 6.10 shows a single SSWD3 interferogram measured at a speed of 452 $\mu m\,s^{-1}$ on April 6, 2005. As can be seen in Panel (b), the region around ZPD was saturated by the atmospheric radiation of the test facility. However, as shown in Panel (c), the cosine wave due to the laser line was not saturated in the wings of the interferogram. Therefore, our analysis focused on an 8 cm section of OPD between 4 and 12 cm.

To simulate PFM1 measurements, 20 scans were generated by SHIFTS at the speeds listed in Table 6.1. The laser line was represented by the simulated astronomical source, where the line was a single spike located at 42.93 cm^{-1} (232 μm) with a solid angle that filled the SSWD3 pixel. The blackbody emission of the Herschel primary mirror was employed to represent the atmospheric emission of the test facility. The thermal time constant of the SSWD3 bolometer was set to 12.38 ms [106]. Otherwise, SHIFTS was executed under the same conditions as outlined in

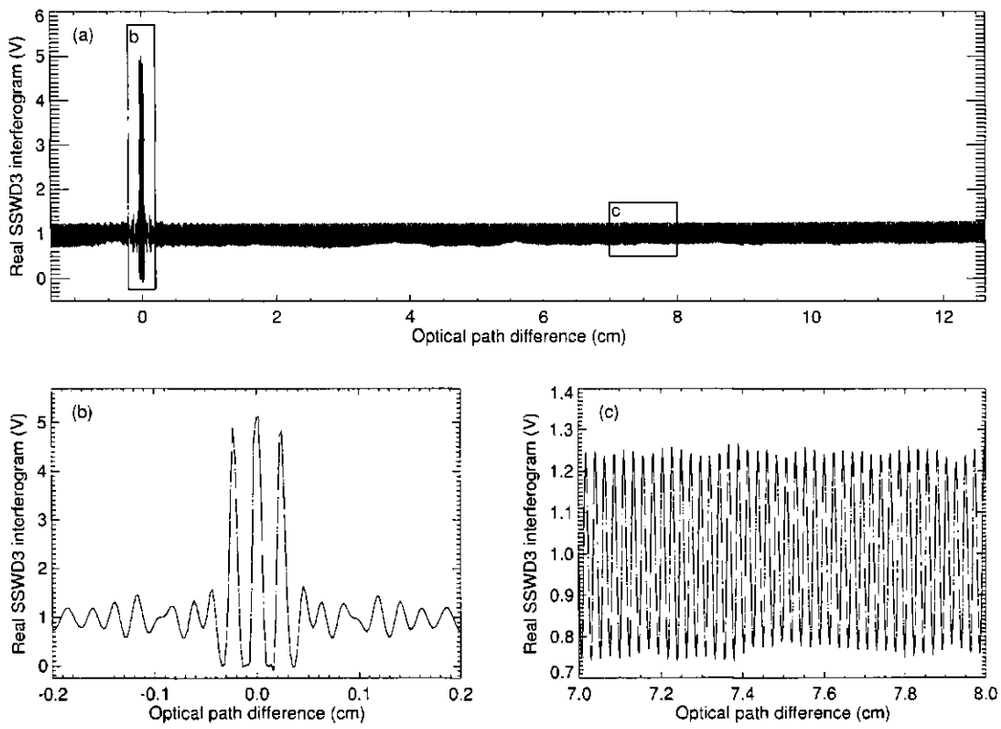

Figure 6.10: Real interferogram due to the laser and the atmosphere. Panel (a) shows a single SSWD3 interferogram measured at 452 $\mu m\,s^{-1}$ on April 6, 2005. The blue boxes marked "b" and "c" denote the regions of the interferogram shown in Panels (b) and (c), respectively.

Section 6.3.

Figure 6.11 shows a single simulated interferogram for a stage speed of 452 $\mu m\,s^{-1}$. Panel (b) shows the region around ZPD, which was not saturated because SHIFTS did not simulate the digitization. Panel (c) shows a high OPD region of the interferogram where, similar to the real data, only a cosine wave was present.

The Fourier transforms were computed for the extracted sections of the 20 real and 20 simulated interferograms. To avoid any phase in the spectrum, the 8 cm window was shifted to ensure the first element in the array was a maximum. As expected, each line appeared as a sparsely sampled sinc function (see Section 2.4.5). To determine the line strength, a sinc function was fitted

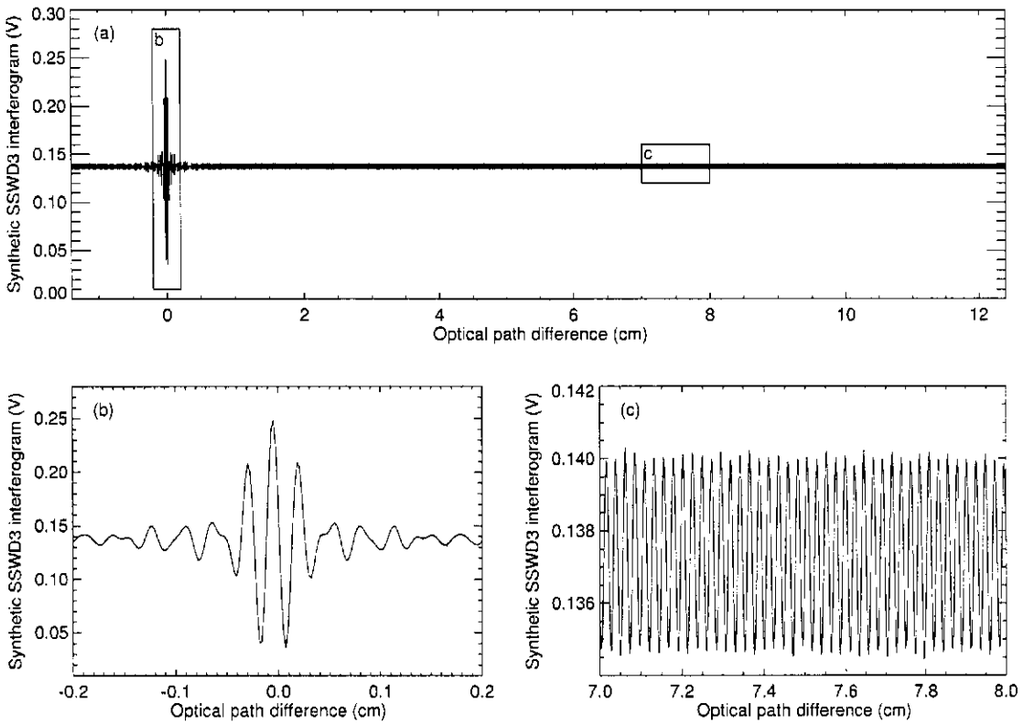

Figure 6.11: Synthetic interferogram due to the laser and the atmosphere. Panel (a) shows a single SSWD3 interferogram measured at 452 $\mu m\, s^{-1}$. The blue boxes marked "b" and "c" denote the regions of the interferogram shown in Panels (b) and (c), respectively.

to each line using the MPFITFUN routine (see Section 6.3.2). The fitted line centers of the real and synthetic data were in close agreement. Given the fitted amplitude and width, a super-sampled sinc function was created out to 1 cm^{-1} on either side of the line. We integrated the area under each sinc function and defined that as the line strength for that measurement.

To compare the real and synthetic line strength, their mean areas were plotted against the theoretical gain curve of the detection system. The mean and the standard deviation were determined for each speed. The real and synthetic data sets were then normalized to the maximum line strength (90 $\mu m\, s^{-1}$). The theoretical gain curve was the magnitude of the product of the transfer functions given by Equations 3.8 and 4.19 and is shown in black in Figure 6.12. Overplotted as

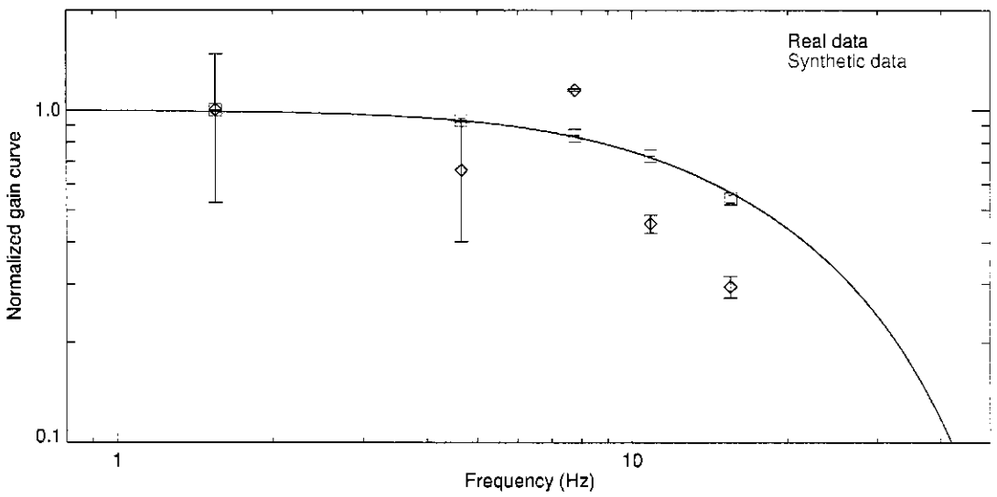

Figure 6.12: Least-squares fit of the area under the curve of the laser measurements at different speeds. The black line was the theoretical gain curve of the transfer function. Each diamond-square pair corresponds to a single stage speed.

diamonds and squares were the real and simulated line strengths, respectively. Both the real and simulated data sets were fit to the theoretical gain curve using an unweighted least-squares fit. Because of the instability in the laser power, the real data follows the gain curve but not very well. In constrast, the synthetic line strengths were in good agreement with the theoretical gain curve.

6.6 Summary

This chapter compared SHIFTS to real SPIRE measurements taken during the first proto-flight model test campaign in 2005. Using three sets of PFM1 measurements, we examined how the stage speed, the temperature of the cryogenic blackbody and the temperatures of the SCAL sources affected the resultant spectra. By investigating laser lines and compensation, we characterized the response expected from SHIFTS. In all cases, the SPIRE spectrometer simulator provided meaningful results which compared well with the real data. Given this confidence in SHIFTS, Chapter 7

employs the simulator to investigate what sort of astronomical objects can be observed with the SPIRE spectrometer.

Chapter 7

Simulated observation of molecular cloud

> *" 'Yes indeed,' said the Unicorn. 'Now you have put a cogent question. What can we measure? Or perhaps I should say "What could we measure?" because (if I may speak for others) we are experts in the theory of measurement, not its practice.' "*
>
> - John Lighton Synge, *Kandelman's Krim*, Jonathan Cape (1957).

This chapter describes the analysis of a simulated astronomical observation produced by the Simulator for the Herschel Imaging Fourier Transform Spectrometer (SHIFTS). Given the agreement between SHIFTS simulations and measured data obtained during from first proto-flight model (PFM1) tests (see Chapter 6), SHIFTS was employed to predict the performance of the Spectral and Photometric Imaging Receiver (SPIRE) spectrometer under nominal operational conditions. The results described herein demonstrate the advantages and challenges associated with use of this instrument. Section 7.1 describes the simple model used to simulate the far-infrared (FIR) emission of a disk of gas and dust. Given the simulated astronomical source (SAS), Section 7.2 analyzes and discusses the data products generated by SHIFTS.

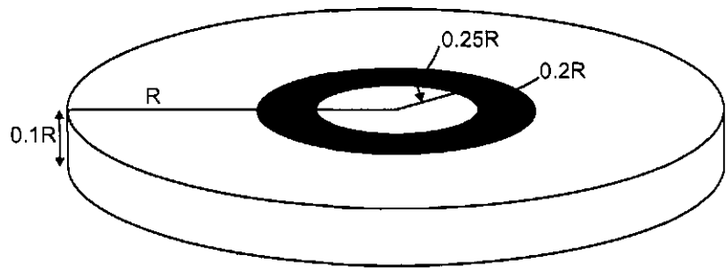

Figure 7.1: Inclined view of the simulated disk. In this figure, the radius R is 1 parsec and the red ring represents the region where carbon monoxide molecules were present.

7.1 Synthetic molecular cloud

One of the primary science goals of the SPIRE instrument is to characterize the early stages of star formation [4, 5]. As indicated in Section 1.1, star formation occurs in the dense regions of molecular clouds. A large fraction of the 200 – 670 μm emission (i.e., the band observed by the SPIRE spectrometer) from these clouds is due to the thermal radiation of dust grains (e.g., silicate and graphite) [9, 17, 157]. In addition to the radiating dust, there are numerous molecular emission lines present at these wavelengths [5]. This section describes the construction of a simple static model composed of continuum and line emission.

The model contained an obscured central luminosity source surrounded by a circular disk of dust. The basic assumptions in the model included the following: the entire disk was optically thin (i.e., no radiation emitted locally was absorbed locally); no stellar extinction occurred between the disk and the Herschel Space Observatory (HSO); the plane of the disk was not inclined with respect to the HSO; and the dust and gas components were at constant densities [15, 158].

Figure 7.1 shows the basic geometry of the model. As can be seen, the radius of the disk was 1 parsec (or pc; see Table A-1) with a thickness one-tenth its radius. At a distance of 1.6 kilo-parsecs from the Earth, the disk subtended an angle of 4.0 arcmin [15]. The distance and radius

were specifically chosen so that the disk filled the field-of-view (FOV) of the SPIRE spectrometer; however, the values were representative of star-forming regions seen in the literature [32, 159, 160]. The disk was split into square blocks 0.06 × 0.06 pc across and 0.1 pc deep. This corresponded to a 7.8 arcsec angular spacing between each block and a solid angle of 1.4×10^{-9} steradians. In addition to the dust component, a ring of carbon monoxide (CO) molecules was located between 0.25 and 0.45 pc (see Section 7.1.2). With each block, the conditions were assumed constant (i.e., each block was isopycnic, isothermal and isotropic).

To create the simulated astronomical source, we specified the initial conditions for the three associated arrays introduced in Section 4.2. The intial value, number of elements and step size of the right ascension and declination were determined from the geometry given above. For the wavenumber grid, the spacing of the SAS spectra, $\Delta\sigma_{\text{sim}}$, was fixed at 0.032 cm^{-1} and the number of elements was set so that the Nyquist frequency was 60 cm^{-1} (see Section 2.4). The spectrum of each block was then calculated using the specific intensities outlined in the following two sections.

7.1.1 Continuum component

To describe the continuum emission, each dust grain was modelled as a greybody [158, 161, 162]. For an optically thin distribution, the total dust emission is governed by

$$S_\sigma = \kappa_o m_d N_d \left(\frac{\sigma}{\sigma_o}\right)^\beta B_\nu(T_{\text{dust}}), \qquad [\text{W m}^{-2}\,\text{Hz}^{-1}\,\text{str}^{-1}] \quad (7.1)$$

where N_d is the column density of dust (in cm^{-2}), m_d is the mass of a single dust grain (in g), σ is the wavenumber (in cm^{-1}), κ_o is the dust opacity per unit mass column density (in $\text{cm}^2\,\text{g}^{-1}$) at a reference wavenumber σ_o (in cm^{-1}), β is the emissivity index (unitless), and $B_\nu(T_{\text{dust}})$ is the blackbody equation (see Equation 1.1) for a dust temperature T_{dust} (in K) [160, 163]. The product of the terms in the above equation, except for $B_\nu(T_{\text{dust}})$, corresponds to the emissivity term, ε_ν, in

Equation 1.1.

To simulate the differential heating of the grains due to the central source, a radial temperature gradient was introduced between the blocks. The temperature of each block was defined as

$$T_{dust} = T_o e^{-r/\gamma}, \qquad [\mathrm{K}] \tag{7.2}$$

where $T_o = 40\,\mathrm{K}$ was the temperature at the center of the cloud, r was the radial distance from the center of the disk (in pc) and $\gamma = 1\ \mathrm{pc}^{-1}$ was a temperature gradient index [158]. Given T_o and γ, the temperature at the edge of the disk was 11.5 K. This range is typical of temperatures seen in star-forming regions [33, 162, 164].

The other terms in Equation 7.1 would ordinarily have various frequency, radius and temperature dependences but were, for simplicity, fixed as constants. Assuming a dust density of 3.0 $\mathrm{g\,cm^{-3}}$ and a grain radius of 0.43 μm, the dust mass was 10^{-12} g [157, 158]. For the reference wavenumber and dust emissivity index, we assumed canonical values of 1000 $\mathrm{cm^{-1}}$ and 2.0, respectively [32, 158, 163]. Given the dust opacities listed in Johnstone *et al.* [32] and Motte *et al.* [160], we adopted a value of $\kappa_o = 0.04\ \mathrm{cm^2\,g^{-1}}$. The column density of CO in molecular clouds such as the Orion Nebula and Cepheus A is on the order of $10^{16}\ \mathrm{cm^{-2}}$ [159, 165]. Given a gas-to-dust ratio of 150 and because our disk model was approximately one-tenth the thickness of the above molecular clouds, the dust column density was set to $6.7 \times 10^{12}\ \mathrm{cm^{-2}}$ [159, 165, 166].

Employing the above values, the effective dust emissivity in Equation 7.1 was 0.01 % at $\sigma = 20\ \mathrm{cm^{-1}}$ [72]. The resultant specific intensities in the simulated disk (approximately 10 to 500 $\mathrm{MJy\,str^{-1}}$) were in agreement with values seen in Motte, André & Neri [160].

7.1.2 Emission line component

In addition to the continuum emission described above, a ring of carbon monoxide molecules was included between 0.25 and 0.45 pc. Due to its ubiquity in star-forming regions, CO is frequently employed as a molecular tracer [167, 168]. To simplify the discussion, only a single isotope, $^{12}C^{16}O$, was included in our model.

Consider the radiative absorption and emission processes in a two energy level system as shown in Figure 7.2. The *Einstein A coefficient*, denoted by $A_{u\ell}$, is defined as the probability per unit time that a system in an upper quantum state u will spontaneously drop to a lower quantum state ℓ and emit a photon with a frequency proportional to the energy difference between the two states. The Einstein B coefficients, $B_{\ell u}$ and $B_{u\ell}$, describe the stimulated absorption and emission of photons in the presence of an external radiation field [169].

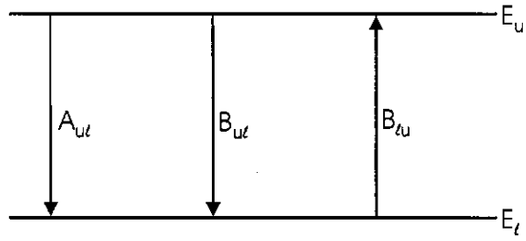

Figure 7.2: Emission and absorption in a two energy level system. The upper energy state, E_u, has a population of N_u and a degeneracy of g_u, while the lower state, E_ℓ, has a population of N_ℓ and a degeneracy of g_ℓ.

As indicated above, we assumed the model was optically thin; the local energy density was therefore sufficiently low that spontaneous emission was the primary radiation source. At far-infrared (FIR) and submillimetre wavelengths, the CO emission lines are caused by discrete changes in the angular momentum quantum number J [168, 170]. For each transition $J_u \rightarrow J_\ell$, the intensity is given by

$$I_u = N_u A_{u\ell} \frac{hc\sigma_{u\ell}}{4\pi}, \qquad [\mathrm{W\,cm^{-2}\,str^{-1}}] \tag{7.3}$$

where $A_{u\ell}$ is the Einstein A coefficient for the rotational transition $J_u \rightarrow J_\ell$ (in $\mathrm{s^{-1}}$), N_u is the population of the upper energy state (in $\mathrm{cm^{-2}}$), $\sigma_{u\ell}$ is the wavenumber of the emitted photon (in

cm^{-1}), h is the Planck constant and c is the speed of light (see Table A-1) [170, 171]. In thermal equilibrium, the population of the energy states is given by the Maxwell-Boltzmann distribution,

$$N_u = \frac{Ng_u}{Q_{\text{rot}}} e^{-E_u/kT_{\text{rot}}}, \qquad [\text{cm}^{-2}] \tag{7.4}$$

where N is the total column density of CO (in cm^{-2}), $g_u = 2J_u + 1$ is the degeneracy of the energy level (a unitless value that desribes the spatial orientations of the angular momentum), Q_{rot} is the rotational partition function (unitless), T_{rot} is the excitation temperature (in K), k is the Boltzmann constant (see Table A-1), and the energy level of the upper state is

$$E_u = J_u(J_u + 1)Bhc, \qquad [\text{J}] \tag{7.5}$$

where B is the rotational constant for CO (see Table A-1) [168, 169, 172, 173]. Given the above equation, the wavenumber of the emitted photon is

$$\sigma_{u\ell} = \frac{E_u - E_\ell}{hc} = 2BJ_u. \qquad [\text{cm}^{-1}] \tag{7.6}$$

For a linear molecule such as CO [174, 175], the rotational partition function is given by

$$Q_{\text{rot}}(T) = \frac{kT_{\text{rot}}}{hcB}. \tag{7.7}$$

To calculate the intensity for each transition, we adopted an excitation temperature of 300 K and, as indicated in Section 7.1.1, a CO column density of 10^{15} molecules per square centimetre [159, 165].

The final value required to compute the line intensity (see Equation 7.3) is the Einstein A coefficient. The coefficients can be determined from spectral line characteristics listed in several online catalogs [176–178]. However, the multiple definitions of the Einstein A coefficient found in the databases frequently leads to confusion [169, 179, 180]. Appendix C compares two of the primary notations seen in the literature and compares the coefficients computed from these databases. As indicated in Appendix C-2, the 2004 edition of the High-resolution Transmission Molecular

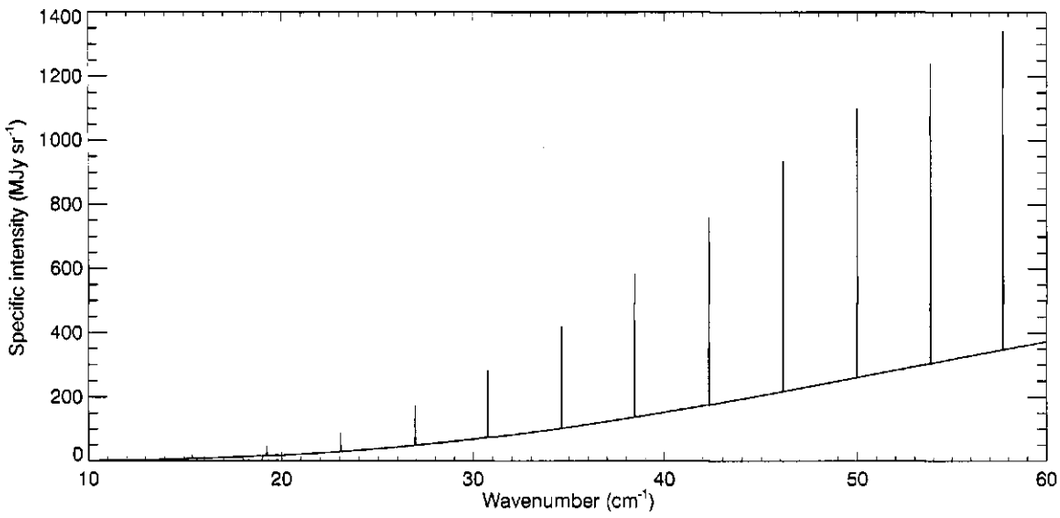

Figure 7.3: Example spectrum of the simulated molecular cloud. Located at a radius of 0.3 pc, the spectrum represents continuum emission at a dust temperature of 27.5 K with CO line emission at a temperature of 300 K.

Absorption (HITRAN) database* explicitly lists the Einstein A coefficent [176, 181]. The CO line intensities were calculated using the Einstein A coefficients from HITRAN2004. Finally, the line intensity was converted to a specific intensity by dividing by the line width noted at the beginning of Section 7.1.

The line and continuum emission were summed to produce the total simulated emission from the entire cloud at each pixel. Figure 7.3 shows an example spectrum for a single SAS pixel at a radius of 0.3 pc. At that radius, the dust temperature was 27.5 K and emission lines were visible since that block was located inside the CO dust ring. With a simulated molecular cloud composed of spectra similiar to Figure 7.3, we proceeded with the SHIFTS simulation.

*Web address: *http://cfa-www.harvard.edu/hitran/*

7.2 Simulated observations of a molecular cloud

As indicated in Section 1.3, one of the motivations for writing SHIFTS was to allow astronomers to explore the capabilities of the SPIRE spectrmeter. We explored these capabilities using our realistic simulation a molecular cloud. This section describes the generation of simulated interferograms and their subsequent analysis.

Several different cases were explored, ranging from an ideal situation to the inclusion of all the noise source simulated by SHIFTS. For each case, we generated a single high resolution scan (i.e., the single-sided scan length equaled 3.5 cm) for a stage speed of 0.05 $\mathrm{cm\,s^{-1}}$.

Figure 7.4 shows the alignment of the spectrometer long and short wavelengths (SLW and SSW, respectively) bands with respect to the simulated disk. As can be seen, the simulated molecular cloud was oriented such that the center of the disk was aligned with the central feedhorns in each spectrometer band (i.e., SLWC3 and SSWD4). While the ring of CO emission lines (denoted by the red crosses) was only present in the second ring of the SLW array, it was present in both the second and third rings of the SSW array.

7.2.1 Data analysis

Once the simulated data products were generated, spectra were computed using the SPIRE data-processing pipeline introduced in Section 6.2. The spectra were then fitted to a theoretical function using the IDL MPFITFUN routine introduced in Section 5.7 [136, 143].

The basic form of the fitting function was given by

$$f_{\mathrm{fit}} = \left[C \left(\frac{\sigma}{\sigma_0} \right)^{\beta} \frac{\sigma^2}{e^{\frac{hc\sigma}{kT}} - 1} \right] + \left[\sum_{i=0}^{N} D_i \,\mathrm{sinc} \left(\frac{2\pi(\sigma - \sigma_i)}{\Delta\sigma} \right) \right] \tag{7.8}$$

where the first term represented the continuum component and the second term represented the line component. Regardless of whether lines were present, the MPFITFUN routine always returned

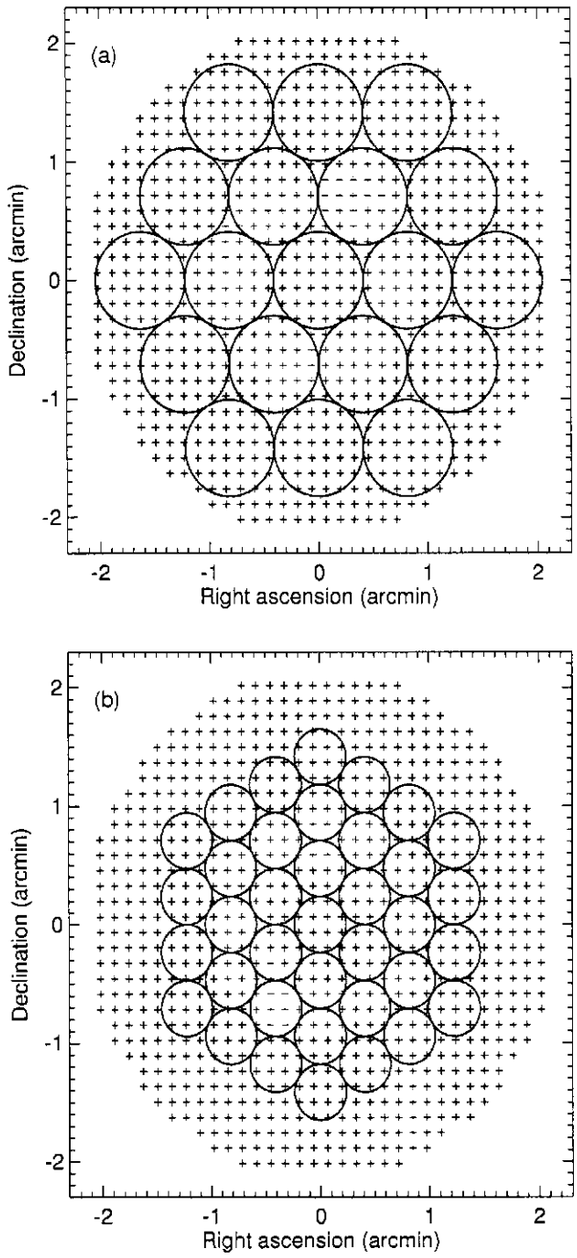

Figure 7.4: Alignment of the spectrometer long and short wavelength arrays with the simulated disk. In both panels, the blue circles represent the entrance apertures of the feedhorns and the crosses represent the centers of the simulated astronomical source pixels (red crosses represent a SAS pixel with both line and continuum emission). Panel (a) shows the SLW array while Panel (b) shows the SSW array.

the dust temperature, emissivity index, the reference wavenumber (all three terms are defined in Section 7.1.1) and a scaling factor denoted by C. The scaling factor represented the product $\kappa_0 m_d N_d$ but will not be listed since it was not possible to separate the three values.

The second term was only included when emission lines were present (i.e., for radii between 0.25 and 0.45 pc). We expected the lines to have a sinc shape due to the instrumental line shape (ILS) of the Fourier transform spectrometer (see Section 2.4.5). The corresponding free parameters for each line i in Equation 7.8 were the width denoted by $\Delta\sigma$, the center of the sinc function denoted by σ_i (both in cm^{-1}) and the amplitude denoted by D_i.

Given the integrated area under each line, we employed a standard radio astronomy analysis technique called *rotation diagrams* to recover the CO temperature and column density [165,174, 175]. To employ the rotation diagram technique, three conditions were first satisfied: the molecular transitions were optically thin, a single excitation temperature defined all transitions, the rotation temperature was much larger than the temperature of the background [174]. To determine the gas temperature and column density, we define a line intensity ratio,

$$L = \frac{4\pi}{hc\sigma A_{u\ell} g_u} \int I_u d\sigma, \qquad [\text{cm}^{-2}] \tag{7.9}$$

where $\int I_u d\sigma$ is integrated line intensity (in $\text{W m}^{-2}\,\text{str}^{-1}$) and the remaining terms are defined in Section 7.1.2. By substituting Equation 7.3 for the integrated line intensity and taking the logarithm of both sides, Equation 7.9 is rewritten as

$$\log_{10}(L) = \log_{10}\left(\frac{N}{Q_{\text{rot}}}\right) - \left(\frac{\log_{10}(e)}{T_{\text{rot}}}\frac{E_u}{k}\right), \qquad [\text{cm}^{-2}] \tag{7.10}$$

which is clearly a linear relation in terms of E_u/k. From the slope, m, and intercept, b, of Equation 7.10, the gas column column density is given by

$$N = Q_{\text{rot}} 10^b, \qquad [\text{cm}^{-2}] \tag{7.11}$$

and the temperature is given by

$$T_{\rm rot} = \frac{\log_{10}(e)}{m}. \qquad \text{[K]} \tag{7.12}$$

From these definitions, the next section calculates the astronomical quantities from ideal SHIFTS-simulated data products of the simulated molecular cloud.

7.2.2 Ideal cases

In the ideal case, the majority of the noise sources outlined in Chapter 4 were not included. The background emission from SCAL and the Herschel primary mirror was ignored; the stage velocity was constant; ideal beamsplitters were employed; pointing errors was ignored; the detector system efficiency was assumed to be unity; electrical and photon noise were ignored; and the bolometer and electrical response was not modelled. However, the transmission efficiency of the two detector bands was included. The band edges were taken from Figure 4.7 and the bandpass was assumed to have unity transmission.

Figure 7.5 shows two interferograms returned by the pipeline after SHIFTS was executed under these conditions. Located at the center of the long wavelength array, the SLWC3 pixel observed a region of the cloud without line emission (see Panel (a) of Figure 7.4); the mean temperature of the SAS pixels incident on the SLWC3 feedhorn was 34.13 K. Its corresponding interferogram is shown in Panel (a). In contrast, the SSWC2 interferogram (located in the third ring of the short wavelength array) in Panel (b) showed evidence of the line features in the wings (see Panel (b) of Figure 7.4). The mean temperature of the SAS pixels incident on the SSWC2 feedhorn was 24.5 K.

Figure 7.6 shows the two spectra corresponding to the intereferograms in the previous figure. The spectra were converted to megajanskies per steradian given Equations 2.31 and 4.4, the transmission efficiency of the beamsplitters, and the speed of light. As expected from Figure 7.4,

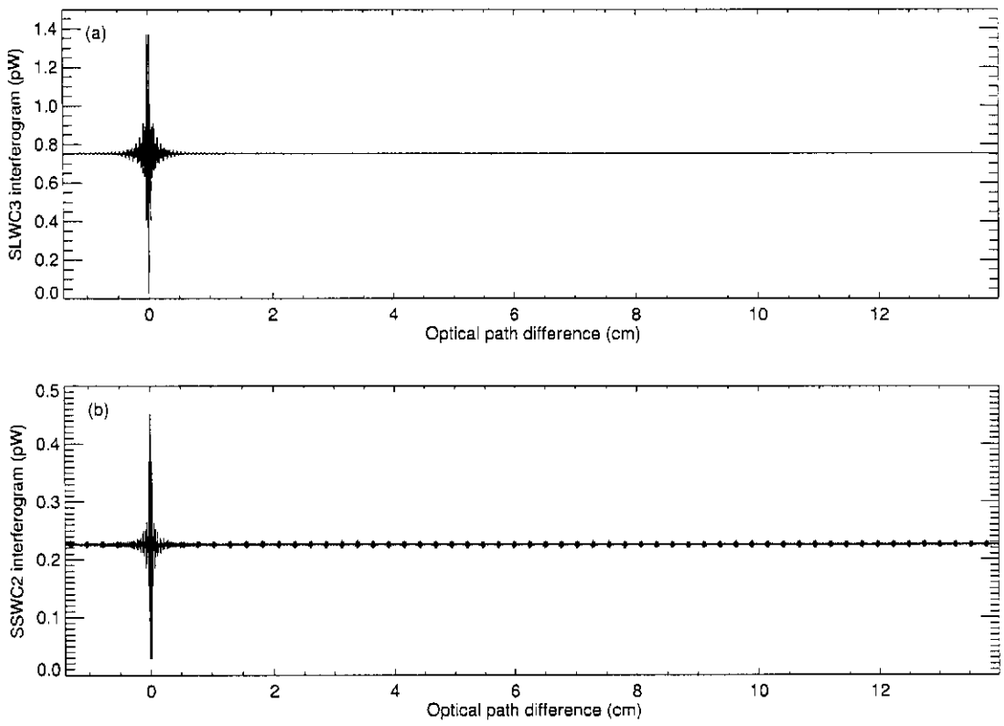

Figure 7.5: Ideal synthetic interferograms of the simulated molecular cloud. Panel (a) shows the SLWC3 interferogram and Panel (b) shows the SSWC2 interferogram.

lines were present in the SSWC2 spectrum but absent from the SLWC3 spectrum. Furthermore, the lines possessed the characteristic sinc profile.

To determine the dust parameters, the SLWC3 spectrum was fit to the theoretical curve (see Section 7.2.1) between 16 and 32 cm^{-1}. The resulting fit (overplotted in blue) differed from the simulated spectra by less than 0.001 %. The SLWC3 fit returned three values: $T_{dust} = 34.13$ K, $\beta = 2.00$ and $\sigma_0 = 984.11$ cm^{-1}. The dust temperature and emissivity index matched exactly to the theoretical values while the reference wavenumber differed by 1.6 %.

In the case of the SSWC2 spectrum, the MPFITFUN routine was fit to the continuum and the five in-band lines. A sixth line is visible at $\sim$54 cm^{-1} but the transmittance of the filter is drop-

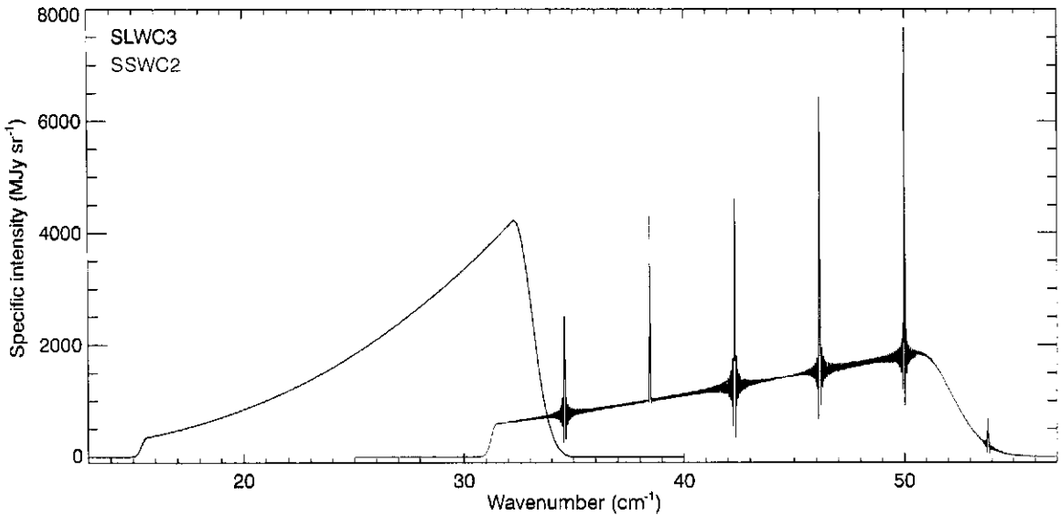

Figure 7.6: Ideal spectra of the simulated modecular cloud. This figure shows the spectra measured by the SLWC3 and SSWC2 bolometers. For both bands, the blue curve represents the fit returned by the MPFITFUN routine.

ping off at that frequency (see Figure 4.7) so that line was not included in the fit. As before, the difference between the fit (overplotted in blue) and the simulated spectrum was on the order of 0.001 %. The returned dust parameters were: $T_{\rm dust} = 24.6\,{\rm K}$, $\beta = 2.00$ and $\sigma_0 = 1026\ {\rm cm}^{-1}$. The agreement with the continuum values was good. As for the lines, the fit returned line centers of 34.60, 38.45, 42.29, 46.14, 49.98 cm^{-1}, in perfect agreement with the line frequencies given by Equation 7.6.

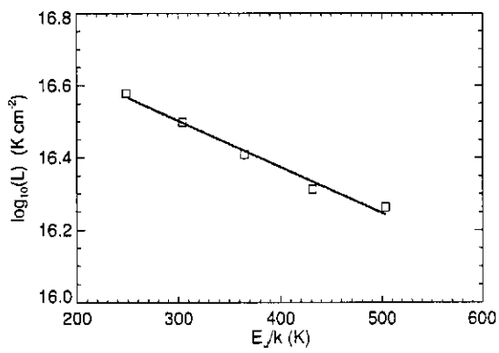

Figure 7.7: Example of rotation diagram analysis. The squares are the integrated line intensities of the five lines seen in the spectrometer short wavelength band of Figure 7.6. The blue line is a linear fit to the squares.

Given the amplitude and width of the sinc function, we determined the integrated line intensity for each line. Following the rotation diagram technique outlined in Section 7.2.1, the

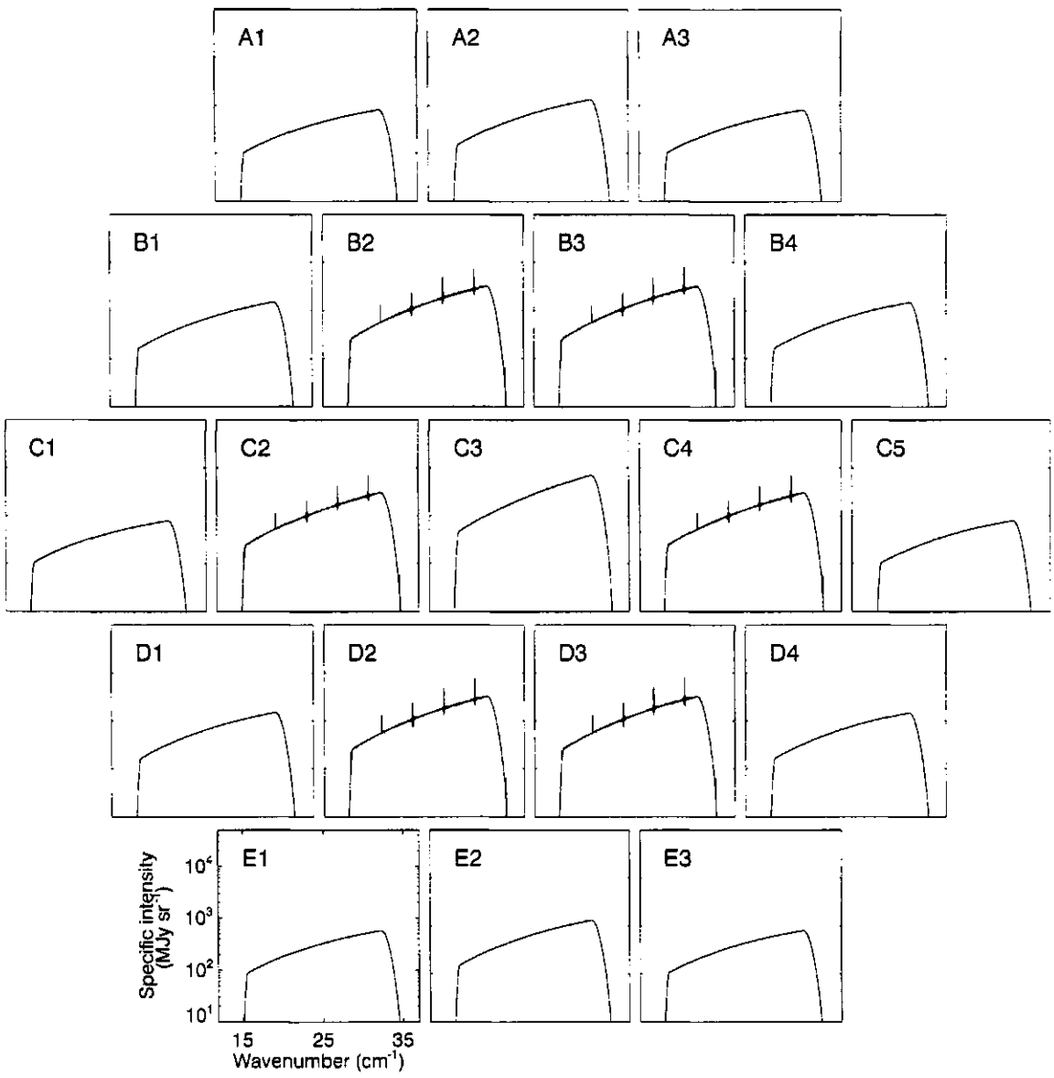

Figure 7.8: Ideal spectrometer long wavelength spectra of the simulated molecular cloud. For ease of comparison, a logarithmic scale is employed and the scale for each panel is identical to Panel E1.

relation between $\log_{10}(L)$ and E_u/k was calculated, as shown in Figure 7.7. From the slope and intercept of the blue line, Equations 7.11 and 7.12 yielded a column density and a gas temperature of 340 K and (9.45×10^{14}) cm^{-2}, respectively. Both these value were in good agreement with the theoretical values given in Section 7.1.2.

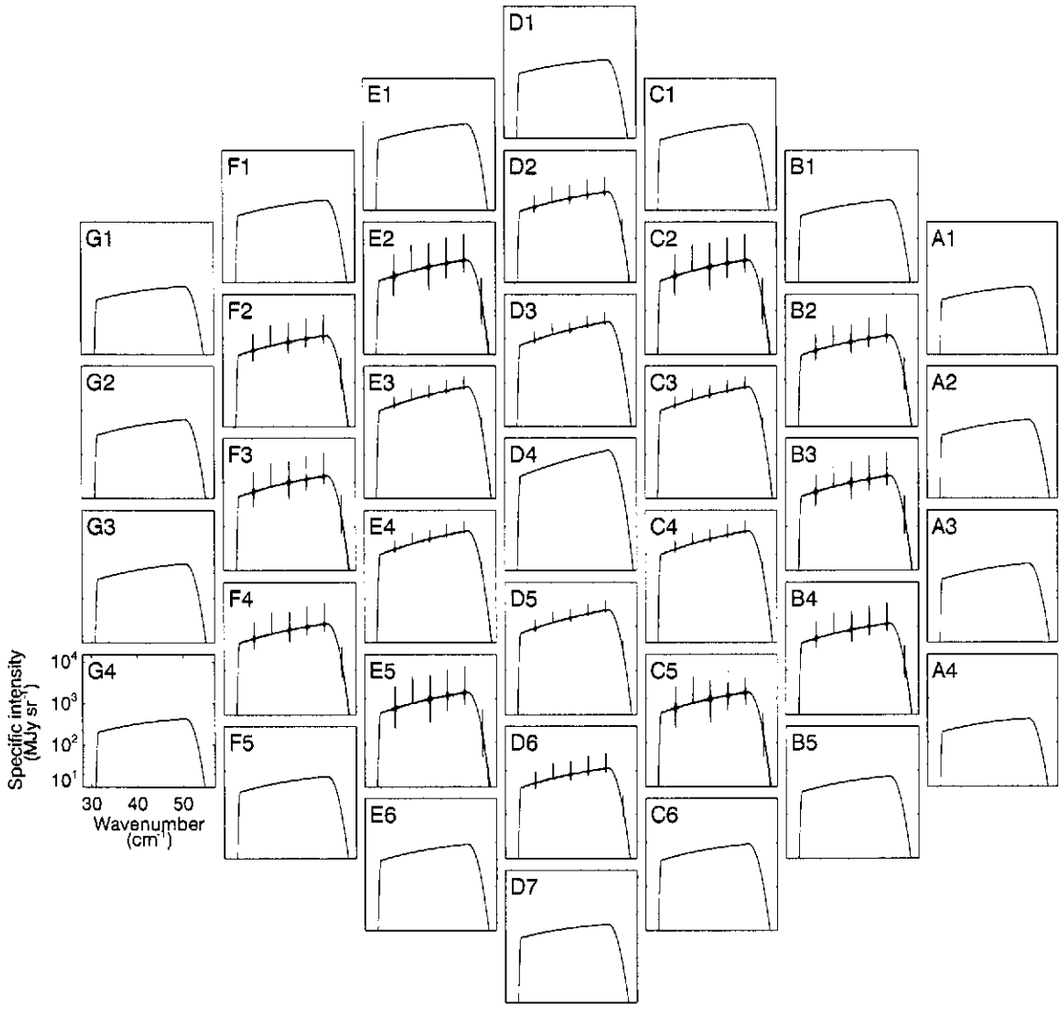

Figure 7.9: Ideal spectrometer short wavelength spectra of the simulated molecular cloud. For ease of comparison, a logarithmic scale is employed and the scale for each panel is identical to Panel G4.

The above analysis was repeated on the spectra of the other 54 bolometers in the two SPIRE spectrometer arrays. The SLW and SSW spectra are shown in Figures 7.8 and 7.9, respectively. Several features are evident in the figures. As was suggested in Figure 7.4, the CO emission lines were only measured in the second ring of the SLW array and the second and third rings of the SSW array. All the measured lines exhibited the sinc shape noted above. Moreover, the strongest

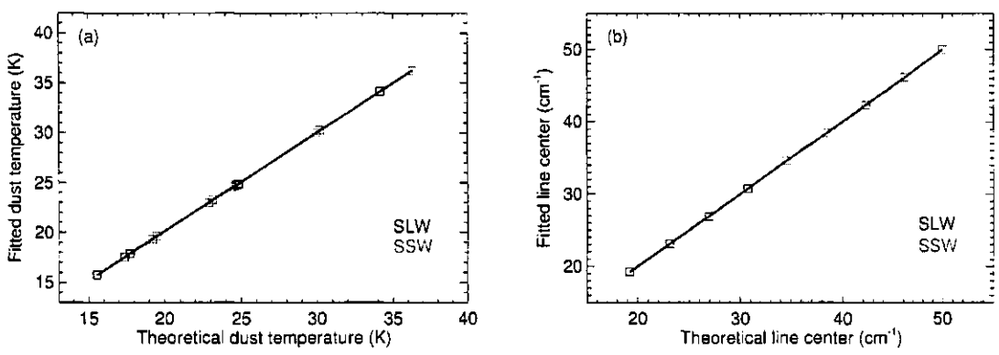

Figure 7.10: Comparison of the theoretical and derived cloud parameters. Panel (a) shows a comparison of the theoretical and derived dust temperatures, while Panel (b) shows a similar comparison for the line centers. In both panels, the blue curve is a least-squares linear fit to the data.

spectra were located at the center of each array, where the dust temperature was hottest.

Once again, a theoretical curve was fit to each spectrum using the MPFITFUN routine. From the continuum component, we determined a mean β for all 56 bolometers of 1.99 ± 0.01 and a mean σ_0 of 1020 ± 46 cm^{-1}. The fit returned a different dust temperature for each spectrum because each feedhorn observed a different section of the simulated cloud (see Equation 7.2). Panel (a) of Figure 7.10 is a comparison of the theoretical dust temperatures (given by the mean temperature of the SAS pixels entering each feedhorn) and the dust temperatures determined from the fit. The slope of a linear fit to the data (shown in blue) was 0.989 ± 0.001.

For each of the 24 spectra where the emission lines were present (18 in SSW, 6 in SLW), the MPFITFUN routine also returned values for the line centers, widths and amplitudes. Panel (b) of

Table 7.1: Derived astronomical quantities.

	Emissivity index β	Reference wavenumber σ_0 (cm^{-1})	CO column density N (10^{15} cm^{-2})	Excitation temperature $T_{\rm rot}$ (K)
Initial value	2	1000	1	300
No noise	1.99 ± 0.001	1020 ± 46	0.84 ± 0.07	323 ± 30
Velocity jitter	2.04 ± 0.02	910 ± 59	0.84 ± 0.08	350 ± 50

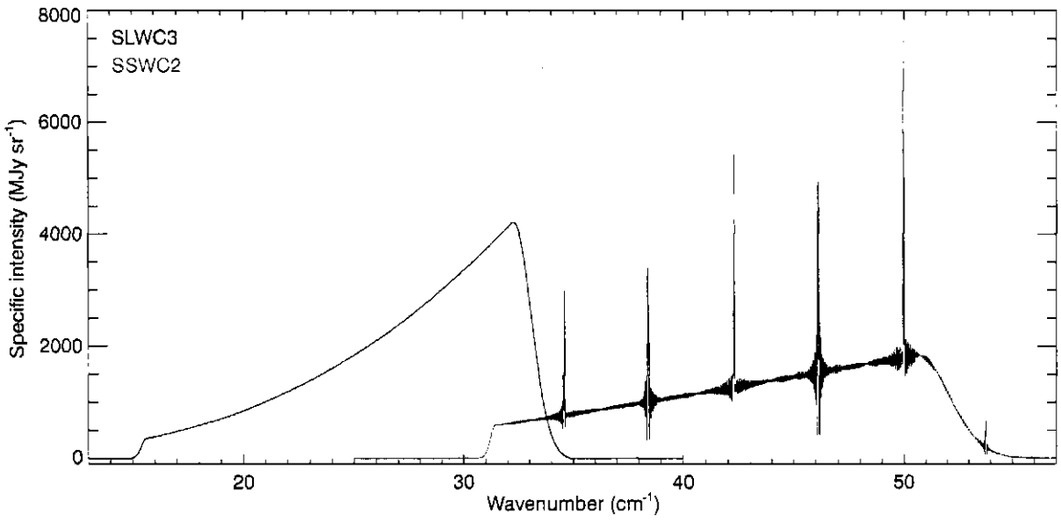

Figure 7.11: Spectra of simulated modecular cloud with velocity jitter included. This figure shows the synthetic spectra measured by the SLWC3 and SSWC2 bolometers. For both bands, the blue curve represents the fit returned by the MPFITFUN routine.

Figure 7.10 shows a comparison of the theoretical line centers (see Equation 7.6) and the line centers determined from the fit. The slope of a linear fit to the data (shown in blue) was 1.000 ± 0.001. Using the line amplitude and width, we determined the integrated line strength for each line in each spectrum. These values were used to determine the gas temperature and column density using the rotation diagram technique demonstrated earlier. Averaging all 24 values, we determined a mean excitation temperature of 323 ± 30 K and a mean CO column density of $(8.4 \pm 0.7) \times 10^{14}$ cm^{-2}. These derived values are summarized in Table 7.1.

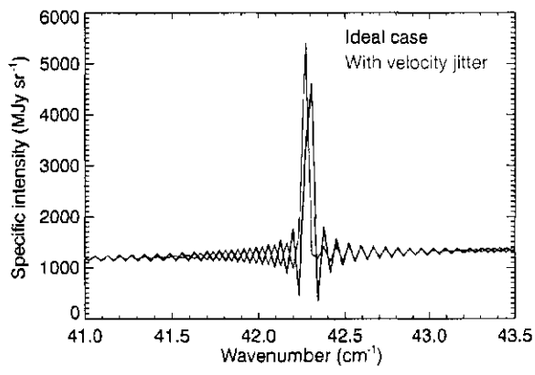

Figure 7.12: Comparison of the line shapes for the ideal and velocity jitter cases. This figure shows Figures 7.6 and 7.11 around the 42 cm^{-1} line.

In addition to the completely ideal case, we also explored a second case

where the velocity jitter was included but all other SHIFTS settings were unchanged. Figure 7.11 shows the SLWC3 and SSWC2 spectra determined under these conditions. Minimal difference was seen between the results shown here and Figure 7.6. To characterize this, Figure 7.12 shows the 42.3 cm^{-1} CO line from both cases. As can be seen, both lines were in close agreement. Similar values for β, σ_o, T_{rot} and N were recovered (see Table 7.1) when the data analysis was repeated. In summary, astronomical quantities were easily recovered from the resultant spectra using a combination of a least-squares fit and rotation diagrams.

7.2.3 Realistic case

While the analysis conducted in the previous section was able to recover the astronomical quantities with reasonable accuracy, the test was idealized. For the purpose of demonstration, it ignored most of the known noise sources present in the SPIRE spectrometer. In contrast, this section uses SHIFTS to simulate the observation of the molecular cloud model with the noise sources included. The results demonstrate the challenges associated with data-processing of real SPIRE data.

Like the previous section, the simulated astronomical source employed in this case was the molecular disk model outlined in Section 7.1. A single high resolution scan was performed at a stage speed of 0.05 $cm\,s^{-1}$. Both the stage velocity jitter and the SCAL thermal drifts were included as outlined in Sections 4.4 and 4.5. The thermal drift of the Herschel primary mirror was included, but the pointing drift of the HSO was ignored. To compensate for the 80 K Herschel primary mirror, the two SCAL sources, SCAL-A and SCAL-B, were heated to 13 and 105 K, respectively, as per Hargrave *et al.* [99]. The beamsplitters and the system efficiency, η_k, were represented by Figures 3.5 and 4.7, respectively. The bolometer thermal time constants were 5.1 and 7.4 ms for the SLW and SSW arrays, respectively. The response of the warm electronics was included, as was

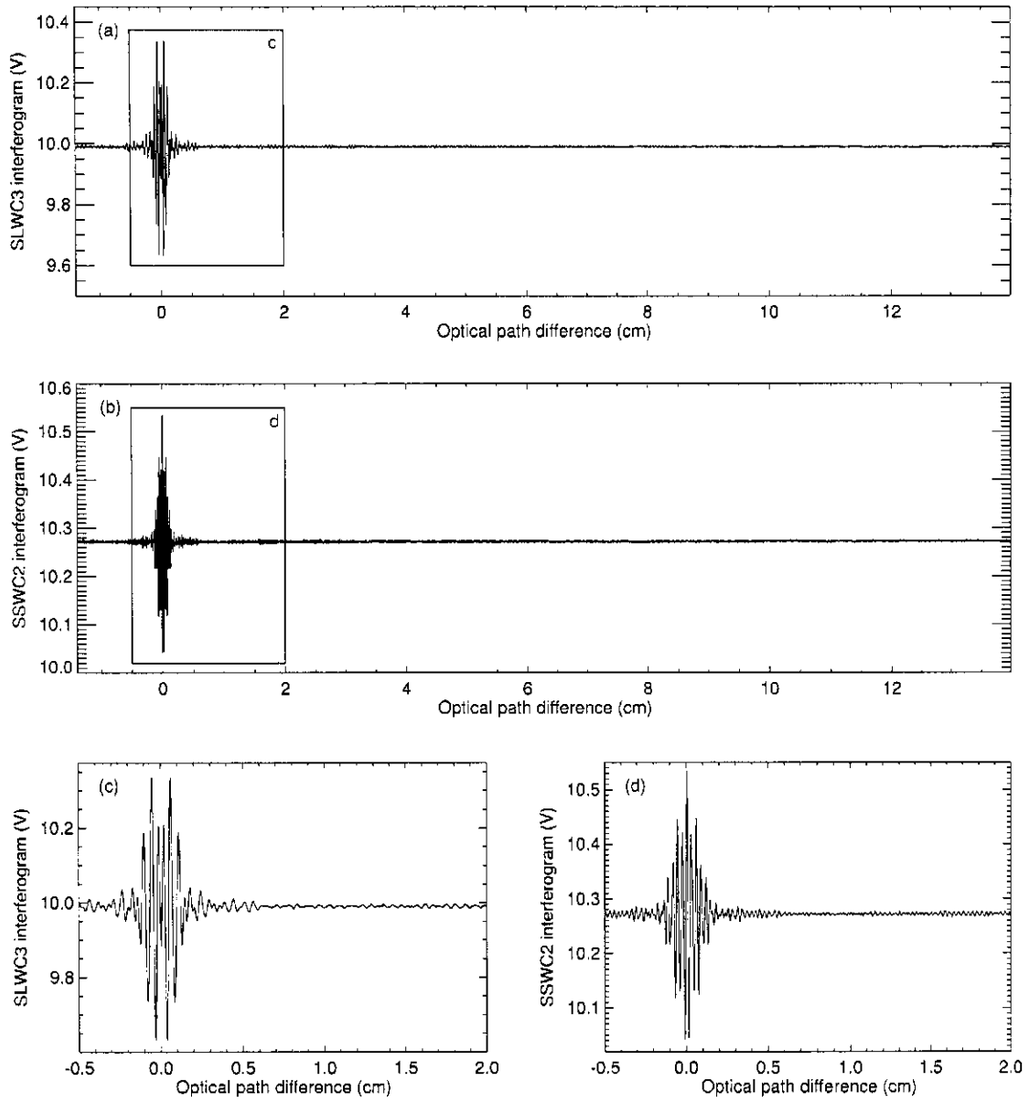

Figure 7.13: Realistic interferograms of the simulated molecular cloud. Panels (a) and (b) show the SLWC3 and SSWC2 interferograms, respectively, generated by SHIFTS under nominal noise conditions. The boxes marked "c" and "d" outline the regions of the interferograms shown in Panels (c) and (d), respectively.

the electrical and photon noise.

The interferograms returned by the pipeline are shown in Figure 7.13. For the sake of comparison, we investigated the same pixels as shown in the previous section. As can be seen by

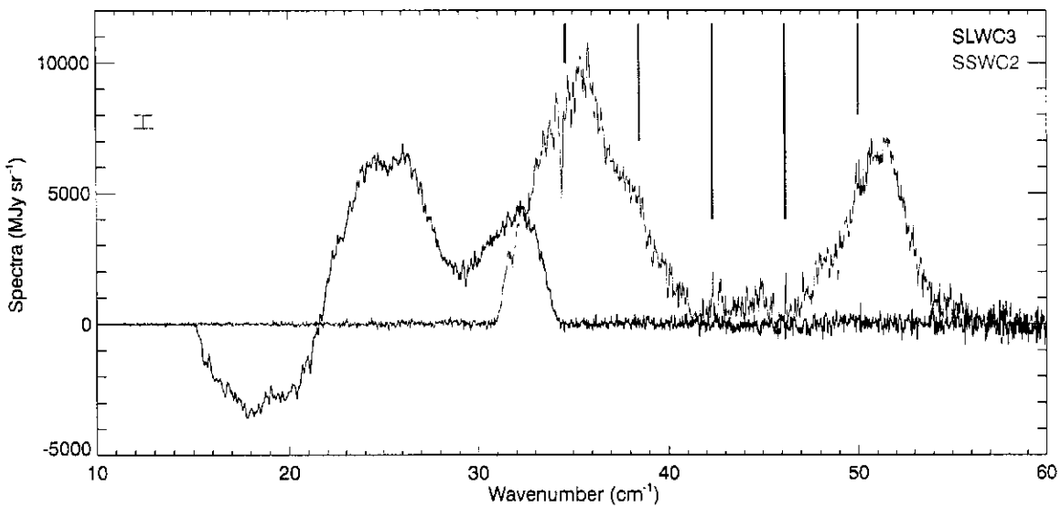

Figure 7.14: Realistic spectra of the simulated molecular cloud. The blue lines represent the theoretical locations of the CO lines in the SSW band; the green bar represents the theoretical error bar.

the large offset, the background signal was well compensated. At the same time, the beat pattern seen in Figure 7.5(b) was not visible Panel (b) of Figure 7.13 because of the presence of photon noise.

Figure 7.14 shows the corresponding spectra after data-processing by the pipeline (see Section 6.2). As can be seen, the spectra no longer had the same spectral shape as Figure 7.6; the dust continuum component and the CO emission lines were not immediately obvious in this figure. In the SLW band, the spectrum switched from SCAL dominance to Herschel primary mirror dominance at approximately 21.5 cm^{-1}. This agreed with the result seen in Figure 5.9 under the same compensation conditions. In the SSW band, two emission features were visible at 42.5 and 46.1 cm^{-1}, a spacing of approximately $2B$.

This spectrum represented the worst case scenario in SPIRE. The simulated astronomical source seen here was at the limit of detectability for a single interferogram. For comparison, estimates in Griffin [85] list a limiting line strength of 6.9×10^{-17} W m^{-2} for a 5-σ 1-hour mea-

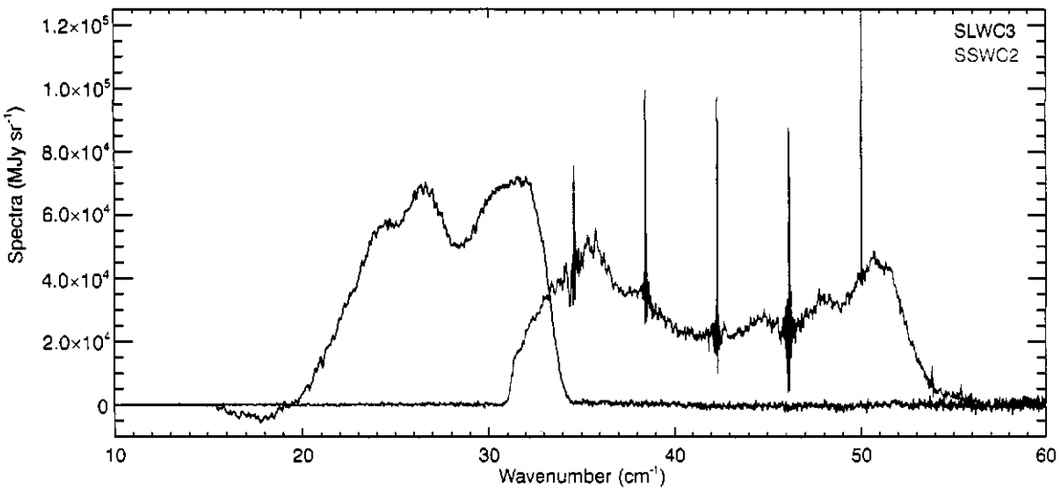

Figure 7.15: Realistic spectra of the simulated molecular cloud shown in Figure 7.14 with the gas and dust column densities increased by an order of magnitude.

surement. For a resolution of 0.04 cm^{-1} (1.2 GHz), this corresponds to a limiting flux density of 5.75 Jy for a 5-σ 1-hour measurement or 70 Jy for a 1-σ 1 s measurement. Accounting for the FOV of a single spectrometer feedhorn (1.7×10^{-8} steradians) and the fact that a single scan lasts approximately one minute, the 1-σ limiting flux density for a single interferogram is approximately 500 MJy str^{-1}. This value (shown as a green error bar in Figure 7.14) agreed with the noise level seen in the SHIFTS-simulated spectrum from a single scan.

To recover astronomical quantities such as the emissivity index and the column density from these two spectra is beyond the scope of this thesis. The data-processing tools to interpret these results have yet to be devised; such work will form an integral part of the PhD thesis of a colleague of mine.

To demonstrate a resultant spectra under a less extreme case, SHIFTS was re-run under the same conditions as above, except that the gas and dust column densities (see Sections 7.1.1 and 7.1.2) were increased by an order of magnitude. As such, the specific intensities of the SAS

spectra were ten times larger. Figure 7.15 shows the SLWC3 and SSWC2 spectra returned by the data-processing pipeline under these conditions. As can be seen, the spectral lines were now clearly visible in the SSWC2 spectrum. In addition, the continuum emission in the SLWC3 spectrum was now dominated by the astronomical source. Moreover, the shape of the SLWC3 spectrum had a similar shape to the spectrum shown in Figure 7.6. This illustrates the feasibility and challenges associated with extracting astrophysical quantities from spectra of this type.

7.3 Summary

This chapter analyzed the capabilities of the SPIRE spectrometer as shown by SHIFTS. In an ideal (i.e. unrealistic) situation, the astronomical quantities of a simple molecular cloud model were easily recovered. However, when all the known noise sources were included, recovery of the astronomical quantities was no longer possible with our current analysis.

Chapter 8

Conclusion

> *" 'What is the meaning of it, Watson?' said Holmes solemnly as he laid down the paper. 'What object is served by this circle of misery and violence and fear? It must tend to some end, or else our universe is ruled by chance, which is unthinkable. But what end? There is the great standing perennial problem to which human reason is as far from an answer as ever.' "*
>
> - Sir Arthur Conan-Doyle, "The Adventure of the Cardboard Box" in *The Complete Sherlock Holmes Volume II*, Doubleday & Company (1930)

This thesis presented the design and implementation of the Simulator for the Herschel Imaging Fourier Transform Spectrometer (SHIFTS) [5, 8]. SHIFTS was written to simulated the performance of the Spectral and Photometric Imaging Receiver (SPIRE) spectrometer, an imaging Fourier transform spectrometer (IFTS) mounted onboard the Herschel Space Observatory (HSO) [4].

Modeling the complexity of the SPIRE spectrometer was a highly involved process (see Chapters 2 and 3). Chapter 4 provided a detailed description of SHIFTS and its operation. Written in version 6.2 of the Interactive Data Language (IDL), the program was split into six primary modules and contained over 2000 lines of code. SHIFTS accounted for all the major components of the SPIRE spectrometer, including the scanning mirror, compensation sources, beamsplitters, low-pass filters, detection system and electronics.

Chapters 5 and 6 described the characterization and qualification of SHIFTS. In Chaper 5, module level testing confirmed that each component of SHIFTS performed as expected. In Chapter 6, we compared the synthetic data products produced by SHIFTS to real data measured during the first SPIRE instrument proto-flight model (PFM1) test campaign conducted at the Rutherford Appleton Laboratory (RAL) in 2005. Under several different observing conditions, we found that the results produced by SHIFTS were qualitatively and quantitively in agreement with the spectral characteristics of the real data.

In Chapter 7, an investigation was conducted on the type of astronomical observations that can be performed with the SPIRE spectrometer and some of the challenges that we expect in subsequent analysis. By observing a simple molecular cloud, it was found that the continuum and line emission characteristics were easily recoverable in an ideal case. Under nominal noise conditions, however, it became more difficult to recover the astronomical quantities.

The results of Chapter 7 highlight some of the challenges associated with using the SPIRE spectrometer. The chief concern is the large background emission of the Herschel primary mirror. While the use of the spectrometer calibrator will compensate for the large modulation produced by the Herschel primary mirror, Figures 7.14 and 7.15 demonstrated that the resulting spectrum will require substantial post-processing before any astronomical quantities can be recovered. An alternative solution to compensation is a cooled mirror, an option being explored for future space missions such as the Japanese Space Infrared Telescope for Cosmology and Astrophysics (SPICA) [182].

Another use of SHIFTS, briefly mentioned in Chapter 6, was the generation of realistic data products for the SPIRE software teams. SHIFTS has already proved helpful in debugging the spectrometer data-processing pipeline under construction by the Astronomical Instrumentation Group (AIG) at the University of Lethbridge. Once the SHIFTS graphical user interface (GUI)

is complete, SHIFTS will be released to the SPIRE consortium, allowing them to test their own software packages. A wider release is planned for the fall of 2006, to coincide with the initial call for Herschel observing proposals.

It is expected that SHIFTS will prove an important tool in our understanding of the SPIRE spectrometer. For instance, SHIFTS will aid in the the data analysis of the final SPIRE instrument test campaign to be conducted this spring. Once fully characterized, the SPIRE spectrometer will provide astronomers with the opportunity to explore the earliest stages of star formation. And then, we can perhaps add another piece to the puzzle that Galileo began assembling over four centuries ago.

Appendix A

Units and constants

Units, unit notation, and equation coherence are the bane of any graduate student in the natural sciences, especially astrophysics. The use of different units by different authors for the same quantity frequently leads to confusion (see Appendix C). To limit this problem, this appendix describes the units and constants employed in this thesis. For reference, Table A-1 lists the physical and mathematical constants [15, 136, 183].

All units in this thesis are defined in Système International (SI) units [184, 185]. Whenever possible, the metre-kilogram-second (MKS) notation is employed instead of the centimetre-gram-second (CGS) notation. The two exceptions are the model parameters of the simulated astronomical model seen in Section 7.1 and the use of debye (D) for the dipole moment (see Appendix C). The prefixes for decimal multiples of units follow the SI convention given by the Bureau International des Poids et Mesures* (BIPM) [184].

Of the seven SI base units, five are employed in this thesis: mass in kilograms (kg), length in metres (m), time in seconds (s), electric current in amperes (A) and thermodynamic temperature

*International Office of Weights and Measures

Table A-1: Physical, astronomical and mathematical constants employed in this thesis.

Quantity	Symbol	Value	Units
Boltzmann constant[a]	k	$1.3806505 \times 10^{-23}$	$\mathrm{J\,K^{-1}}$
Permeability of free space[a]	μ_o	$4\pi \times 10^{-7}$	$\mathrm{m\,kg^{-1}\,C^{-2}}$
Permittivity of free space[a]	$\epsilon_o = \frac{1}{\mu_o c^2}$	$8.854187817 \times 10^{-12}$	$\mathrm{C^2\,N^{-1}\,m^{-2}}$
Planck constant[a]	h	$6.62600693 \times 10^{-34}$	$\mathrm{J\,s}$
Rotational constant of carbon monoxide[b]	B	1.92252896	$\mathrm{cm^{-1}}$
Speed of light[a] (in a vacuum)	c	2.99792458×10^{8}	$\mathrm{m\,s^{-1}}$
Parsec[c]	pc	3.086×10^{16}	m
Base of natural logarithm[d]	e	2.7182818284590451	
Ratio of circumference to diameter[d]	π	3.1415926535897931	

[a] Source: Mohr & Taylor [183].
[b] Source: Varberg & Evenson [168].
[c] Source: Carroll & Ostlie [15].
[d] Source: Liepman [186].

in kelvin (K). Given the base units, several common derived units are also employed: force in newtons ($\mathrm{N = kg\,m\,s^{-2}}$), energy in joules ($\mathrm{J = N\,m = kg\,m^2\,s^{-2}}$), power in watts ($\mathrm{W = J\,s^{-1} = kg\,m^2\,s^{-3}}$), electric potential difference in volts ($\mathrm{V = W\,A^{-1} = kg\,m^2\,s^{-3}\,A^{-1}}$) and electric charge in coulombs ($\mathrm{C = A\,s}$) [184, 185]. To denote the flux density (i.e., the power per unit area per unit frequency interval), we employ the radio astronomy unit of janskies ($1\ \mathrm{Jy} = 10^{-26}\ \mathrm{W\,m^{-2}\,Hz^{-1}}$) [15].

In physics, the spectral scale of electromagnetic waves is generally described in terms of wavelength (i.e., distance between crests at any instant of time) or frequency (i.e., oscillations per time interval at any position in space) [62]. The conversion between the two units is given by

$$c = \nu\lambda, \qquad [\mathrm{m\,s^{-1}}] \tag{A-1}$$

where λ is the wavelength (in m), ν is the frequency (in hertz, or Hz) and c is the speed of light (see Table A-1) [62, 183]. In far-infrared (FIR) and sub-millimetre astronomy, wavelengths are typically given in microns ($1\ \mu\mathrm{m} = 10^{-6}$ m) or millimetres (mm), and frequencies in gigahertz ($1\ \mathrm{GHz} = 10^{9}$ Hz) or terahertz ($1\ \mathrm{THz} = 10^{12}$ Hz) [169, 187]. Complementing ν and λ, the angular frequency

and the angular wavenumber are occasionally employed. The angular frequency is given by

$$\omega = 2\pi\nu, \qquad [\text{radians}\,\text{s}^{-1}] \tag{A-2}$$

while the angular wavenumber is given by

$$k = \frac{2\pi}{\lambda}. \qquad [\text{m}^{-1}] \tag{A-3}$$

Due to the prominence of Fourier transform spectroscopy in this thesis, we introduce a fifth notation: wavenumber denoted by σ. As shown in Chapter 2, wavenumber in inverse centimetres (cm^{-1}) is the natural unit of spectral scale in FTS because the optical path difference (OPD) is typically measured in centimetres [49]. The conversion from wavelength or frequency to wavenumbers is given by

$$\sigma = \frac{1}{\lambda} = c\nu. \qquad [\text{cm}^{-1}] \tag{A-4}$$

For dimensionless geometric quantities, we generally follow the SI system and define the plane angle in radians and the solid angle in steradians (or sr) [184]. In figures, the plane angle is given in degrees, where 360° equals 2π radians [188]. When stating positions on the celestial sphere, the equatorial coordinate system is employed. In this system, the latitude is given by the declination (in degrees, arcminutes and arcseconds) denoted by δ and the longitude by the right ascension (in hours, minutes and seconds) denoted by α [15]. However, the declinations and right ascensions seen in this thesis are always small so both values are simply given by seconds of arc (where 1 arcsec = $\frac{1}{3600}$ degrees).

Appendix B

Analysis of spectrometer calibrator and spectrometer mechanism data

Appendix B describes the analysis of spectrometer mechanism (SMEC) and spectrometer calibrator (SCAL) data. The results of the analysis were integral to the development of the Simulator for the Herschel Imaging Fourier Transform Spectrometer (SHIFTS). The data analyzed below was measured during the first proto-flight model (PFM1) test campaign conducted at the Rutherford Appleton Laboratory (RAL) in Oxfordshire, England in 2005. Section 6.1 provides a general overview of the PFM1 tests; this appendix focuses solely on the SMEC and SCAL subsystem data.

B-1 Spectrometer mechanism

As indicated in Section 3.5, SMEC provides the optical retardation for the SPIRE spectrometer. Section 4.4 indicates that to model properly SMEC's effect on a measured interferogram, the stage noise profile must be understood. This section describes the analysis of measured data and the computation of a noise profile.

Table B-1: Spectrometer mechanism data measured during the first proto-flight model test campaign in 2005. Values were determined from a 3.3 cm segment of each scan sampled at 226.12 Hz. The scans measured in March used one set of feedback loop settings while scans measured in April used another set.

Date(s)	Number of scans	Average time per scan (s)	Average stage speed (μm s^{-1})	Average standard deviation (μm s^{-1})
March 8	16	72.91	452.59	29.46
April 6	4	364.87	90.45	39.39
April 5-8	34	121.62	271.35	36.06
April 6,7	8	72.97	452.25	35.46
April 6	4	52.12	633.16	34.40
April 6,7	8	36.48	904.56	32.28

Table B-1 summarizes the measured values of 74 high resolution scans taken with the SMEC development model during the PFM1 tests. High resolution scans were employed because they provided a model profile that represents as much of the stage scan length as possible. Each scan was measured from 0.5 to 4.0 cm at a sampling frequency of 226.12 Hz. Zero path difference (ZPD; introduced in Section 2.3.2) was located at 0.823 cm so the mechanical path difference (MPD) varied between -0.323 to 3.177 cm.

Velocity error

The PFM1 data were analyzed by calculating the velocity error for each scan. To avoid the acceleration and deceleration phases at the beginning and end of the scans, only mechanical path difference (MPD) measurements between -0.223 and 3.077 cm were employed. Moreover, we denoted the non-evenly spaced stage position by the variable z to distinguish from the evenly spaced positions denoted by x in Chapter 2.

Figure B-1 shows the analysis of the velocity error for a single forward scan taken on April 6, 2005. Following the definition of forward and reverse given in Section 4.4, and first and third scans in Panel (a) are forward scans and the second and fourth scans are reverse scans. As indicated

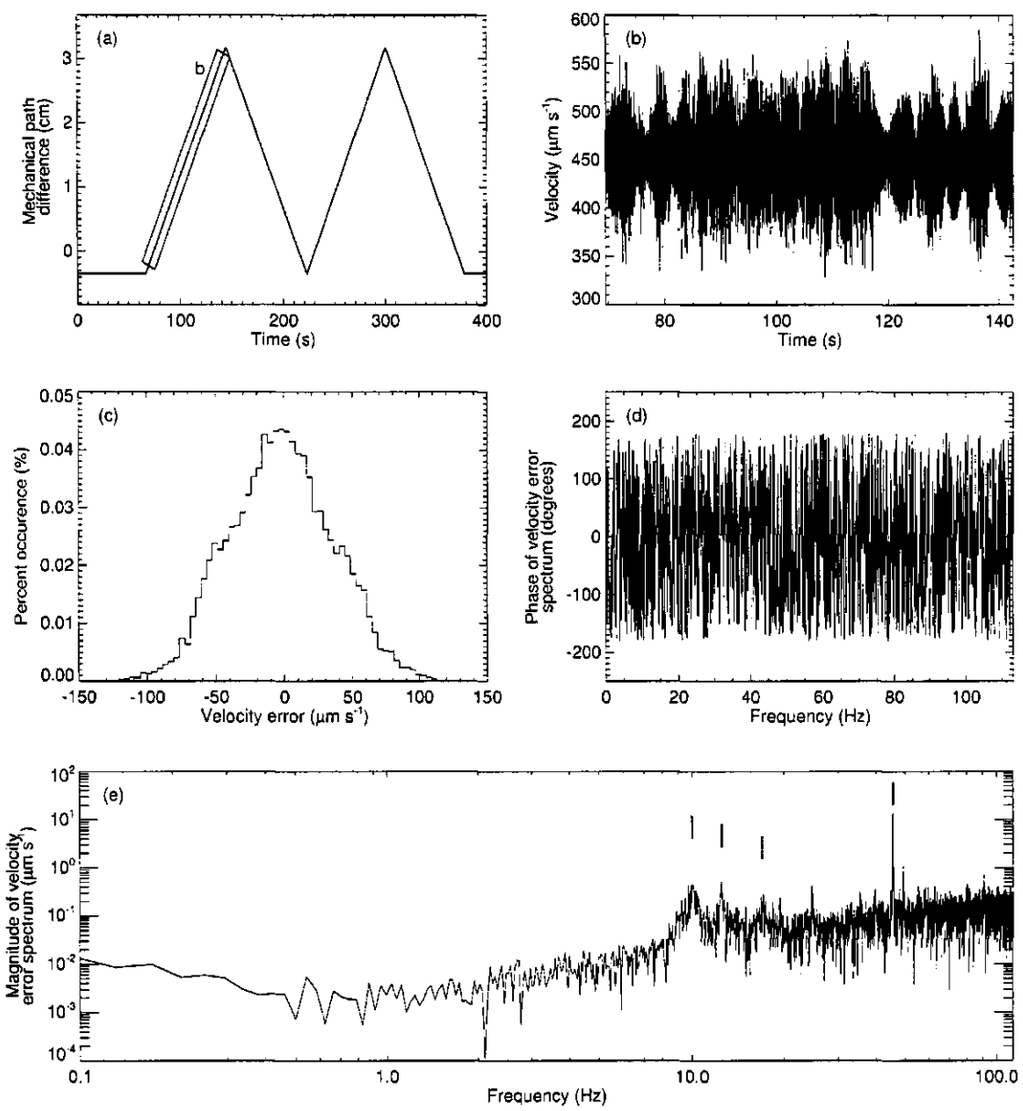

Figure B-1: Analysis of the velocity error from a single spectrometer mechanism scan measured on April 6, 2005 during the first proto-flight model test campaign. Panel (a) shows four scans taken at a speed of 452 $\mu m\,s^{-1}$. The blue box represents the 3.3 cm segment used in the analysis. Panel (b) shows the velocity of the segment from Panel (a). Panel (c) shows the distribution of the velocity error of the segment; the bin size is 4 $\mu m\,s^{-1}$. Panels (d) and (e) show the phase and magnitude of the Fourier transform of the velocity error, respectively. For clarity, only every fifth point is plotted in Panel (d). The red and blue lines in Panel (e) denote important spectral features.

by the blue box, a 3.3 cm segment of the position, $z(t)$, was extracted. From that segment, the velocity between each pair of position values, i and i + 1, was determined,

$$v_i = \frac{\Delta z_i}{\Delta t_i} = \frac{z_{i+1} - z_i}{t_{i+1} - t_i}, \qquad [\mu m\, s^{-1}] \tag{B-1}$$

as shown in Panel (b). The velocity error was defined as

$$\Delta v_i = v_i - \bar{v}, \qquad [\mu m\, s^{-1}] \tag{B-2}$$

where $\bar{v}$ was the mean velocity of the 3.3 cm segment. The distribution of the velocity error is shown in Panel (c) for a bin size of 4 $\mu m\, s^{-1}$. For this single scan, the stage speed was 452.19 $\pm$ 37.99 $\mu m\, s^{-1}$.

Panels (d) and (e) show the phase and magnitude, respectively, of the Fourier transform of the velocity error (computed using Equations 2.16 and 2.15, respectively). The frequency grid used in Panels (d) and (e) was determined using variations of Equations 2.35 and 2.42. The frequency interval is given by

$$\Delta f = \frac{1}{2T}, \qquad [\text{Hz}] \tag{B-3}$$

where T is half the scan time (in s), and the Nyquist frequency is given by

$$f_N = \frac{1}{2\Delta t}, \qquad [\text{Hz}] \tag{B-4}$$

where Δt is the sampling interval (in s). Given the 226.12 Hz sampling frequency and 72.91 s scan time, $\Delta f = 0.014$ Hz and $f_N = 113.06$ Hz. As can be seen, the phase was entirely random, a fact we exploited to simulate the stage position (see Section 4.4). To clearly display the low frequency features, Panel (e) utilized positive-definite logarithmic axes.

Several features are immediately apparent in Panel (e): the broad peaks at 10, 12.5 and 17 Hz (marked by the red vertical lines) and the sharp feature at 45.5 Hz (marked by the blue

vertical line). Analysis by the Laboratoire d'Astrophysique de Marseille (LAM) in Marseille, France suggested that the broad peaks were due to microvibrations and the peak at 45.5 Hz was a mechanical resonance of the stage.

Variation in spectra

Although Panel (e) of Figure B-1 was representative of the PFM1 velocity error spectra, different scan conditions produced different spectra. Figure B-2 shows the noise profiles under various scan conditions. Each spectrum in Figure B-2 was computed using the root-mean-square (RMS). The RMS spectrum at a frequency f_j is given by

$$\mathrm{RMS_j} = \sqrt{\frac{1}{\Delta f N}\sum_{i=1}^{N}(\mathcal{R}_i^2 + \mathcal{I}_i^2)}, \qquad [\mu\mathrm{m\,s^{-1}\,Hz^{-1/2}}] \qquad \text{(B-5)}$$

where N is the number of points and $\mathcal{R}_i$ and $\mathcal{I}_i$ are the real and imaginary components of the spectrum i, respectively. The inclusion of the frequency interval acts as a normalization constant, allowing different speeds or scan lengths to be compared [189].

Panel (a) of Figure B-2 shows the RMS spectra for forward scans taken at 452 $\mu\mathrm{m\,s^{-1}}$. The red line corresponds to 8 scans taken on March 8, 2005 while the black line corresponds to 8 scans taken on April 6 and 7, 2005. Following the measurements on March 8, 2005, the PID settings of the digital feedback loop were changed to push the spectral feature at 2.5 Hz out to a higher frequency. The spectra in Panels (b) and (c) both operated on the latter PID settings.

Panel (b) shows spectra from forward and reverse scans taken on April 6 and 7, 2005 at 452.2 $\mu\mathrm{m\,s^{-1}}$. As can be seen, for frequencies above 2 Hz, the two spectra were in good agreement. Below 2 Hz, the reverse scan (shown in red) has a larger velocity error. A similar result is seen in Panel (c), which shows the spectra for different speeds. Again, the spectra were in good agreement for frequencies above 2 Hz. However, at 0.1 Hz, the spectra differed by as much as a factor of 50.

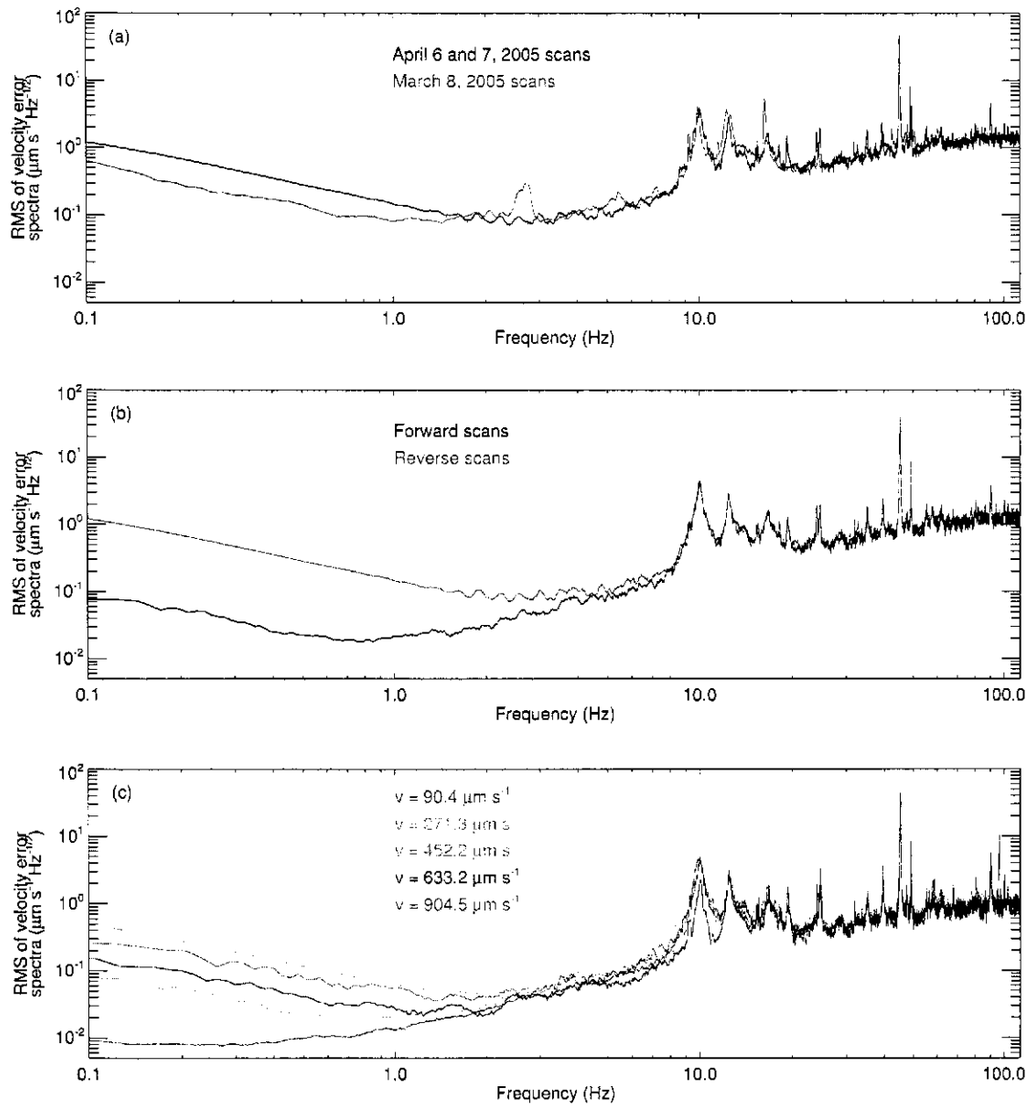

Figure B-2: Comparison of spectrometer mechanism velocity error under different scan conditions. Panel (a) shows spectra from up scans taken at 452.2 $\mu m\,s^{-1}$ using different feedback loop settings. Panel (b) shows spectra from up and down scans taken on April 6 and 7, 2005 at 452.2 $\mu m\,s^{-1}$. Panel (c) shows spectra measured at different speeds between April 5 and 8, 2005. For clarity, the spectra were smoothed by a ten point wide averaging function.

Table B-2: Spectrometer calibrator data measured during the first proto-flight model test campaign in 2005. Values were determined from 250 s measurements sampled at 1 Hz.

Date(s)	Number of scans	Average temperature (K)		Average standard deviation (mK)	
		SCAL-A	SCAL-B	SCAL-A	SCAL-B
March 10	2	24.168	5.022	2.5	3.7
March 24	19	38.153	6.518	3.8	1.9
March 31	13	6.165	36.155	3.8	4.2

The variations between the latter spectra had several causes, including the 2.5 kHz update rate of the digital feedback loop, the 226.12 Hz sampling rate, the distance between encoder fringes (4 μm), the speed and the static friction. However, the interaction between these factors was beyond the scope of this thesis. And since it was not practical to maintain a catalog of velocity error spectra for every possible scan condition, a single model spectrum was used to simulate the SMEC position. Because the nominal stage speed is 0.05 cm s^{-1}, the model profile employed in SHIFTS was the RMS spectrum for the eight 452 μm s^{-1} scans measured on April 6 and 7, 2005. Figure 4.3 shows the model profile, calculated using Equation B-5.

B-2 Spectrometer calibrator

The spectrometer calibrator is used by the SPIRE spectrometer to compensate for the large background emission of the Herschel primary and secondary mirrors; its operation is described in Section 3.3. As outlined there, SCAL is composed of two sources (denoted SCAL-A and SCAL-B) that are independently heated to temperatures as high as 120 K [100]. This section describes the analysis of SCAL data from the PFM1 test campaign and the determination of a noise profile using the same techniques as outlined above for SMEC. This noise profile was used in SHIFTS to simulate realistic temperature errors in the SCAL timeline (see Section 4.5).

Table B-2 summarizes the temperature measurements of the SCAL cryogenic qualification

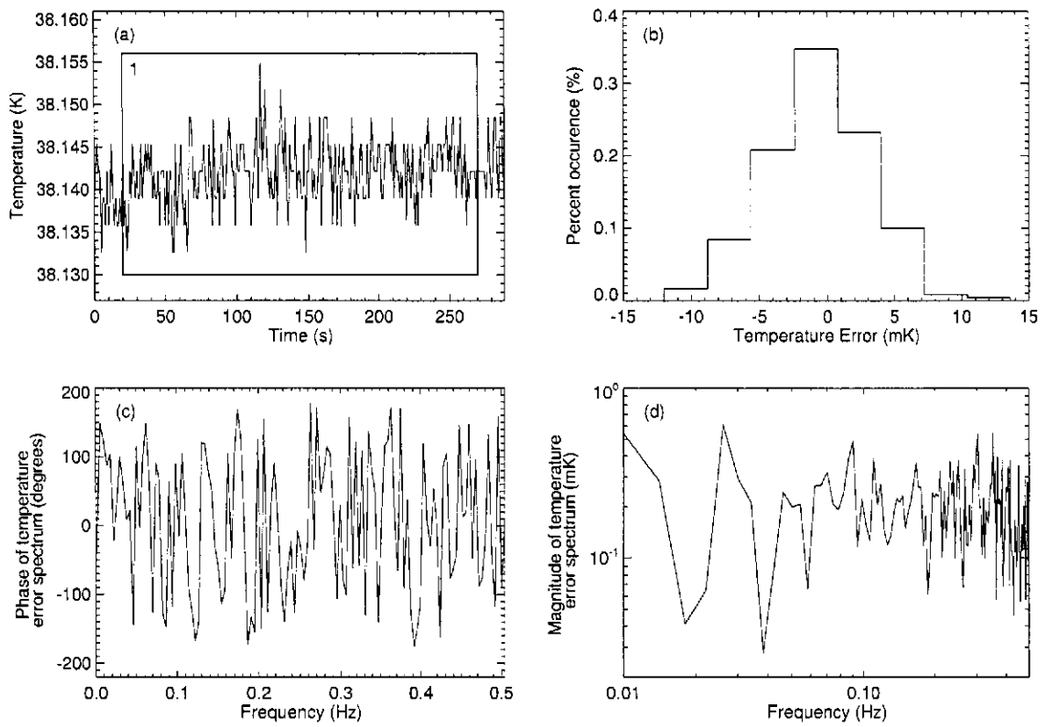

Figure B-3: Analysis of the temperature error from spectrometer calibrator data measured on March 24, 2005 during the first proto-flight model test campaign. Panel (a) shows the temperature of the SCAL-A source; the blue box marked 1 denotes the 250 s segment used in the analysis. Panel (b) shows the distribution of the temperature error for a bin size of 3.2 mK. Panels (c) and (d) show the phase and magnitude of the Fourier transform of the temperature error, respectively.

model (CQM) during the PFM1 test campaign in 2005. Each of the 34 temperature measurements were extracted from housekeeping timelines varying in length between 298 and 1318 s. A 250 s segment between 20 and 270 s was extracted from each measurement. As can be seen, the temperatures for the 250 s samples were very stable, with errors of less than 0.1 %. This high thermal stability meant that a high sampling frequency was unnecessary (unlike the stage sampling); as such, the temperature of the sources was only measured once per second.

Figure B-3 shows the analysis of the temperature error of SCAL-A measured between 17:46 and 17:52 on March 24, 2005. The temperature of the segment is shown in Panel (a), with

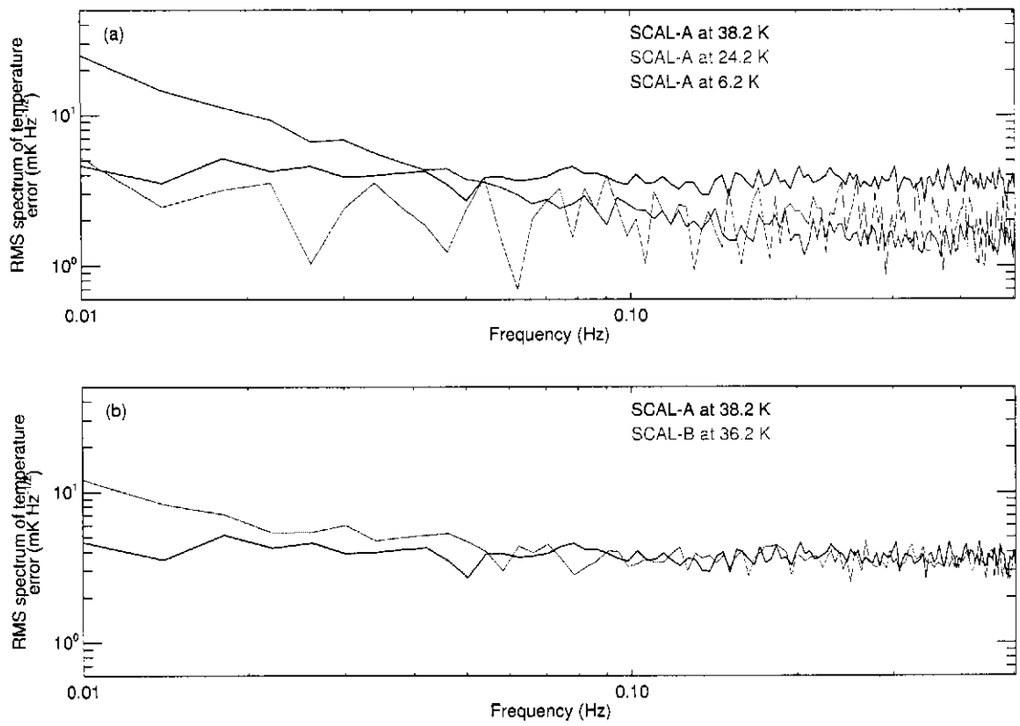

Figure B-4: Comparison of spectrometer calibrator temperature errors under different conditions. Panel (a) shows temperature error spectra of SCAL-A at different temperatures, while Panel (b) shows spectra for SCAL-A and SCAL-B at approximately the same temperature.

the 250 s segment highlighted by the blue box marked 1. As can be seen, the temperatures were digitized, with a resolution of approximately 3.2 mK (slightly smaller than the resolution of the thermometers introduced in Section 3.3). The temperature error was defined as

$$\Delta T_i(t) = T_i(t) - \overline{T}, \qquad [\mathrm{K}] \tag{B-6}$$

where $\overline{T}$ was the mean temperature (in K) and T_i was the temperature (in K) for the time interval i. The distribution of the temperature error is shown in Panel (b) for a bin size of 3.2 mK. The temperature of this measurement was 38.142 K with a one standard deviation error of 4 mK.

From the temperature error, the lower two panels of Figure B-3 were computed in an identical fashion to the velocity error for SMEC in the previous section. Given the 250 s sample

length and the 1 Hz sampling interval, the frequency interval and Nyquist frequency in the spectral domain were 0.004 Hz and 0.5 Hz, respectively (see Equations B-3 and B-4). Similar to the velocity error, the phase of the temperature error spectrum in Panel (c) was random.

The magnitude of the temperature error spectrum shown in Panel (d) was representative of the spectra from the SCAL measurements listed in Table B-2. For comparison, Figure B-4 shows spectra for one SCAL source at different temperatures and for different SCAL sources at approximately the same temperature. Like the velocity error, the RMS spectra were computed using Equation B-5. As can be seen, there was little variation between the spectra. In Panel (a), a higher error was seen for hot temperatures at high (greater than 0.1 Hz) frequencies while a higher error was seen for low temperatures at low (less than 0.1 Hz) frequencies. Even less variation was seen in the comparison between SCAL-A and SCAL-B, as shown in Panel (b). The results indicated that even though the two sources were of different physical sizes (as noted in Section 3.3), their thermal properties, as manifested by the temperature error spectra, were essentially the same.

As indicated in the previous section, it was not practical to maintain a catalogue of SCAL profiles for each temperature. As such, the RMS spectra of SCAL-A at a temperature of 38.2 K (the black line in Panels (a) and (b) in Figure B-4) was chosen as the model profile in SHIFTS.

Appendix C

The Einstein A coefficient

Due to the importance of spectroscopy in astronomical and atmospheric modeling, online databases of spectral line characteristics were developed over the past several decades [176, 177]. These databases contain numerous spectral values (e.g., line frequencies and intensities, broadening paramters); some even include the Einstein A coefficient. As defined in Section 7.1.2, the Einstein A coefficient is the probability per unit time that a system in an upper quantum state, u, will spontaneously drop to a lower quantum state, ℓ, and emit a photon with a frequency proportional to the energy difference between the two states [169]. Chapter 7 employed the Einstein A coefficients to calculate the line intensity of rotational transitions of carbon monoxide (CO). Unfortunately, the multiple definitions of the Einstein A coefficient in the literature frequently lead to confusion when modeling the line intensity [179, 180].

This appendix describes the two common notations of the Einstein A coefficient and then compares the coefficients determined from three online database to establish their agreement. It is important to note that in the literature, each author employs a specific set of symbols to describe the Einstein A coefficient. For the sake of clarity, we employ a common symbol set in this appendix

whenever possible.

C-1 Comparison of notations

This section describes and compares the two common notations used by the online databases: Rothman *et al.* [190] and Turner [175]. A careful analysis of each definition (Equations C-1 and C-3) reveals that unit coherence is not respected. This problem exists because both notations are defined in terms of the electric dipole moment (in units of debye, or D). When defining the force between two charges in centimetre-gram-second (CGS) electostatic units, the permittivity of free space, in units of $C^2\,N^{-1}\,m^{-2}$ (see Table A-1), is replaced by the dimensionless $\frac{1}{4\pi}$ [181]. While some older papers include the factor of ϵ_o (e.g., see Hilborn [180] or Tatum [191]), modern spectroscopists prefer the unrationalized CGS notation in which ϵ_o is ignored [192]. In unrationalized CGS units, debye corresponds to ergs cm^3 (where 1 erg = 10^{-7} joules) [181, 185, 190, 191].

Rothman *et al.* [190] lists the Einstein A coefficient for a transition from an upper state η' to a lower state η as

$$A_{\eta'\eta} = \left(\frac{64\pi^4\sigma_{\eta'\eta}^3}{3h}\right)\frac{g_\eta}{g_{\eta'}}\mathfrak{R}_{\eta\eta'}, \qquad [s^{-1}] \tag{C-1}$$

where $\sigma_{\eta'\eta}$ is the spectral line transition wavenumber (in cm^{-1}), $g_{\eta'}$ and g_η are the statistical weights of the upper and lower states, respectively, and $\mathfrak{R}_{\eta\eta'}$ is the weighted transition-moment squared (in debye^2). The weighted transition-moment squared is given by

$$\mathfrak{R}_{\eta\eta'} = \frac{1}{g_\eta}\sum_{\zeta,\zeta'}|R_{(\eta\zeta)(\eta'\zeta')}|^2, \qquad [D^2] \tag{C-2}$$

where $R_{(\eta\zeta)(\eta'\zeta')}$ is the transition moment (in D), and ζ' and ζ are undefined (see below).

In Turner [175], the Einstein A coefficient is given by

$$A = \left(\frac{64\pi^4\sigma_{u\ell}^3}{3h}\right)\frac{S\mu_{u\ell}^2}{g_u}, \qquad [s^{-1}] \tag{C-3}$$

where u designates the upper energy level given by angular momentum quantum number J_u, ℓ designates the lower energy level given by J_ℓ, $\sigma_{u\ell}$ is the spectral transition line frequency (in cm^{-1}), S is the line strength, $\mu_{u\ell}$ is the relevant dipole moment component and $g_u = 2J_u + 1$ is the rotational degeneracy of the upper level. Though Turner [175] does not state the units for either S or μ_{ui}, Pickett *et al.* [177] lists μ_{ui} with units of debye. As will be shown below, S is unitless. Equation C-3 is also seen in Cummins, Linke & Thaddeus [171] and Phillips [173].

Equations C-1 and C-3 provide similar definitions for the Einstein A coefficient. But while the parenthetical term is identical in both equations, the other term does not agree. Rothman *et al.* lists the Einstein A coefficient for the general case of a transition of the system from one quantum state to another quantum state [193, 194]. In contrast, Turner's equation describes changes in the rotational quantum number J due to a component of the electric dipole moment [173, 175].

To unify these notations, we first convert Rothman *et al.* into an equivalent form. Following the analysis of Gamache & Rothman [194], we define a second transition moment with different subscripts, $R_{\eta\eta'}$, which is equivalent to the electric dipole moment [190, 194, 195]. The square of $R_{\eta\eta'}$ is proportional to the probability of the system undergoing a transition from a state η to a state η'. Gamache & Rothman [194] labels quantum states using two values: non-degenerate states are denoted by η while degenerate states are denoted by ζ. The two transition moments, $R_{\eta\eta'}$ and $R_{(\eta\zeta)(\eta'\zeta')}$, are related by

$$|R_{\eta\eta'}|^2 = \frac{1}{g_{\eta'}} \sum_{\zeta,\zeta'} |R_{(\eta\zeta)(\eta'\zeta')}|^2. \qquad [\mathrm{D}^2] \tag{C-4}$$

Inserting Equations C-2 and C-4 into Equation C-1 yields

$$A_{\eta'\eta} = \left(\frac{64\pi^4 \sigma_{\eta'\eta}^3}{3h} \right) |R_{\eta\eta'}|^2. \qquad [\mathrm{s}^{-1}] \tag{C-5}$$

A similar treatment of the Einstein A coefficient is given in Condon & Shortley [196], Gordy &

Cook [197], Harmony [193], Herzberg [198], Kroto [199] and Townes & Schawlow [200].

We now follow Gordy & Cook [197] and introduce the unitless line strength,

$$\lambda_g(J_\ell,\tau_\ell;J_u,\tau_u) = \sum_{FM_\ell M_u} |\langle J_u,\tau_u,M_u|\Phi_{Fg}|J_\ell,\tau_\ell,M_\ell\rangle|^2, \tag{C-6}$$

where J_u, τ_u and M_u are quantum numbers corresponding to the upper state u; J_ℓ, τ_ℓ and M_ℓ are quantum numbers corresponding to the lower state ℓ; and Φ_{Fg} is the cosine of the angle between the space-fixed axes $F = X,Y,Z$ and the body-fixed principal axes of inertia $g = x,y,z$. Summing over M_u yields

$$\lambda_g(J_\ell,\tau_\ell;J_u,\tau_u) = (2J_u+1)\sum_{FM_\ell} |\langle J_u,\tau_u,M_u|\Phi_{Fg}|J_\ell,\tau_\ell,M_\ell\rangle|^2. \tag{C-7}$$

From the definition of the components of the dipole moment, $\mu_F = \sum_g \mu_g \Phi_g$, we write

$$\sum_{FM_\ell} |\langle J_u,\tau_u,M_u|\mu_F|J_\ell,\tau_\ell,M_\ell\rangle|^2 = \mu_g^2 \sum_{FM_\ell} |\langle J_u,\tau_u,M_u|\Phi_{Fg}|J_\ell,\tau_\ell,M_\ell\rangle|^2, \quad [D^2] \tag{C-8}$$

where μ_g is a component of the dipole moment in one direction of the principal axes of inertia and μ_F is the dipole moment in one space-fixed axis (both in debye). For a rotor in the absence of any external fields,

$$\sum_{FM_\ell} |\langle J_u,\tau_u,M_u|\mu_F|J_\ell,\tau_\ell,M_\ell\rangle|^2 = |\langle J_u,\tau_u|\mu|J_\ell,\tau_\ell\rangle|^2, \quad [D^2] \tag{C-9}$$

where $\langle J_u,\tau_u|\mu|J_\ell,\tau_\ell\rangle$ is the expectation value of the dipole moment vector. Therefore, for a single transition,

$$|\langle J_u,\tau_u|\mu|J_\ell,\tau_\ell\rangle|^2 = \frac{\mu_g^2 \lambda_g(J_\ell,\tau_\ell;J_u,\tau_u)}{(2J_u+1)}. \quad [D^2] \tag{C-10}$$

As can be seen in Equation C-10, the line strength describes the ratio of the weighted square of the expectation value of the dipole moment vector and the square of one component of the dipole moment. Denoting the line strength by S and the square of the expectation value of the dipole

moment vector by $|R_{\eta\eta'}|^2$, the synthesis of Rothman *et al.* and Turner is given by

$$\underbrace{\frac{g_\eta}{g_{\eta'}}\mathfrak{R}_{\eta\eta'} = |R_{\eta\eta'}|^2}_{\text{Rothman } et\ al.} = \underbrace{\frac{S\mu_{u\ell}^2}{g_u}}_{\text{Turner}}. \qquad [\text{D}^2] \tag{C-11}$$

C-2 Comparison of catalog values

With an understanding of the various notations of the Einstein A coefficients, this section compares the Einstein A coefficients calculated from three separate databases:

1. Gestion et Etude des Informations Spectroscopiques Atmosphériques* (GEISA)
2. High-resolution Transmission Molecular Absorption Database† (HITRAN; 2000 and 2004 editions)
3. Jet Propulsion Laboratory (JPL) Molecular Spectroscopy Catalog‡

By way of example, two rotational transitions of carbon monoxide, $6 \longrightarrow 5$ and $2 \longrightarrow 1$, were selected and are summarized in Table C-1.

The 2004 edition of HITRAN was used as the baseline because it explicitly includes values for the Einstein A coefficient [176]. GEISA and the 2000 edition of HITRAN list the weighted square of the transition moment for a reference temperature of 296 K. In those cases, the Einstein A coefficients were determined using Equation C-1 [178,201]. Unlike GEISA and HITRAN, the JPL catalog lists neither the Einstein A coefficient nor the weighted square of the transition moment [177]. Instead, the Einstein A coefficients were determined from the line intensity,

$$I_{u\ell}(T_o) = \left(\frac{8\pi^3}{3h}\right)\sigma_{u\ell}\frac{S\mu_{u\ell}^2}{Q_{\text{rot}}}\left[e^{-E_\ell/kT_{\text{rot}}} - e^{-E_u/kT_{\text{rot}}}\right], \quad [\text{nm}^2\,\text{MHz}] \tag{C-12}$$

where $\sigma_{u\ell}$ is the wavenumber of the emitted photon (see Equation 7.6), Q_{rot} is the rotational partition function (see Equation 7.7) for an excitation temperature T_{rot} (in K), E_ℓ and E_u are the lower

*Management and Study of Atmospheric Spectroscopic Information; web address: *http://ara.lmd.polytechnique.fr/public/products/GEISA/HTML-GEISA/*

†Web address: *http://cfa-www.harvard.edu/hitran/*

‡Web address: *http://spec.jpl.nasa.gov*

Table C-1: Einstein A coefficients calculated for two rotational transitions of carbon monoxide. Given Equation 7.6, the 2 → 1 transition corresponds to a frequency of 230.64 GHz (7.690 cm^{-1}) and the 6 → 5 transition corresponds to a frequency of 691.91 GHz (23.065 cm^{-1}).

Database	Transition ($u \rightarrow \ell$)	$\mathfrak{R}_{\eta\eta'}$ (10^{-3} D^2)	Einstein A coefficient (s^{-1})
HITRAN 2004	2 → 1	N/A[a]	6.857×10^{-7}
	6 → 5	N/A[a]	2.120×10^{-5}
HITRAN 2000	2 → 1	8.037	6.877×10^{-7}
	6 → 5	6.531	2.127×10^{-5}
GEISA	2 → 1	8.040	6.880×10^{-7}
	6 → 5	6.530	2.126×10^{-5}
JPL	2 → 1	7.830[b]	6.912×10^{-7}
	6 → 5	6.395[c]	2.082×10^{-5}

[a] Not available.
[b] Calculated from a line intensity of $I_{21}(T_o) = 10^{-4.1197}$ nm^2 MHz.
[c] Calculated from a line intensity of $I_{65}(T_o) = 10^{-2.8193}$ nm^2 MHz.

and upper energy levels, respectively (see Equation 7.5), h is the Planck constant, c is the speed of light and b is the rotational constant for CO (see Table A-1) [173, 175, 177].

The line intensity (derived in Penner [202]) is listed for a reference temperature of T_o = 300 K [177]. However, the right-hand side of Equation C-12 is defined for any temperature so $S\mu^2_{u\ell}$ was determined for the GEISA and HITRAN temperature of 296 K [177]. The Einstein A coefficients were then calculated using Equation C-3. For example, the line intensity for the 2 → 1 transition is $10^{-4.1197}$ nm^2 MHz; Equation C-12 returns a value of $S\mu^2_{21} = (2.424 \times 10^{-2})$ D^2. Turner's unit of $S\mu^2_{21}$ was converted to $\mathfrak{R}_{12} = (7.830 \times 10^{-3})$ D^2 by applying the statistical weights given in Equation C-11.

Even though no uncertainties are listed in the catalogs, the agreement between the values is good; all the calculated values differed from each other by less than 1 %.

References

[1] T. Bulfinch. *Bulfinch's Mythology: the Age of Fable, the Age of Chivalry, the Legends of Charlemagne*. Random House: New York, NY (1934).

[2] G. B. Grinnell. *Blackfoot Lodge Tales: The Story of a Prairie People*. University of Nebraska Press: Lincoln, NE (1962).

[3] G. Galilei. *The Sidereal Messenger*. University of Chicago Press: Chicago, IL (1989). Translated by A. van Helden (originally published as "Sidereus Nuncius" in 1610).

[4] G. L. Pilbratt. "Herschel Mission: Status and Observing Opportunities." In *Optical, Infrared, and Millimeter Space Telescopes* (edited by J. C. Mather), **5487**:401–412. Proceedings of the International Society for Optical Engineering (2004).

[5] M. Griffin, B. Swinyard, and L. Vigroux. "The Herschel-SPIRE Instrument." In *Optical, Infrared and Millimeter Space Telescopes* (edited by J. C. Mather), **5487**:413–424. Proceedings of the International Society for Optical Engineering (2004).

[6] A. Poglitsch, *et al.* "The Photodetector Array Camera & Spectrometer (PACS) for the Herschel Space Observatory." In *Optical, Infrared, and Millimeter Space Telescopes* (edited by J. C. Mather), **5487**:425–435. Proceedings of the International Society for Optical Engineering (2004).

[7] T. de Graauw and F. P. Helmich. "Herschel-HIFI: The Heterodyne Instrument for the Far-Infrared." In *The Promise of the Herschel Space Observatory* (edited by G. L. Pilbratt, *et al.*), **SP-460**:45–51. Proceedings of the European Space Agency Symposium in Toledo, Spain (2001).

[8] J. V. Lindner, D. A. Naylor, and B. M. Swinyard. "Simulation of the Performance of ESA's Herschel/SPIRE Imaging Fourier transform spectrometer." In *Optical, Infrared, and Millimeter Space Telescopes* (edited by J. C. Mather), **5487**:469–480. Proceedings of the International Society for Optical Engineering (2004).

[9] E. F. van Dishoeck and F. P. Helmich. "Scientific Drivers for future high-resolution far-infrared spectroscopy in space." In *Submillimetre and Far-infrared Space Instrumentation*, **ESA SP-388**:3–12. Proceedings of the 30th ESLAB symposium (1996).

[10] W. Herschel. "Catalogue of One Thousand new Nebulae and Clusters of Stars." *Philosophical Transactions of the Royal Society of London*, **76**:457–499 (1786).

[11] J. Bally, *et al.* "Externally illuminated young stellar environments in the Orion nebula: *Hubble Space Telescope* planetary camera and ultraviolet observations." *The Astronomical Journal*, **116**(1):293–321 (1998).

[12] J. E. Dyson and D. A. Williams. *The Physics of the Interstellar Medium*. The Graduate Series in Astronomy, 2nd edition. Institute of Physics Publishing: Bristol, England (1997).

[13] W. Herschel. "On Nebulous Stars, properly so called." *Philosophical Transactions of the Royal Society of London*, **81**:71–88 (1791).

[14] W. Herschel. "Experiments on the Refrangibility of the Invisible Rays of the Sun." *Philosophical Transactions of the Royal Society of London*, **90**:284–292 (1800).

[15] B. W. Carroll and D. A. Ostlie. *An Introduction to Modern Astrophysics*. Addison-Wesley: Reading, MA (1996).

[16] F. H. Shu, F. C. Adams, and S. Lizano. "Star Formation in Molecular Clouds: Observation and Theory." *Annual Review of Astronomy and Astrophysics*, **25**:23–81 (1987).

[17] P. André and F. Motte. "FIRST and the earliest stages of star formation." In *Star Formation from the small to the large scale*, **ESA SP-445**:219–226. Proceedings of the 33th ESLAB symposium (2000).

[18] R. Bowers and T. Deeming. *Astrophysics II: Interstellar Matter and Galaxies*. Jones and Bartlett Publishers: Boston, MA (1984).

[19] D. Leverington. *A History of Astronomy from 1890 to present*. Springer: London, England (1995).

[20] R. J. Trumpler. "Absorption of light in the galactic system." *Publications of the Astronomical Society of the Pacific*, **42**(248):214–227 (1930).

[21] H. Karttunen, *et al.* *Fundamental Astronomy*. 4th edition. Springer-Verlag: Berlin, Germany (2003).

[22] C. A. Beichman. "The IRAS view of the galaxy and the solar system." *Annual Review of Astronomy and Astrophysics*, **25**:521–563 (1987).

[23] S. Chandrasekhar. *Radiative Transfer*. Dover Publications: New York, NY (1960).

[24] W. L. Wolfe. *Handbook of Military Infrared Technology*. US Government Printing Office: Washington, DC (1965).

[25] E. Churchwell, M. G. Wolfire, and D. O. S. Wood. "The infrared emission from dust surrounding newly formed O stars." *The Astrophysical Journal*, **354**:247–261 (1990).

[26] B. Nisini, *et al.* "High-J CO Line Emission from Young Stellar Objects: From ISO to First." In *The Far Infrared and Submillimeter Universe* (edited by G. Pilbratt, S. Volonte, and A. Wilson), **SP-401**:321–324. Proceedings of an ESA Symposium devoted to ESA's "FIRST" mission (1997).

[27] J. W. V. Storey, D. M. Watson, and C. H. Townes. "Far-infrared observations of shocked CO in Orion." *The Astrophysical Journal*, **247**:136–143 (1981).

[28] D. A. Allen. "Infrared Astronomy: an Assessement." *Quarterley Journal of the Royal Astronomical Society*, **18**:188–198 (1977).

[29] H. J. Walker. "A brief history of infrared astronomy." *Astronomy and Geophysics*, **41**(5):5.10–5.13 (2000).

[30] W. S. Holland, *et al.* "SCUBA: a common-user submillimetre camera operating on the James Clerk Maxwell Telescope." *Monthly Notices of the Royal Astronomical Society*, **303**(4):659–672 (1999).

[31] M. Griffin, B. Swinyard, and L. Vigroux. "The SPIRE Instrument for FIRST." In *UV, Optical and IR Space Telescopes and Instruments* (edited by J. B. Breckinridge and P. Jakobsen), **4013**:142–151. Proceedings of the International Society for Optical Engineering (2000).

[32] D. Johnstone, *et al.* "Large-area mapping at 850 microns. II. Analysis of the clump distribution in the ρ Ophiuchi molecular cloud." *The Astrophysical Journal Supplement Series*, **545**(2):327–339 (2000).

[33] D. Johnstone, J. D. Francesco, and H. Kirk. "An Extinction Threshold for Protostellare Cores in Ophiuchus." *The Astrophysical Journal*, **611**(1):L45–L48 (2004).

[34] A. E. Visser and J. S. Richer. "Completion of a SCUBA survey of Lynds dark clouds and implications for low-mass star formation." *The Astrophysical Journal*, **124**(5):2756–2789 (2002).

[35] D. B. Gallagher, W. R. Irace, and M. W. Werner. "The Development and Mission of the Space Infrared Telescope Facility (SIRTF)." In *Optical, Infrared, and Millimeter Space Telescopes* (edited by J. C. Mather), **5487**:13–25. Proceedings of the International Society for Optical Engineering (2004).

[36] H. Murakami. "ASTRO-F Infrared Sky Survey Mission." In *Optical, Infrared, and Millimeter Space Telescopes* (edited by J. C. Mather), **5487**:330–337. Proceedings of the International Society for Optical Engineering (2004).

[37] H. Shibai. "ASTRO-F mission." *Advances in Space Research*, **34**(3):589–593 (2004).

[38] G. L. Pilbratt. "The Herschel mission, scientific objectives, and this meeting." In *The Promise of the Herschel Space Observatory* (edited by G. L. Pilbratt, *et al.*), **SP-460**:11–20. Proceedings of the European Space Agency Symposium in Toledo, Spain (2001).

[39] G. R. Fowles and G. L. Cassiday. *Analytical Mechanics*. Thomson Learning: Toronto, ON (1999).

[40] "Herschel-SPIRE Memorandum of Understanding: Canadian Contribution to the Herschel-SPIRE Instrument Project." Technical Report SPIRE-UCF-PRJ-001614, University of Lethbridge, Lethbridge, AB (2003).

[41] L. D. Spencer, *et al.* "A Fourier transform spectrometer for ground testing of the Herschel/SPIRE instrument." In *Optical, Infrared, and Millimeter Space Telescopes* (edited by J. C. Mather), **5487**:501–512. Proceedings of the International Society for Optical Engineering (2004).

[42] The answer to the ultimate question of life, the universe and everything.

[43] T. Lim, *et al.* "First Results from Herschel-SPIRE Performance Tests." In *Optical, Infrared and Millimeter Space Telescopes* (edited by J. C. Mather), **5487**:460–468. Proceedings of the International Society for Optical Engineering (2004).

[44] B. Sibthorpe, A. Woodcraft, and M. Griffin. "A software simulator for the Herschel-SPIRE imaging photometer." In *Optical, Infrared, and Millimeter Space Telescopes* (edited by J. C. Mather), **5487**:491–500. Proceedings of the International Society for Optical Engineering (2004).

[45] B. M. Swinyard, *et al.* "The Imaging FTS for Herschel SPIRE." In *IR Space Telescopes and Instruments* (edited by J. C. Mather), **4850**:698–709. Proceedings of the International Society for Optical Engineering (2003).

[46] B. M. Swinyard, *et al.* "The FIRST-SPIRE Spectrometer: A Novel Imaging FTS for the Sub-Millimetre." In *UV, Optical and IR Space Telescopes and Instruments* (edited by J. B. Breckinridge and P. Jakobsen), **4013**:196–207. Proceedings of the International Society for Optical Engineering (2000).

[47] B. Swinyard. "Simulations of the FTS Performance." Technical Report SPIRE-RAL-NOT-000413, Rutherford Appleton Laboratory, Oxfordshire, England (2000).

[48] I. Grattan-Guiness. *Joseph Fourier, 1768-1830*. The MIT Press: Cambridge, MA (1972).

[49] S. P. Davis, M. C. Abrams, and J. W. Brault. *Fourier Transform Spectroscopy*. Academic Press: St. Louis, MO (2001).

[50] D. C. Champeney. *Fourier Transforms and their Physical Applications*. Academic Press: St. Louis, MO (1973).

[51] R. M. Bracewell. *Fourier Transforms and Its Applications*. McGraw-Hill Book Co: New York, NY (1965).

[52] J. W. Brown and R. V. Churchill. *Complex Variables and Applications*. 6th edition. McGraw-Hill: New York, NY (1996).

[53] E. O. Brigham. *The Fast Fourier Transform*. Prentice-Hall: Englewood Cliffs, NJ (1973).

[54] J. F. James. *A Student's Guide to Fourier Transforms*. 2nd edition. Cambridge University Press: Cambridge, England (2002).

[55] R. J. Bell. *Infrared Fourier Transform Spectroscopy*. Academic Press: New York, NY (1972).

[56] P. R. Griffiths and J. A. de Haseth. *Fourier Transform Infrared Spectroscopy*. John Wiley and Sons: New York, NY (1986).

[57] E. V. Loewenstein. "The History and Current Status of Fourier Transform Spectroscopy." *Applied Optics*, **5**(5):845–853 (1966).

[58] J. S. Walker. *Fourier Analysis*. Oxford University Press: Oxford, England (1988).

[59] M. L. Forman, W. Steel, and G. A. Vanasse. "Correction of Asymmetric Interferograms Obtained in Fourier Spectroscopy." *Journal of the Optical Society of America*, **56**(1):59–64 (1966).

[60] M. Born and E. Wolf. *Principles of Optics: Electromagnetic Theory of Propagation, Interference and Diffraction of Light*. 6th edition. Cambridge University Press: Cambridge, England (1980).

[61] T. Young. "The Bakerian Lecture: On the Theory of Light and Colours." *Philosophical Transactions of the Royal Society of London*, **92**:12–48 (1802).

[62] R. A. Serway. *Physics for Scientists and Engineers, with Modern Physics*. 4th edition. Saunders College Publishing: Philadelphia, PA (1996).

[63] B. Jaffe. *Michelson and the Speed of Light*. Anchor Books: Garden City, NY (1960).

[64] A. A. Michelson and E. W. Morley. "On the Relative Motion of the Earth and the Luminiferous Ether." *The American Journal of Science*, **34**(203):333–345 (1887).

[65] A. A. Michelson. "Radiation in a Magnetic Field." *The Astrophysical Journal*, **6**(6):131–138 (1897).

[66] K. Dohlen, *et al.* "Optical Design of the SPIRE Instrument for FIRST." In *UV, Optical and IR Space Telescopes and Instruments* (edited by J. B. Breckinridge and P. Jakobsen), **4013**:119–128. Proceedings of the International Society for Optical Engineering (2000).

[67] E. Hecht. *Optics*. 4th edition. Addison-Wesley: San Fransisco, CA (2002).

[68] H. Rubens and R. W. Wood. "Focal Isolation of Long Heat-Waves." *Philosophical Magazine*, **21**(6):249–261 (1911).

[69] J. Connes and P. Connes. "Near-Infrared Planetary Spectra by Fourier Spectroscopy. I. Instruments and Results." *Journal of the Optical Society of America*, **56**(7):896–910 (1966).

[70] H. Nyquist. "Certain topics in telegraph transmission theory." *Transactions of the American Institute of Electrical Engineers*, **47**:617–644 (1928).

[71] R. S. Longhurst. *Geometrical and Physical Optics*. 2nd edition. John Wiley & Sons: New York, NY (1967).

[72] D. A. Naylor. Astronomy Instrument Group, University of Lethbridge, Lethbridge, AB. *Personal Communication* (2005).

[73] J. W. Cooley and J. W. Tukey. "An Algorithm for the Machine Calculation of Complex Fourier Series." *Mathematical Computation*, **19**:297–301 (1965).

[74] M. K. Tahic and D. A. Naylor. "Apodization Functions for Fourier Transform Spectroscopy." In *Fourier Transform Spectroscopy*. Optical Society of America (2005).

[75] R. H. Norton and R. Beer. "New apodizing functions for Fourier spectrometry." *Journal of the Optical Society of America*, **66**(3):259–264 (1976).

[76] F. J. Harris. "On the Use of Windows for Harmonic Analysis with the Discrete Fourier Transform." *Proceedings of the IEEE*, **66**(1):51–83 (1978).

[77] M. K. Tahic. *Fourier transform spectroscopy of the Orion Molecular Cloud*. MSc thesis, University of Lethbridge, Lethbridge, AB (2004).

[78] I. M. Chapman and D. A. Naylor. "Development of a Freely-Distributed, Customizable Atmospheric Radiative Transfer Model." In *Fourier Transform Spectroscopy topical meeting*. Optical Society of America: Alexandria, VA (2004).

[79] L. D. Spencer. *Spectral characterization of the Herschel SPIRE Photometer*. MSc thesis, University of Lethbridge, Lethbridge, AB (2005).

[80] M. L. Forman. "Spectral interpolation: zero fill or convolution." *Applied Optics*, **16**(11):2801 (1977).

[81] D. Griffin, M. Griffin, and B. Swinyard. "SPIRE Design Description." Technical Report SPIRE-RAL-PRJ-000620, Rutherford Appleton Laboratory, Oxfordshire, England (2003).

[82] P. Hargrave and I. Walker. "End Item Data Package: SPIRE Instrument Beam dividers." Technical Report SPIRE-UCF-DOC-002126, Cardiff University, Cardiff, Wales (2004).

[83] M. E. Caldwell, *et al.* "Beam pattern (diffraction) aspects in design of the SPIRE instrument." In *UV, Optical and IR Space Telescopes and Instruments* (edited by J. B. Breckinridge and P. Jakobsen), **4013**:210–220. Proceedings of the International Society for Optical Engineering (2000).

[84] D. H. Martin and J. W. Bowen. "Long-Wave Optics." *IEEE Transactions on Microwave Theory and Techniques*, **41**(10):1676–1690 (1993).

[85] M. Griffin. "SPIRE Sensitivity Models." Technical Report SPIRE-QMW-NOT-000642, Cardiff University, Cardiff, Wales (2004).

[86] K. Dohlen, A. Origné, and M. Ferlet. "Optical alignment verification of the Herschel-SPIRE instrument." In *Optical, Infrared and Millimeter Space Telescopes* (edited by J. C. Mather), **5487**:448–459. Proceedings of the International Society for Optical Engineering (2004).

[87] P. Hargrave. "Filters - Interface Control Document." Technical Report SPIRE-UCF-PRJ-001151, Cardiff University, Cardiff, Wales (2003).

[88] B. Stobie and D. Ferrand. "SPIRE BSM Hardware and software integration process." In *Optical, Infrared and Millimeter Space Telescopes* (edited by J. C. Mather), **5487**:513–522. Proceedings of the International Society for Optical Engineering (2004).

[89] I. Pain, *et al.* "The SPIRE Beam Steering Mirror: a cryogenic 2 axis mechanism for the Herschel Space Observatory." In *IR Space Telescopes and Instruments* (edited by J. C. Mather), **4850**. Proceedings of the International Society for Optical Engineering (2003).

[90] P. A. R. Ade, P. Hamilton, and D. A. Naylor. "An Absolute Dual Beam Emission Spectrometer." In *Fourier Transform Spectroscopy: New Methods and Applications*, pp. 90–92. Optical Society of America: Santa Barbara, CA (1999).

[91] D. A. Naylor, *et al.* "Mach-Zehnder Fourier Transform Spectrometer for astronomical spectroscopy at submillimter wavelengths." In *Millimeter and Submillimeter Detectors for Astronomy* (edited by T. G. Phillips and J. Zmuidzinas), **4855**:540–51. Proceedings of the International Society for Optical Engineering (2003).

[92] D. K. Lambert and P. L. Richards. "Martin-Puplett interferometer: an analysis." *Applied Optics*, **17**(10):1595–1602 (1978).

[93] D. H. Martin and E. Puplett. "Polarised interferometric spectrometry for the millimetre and submillimetre spectrum." *Infrared Physics*, **10**:105–109 (1970).

[94] J. Bock, G. Lilienthal, and B. Swinyard. "Herschel SPIRE Detector Subsystem Specification Document." Technical Report SPIRE-JPL-PRJ-000456, Jet Propulsion Laboratory, Pasadena, CA (2003).

[95] A. Eflving and I. Rasmussen. "Herschel pointing accuracy and calibration procedures." Technical Report SCI-PT-19552, European Space and Technology Centre, Noordwijk, the Netherlands (2003).

[96] J. Fischer, *et al.* "Cryogenic far-infrared laser absorptivity measurements of the Herschel Space Observatory telescope mirror coatings." *Applied Optics*, **43**(19):3765–3771 (2004).

[97] E. Sein, *et al.* "A Φ 3.5 M SiC telescope for HERSHEL Mission." In *IR Space Telescopes and Instruments* (edited by J. C. Mather), **4850**:606–618. Proceedings of the International Society for Optical Engineering (2003).

[98] P. C. Hargrave. Astronomy Instrumentation Group, Cardiff University, Cardiff, Wales. *Personal Communication* (2005).

[99] P. C. Hargrave, *et al.* "In-Flight Calibration Sources for Herschel-SPIRE." In *IR Space Telescopes and Instruments* (edited by J. C. Mather), **4850**:638–649. Proceedings of the International Society for Optical Engineering (2003).

[100] P. Hargrave and M. Griffin. "Spectrometer Calibrator Subsystem Design Description." Technical Report SPIRE-QMW-PRJ-001104, Cardiff University, Cardiff, Wales (2001).

[101] J. E. Chamberlain. *The Principles of Interferometric Spectroscopy*. John Wiley and Sons: Chichester, England (1979). Edited by G. W. Chantry and N. W. B. Stone.

[102] "Cernox RTD thermistors." Product information from Lakeshore Corporation, Westerville, OH. Web address: *http://www.lakeshore.com/temp/sen/crtd.html*.

[103] K. J. Åström and T. Hägglund. "The future of PID control." *Control Engineering Practice*, **9**(11):1163–1175 (2001).

[104] C. Lee, P. A. R. Ade, and C. V. Haynes. "Self supporting filters for compact focal plane designs." In *Submillimetre and Far-Infrared Space Instrumentation*, **SP-388**:81–83. Proceedings of the 30th ESLAB Symposium: Noordwijk, The Netherlands (1996).

[105] R. Ulrich, K. F. Renk, and L. Genzel. "Tunable Sumillimeter interferometers of the Fabry-Perot type." *IEEE Transactions on Microwave Theory and Techniques*, **11**(5):363–371 (1963).

[106] T. Fulton. "SPIRE Detector Response and Glitch Characterization." Technical Report SPIRE-UOL-REP-002207, University of Lethbridge, Lethbridge, AB (2005).

[107] D. Pouliquen. "Herschel-SPIRE Spectrometer mirror mechanism design description." Technical Report LAM-PJT-SPI-NOT-200008, Laboratoire d'Astrophysique de Marseille, Marseille, France (2001).

[108] "Exposed linear encoders." Product information from Heidenhain Corporation, Schaumburg, IL. Web address: *http://www.heidenhain.com/Products/ExposedLinear/lip.htm*.

[109] D. A. Naylor, *et al.* "Data processing pipeline for a time-sampled imaging Fourier transform spectrometer." In *Imaging Spectrometry X* (edited by S. S. Shen and P. E. Lewis), **5546**:61–72. Proceedings of the International Society for Optical Engineering (2004).

[110] P. Hargrave and C. Tucker. "End Item Data Package: SPIRE 300mK Spectrometer filters - PFM." Technical Report HSO-CDF-EIDP-055, Cardiff University, Cardiff, Wales (2004).

[111] M. J. Griffin, J. J. Bock, and W. K. Gear. "Relative performance of filled and feedhorn-coupled focal-plane architecture." *Applied Optics*, **41**(31):6543–6554 (2002).

[112] T. Lim. Space Science and Technology Division, Rutherford Appleton Laboratory, Oxfordshire, England. *Personal Communication* (2004).

[113] G. Chattopadhyay, *et al.* "Feedhorn Coupled Bolometer Arrays for SPIRE: Design, Simulation, and Measurements." *IEEE Transactions on Microwave Theory and Techniques*, **51**(10):2139–2146 (2003).

[114] B. Rownd, *et al.* "Design and performance of feedhorn-coupled bolometer arrays for SPIRE." In *Millimeter and Submillimeter Detectors for Astronomy* (edited by T. G. Phillips and J. Zmuidzinas), **4855**:510–519. Proceedings of the International Society for Optical Engineering (2003).

[115] D. A. Harper, *et al.* "Heat trap: an optimized far infrared field optics system." *Applied Optics*, **15**(1):53–60 (1976).

[116] J. A. Murphy. "Aperture Efficiencies of Large Axisymmetric Reflector Antennas Fed by Conical Horns." *IEEE Transactions on Antennas and Propagation*, **36**(4):570–575 (1988).

[117] J. A. Murphy and R. Padwan. "Radiation patterns of few-moded horns and condensing lightpipes." *Infrared Physics*, **31**(5):291–299 (1991).

[118] K. Rohlfs. *Tools of Radio Astronomy*. Astronomy & Astrophysics Library. Springer-Verlag: Berlin, Germany (1986).

[119] J. Glenn. Center for Astrophysics and Space Astronomy, University of Colorado, Boulder, CO. *Personal Communication* (2005).

[120] R. A. Waldron. *The Theory of Waveguides and Cavities*. Maclaren & Sons Ltd: London, England (1967).

[121] J. C. G. Lesurf. *Millimetre-wave Optics, Devices and Systems*. IOP Publishing Ltd: Bristol, England (1990).

[122] N. Marcuvitz. *Waveguide Handbook*. IEE Electromagnetic Waves Series 21. Peter Peregrins Ltd: London, England (1986).

[123] J. L. Doane. "Propagation and mode coupling in corrugated and smooth-walled circular waveguides." In *Infrared and Millimeter Waves, Volume 13: Millimeter Components and Techniques, Part IV* (edited by K. J. Button), pp. 123–170. Academic Press: Orlando, FL (1985).

[124] F. R. Arams. *Infrared-to-millimeter wavelength detectors*. Artech House: Norwood, MA (1973).

[125] P. Davis, T. Fulton, and D. Naylor. "Band edges of the SPIRE PFM1 spectrometer." Technical Report SPIRE-UOL-REP-002420, University of Lethbridge, Lethbridge, AB (2005).

[126] J. Glenn, *et al.* "Numerical optimization of integrating cavities for diffraction-limited millimeter-wave bolometer arrays." *Applied Optics*, **41**(1):136–142 (2002).

[127] A. D. Turner, *et al.* "Silicon nitride micromesh bolometer array for submillimeter astrophysics." *Applied Optics*, **40**(28):4921–31 (2001).

[128] M. Griffin, *et al.* "SPIRE - a bolometer instrument for FIRST." In *Advanced Technology MMW, Radio, and Terahertz Telescopes* (edited by T. G. Phillips), **3357**:404–415. Proceedings of the International Society for Optical Engineering (1998).

[129] P. L. Richards. "Bolometers for infrared and millimeter waves." *Journal of Applied Physics*, **76**(1):1–24 (1994).

[130] W. Holland, W. Duncan, and M. Griffin. "Bolometers for Submillimeter and Millimeter Astronomy." In *Single-Dish Radio Astronomy: Techniques and Applications* (edited by S. Stanimirović, *et al.*), **278**:463–491. ASP Conference Series (2002).

[131] R. V. Sudiwala, M. J. Griffin, and A. L. Woodcraft. "Thermal modelling and characterisation of semiconductor bolometers." *International Journal of Infrared and Millimeter Waves*, **23**(4):545–573 (2002).

[132] H. T. Nguyen, *et al.* "A Report on Laboratory Performance of the Spectroscopic Detector Arrays for SPIRE/HSO." In *Millimeter and Submillimeter Detectors for Astronomy II* (edited by J. Zmuidzinas, W. S. Holland, and S. Withington), **5498**:196–207. Proceedings of the International Society for Optical Engineering (2004).

[133] D. Naylor, T. Fulton, and P. Davis. "Phase study of SPIRE PFM1 Spectrometer Data." Technical Report SPIRE-UOL-REP-002421, University of Lethbridge, Lethbridge, AB (2005).

[134] E. L. Dereniak and D. G. Crowe. *Optical Radiation Detectors*. John Wiley and Sons: New York, NY (1984).

[135] F. Pinsard. "Herschel/SPIRE Detector Control Unit Design document." Technical Report SPIRE-SAP-PRJ-001243, Commissariat à l'Energie Atomique Service d'Astrophysique, Saclay, France (2005).

[136] "Interactive Data Language." Product information from Research Systems Inc., Boulder, CO. Web address: *http://www.rsinc.com/idl*.

[137] N. Dale, C. Weens, and M. Headington. *Programming and Problem Solving with C++*. 2nd edition. Jones and Bartlett Publishers: Sudbury, MA (2000).

[138] P. Léna. *Observational Astrophysics*. Springer-Verlag: Berlin, Germany (1988). Translated by A. R. King (originally published as "Astrophysique: Méthodes physique de l'observation" in 1986).

[139] B. Swinyard and M. Griffin. "Operating Modes for the SPIRE Instrument." Technical Report SPIRE-RAL-PRJ-000320, Rutherford Appleton Laboratory, Oxfordshire, England (2003).

[140] B. Swinyard. "Implications of reduced SMEC scan speed range." Technical Report SPIRE-RAL-NOT-001543, Rutherford Appleton Laboratory, Oxfordshire, England (2003).

[141] "CDR Herschel Micro-Vibration Analysis Report." Technical Report H-P-2-ASP-AN-0773, Systems Mechanical Analyses team, Alcatel Space (2004).

[142] J.-P. Baluteau. Laboratoire d'Astrophysique de Marseille, Marseille, France. *Personal Communication* (2005).

[143] W. H. Press, *et al. Numerical Recipes: The Art of Scientific Computing*. Cambridge University Press: Cambridge, England (1986).

[144] S. K. Park and K. W. Miller. "Random number generators: Good ones are hard to find." *Communications of the Association for Computing Machinery*, **31**(10):1192–1201 (1988).

[145] G. E. P. Box and M. E. Muller. "A Note on the Generation of Random Normal Deviates." *Annals of Mathematical Statistics*, **29**(2):610–611 (1958).

[146] P. Hargrave. "Spectrometer Calibrator Flight Model & Flight Space Interface Control Document." Technical Report SPIRE-UCF-PRJ-001149, Cardiff University, Cardiff, Wales (2004).

[147] M. J. Eccles, M. E. Sim, and K. P. Tritton. *Low light level detectors in astronomy*. Cambridge University Press: Cambridge, England (1983).

[148] J. C. G. Lesurf. *Information and Measurement*. 2nd edition. CRC Press: Boca Baton, FL (2001).

[149] R. N. Bracewell. "The Fourier Transform." *Scientific American*, **260**(6):86–95 (1989).

[150] R. J. Hanisch, *et al.* "Definition of the Flexible Image Transport System (FITS)." *Astronomy and Astrophysics*, **376**(1):359–380 (2001).

[151] P. A. Collins, *et al.* "A Ground Calibration Facility for HERSCHEL-SPIRE." In *IR Space Telescopes and Instruments* (edited by J. C. Mather), **4850**:628–637. Proceedings of the International Society for Optical Engineering (2003).

[152] P. Hargrave. "SPIRE AIV Cryogenic Black Body Source and Filter Stack." Technical Report HSO-CDF-EIDP-069, Cardiff University, Cardiff, Wales (2003).

[153] A. Rebolledo, P. Davis, and T. Fulton. "SPIRE Fourier Transform - User Guide." Technical Report SPIRE-UOL-DOC-002495, University of Lethbridge, Lethbridge, AB (2005).

[154] "Java Technology." Product information from Sun Microsystems, Santa Clara, CA. Web address: *http://java.sun.com/*.

[155] "FIR series Optically Pumped Far Infrared Lasers." Product information from Edinburgh Instruments, Livingston, Scotland. Web address: *http://www.edinst.com/fir.htm*.

[156] M. Inguscio, *et al.* "A review of frequency measurements of optically pumped lasers from 0.1 to 8 THz." *Journal of Applied Physics*, **60**(12):R161–R192 (1986).

[157] A. Li and B. T. Draine. "Infrared emission from interstellar dust. II. The diffuse interstellar medium." *The Astrophysical Journal*, **554**(2):778–802 (2001).

[158] J. Lindner. "Dusty galaxies: modelling spectral energy distributions." *Canadian Undergraduate Physics Journal*, **2**(2):7–12 (2003).

[159] P. F. Goldsmith, E. A. Bergin, and D. C. Lis. "Carbon monoxide and dust column densities: the dust-to-gas ratio and structure of three giant molecular cloud cores." *The Astrophysical Journal*, **491**:615–637 (1997).

[160] F. Motte, P. André, and R. Neri. "The initial conditions of star formation in the ρ Ophiuchi main cloud: wide-field millimeter continuum mapping." *Astronomy and Astrophysics*, **336**:150–172 (1998).

[161] M. A. Gordon. "Dust emission as a quantitative probe of star-forming regions." *Astronomy and Astrophysics*, **301**:853–864 (1995).

[162] J. Glenn and T. R. Hunter. "A comparison of tracers of cool gas in galaxies and the $^{12}CO/^{13}CO$ luminosity ratio in luminous infrared galaxies." *The Astrophysical Journal Supplement Series*, **135**(2):177–182 (2001).

[163] R. H. Hildebrand. "The Determination of Cloud Masses and Dust Characteristics from Submillimetre Thermal Emission." *Quarterley Journal of the Royal Astronomical Society*, **24**:267–282 (1983).

[164] J. P. Bernard, *et al.* "PRONAOS observations of MCLD 123.5+24.9: cold dust in the Polaris cirrus cloud." *Astronomy and Astrophysics*, **347**:640–649 (1999).

[165] E. Serabyn and E. W. Weisstein. "Fourier transform spectroscopy of the Orion Molecular Cloud Core." *The Astrophysical Journal*, **451**:238–251 (1995).

[166] R. Chini, *et al.* "Dust filaments and star formation in OMC-2 and OMC-3." *The Astrophysical Journal*, **474**:L135–L138 (1997).

[167] D. Johnstone, A. M. S. Boonman, and E. F. van Dishoeck. "Astrochemistry of sub-millimeter sources in Orion." *Astronomy and Astrophysics*, **412**:157–174 (2003).

[168] T. D. Varberg and K. M. Evenson. "Accurate far-infrared rotational frequencies of carbon monoxide." *The Astrophysical Journal*, **385**:763–765 (1992).

[169] P. F. Bernath. *Spectra of Atoms and Molecules*. 2nd edition. Oxford University Press: Oxford, England (2005).

[170] D. M. Watson, *et al.* "Detection of CO $J = 21 \rightarrow 20$ (124.2 μm) and $J = 22 \rightarrow 21$ (118.6 μm) emission from the Orion Nebula." *The Astrophysical Journal*, **239**:L129–L132 (1980).

[171] S. E. Cummins, R. A. Linke, and P. Thaddeus. "A Survey of the Millimeter-Wave Spectrum of Sagittarius B2." *The Astrophysical Journal Supplement Series*, **60**:819–878 (1986).

[172] R. P. Feynman, R. B. Leighton, and M. Sands. *The Feynman Lectures on Physics*. Addison-Wesley: Reading, MA (1963).

[173] R. Phillips. *Radiative Transfer Modelling of Star Formation Regions*. PhD thesis, University of Kent at Canterbury, Canterbury, England (1999).

[174] G. A. Blake, *et al.* "Molecular abundances in OMC-1 - The chemical composition of interstellar molecular clouds and the influence of massive star formation." *The Astrophysical Journal*, **315**:621–645 (1987).

[175] B. E. Turner. "A molecular line survey of Sagittarius B2 and Orion-KL from 70 to 115 GHz. II - Analysis of the data." *The Astrophysical Journal Supplement Series*, **76**:617–686 (1991).

[176] L. S. Rothman, *et al.* "The HITRAN 2004 Molecular Spectroscopic Database." *Journal of Quantitative Spectroscopy and Radiative Transfer*, **96**(2):139–204 (2005).

[177] H. M. Pickett, *et al.* "Submillimeter, millimeter, and microwave spectral line catalog." *Journal of Quantitative Spectroscopy and Radiative Transfer*, **60**(5):883–890 (1998).

[178] N. Jacquinet-Husson, *et al.* "The 2003 edition of the GEISA/IASI spectroscopic database." *Journal of Quantitative Spectroscopy and Radiative Transfer*, **95**(4):429–467 (2005).

[179] M. Harwit. *Astrophysical Concepts*. 2nd edition. Springer-Verlag: New York, NY (1988).

[180] R. C. Hilborn. "Einstein coefficients, cross sections, f values, dipole moments, and all that." *American Journal of Physics*, **50**(11):982–986 (1982).

[181] M. Šimečková, *et al.* "Einstein A-coefficients and statistical weights for molecular absorption transitions in the HITRAN database." *Journal of Quantitative Spectroscopy and Radiative Transfer*, **98**(1):130–155 (2006).

[182] T. Onaka and T. Nakagawa. "SPICA: A 3.5 m space infrared telescope for mid- and far-infrared astronomy." *Advances in Space Research*, **36**(6):1123–1127 (2005).

[183] P. J. Mohr and B. N. Taylor. "CODATA recommended values of the fundamental physical constants: 2002." *Reviews of Modern Physics*, **77**(1):1–107 (2005).

[184] "Le Système international d'unités (SI)." 7th edition, Bureau International des Poids et Mesures, Sèvres Cedex, France (1998). Web address: *http://www.bipm.org/utils/en/pdf/si-brochure.pdf*.

[185] B. N. Taylor. "Guide for the Use of the International System of Units (SI)." NIST Special Publication 811, National Institute of Standards and Technology, Gaithersburg, MD (1995). Web address: *http://physics.nist.gov/cuu/pdf/sp811.pdf*.

[186] D. S. Liepman. "Mathematical constants." In *Handbook of Mathematical Functions with Formulas, Graphs, and Mathematical Tables* (edited by M. Abramowitz and I. A. Stegun), pp. 1–4. Dover Publications: New York, NY (1965).

[187] I. S. Glass. *Handbook of Infrared Astronomy*. Cambridge Observing Handbooks for Research Astronomers. Cambridge University Press: Cambridge, England (1999).

[188] C. H. Edwards and D. E. Penney. *Calculus with analytic geometry and early transcendentals*. 5th edition. Prentice Hall: Upper Saddle River, NJ (1997).

[189] D. Freedman, *et al.* *Statistics*. 2nd edition. W. W. Norton and Company: New York, NY (1991).

[190] L. S. Rothman, *et al.* "The HITRAN Molecular Spectroscopic Database and HAWKS (HITRAN Atmospheric Workstation): 1996 Edition." *Journal of Quantitative Spectroscopy and Radiative Transfer*, **60**(5):665–710 (1998).

[191] J. B. Tatum. "The interpretation of intensities in diatomic molecular spectra." *The Astrophysical Journal Supplement Series*, **14**:21–56 (1967).

[192] L. S. Rothman. Atomic and Molecular Physics Division, Harvard-Smithsonian Center for Astrophysics, Cambridge, MA. *Personal Communication* (2005).

[193] M. D. Harmony. *Introduction of Molecular Energies and Spectra*. Holt, Rinehart & Winston: New York, NY (1972).

[194] R. R. Gamache and L. S. Rothman. "Extension of the HITRAN database to non-LTE applications." *Journal of Quantitative Spectroscopy and Radiative Transfer*, **48**(5-6):519–525 (1992).

[195] J. J. Sakurai. *Modern Quantum Mechanics*. 2nd edition. Pearson Education: Delhi, India (1994).

[196] E. U. Condon and G. H. Shortley. *The Theory of Atomic Spectra*. 2nd edition. Cambridge University Press: Cambridge, England (1963).

[197] W. Gordy and R. L. Cook. *Microwave Molecular Spectroscopy*. 3rd edition. John Wiley & Sons: New York, NY (1984).

[198] G. Herzberg. *Molecular Spectra and Molecular Structure: I. Spectra of Diatomic Molecules*. 2nd edition. D. Van Nostrand Company: Princeton, NJ (1950).

[199] H. W. Kroto. *Molecular Rotation Spectra*. 2nd edition. Dover Publications: New York, NY (1992).

[200] C. H. Townes and A. L. Schawlow. *Microwave Spectroscopy*. McGraw-Hill Book Company: New York, NY (1955).

[201] L. S. Rothman, *et al.* "The HITRAN molecular spectroscopic database: edition of 2000 including updates through 2001." *Journal of Quantitative Spectroscopy and Radiative Transfer*, **82**(1-4):5–44 (2003).

[202] S. S. Penner. *Quantitative Molecular Spectroscopy and Gas Emissivities*. Addison-Wesley: Reading, MA (1959).